## Title
Reduction of radiation dose to radiosensitive organs and its tradeoff with image quality in Computed Tomography



## Author
Zhang, Di

## Publication Date
2012

Peer reviewed|Thesis/dissertation

UNIVERSITY OF CALIFORNIA

Los Angeles

# Reduction of radiation dose to radiosensitive organs and its tradeoff with image quality in Computed Tomography

A dissertation submitted in partial satisfaction of the

requirements for the degree Doctor of Philosophy

in Biomedical Physics

by

Di Zhang

2012

ABSTRACT OF THE DISSERTATION

Reduction of radiation dose to radiosensitive organs and its tradeoff with image quality in Computed Tomography

By

Di Zhang

Doctor of Philosophy in Biomedical Physics

University of California, Los Angeles, 2012

Professor Michael McNitt-Gray, Chair

Computed Tomography (CT) has been used for medical diagnosis for the past four decades and has made significant contributions to patient healthcare by providing fast and accurate diagnostic information. Besides the extraordinary medical benefits it has brought to society, it delivers radiation dose to the patients, which can be potentially hazardous. Therefore, it has been a significant interest in both scientific research and clinical practice to reduce radiation dose to the patients during CT scans, while still maintaining the diagnostic performance, so that the information provided through this procedure is not compromised and appropriate medical determinations can be made at the minimum cost.

In this research work, a Monte Carlo based simulation package was used to estimate radiation dose to individual radiosensitive organs of patients with a range of body habitus. This package is exam and protocol specific, and it takes into account technical details of CT scanners such as spectra, bowtie filtration, and beam geometry. Modifications were made to the Monte Carlo simulation package to perform detailed radiation dose assessments for both patients and phantoms. These include the estimate of radiation dose to individual organs, the peak radiation dose to a wide spread tissue (such as peak skin dose), and surface dose distribution in a complex CT irradiation environment. Meanwhile, the effect of a variety of traditional dose reduction methods, such as tilting the gantry in brain perfusion scans, was also investigated.

In addition to the traditional dose reduction techniques that are already being utilized in the clinic, an innovative method to reduce organ dose while maintaining image quality was investigated. The distribution of radiation dose within the scan volume was demonstrated to be dependent on the Tube Start Angle (TSA). A change of TSA can cause a shift of dose distribution along the longitudinal axis. This results in variations in the measurement of surface dose during helical scans. This dose variation along the longitudinal direction for patients in CT imaging inspired a novel innovation to reduce organ dose while maintaining image quality by adjusting the TSA and table height in CT exams. Monte Carlo simulations were performed to demonstrate the effectiveness of this method for different patients under various scenarios, including conventional fixed tube current CT scans, and tube current modulated (TCM) scans. Besides the dose benefit this new method brings, its effect on image quality was investigated and demonstrated that there was no significant compromise on the image quality.

Despite the efforts to reduce radiation dose while maintaining image quality, the ultimate tradeoff in the goal of maximizing the benefit to risk ratio in CT examinations is the tradeoff between radiation dose and *diagnostic outcome*. As radiation dose is decreased, the image quality may be degraded. However, the diagnostic outcome does not necessarily have to be compromised. In other words, the image quality used for specific CT clinical tasks today may have room to be degraded and still be able to maintain accuracy of diagnostic outcomes. In order to investigate this tradeoff between radiation dose and diagnostic outcome for a specific clinical task (appendicitis was selected in this dissertation), a preliminary observer study was conducted to determine the difference of diagnostic performance at various dose levels. Images at reduced radiation dose levels were simulated by adding noise to the projection data using a calibrated method. These methods were employed for a group of patients with right lower quadrant pain who were scanned because of a suspected appendicitis. The results of Receiver Operation Characteristic (ROC) analysis suggested that there was no significant difference between radiation dose levels of 100%, 70% and 50%. Detailed analysis of patient organ (liver) dose demonstrated that the diagnostic performance is nearly perfect when the liver dose is higher than 10mGy. The interrelationship between a simple image quality metric (noise), organ dose, and patient size was also investigated.

In summary, this work assessed dose reduction tools available today that do not affect image quality, proposed a new method to reduce organ dose while maintaining image quality, and evaluated the method to reduce radiation dose, which affects image quality but could

maintain diagnostic outcome by investigating the tradeoff between radiation dose and diagnostic outcome, as well as their correlation with image quality metrics (noise).

The dissertation of Di Zhang is approved.

Christopher Cagnon

John DeMarco

Matthew Brown

Jianwei Miao

Michael McNitt-Gray, Committee Chair

University of California, Los Angeles

2012

I dedicate this dissertation to my wife Wei Sha, my son Oscar Zhang, my father Xingui Zhang and my mother Lan Chen.

It’s been a fortune for me to have this journey with you.

**Table of Contents**

**Acknowledgments**

First and foremost I would like to thank Dr. Michael McNitt-Gray for everything in the past five years. Throughout my graduate studies at UCLA, Mike has always been tremendously supportive and encouraging. I joined Mike's group on day one of my UCLA career. Therefore I have been actively involved in research activities from my first year at UCLA. Mike's creative and critical approach to scientific problems deeply inspired me and helped me to grow to a scientist. Mike was not only my academic advisor; he also gave me endless guidance and support on my career, my family, my understanding of American culture, and life in general. His vision, breadth of mind, and kindness influenced me in many ways and they will benefit me throughout the future days of my life.

I am also extremely grateful for the advices and effort devoted to this work from my committee members. I was very fortunate to be able to work closely with my other two mentors and friends during the past five years: Dr. John DeMarco and Dr. Chris Cagnon. I deeply appreciate John's previous work which established the foundation of all the Monte Carlo studies. Without John's dedication and wisdom, our research group would not have gotten to this point. I enjoyed all the radiation therapy sessions with John at Medical Plaza 200. John's solid knowledge background, rigorous attitude and unique sense of humor set an example for being a perfect scientist, which I will strive to achieve. I'm very grateful for Chris' willingness to dive in the data for a thorough discussion whenever necessary and his skills to provide insightful suggestions and advices from a clinical perspective. His passion and eloquence were very impressive and he always has an interesting point on every topic I could name. He has a unique sense of optimism which is infectious. I enjoyed every refreshing conversation we had, both about science and about culture. I would like to thank Dr. Matt Brown for supervising my research work and for providing extremely helpful solutions for the implementation of my

research projects. Matt initialed the QIWS (Quantitative Imaging Working Station) platform and it has been an incredible beneficial tool for all of our research activities. He is a combination of a great scientist with sharp visions a great business man with extraordinary business development skills. I am grateful for his guidance and advices. I would like to express my appreciation to Dr. Jianwei Miao for sitting in my committee and his endurance to support my research work despite his unfamiliarity to the field of medical imaging. His insightful questions during my first oral examination helped me to enhance my study design for this dissertation.

I would like to take this opportunity to express my most sincere gratitude to Dr. Matilda Jude, Dr. Edward Zaragoza, Dr. Grace Kim, Dr. Margaret Lee, Dr. Maitraya Patel, Dr. Denise Andrews-Tang, Dr. Laura Doepke, Dr. Michael Douek, and Dr. Cheryce Poon for their generous support on my main dissertation research project. Matilda has devoted tremendous amount of efforts to this project, from the initial discussion about the idea, to the study design, data collection, and data analysis. Without her expertise as a radiologist, I could not have completed this project. Matilda has the most beautiful smile and I always enjoyed chatting with her. Ed provided a lot of valuable advices in the study design. I appreciate his contribution and involvement in this project given his very busy schedule. Grace is a great scientist in statistics. She had such an important role in every single process of this project and the offered irreplaceable help. I want to thank Grace for her rigorous insight, which always pushed me towards the next level in order to make a better interpretation of the data.

I would also like to thank all of the professors and students in the Biomedical Physics (BMP) program and the MedQIA research group for their accompanying and support. Specifically, I appreciate Dr. Jonathan Goldin's critiques of my research work, which pushed me to approach my study in a more comprehensive fashion. I want to Richie Pais and Bharath Ramakrishna for their kind helps relating to QIWS. Specifically, I would like to thank David

Qing, a part time MedQIA employer, for helping me setting up the experiment for my project on QIWS. I enjoyed the friendship with all the BMP students and all the fun activities we had together. I would like to thank Terry Moore and Reth Thach for all the assistance as I progressed in the BMP program toward the doctoral degree.

I owe a big thank to my lab mates and friends who has been with me for the past years. First, I thank Dr. Erin Angel not only for being extremely helpful to get me up to speed in my first two years in the group, but also for providing tremendous guides and suggestions in finding my first industrial job. As a colleague in the company I currently work in, she helped me in numerous ways to get me started in another new environment. I also want to express my sincere gratitude to Maryam Khatonabadi for carrying out the observer studies for my dissertation while I was having a summer internship out of town, and for all the warm support on other research projects as well as life in general. Finally, I am very grateful for my partner Dr. Adam Turner's accompanying during graduate study. We stepped and advanced side by side in our graduate career and had a lot of victories. His work laid the ground for a lot of the methods I used. Without his extraordinary contribution to the research field, I would not have achieved half of the work I've done today.

Life is a journey, with highs and lows. I was fortunate to have my family by my side in this journey. I am grateful for all the unselfish love from my father Xingui Zhang, my mother Lan Chen, my father in law Defang Sha and my mother in law Zhenhua Wang. I would like to particularly thank those individuals who showed support during the difficult times in my life. I owe the biggest thank you to my wife Wei Sha. I would like to thank her for having faith on us no matter under what circumstances. It has been an amazing ride with Wei in the past 10 years. With the new member Oscar Zhang who will join the family very soon, I am eagerly looking forward to the new chapter in our lives.

I would like to acknowledge the following grants and fellowships for funding portions of this work:

- UCLA Dissertation Year Fellowship (2011-2012)
- UCLA Affiliates Scholarship (2010-2012)
- UCLA Dr. Ursula Mandel Scholarship (2010-2011)
- National Institute of Biomedical Imaging and Bioengineering - R01 EB004898 (2007-2010)

The following are chapter-specific acknowledgments:

- Chapter 4 is based on the research published in the journal *American Journal of Roentgenology* and presented at the Radiological Society of North America (RSNA) Annual Meeting in Chicago, IL in December 2010:

  Zhang D, Cagnon CH, Villablanca PJ, Cody DD, Stevens DM, Zankl M, DeMarco JJ, McCollough CH, Turner AC, Khatonabadi M, and McNitt-Gray MF, "Peak skin and eye lens radiation dose from brain perfusion CT based on Monte Carlo simulations," AJR. **198**, 412-417, 2012.

  Zhang D, Cagnon CH, DeMarco JJ, Turner AC, Khatonabadi M, McNitt-Gray MF, "Estimating Radiation Dose to Eye Lens and Skin from CT Brain Perfusion Examinations: A Monte Carlo Study". Radiological Society of North America annual meeting, November, 2010

- Chapter 5 is partially based on research presented at the Radiological Society of North America (RSNA) Annual Meeting in Chicago, IL in December, 2010:

  Zhang D, Zankl M, McNitt-Gray, MF. "How Do CTDI and TG111 Small Chamber Dose Perform in Estimating Radiation Dose to Eye Lens and Skin from CT Brain Perfusion Examinations for Patients with Various Sizes: A Monte Carlo Study". Radiological Society of North America annual meeting, December, 2010.

- Chapter 6 is based on the research published in the journal *Medical Physics.* This work was awarded the 2009 Norm Baily Award from the Southern California Chapter of the American Association of Physicists in Medicine (AAPM):

  Zhang D, Savandi AS, Demarco JJ, Cagnon CH, Angel E, Turner AC, Cody DD, Stevens DM, Primak AN, McCollough CH, McNitt-Gray MF. "Variability of surface and center position radiation dose in MDCT: Monte Carlo simulations using CTDI and anthropomorphic phantoms", Medical Physics, 36(3):1025-38, 2009.

- Chapter 7 is based on the research published in the journal *Medical Physics* and presented at the American Association of Physicists in Medicine (AAPM) Annual Meeting in Anaheim, CA, in July 2009:

  Zhang D, Zankl M, DeMarco JJ, Cagnon CH, Angel E, Turner AC, McNitt-Gray MF. "Reducing radiation dose to selected organs by selecting the tube start angle in MDCT helical scans: a Monte Carlo based study", Medical Physics, 36(12), 5654-64, 2009.

  Zhang D, DeMarco JJ, Cagnon CH, Angel E, Turner AC, Zankl M, McNitt-Gray MF. "Reducing Dose to a Small Organ by Varying the Tube Start Angle in a Helical CT Scan". American Association of Physics in Medicine annual meeting, July, 2009.

- Chapter 8 is partially based on the research presented at The First International Meeting on Image Formation in X-Ray Computed Tomography in Salt Lake City, UT in June 2009:

  Zhang D, Cagnon CH, DeMarco JJ, Turner AC, McNitt-Gray MF. "Novel strategies to reduce patient organ dose in CT without reducing tube output". The First International Meeting on Image Formation in X-Ray Computed Tomography, June 09, 2010.

- Chapter 9 is partially based on the research presented at European Congress of Radiology Annual Meeting in Vienna, Austria in March, 2012:

  Zhang D, Khatonabadi M, Kim H, Jude M, Zaragoza E, Lee M, Patel M, Poon C, Douek M, Andrews-Tang D, Doepke L, McNitt-Gray S, Cagnon CH, DeMarco JJ, McNitt-Gray MF. "The effect of patient organ dose reduction on diagnostic accuracy of a CT clinical task". European Congress of Radiology annual conference, Vienna, March, 2012.

  Zhang D, Khatonabadi M, Kim H, Jude M, Zaragoza E, Lee M, Patel M, Poon C, Douek M, Andrews-Tang D, Doepke L, McNitt-Gray S, Cagnon CH, DeMarco JJ, McNitt-Gray MF. "The effect of CT dose reduction on performance of a diagnostic task". European Congress of Radiology annual conference, Vienna, March, 2012.

VITA

| | |
|---|---|
| 2004 | B.S., Engineering Physics<br>Tsinghua University<br>Beijing, China |
| 2006 | M.S., Engineering Physics<br>Tsinghua University<br>Beijing, China |
| 2006-07 | Graduate Student Researcher<br>Rensselaer Polytechnic Institute<br>Troy, New York, USA |
| 2007-11 | Graduate Student Researcher<br>University of California, Los Angeles<br>Los Angeles, California, USA |
| 2009 | Norm Baily Award<br>Southern California Chapter of the AAPM<br>Los Angeles, California, USA |
| 2009 | M.S., Biomedical Physics<br>University of California, Los Angeles<br>Los Angeles, California, USA |
| 2010-11 | Dr. Ursula Mandel Scholarship<br>University of California, Los Angeles<br>Los Angeles, California, USA |
| 2011-12 | UCLA Dissertation Year Fellowship<br>University of California, Los Angeles<br>Los Angeles, California, USA |
| 2011 | Sylvia Sorkin Greenfield Award<br>UCLA Biomedical Physics Interdepartmental Graduate Program<br>Los Angeles, California, USA |

SELECTED PUBLICATIONS

Zhang D, Cagnon CH, Villablanca PJ, Cody DD, Donna MS, Zankl M, DeMarco JJ, McCollough CH, Turner AC, Khatonabadi M, McNitt-Gray MF. “Peak Skin and Eye Lens Dose from Neuro-Perfusion CT Examinations Based On Monte Carlo Simulations”. AJR, 198(2), 412-7, 2012.

Turner AC, Zhang D, Khatonabadi M, Zankl M, DeMarco JJ, Cagnon CH, Cody DD, Stevens DM, McCollough CH, McNitt-Gray MF. "The feasibility of patient size-corrected, scanner-independent organ dose estimates for abdominal CT exams". Medical Physics, 38(2), 820-9, 2011.

Mathieu KB, McNitt-Gray MF, Zhang D, Kim HJ, Cody DD. “Precision of dosimetry-related measurements obtained on current multidetector computed tomography scanners”. Medical Physics, 37(8), 4102-09. 2010.

Turner AC, Zankl M, DeMarco JJ, Cagnon CH, Zhang D, Angel E, Cody DD, Stevens DM, McCollough CH, McNitt-Gray MF. "The feasibility of a scanner-independent technique to estimate organ dose from MDCT scans: Using CTDIvol to account for differences between scanners". Medical Physics, 37(4), 1816-25, 2010.

Chawla SC, Federman N, Zhang D, Nagata KT, Nuthakki S, Angel E, McNitt-Gray MF, Boechat MI. “Estimated cumulative radiation dose from PET/CT in Pediatric Patients with Malignancies - A five year retrospective review”. Pediatric Radiology, 2010 May;40(5):681-6

Zhang D, Zankl M, DeMarco JJ, Cagnon CH, Angel E, Turner AC, McNitt-Gray MF. “Reducing radiation dose to selected organs by selecting the tube start angle in MDCT helical scans: a Monte Carlo based study”, Medical Physics, 36(12), 5654-64, 2009

Turner AC, Zhang D, Kim HJ, DeMarco JJ, Cagnon CH, Angel E, Cody DD, Stevens DM, Primak AN, McCollough CH, McNitt-Gray MF. “A method to generate equivalent energy spectra and filtration models based on measurement for multidetector CT Monte Carlo dosimetry simulations”, Medical Physics, 36(6), 2154-64, 2009.

Zhang D, Savandi AS, Demarco JJ, Cagnon CH, Angel E, Turner AC, Cody DD, Stevens DM, Primak AN, McCollough CH, McNitt-Gray MF. “Variability of surface and center position radiation dose in MDCT: Monte Carlo simulations using CTDI and anthropomorphic phantoms”,Medical Physics, 36(3):1025-38, 2009

Ding A, Zhang D, Xu XG. “Training software using virtual-reality technology and pre-calculated effective dose data”, Health Physics, 96(5):594-601, 2009.

## Chapter 1 Background and Motivation

Since x-ray was discovered by Roentgen at 1895, it has been used for medical imaging to understand patient anatomy without surgical procedures. The x-ray photons are attenuated differently by various tissues and structures within human body, therefore generating a contrast on the image reflecting anatomy, which can be used for medical diagnosis. Conventional radiography which uses a plain film reduces the 3D anatomy of the patient into a 2D projection image. Therefore, the information with respect to the dimensional parallel to the x-ray beam is lost. The introduction of CT in the 1970s, however, overcame this limitation. A CT scanner acquires projection images from 360 degrees and post-processes the projection data using reconstruction algorithms to form cross-section images. So the superposition of structures in-plane is eliminated in CT. In other words, CT was able to yield images with each representing a single slice of the body (tomography). This revolutionary advance in medical imaging has added another dimension of information for medical images and has contributed tremendous value to diagnostic value that can be obtained using x-ray. In addition, the inherent high-contrast resolution in CT has made it feasible to distinguish tissues with very small density difference, which added to its power to identify anatomical abnormalities.

Over more than 30 years of advances in technologies, including x-ray generation, filtration design, detector, firmware, and post-processing, CT has developed into a medical imaging modality with the capability of obtaining excellent resolution for both high contrast and low contrast tasks, as well as the capability to perform volumetric imaging by the implementation of multi-row detectors (MDCT). It has been a major diagnostic tool and has been

impacting patient healthcare throughout the entire world. Today CT is routinely used as a key component in Radiology and Oncology departments for many areas of medical applications. To name a few, within Radiology department, it is used in head scans to detect infarction, hemorrhage, or trauma; it is used in thoracic scans for detecting both acute and chronic changes in the lung parenchyma; it is used in Cardiology to diagnose cardiovascular diseases; it is used in abdomen or pelvic scans to determine the stage of cancer and to follow progress; it is also used in extremity scans to image complex fractures, especially one around joints because of its ultra-high spatial resolution. Within Oncology department, CT is used to obtain attenuation properties for body tissues in order to perform necessary calculations of radiation dose distribution in treatment planning.

CT scanners use x-ray tubes to generation photons. In this process, electrons are emitted from cathode via thermionic emission and are accelerated within the tube towards anode driven by the potential difference between the cathode and the anode. The highly energetic electrons then interact with matter (usually tungsten) and convert their kinetic energy into heat and electromagnetic radiation (photons) through the process of bremsstrahlung. Figure 1 shows the physical look of the anode. The fluence of photons depends on kVp and mAs. kVp is defined as the peak tube potential between the cathode and the anode. It determines the highest energy of photons within the beam. mAs is the multiplication of tube current (the rate of the charge of electrons from the cathode to the anode) and exposure time. mAs is proportional to the fluence of the x-ray beam.

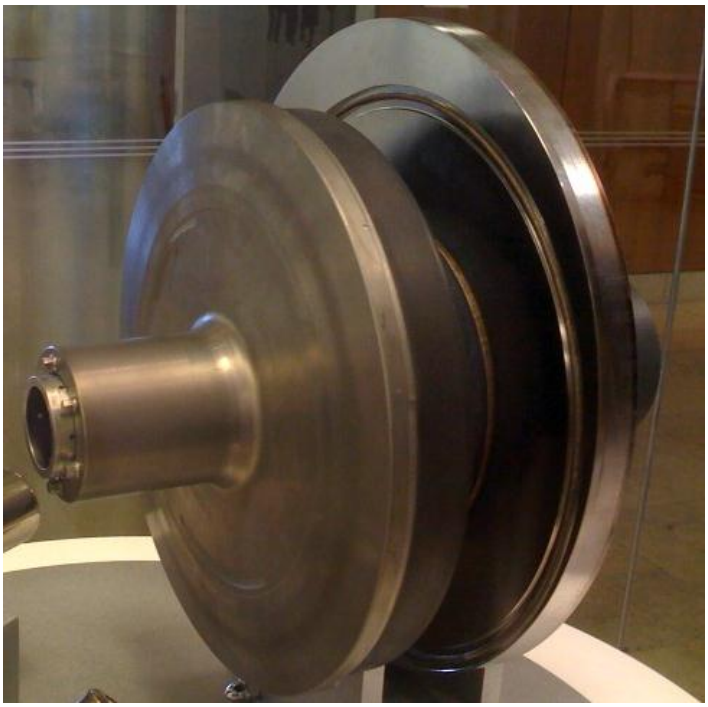

**Figure 1.1 Example image of an anode.**

During the CT scan a patient lies on the table while the x-ray tube and the detector ring spin in the gantry in a very fast speed (as fast as 0.27s/rotation for certain manufacturer). Fan shaped beams are used in modern CT scanners as shown in figure 2. There are two different scan modes with respect to the pattern of the movement of the bed: axial scan and helical scan. In axial scan, the bed moves incrementally after every rotation so the anatomy is captured section by section; in helical scan, the bed moves continuously while the tube and detector are rotating. Under helical scan mode, pitch is defined as the advance of the table in a rotation divided by the nominal collimation width in z direction. Helical scan was introduced in 1990s and it has dramatically increased the time efficiency of CT scans.

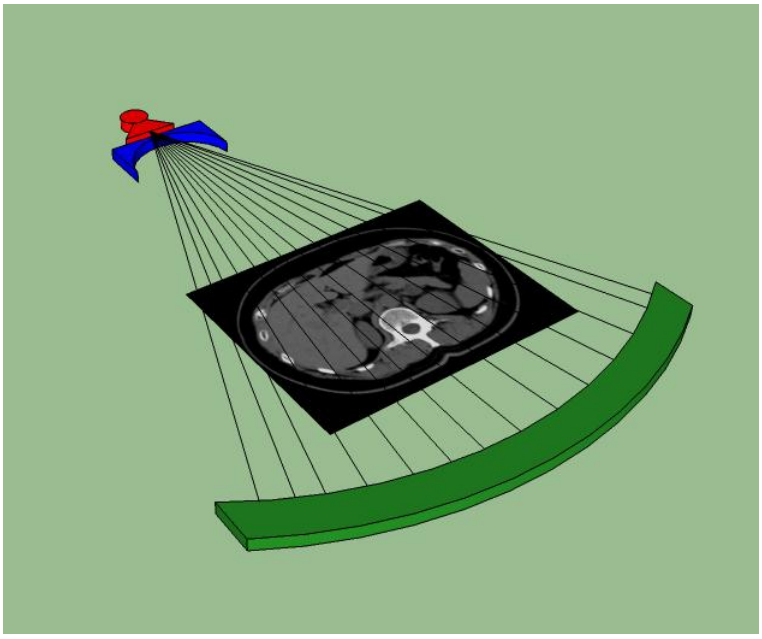

**Figure 1.2 Fan beam geometry of modern CT scanners.**

## 1.1 Concerns about risks from radiation in CT exams

As a medical imaging modality using ionizing radiation, CT inevitably delivers radiation dose to patients. By interacting with human tissues (mostly water) through photoelectric effect or Compton scatter, the photons cause potential damage to tissues by either direct effect or indirect effect. Direct effect refers to photons' interaction with the atoms of the DNA molecule or other cellular component critical to the survival of the cell. Indirect effect refers to the damage to the cell by ionized molecules generated from the interaction of photons and water molecule. Since in CT the mAs is usually much higher than that was used in radiography (and therefore more photons are penetrating the patient), the increase of radiation dose is not trivial. Absorbed dose with the unit of Gray is used as the physical metric to quantify radiation dose, which is defined as the energy deposited (in the unit of Joule) per unit mass (in the unit of kilogram). Absorbed

dose to each individual radiosensitive organ is a meaningful quantity to estimate organ specific risks[1-4].

The number of CT scans in United States has increase from 18.3 million in 1993 to 62.0 million in 2006, with an estimated annual growth rate of 10%[5,6]. Especially since the introduction of MDCT in mid 1990s, the use of CT has increased dramatically due to its improved capacity. In clinical practice, CT exams consists 15% of the total number of radiological imaging procedures, but it contributes to 50% of the population radiation exposure from medical procedures, and it contributes to 25% of the population radiation exposure from all sources, including background radiation. This has lead to concerns about the potential risks of radiation hazards to patients.

There are two kinds of effects that may be introduced to patients exposed to radiation: deterministic effect and stochastic effect. Deterministic effect has a threshold of radiation dose, above which certain acute damage will happen after the exposure, and the severity is dependent on radiation dose. This type of effect includes cataract, erythema (skin reddening), infertility, and so on. The threshold for deterministic effect varies depending on different damage and type of tissue cells, but the lowest is around 1Gy, such as epilation (loss of hairs). In most of the cases, the radiation dose a patient receives from CT scan is well below this magnitude, but for certain type of protocols, such as CT perfusion studies, the dose can be close, or even beyond this threshold. This will be discussed in further detail in Chapter 4 and 5. Figure 1.3 shows some examples of patients suffering from epilation, one of the deterministic effects of radiation, after

CT brain perfusion examinations. Other scenarios where deterministic effect may happen are accidents in CT exams caused by operational errors[7]. Figure 1.4 shows an example of a pediatric patient suffering from erythema due to operational errors.

**Figure 1.3 Some examples of patients suffering from epilation after brain perfusion CT examinations (from New York Times magazine).**

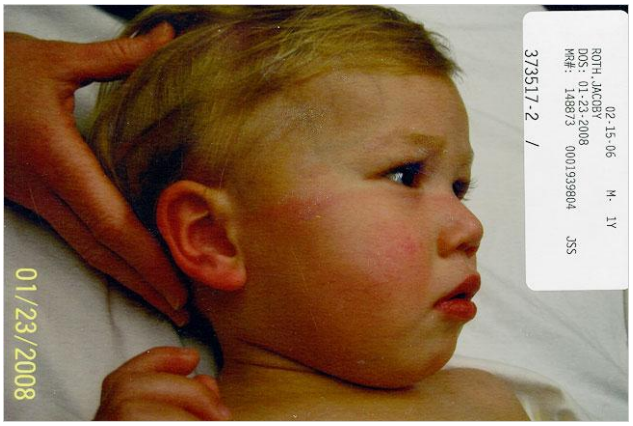


**Figure 1.4 An example of a pediatric patient suffering from erythema due to operational errors[8].**

Stochastic effects, on the other hand, do not have a threshold. The probability of its occurrence depends on absorbed dose. However, the severity is independent of dose. This effect is caused by the damage to DNA, which affects the integrity of genetic information. Although most of the cells that have DNA damage will either fix themselves or take an action to a programmed death (apoptosis), some mutations can remain and proliferate to other cells. These mutations can potentially cause the development of cancer over a long period of time (up to tens of years), which is the process of carcinogenesis. The concern for carcinogenesis is a big concern particularly for pediatric patients, since the pediatric patients are more radio-sensitive to radiation[9-11], and they have a longer life spam to develop cancer. The radiation dose from most of the CT exams falls into the range of stochastic effect. However, there is not a single perfect risk model of carcinogenesis for radiation dose at this range, since it requires intensive epidemiological studies which tracks radiation dose to a very large number of individuals and monitor their conditions over years in order to yield meaningful results. The risk model that is currently used is based on the data from nuclear bomb survivors from Japan. The radiation dose

to the majority of these patients is in general higher than the dose delivered by CT exams (<100 mGy), so the risk estimates were extrapolated assuming Linear No Threshold model (LNT). The most widely used and arguably most comprehensive risk models that take these data into account are the published report VII of The Biological Effects of Ionizing Radiations (BEIR VII)[2], based on which age and gender specific risks can be assessed based on radiation dose to individual organs. Using the data in BEIR VII report, Berrington et al. concluded that 29,000 future cancers could be related to CT scans performed in the U.S. in 2007[12].

The concerns over the potential risks from CT exams naturally led to the question: should the risk be taken into account during clinical practice when a physician is ordering a CT exam? Despite the controversy of this topic, it is a fact that the fast and accurate diagnostic capability that CT provides offers extremely valueable information for a physician to make appropriate medical determinations. CT has benefited patients and has saved a lot of lives under a variety of clinical circumstances, for example, to determine if an immediate surgery is needed for a patient with lower quadrant abdominal pain (suspected appendicitis). Furthermore, BEIR VII report itself comes with multiple approximations and assumptions about the Lifetime Attributable Risk (LAR), and the risk estimates have huge error bars[2]. In fact, the report itself admitted that 'because of the various sources of uncertainty it is important to regard specific estimates of LAR with a healthy skepticism' at page 278. Using the risk estimates from BEIR VII report, O'Connor et al showed in their study that 863,000 annual deaths would be expected from background radiation for residence in Colorado[13].

Nonetheless, it is imperative to maximize the benefit to risk ratio for every CT exam. Several campaigns have been carried out to promote delivering just enough dose to the patients for necessary diagnostic information, such as Image Gently and Image Wisely[14,15]. Meanwhile, several government entities, or organizations have initiated stricter regulations against the excessive or unnecessary use of radiation exposure, including FDA and Joint Commission[16,17]. The state of California has passed a law regarding the recording and reporting of radiation dose from CT, commencing July 1st, 2012[18].

### 1.2 Estimating radiation dose from CT

A variety of methods and metrics are being used to estimate radiation dose from CT, including standardized phantom measurements, small dosimeter measurements, and Monte Carlo method based simulation estimates. Standardized phantom measurements are the current metric that is routinely used today to quantify radiation output from CT scanners. However, this metric only still represent radiation dose to phantoms. Small dosimeter measurements were often used to estimate patient dose. However, small dosimeters are limited by the factor that it could not be placed inside patient body. On the other hand, Monte Carlo method based simulations are capable of estimating radiation dose to individual patient organs or even dose distribution within patient models. This method provides dose information in a much more detailed level.

#### 1.2.1. Standardized phantom measurements

The metric to quantify radiation dose from CT is the Computed Tomography Dose Index (CTDI), which is a measure of the amount of radiation delivered from a series of contiguous

axial scans in two cylindrical homogenous standardized polymethyl methacrylate (PMMA) phantoms with different sizes. One of them is16 cm diameter which represents head or pediatric body, while the other one is 32 cm diameter representing adult body (shown in Fig. 1.5). CTDI is routinely used in clinic and is also widely used in academic research. This metric is practically measured with the use of a 100 mm long pencil ion chamber with a single axial scan performed at the center of the phantom[19]. It is calculated using the following equation[20]:

$$CTDI = \frac{f \times C \times E \times L}{NT} \qquad \text{Eq. 1.1}$$

, where f represents the conversion coefficient from exposure to air kerma (8.7mGy/R); and C is the calibration factor for the electrometer (usually it's a value very close to 1); E represents the measured value of exposure in the unit of Roentgens; L is the active length of the ionization chamber (100 mm); NT represents the nominal beam width, where N is the number of detector rows, and T is the width of each detector row in z direction. The factor of L/NT in this equation is used to compensate the fact that the 100 mm long ion chamber is partially irradiated by the x-ray beam. Although there is only one single axial scan in conventional CTDI measurements, it can be proven that this exposure is mathematically equivalent to the average dose in the center slice of a series of several contiguous scans[1,20,21].

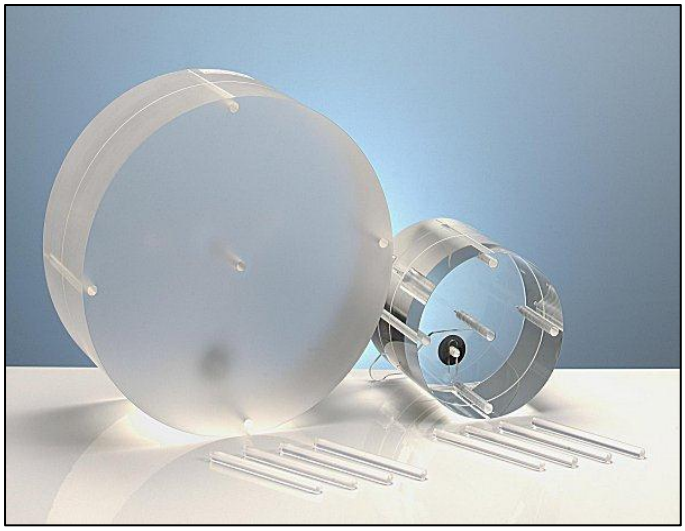

**Figure 1.5 16 cm diameter "head" and 32 cm diameter "body" CTDI phantoms composed of PMMA and containing pre-drilled holes at center and four periphery positions.**

Since the x-ray photons are attenuated differently on different locations within the CTDI phantoms, in order to take the spatial variation of dose distribution within the phantoms into account, both CTDI phantoms were designed to have 5 holes (1 central, 4 peripheral) where either PMMA rods or the ion chamber can be inserted. Therefore $CTDI_{center}$ and $CTDI_{periphery}$ can be obtained by switching the locations of the rods and the ion chamber. Figure 1.6 shows some typical values for $CTDI_{center}$ and $CTDI_{periphery}$ for both 32 cm and 16 cm phantom to illustrate the in-plane in-homogeneity. The weighted CTDI ($CTDI_w$) represents an averaged dose to the whole phantom and was defined as:

$$CTDI_W = {}^1\!/_3\, CTDI_{center} + {}^2\!/_3\, CTDI_{periphery} \qquad \text{Eq. 1.2}$$

In order to account for the non-contiguity in helical CT scans, the volume CTDI ($CTDI_{vol}$) was proposed and was defined as:

$$CTDI_{vol} = \frac{CTDI_W}{pitch} \quad \text{Eq. 1.3}$$

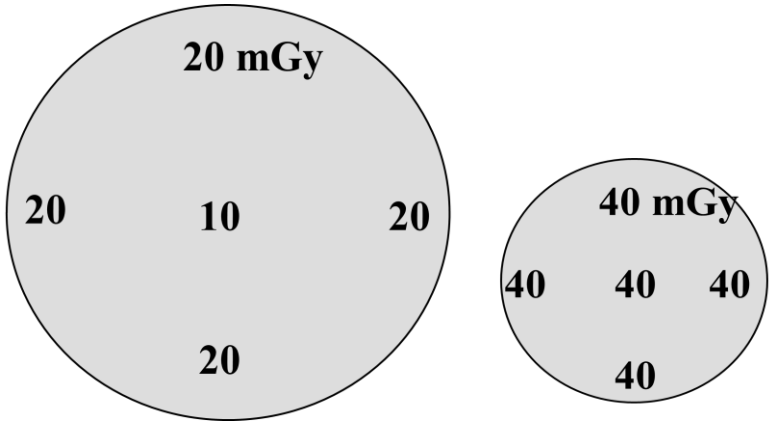


**Figure 1.6 The spatial variation of radiation dose within both (a) 32 cm and (b) 16 cm phantoms. Reprinted from M.F. McNitt-Gray[20].**

Finally, in order to account for the scan length, Dose Length Product (DLP) was proposed and was defined as:

$$DLP = CTDI_{vol} \times scan\ length \quad \text{Eq. 1.4}$$

CTDI metric has been a robust CT dose metric until recent years when newer generation CT scanners are equipped with wider and wider beam width. When the beam width in z axis is wide enough that the 100 mm long ion chamber could not include the majority of the scatter tails in phantoms (shown in Fig 1.7), the mathematical equivalency between the dose under a single axial scan at the phantom center and the dose at the center slice of a series of contiguous scans is not valid anymore[22-24]. For example, the widest beam width from diagnostic scanners currently on the market is 160 mm (Toshiba Aquilion ONE), which is already wider than the 100 mm long

ion chamber without the scatter tails. In order to address this issue, the American Association of Physicists in Medicine (AAPM) Task Group 111 has proposed a new CT dose metric under a new paradigm[25]. This paradigm is being tested and validated by AAPM Task Group 200. According to this new paradigm, a small volume ion chamber is used when the prescribed scan (even it is a helical scan) is performed on a phantom. However, in practice, there is significant variation for the distribution of radiation dose along the longitudinal direction. This causes large uncertainties when the small volume ion chamber is placed at peripheral positions of the phantom for dose estimation. This is a current challenge faced by the new TG111 CT dose metric. This challenge will be thoroughly investigated in Chapter 6. In addition, several methods to overcome this limitation will be presented and analyzed in Chapter 6.

Another limitation of CTDI is that it is defined to be equal to the average dose in the center slice of a series of several contiguous scans. Therefore it works for both contiguous axial scans and helical scans, which covers the majority of clinical CT scan protocols. However, for scenarios where there is no table motion, CTDI overestimate radiation dose since it assumes scatters from adjacent scans which do not exist in this case. For example, for the estimation of radiation dose from CT brain perfusion scans, CTDIvol overestimates the skin dose that actually delivered to the patients. This will be demonstrated and discussed in further detail in Chapter 4 and Chapter 5.

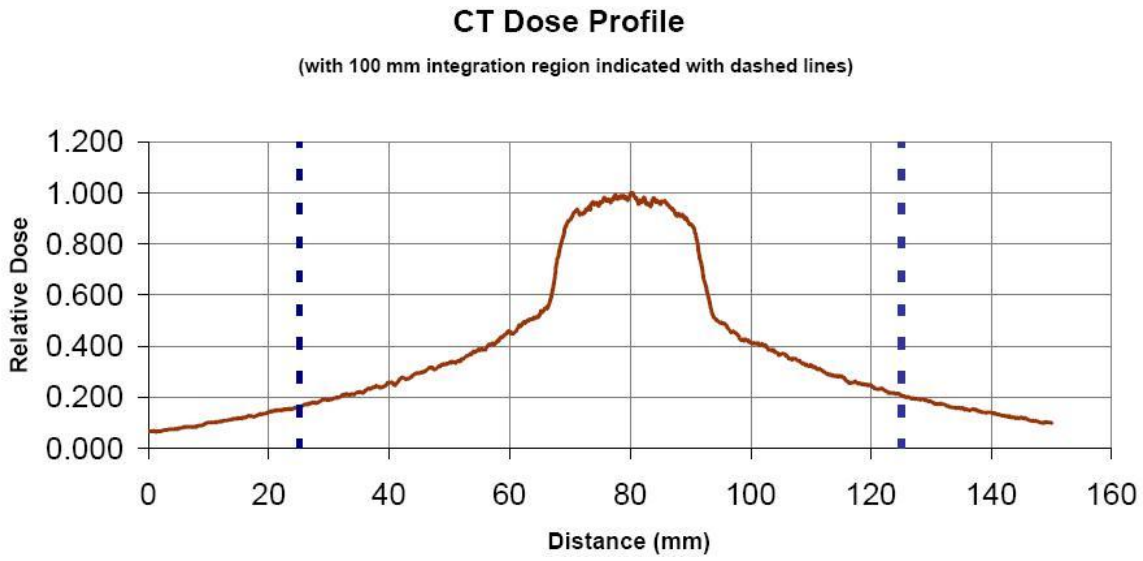


**Figure 1.7 The beam profile in the center of phantom along z axis. It is shown that the 100mm ion chamber could not capture the entire scatter tails on both side.**

### 1.2.2. Small dosimeter measurements

Although $CTDI_{vol}$ is routinely reported on scanner consoles in clinical practice, it is not patient dose[26]. CTDI is a good metric to quantify the output radiation of the CT scanners by taking lots of technical factors into account, including spectra, bowtie filtration, and so on. However, since the standard size homogeneous CTDI phantoms cannot assimilate heterogeneous patient population with a variety of different size, CTDI does not represent radiation dose that patients receive from CT exams. Direct measurements of dose using small dosimeters on either anthropomorphic phantoms[27-34] or patients take patient geometry and materials into account. These dosimeters used in this method include small ionization chambers, Thermoluminescence Detectors (TLD), Metal Oxide-Silicon Semiconductor Field Effect Transistor (MOSFET) detectors, and Optically Stimulated Luminescence (OSL) detectors.

There are several limitations for the direct measurements using small dosimeters. First, for measurements on patients, it is impossible to place the small chambers inside a patient's body for organ dose estimation. For measurements on phantoms, the anthropomorphic phantoms usually consist of only several materials and sometimes even less. The anatomical and composition heterogeneity is far less complex than that of real patients. Second, most of these dosimeters (with the exception of ion chamber) have strong energy dependency[35-37]. Therefore the measured result is not perfectly reliable across different energy regions, such as between 80 kVp and 140 kVp. As a matter of fact, it is even not perfectly reliable between different locations in the same phantom, such as between peripheral and center of the phantom, because the energy spectra are slightly different at these two locations due to beam hardening effect. Third, the uncertainty of tube start angle could cause large error bars during repeated scans for measurements using small dosimeter. This is also mentioned in 1.2.1 and will be discussed in further detail in Chapter 6.

### 1.2.3. Effective Dose

Effective dose (ED) was introduced as a health physics concept by the International Commission on Radiation Protection (ICRP) to account for the various radiosensitivities of the tissues that absorb energy from radiation[9,11]. This quantity is defined as an estimate of the whole-body radiation dose that would result in an equivalent stochastic risk as the partial-body imaging procedure, and is mathematically defined as a weighted average of the dose to several radiosensitive tissues ($D_T$):

$$ED = \sum_T (\omega_T \times \omega_R \times D_T) \quad \text{Eq. 1.5}$$

where $\omega_T$ is a tissue-specific radiosensitivity factor whose value is specified by the ICRP based on epidemiological studies and $\omega_R$ is a radiation weighting factor that account for the relative biological damage imparted from the energy deposition of different types of particles. The tissue weights, $\omega_T$, were developed based on a detriment model by taking into account life lost, lethality and loss of quality of life for a composite population. It is averaged between males and females as well as across ages. The radiation weighting factor, $\omega_R$, for x-ray photons is equal to 1. Effective dose is measured in units denoted Sieverts (Sv). Although effective dose is a viable tool to assess occupational radiation dose, or radiation dose to a population, organ dose is a more descriptive metric for individual CT dosimetry, since it takes into account the patient specific information, such as size and age. In addition, organ dose allows the need to take into account the partial irradiation in CT scans.

### 1.2.4. Monte Carlo method based estimates

Monte Carlo method based simulations are considered to be a much more accurate approach to estimate the radiation transport and therefore the organ dose from CT. It takes into account spectra, filtration, scanner geometry, beam shape, patient anatomy and composition, as well as all the other delicate details of the characteristics about the transport of photons. Several research groups have developed methodologies to estimate radiation dose from CT using Monte Carlo methods[38-44]. While most of the groups use well established Monte Carlo code for the simulations of particle transport, some group have tried to write their own Monte Carlo code[38].

Besides the simulation of the transport, the accuracy of Monte Carlo method based simulations is also limited by the inputs to the code, including the CT source model and the patient model.

For the CT source model, depending on the availability of the technical factors of the CT scanners, which are usually proprietary, different levels of approximations are used by different research groups. For example, Gu et al. used 12 fixed sources along 360 degrees to approximate a full circle of continuous irradiation[40]. For patient models, there are models with different levels of complexities ranging from hermaphroditic mathematical phantoms consisted of simple geometric shapes (such as MIRD phantoms show in Fig. 1.8a) to fully voxelized patients with a variety of body habitus and physical size (such as GSF family phantoms shown in Fig. 1.8b and RPI pregnant female phantoms shown in Fig. 1.8c). A widely used Monte Carlo CT dose package ImPACT CT Patient Dosimetry Calculator was approximated from single row detector geometries and contiguous axial scans (not direct simulation on the helical path of the CT source) using MIRD phantom[45]. A UCLA Monte Carlo CT Dose Simulation Package which uses more reliable source and patient models will be discussed in detail in Chapter 3.

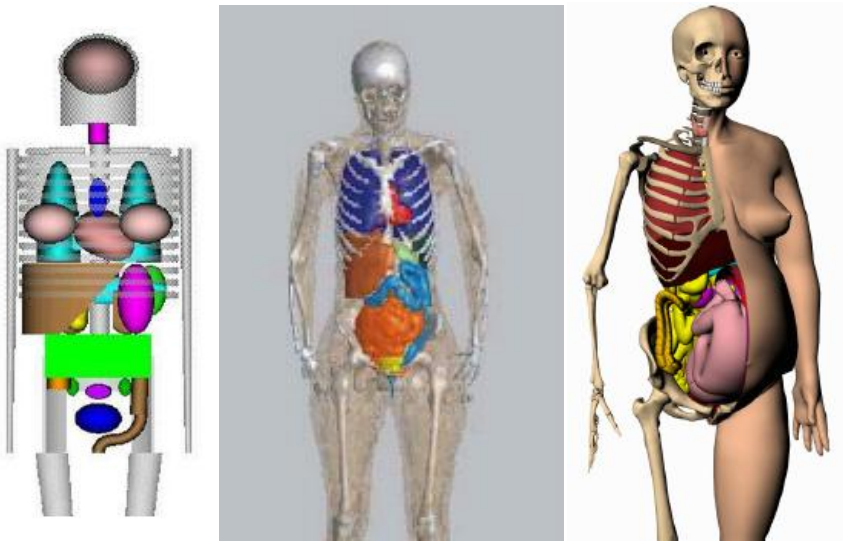

**a)** **b)** **c)**

**Figure 1.8 a) MIRD mathematical phantom; b) Irene from GSF family phantom; c) RPI-9 pregnant female phantom.**

While a lot of efforts have been made to estimate patient organ dose using Monte Carlo method, organ dose is mainly used for the evaluation of stochastic effects, which relate to long term carcinogenesis. For the evaluation of deterministic effects, such as the estimation of skin dose in brain perfusion scans, the averaged dose to skin tissue is not an ideal metric because only a very small portion of skin tissue is exposed to radiation in brain perfusion CT exams. The more relevant and important metric in this case is the peak skin dose, which indicates the maximum radiation dose delivered to an area of local skin tissues. Chapter 4 and Chapter 5 will specifically investigate the peak skin dose to patients from CT perfusion exams by using a mesh tally technique which is capable of estimating radiation dose distribution within the patient anatomy.

## 1.3 Reducing radiation dose from CT

Radiation dose from CT is determined by many factors[20], including kVp, mAs, collimation, pitch, slice thicknesses, reconstruction techniques, and so on. There is a variety of different approaches to reduce radiation dose. The strategies for dose reduction are highly related to the specific patient size and body habitus. They can be divided into two different categories: dose reduction methods that do not affect image quality, and dose reduction methods that do affect image quality. The techniques in the first category include the use of tube current modulation, and the use of new computational algorithms, including noise suppressing algorithms and reconstruction algorithms[46]. The techniques in the second category include the decrease of kVp and the decrease of mAs. These dose reduction approaches should be used based on specific clinical applications and patient properties.

### 1.3.1. Techniques to reduce CT radiation dose while maintaining image quality

Tube Current Modulation (TCM) refers to the change of mAs during the rotation of the x-ray tube to take advantage of the fact that the attenuation properties of body from different projections are different. Theoretically, this technique does not impair the image quality because the projection with the most noisy signal determines the noise of the final image[47]. The results of studies using Monte Carlo simulations showed that the use of TCM generally has promising dose reduction across different size of patients[48-50]. However, for very large size patients, TCM may introduce higher doses[50].

Filter-Backprojection (FBP) algorithm is currently used by almost all commercial CT scanners. New algorithms for dose reduction purposes include spatial domain based filters, raw-data based filters, and iterative reconstruction algorithms. Spatial domain filters were suggested

to be able to maintain the same image quality for CT images at a lower dose cost for the detection of liver lesions[51]or for soft tissue interpretations[52]. Applications of raw-data based filters have also been reported for the reduction of CT dose[53]. Iterative reconstruction algorithms were also demonstrated to have the potential for improving image quality and reducing radiation dose in CT because it is able to incorporate the physical model of CT systems so various artifacts can be better corrected. It is also superior to conventional reconstruction algorithms in processing insufficient data such as reduced projections so that radiation dose can be significantly reduced[54,55].

Other methods to reduce radiation dose while maintaining image quality in specific exams include the adjustment of scan location and gantry angle in CT brain perfusion scans. The effectiveness of these easily implementable techniques will be investigated and evaluated in Chapter 4.

In addition to these techniques, a novel method to reduce organ dose while maintaining image quality by exploiting the surface dose variation from CT scans will be thoroughly investigated in Chapter 7. Furthermore, this technique can be combined with the adjustment of table height to achieve significant dose reductions in CT scans. This will be investigated in Chapter 8.

### 1.3.2. Techniques to reduce CT radiation dose that affect image quality

Lowering kVp and optimizing the energy spectra is currently an active area of research[56-61]. Specifically, these studies have shown that 80 kVp and 100 kVp can provide higher iodine

contrast to noise ratio and offer dose reduction compared to 120 kVp. While kVp is decreased, the mAs must be increased in order to compensate for the loss of photon fluence and therefore the loss of image quality. A recent study concluded that increasing the mAs by 3~4 times while changing from 120 kVp to 80 kVp could approximately deliver the same organ dose to patients[62]. Therefore in clinical practice if the increase of mAs is less than 3 times, patient organ dose is decreased.

Reduction of mAs is a direct way to reduce CT radiation dose since dose is proportional to mAs. However, any decrease in mAs should be considered with caution because it results in the increase of noise and therefore could potentially impair the diagnostic outcome. This is especially true for abdomen examinations because the low contrast resolution can be easily affected by the increase of noise[63]. Assessments of image quality using observer studies have been reported in several studies using scores regarding different aspects of image quality. Some of them suggested that it is possible to reduce tube current without markedly affecting image quality[64-69], while others concluded that reduced tube current significantly affect reader's evaluation of image quality[70,71]. While the results from these works are very informative, they are limited either by too few number of mAs levels[65,68,69], design of the experiment (using scores on the image quality instead using the outcome of specific diagnostic tasks)[68,69], or more importantly, the absence of detailed information about radiation dose. In all of these studies either mAs or CTDI was used as the metric for radiation dose, while these factors only represent the output of the tube, instead of the radiation dose to the patients. For example, a smaller patient receives higher dose than a larger patient using the same scan protocol.

In Chapter 9 of this dissertation, the feasibility of the method to reduce radiation dose that yields lower image quality, but still maintaining diagnostic performance will be investigated. The tradeoff between organ dose (risk) and diagnostic performance (benefit) in the diagnosis of a specific clinical task will be studied by conducting an observer study.

### 1.4 Discussion

CT as a medical imaging modality is beneficial to patients. On the other hand it has raised concerns about the potential risks it may introduce to patients. It is in great need to develop methods that could precisely quantify and evaluate the reduction of radiation dose from CT, so that the benefit to risk ratio from these exams can be optimized. Meanwhile, the CT dose reduction should be investigated in the context that the goal of a CT exam is to obtain diagnostic information, rather than image esthetics. Some CT dose reduction techniques do not change the quality of the images at all, while others do change the image quality, but not necessarily change the diagnostic performance. The purposes of this dissertation is to use a well validated CT dose estimation tool to evaluate the radiation dose and related dose reduction technique for brain perfusion CT exams (Chapter 4 and Chapter 5); to propose a new methodology to reduce organ dose without changing the tube output (Chapter 6 to 8); to put the CT dose reduction in the context of clinical goal and investigate how much the change of dose and image quality would affect the diagnostic performance (Chapter 9).

## Chapter 2 Specific Aims

The goal of this research is to investigate methods to reduce organ dose while maintaining image quality, as well as to explore the dose reduction methods that causes lower image quality but could maintain diagnostic outcome by investigating the tradeoffs between radiation dose and diagnostic performance for a specific clinical CT task. First, radiation dose from CT brain perfusion exams, where the concern about radiation dose has been address tremendously in public, is accurately estimated. Second, a method is proposed to reduce organ dose in CT without the change of tube output. This method should have minimal impact on image quality. Its dose benefit is studied and its implication to image quality is investigated. Third, the tradeoff of organ dose and observer performance is studied by observer perceptions for a specific task. This method has more implications on image quality but it's sought to minimize radiation dose without compromising diagnostic outcome. Meanwhile, image noise is investigated to study their correlations with observer performances. This would potentially provide the link between diagnostic outcomes and organ dose, or even risks, through the use of quantitative image quality metrics. To carry out this study, the specific aims are:

**Specific Aim 1:** To accurately estimate eye lens dose and peak skin dose from CT brain perfusion examinations and to demonstrate the overestimation of radiation dose if the CTDI from this procedure is used as patient dose.

**Specific Aim 2:** To explore dose reduction to specific radiosensitive organs without the change of tube output using existing or constructively feasible scanner capabilities, such as controlling

tube start angle and table height, as well as to investigate their effects on image quality using measurements in phantoms.

**Specific Aim 3:** To investigate the tradeoff of between diagnostic performance and organ dose using various levels of mAs, based on results from observer studies and accurate model of MDCT.

## Chapter 3 Monte Carlo MDCT Dose Simulation Package

Monte Carlo simulations were performed for all the dosimetry simulations for radiation dose estimations discussed in this dissertation.

### 3.1 Monte Carlo Method

Monte Carlo methods were developed in the 1940s for the nuclear weapon projects in the Los Alamos National Laboratory, and they were named in homage to the Monte Carlo Casino in Monaco. They are a class of computational tools that nowadays are used widely in the areas of finance, energy, transportation, environment or engineering in terms of physical and mathematical systems, especially systems with many coupled degrees of freedom with significant uncertainty in inputs, such as fluids, cellular structures, and radiation transport. These problems are usually too complicated to be solved analytically (e.g., solving equations). Therefore in contrast to a deterministic approach, Monte Carlo method based algorithms use repeated random sampling and probability statistics to investigate the problems. First, a probability distribution is established based on mathematical or physical property of the model that has inherent uncertainty. Then the result is calculated over and over again, each time using a different set of random values from the probability functions. Before the computation is finished, Monte Carlo simulation could involve a very large number of recalculations, depending on the requirement of desired accuracy. The results yield distributions of possible outcome values. The way Monte Carlo methods are applied varies widely from field to field. There are dozens of different kinds of codes or packages in each field of application. In radiation transport

simulations specifically, some of the most widely used Monte Carlo packages are GEANT4[69,72], EGS[47], and MCNP/MCNPX[73,74].

### 3.2 MCNP/MCNPX

MCNPX (Monte Carlo N-Particle eXtended) is a general-purpose Monte Carlo radiation transport code for modeling the interaction of radiation with nearly all particles at nearly all energies. It was extended from MCNP, which was designed for photon, electron and neutron particles. The applications of MCNP/MCNPX range from nuclear medicine, radiation protection, accelerator applications, homeland security to medical physics, nuclear reactor, and much more. MCNPX was written in FORTRAN codes. It supports both Linux and Windows systems, as well as parallel computations.

The users need to provide information about the source (type, size, shape, and distribution of radiation particle) and the geometry (size, shape, material composition, and density). This information will be fed into MCNPX as a text file called an input file in a specified format. MCNPX tracks each primary particle and all the subsequent secondary particles when simulating their interactions with matters within the geometry based on prior embedded knowledge regarding to the probability of interactions of the atoms (e.g., cross section), until the particle leaves the geometry model or falls below the energy threshold for tracking purpose. This process is repeated a very large number of times to yield results that are statistically meaningful. The simulation process for each particle is independent from each other. Different types of tallies (such as energy fluence or dose) can be defined in the input file, and

results are reported in an output file for each defined tally region, along with the standard deviation for estimation of relative errors.

### 3.3 UCLA CT Dose Estimation Package

Although MCNPX provides a large variety of flexibility to define the shape and type of radiation source, it does not accommodate the sophistication of a CT fan-shaped beam radiation source, neither a ring source (for axial scans), nor helical source (for helical scans). In addition, the 'moving' bowtie shaped filter cannot be defined directly in provided capabilities. Therefore, the source FORTRAN code of MCNPX (source.f) was modified to take into account of the details of the geometry of the CT sources.

Several modules were implemented in the source.f file to model all the details of the initialization of each primary particle. These include CT source model and CT scan model. As illustrated in Figure 3.1, CT source model include the photon spectra, scanner parameters such as fan angel and source to isocenter distance, and bowtie filtration. CT scan model include everything that defines the path of the source, such as scan start location, scan stop location, pitch, and nominal collimation.

The main goal of these modules is to initialize the parameters of each primary particle. These parameters include the definition of the definition of the definition of the energy of the particle, the initial location and direction of flight of the particle, as well as the definition of the bowtie filtration. More specifically, when a new photon is created, source.f assigns it an energy value. Then the photon is initiated to have its 3-D spatial position (x,y,z) and, as well as 3-D

components of a unit vector (u,v,w) pointing in the direction of the photon's trajectory. These parameters are then used by other MCNPX files to transport the photon and tally energy deposition and dose from pre-defined phantom or patient geometry. The subroutine of source.f is executed once for each primary particle, and based on defined probability functions in source.f, the initial condition for each particle is different. The phantom or patient geometry is defined within the geometry model, which is also shown in Figure 3.1. It should be noted that both CT source model and CT scan model are implemented in the source.f file, while the geometry model is implemented in the input file. The patient model includes patient geometry, tissue composition, and tissue density.

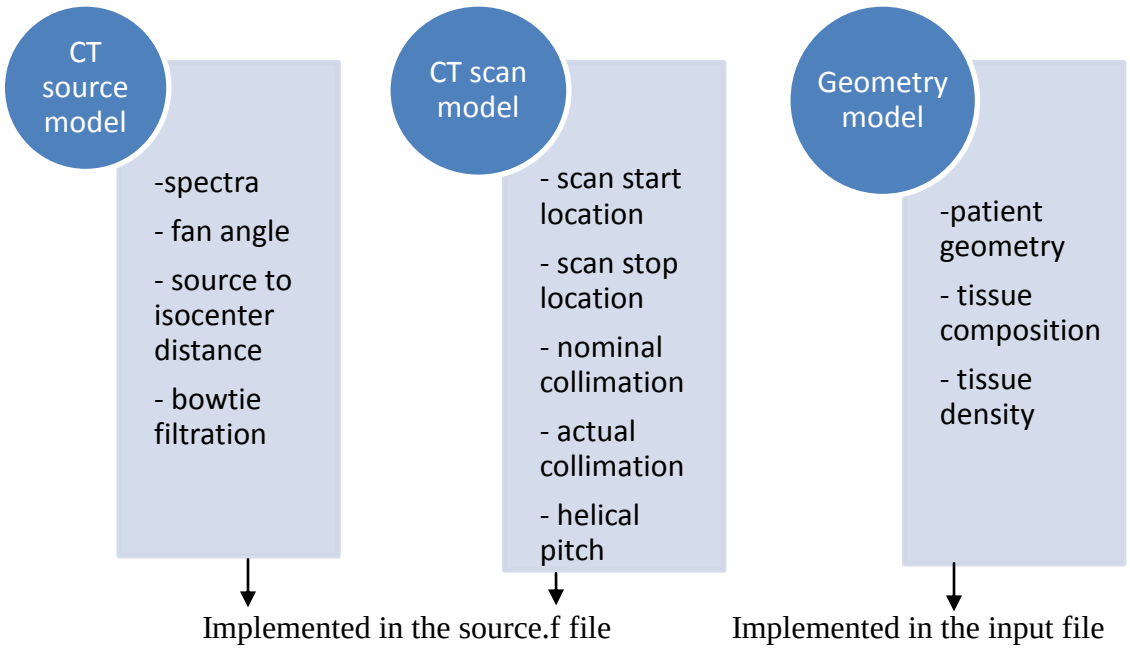


**Figure 3.1 CT source model and CT scan model in source.f of UCLA CT Dose Estimation Package.**

### 3.3.1. CT Source Modeling

The CT source model is related to the definition of the energy and filtration for each individual photon. The energy spectrum is kVp and scanner model dependent, and it was generated using equivalent source method that was published previously[75]. The energy spectrum is described by an energy probability density function (PDF). The Monte Carlo algorithm calls for sampling from the energy PDF to select a value for the current photon. Since the random number generator used in source.f (rang()) selects a value in the range of [0,1) uniformly (i.e., all decimal values have the same chance of being selected), it is necessary to use the Inverse Transform Method to properly sample the photon energy PDF. This method transforms the uniform PDF in random number space (ξ) to the energy PDF in photon energy space (E) by equating the respective PDFs:

$$p(E)\,dE = q(\xi)\,d\xi$$

Where *p(E)* and *q(ξ)* represent the probability function in energy spectra space and random number space. Given that $q(\xi) = 1$ is equal for all ξ's, thus:

$$p(E)\,dE = d\xi$$

$$\int_a^E p(E)\,dE = \int_0^\xi d\xi$$

$$\int_a^E p(E)\,dE = \xi$$

Now if a = Emin and E = Emax, then:

$$\int_{E_{\min}}^{E_{\max}} p(E)\,dE = P(E)$$

where P(E) is, by definition, the energy cumulative distribution function (CDF). Substitution from above gives:

$$P(E) = \xi$$

So:

$$E = P^{-1}(\xi)$$

If p(E), and therefore P(E), is a known continuously differentiable function, then a random photon energy can be obtained analytically using a randomly generated number from a uniform sample.

The photon energy spectra used in source.f is not a continuous function, thus a discrete form of the above Inverse Transform Method is used. This method utilizes a discrete CDF such that:

$$CDF(E) = P(E) = \sum_{i=0}^{E} p(E_i)$$

As illustrated by Figure 3.2, in source.f the discrete method works using the following algorithm:

1. Randomly generate a number, ξ, between 0 and 1
2. Find the smallest discrete index value, i, such that CDF(E) > ξ
3. Set the current photon's energy equal to the product of i and the energy interval used between each index value in the CDF (in MeV). Mathematically, this states:

$$energy\,[Mev] = i \times \frac{kVp}{number\,of\ discrete\ spectrum\,values} \times 0.001 \frac{MeV}{keV}$$

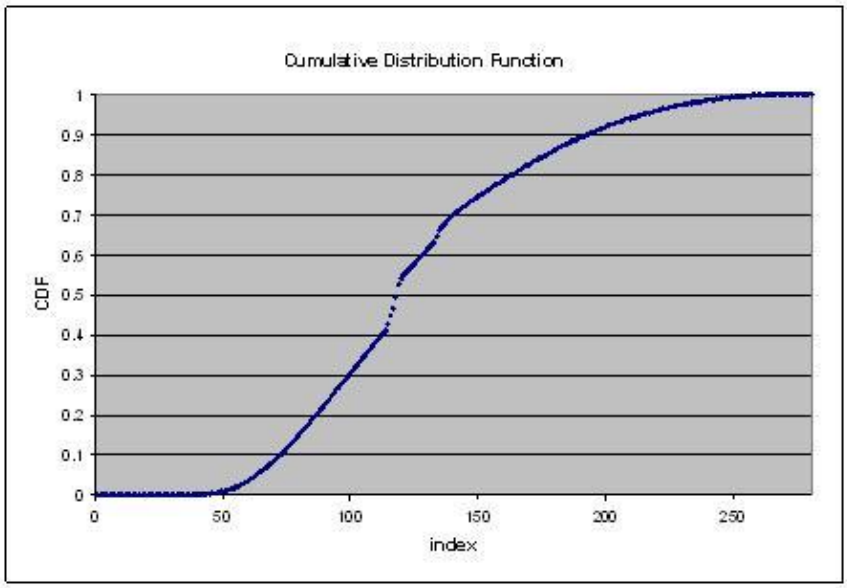


(a)

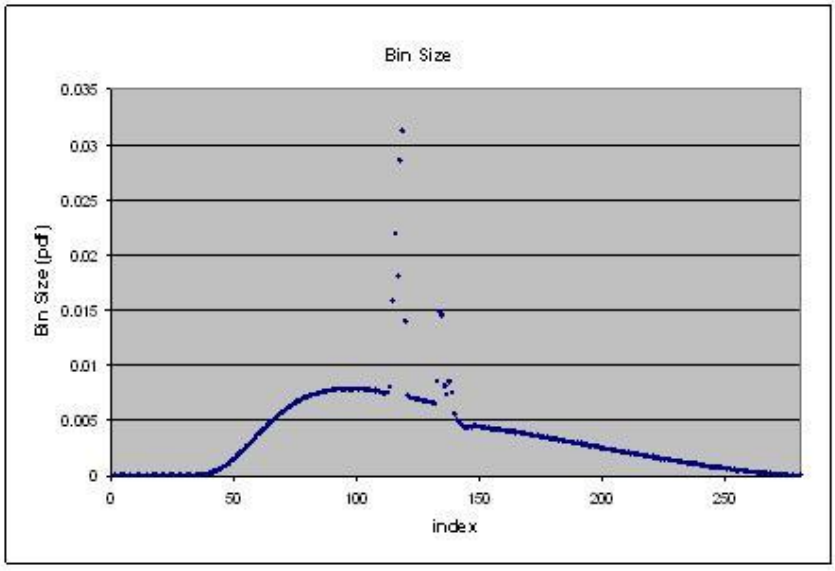


(b)

**Figure 3.2 Illustration of random sampling for initial energy of the partice. a) Cumulative Distribution function; b) Probability Density Function.**

Figure 3.2 shows that energies with higher probabilities of occurrence are randomly chosen more frequently by a uniform random number generator than energies with lower probabilities of occurrence.

After the initialization of the energy for a particle, the particle needs to go through the scanner filtration, including inherent filtration and bowtie filtration, as shown in Figure 3.3. Since the location of the source is different for each individual particle, it is impossible to explicitly model filtration in the geometry. Alternatively, the weight (wgt) feature in MCNPX was used to take the filtration into account. By defining the weight of a particle, the user can modify its contribution to the tally result. Filtration information (including both inherent filter and bowtie filter) was generated using equivalent source method[75] and was saved in text files which can be read in by MCNPX to determine the weight factor for each particle. Based on the direction of the particle, the pathlength of the particle travel through the filter can be calculated (x); with the information about the composition of the filtration material, the attenuation coefficient of the filtration (μ) could be calculated. Therefore the total attenuation factor from the filtration for each particle could be calculated assuming exponential attenuation: $e^{-\mu x}$. This factor is applied as the weigh parameter in MCNPX.

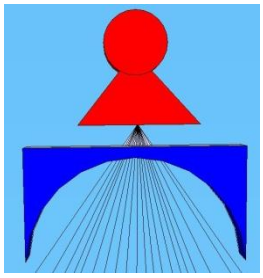

**Figure 3.3 X-ray source and bowtie filtration of a CT source.**

### 3.3.2. CT scan modeling

After the energy of the photon is specified, the initial location of the particle was uniformly sampled from a predefined path, which depends on the parameters of the CT scanner, as well as the scan protocol, including scan start and stop location, source to iso-center distance, nominal collimation, and pitch (if it's a helical scan). There are a variety of options to choose from when setting the source motion: helical scan, single axial scan, contiguous axial scan, or fixed source scan. Each of these options allows the source to exist in a set of specific positions, from which the codes in source.f randomly samples with a uniform probability. The pathways for each mode of source motion were specifically defined based on the scan parameters. Simulating a very large number of photon histories will theoretically sample the entire path.

After the energy and location is initialized, the initial direction of the particle was specified by the definition of a vector within the range of assigned trajectories. The assigned trajectories depend on the source to iso-center distance, fan angle, and actual collimation width. These parameters confine the direction of the particle to be within a rectangle at the plane perpendicular to the source to iso-center line, as shown in Figure 3.4. A point within this

rectangle is uniformly sampled in a random fashion, then the vector connecting the iso-center and the sampled point is defined as the particle's initial trajectory.

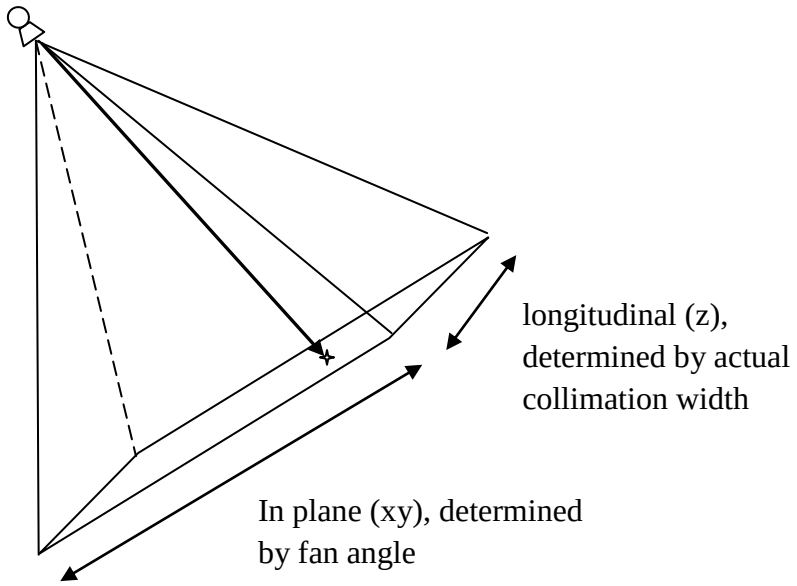


**Figure 3.4 The trajectory representing the initial direction of the emitting particle is defined by randomly sampling a point within a rectangle, which was determined by the geometry of the CT scanner.**

### 3.3.3. Geometry modeling and tallying

The geometry of the radiation transport environment is defined in the input file. Two different types of geometry could be used in MCNPX: shape based geometry and voxel based geometry. Shape based geometry uses definable geometric surfaces (such as plane, circle, cone) to construct volume units (called "cells"). Each cell's chemical composition and density need to be specified to provide its attenuation characteristics for radiation transport. An example of shape based geometry is the MIRD phantom mentioned in 1.2.3. UCLA CT Dose Simulation Package uses shape based geometry for all the CTDI simulations. Voxel based geometry is composed of a large number of voxels, with each voxel representing a small volume in the space with its

specific chemical composition and density. An example of voxel based geometry is GSF family phantom mentioned in 1.2.3. UCLA CT Dose Simulation Package uses voxel based geometry for all the patient dose estimations. The composition and density for each tissue type in patient models are from the ICRU Report 44 organ composition tables [76].

According to the needs, different types of tallies could be defined in the input file. These include fluence and/or energy fluence through a surface, total deposited energy and/or average dose within a cell (or a collection of cells for voxel based geometry), mesh tally which yields the dose distribution within a defined volume. In this dissertation, CTDI simulations were realized using average dose tally within a cell defined as active volume of the ionization chamber; organ dose simulations were implemented using average dose tally within a collection of cells which defines an individual organ; peak skin dose were implemented using the mesh tally feature.

### 3.3.4. Summary of the workflow of UCLA CT Dose Simulation Package

Figure 3.5 summarizes the workflow of UCLA CT Dose Simulation Package. The initialization of the status for each primary photon is implemented in the source.f file. First, the energy of the photon is initialized using the method described in 3.3.1 based on the spectra information. Then the location of the photon is initialized using the method described in 3.3.2 based on scan parameters such as scan mode (helical, axial, contiguous axial, or fixed source), scan start and stop location, nominal collimation, and pitch (for a helical scan). After the initialization of the photon location, the direction of flight is initialized also based on the method in 3.3.2 using parameters including source to iso-center, fan angle, and actual collimation width.

When the initialization of the photon is finished, the information of the photon, together with the information of the geometry defined in the input file, are fed into the radiation transport process controlled by all the other MCNPX Fortran files. This process is repeated for a very large number of times (defined as NPS in the input file) in order to achieve statistical significance. Finally, based on the type of tally that was defined in the input file, corresponding results can be obtained in the output files of MCNPX.

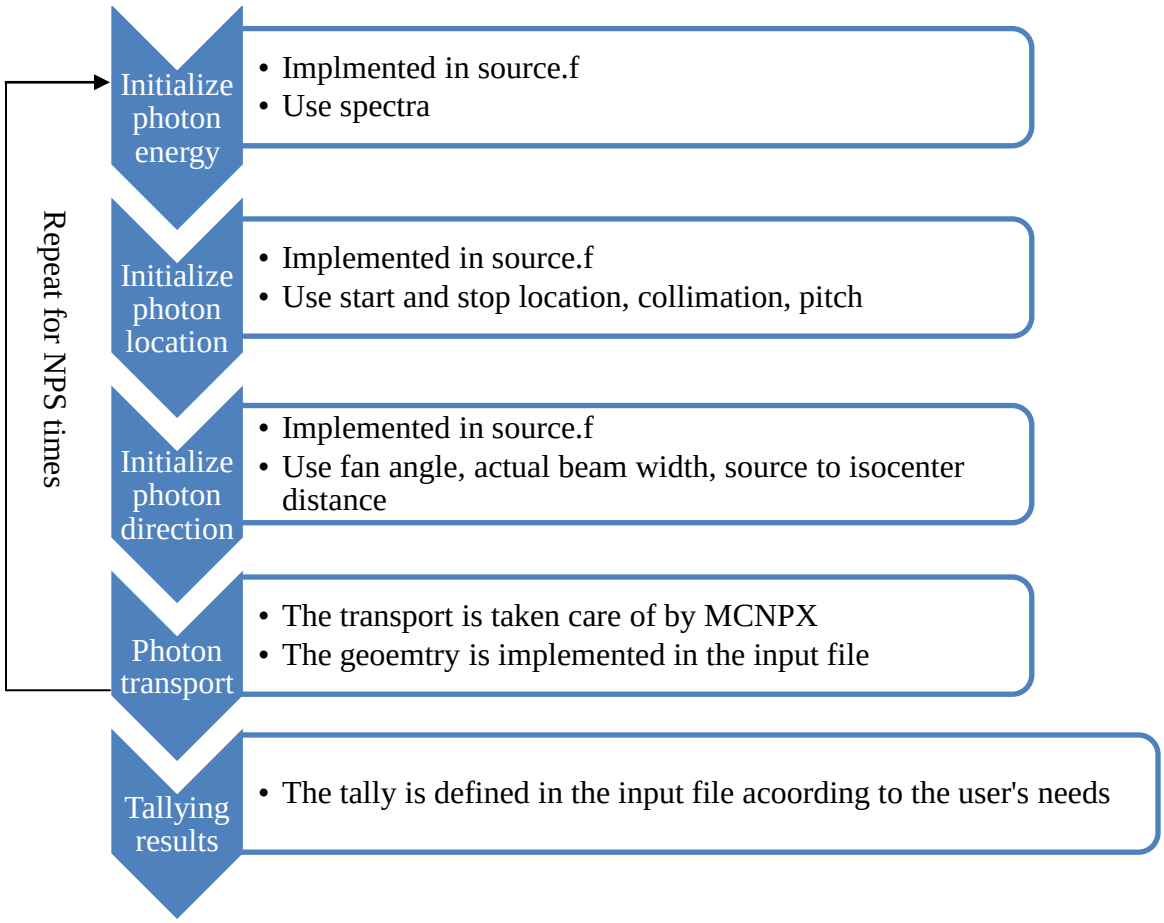


**Figure 3.5 The overall workflow of MCNPX simulation for the UCLA CT Dose Simulation Package. The initialization and photon transport are repeated for NPS times before the tallying results can be obtained.**

### 3.4 Dose Estimation and Validation

Under the condition of Charged-Particle Equilibrium (CPE), which means the charge of particles entering a small volume is equal to the charge of particles exiting that small volume, dose (D) is equal to Collision Kerma ($K_c$)[77]. MCNPX can estimate results in any region of interest (ROI) defined in the geometry. These results can be under different forms depending on how they were specified in the input file. For example, F1 tally scores the fluence of particles, and F6 tally scores the energy deposition with the ROI. In the UCLA CT Dose Simulation Package, *F4 tally was used to estimate the energy fluence (Ψ) within the ROI by track-length estimate method[74]. Energy fluence can then be converted to $K_c$ by using energy dependent and material dependent mass absorption coefficient ($\mu_{en}/\rho$):

$$D \xrightarrow{CPE} K_c = \int_{E=0}^{E_{max}} \Psi'(E) \cdot \left(\mu_{en}/\rho\right)_{E,material} dE$$

This was achieved by using DE and DF cards in MCNPX.

A normalization methodology published previously was used to convert the raw MCNPX output to absolute dose values[41]. Normalization Factors that are kVp and collimation specific were generated by measurements and simulations in air at isocenter and were applied to raw MCNPX results for other more complex geometries, such as CTDI or patient simulations.

CTDI simulation results were benchmarked with measurements for all the different CT scanner models from various manufacturers in order to validate different factors during the

modeling process, such as geometry, spectra, and bowtie filtration. The agreement between measurements and simulations were within 6% for all different combinations of scanning parameters for each CT scanner model[75].

### 3.5 Parallelization of the Package

Due to the repeated sampling nature of Monte Carlo methods and the complex geometry of CT scanners as well as the patient models, the MCNPX simulations often take very long time to run. In order to circumvent this limitation, it is imperative to take the advantage of the power of parallel computation and make the workflow more efficient. MCNPX comes with the parallel FORTRAN coding that implement Message Passing Interface (MPI) protocols to help the communications between different computing units and therefore facilitate the overall computational performance. Therefore, MCNPX can be compiled with the capability of parallel computation. However, the modifications to the source (source.f) also need to be parallelized so that it can function in a parallel computing environment.

In order to achieve that goal, the structure of the source.f code was modified to make sure that all the parameters, including the geometry information such as source to iso-center distance, spectra information as well as the bow-tie filtration information can be passed into different computing units. After these modifications, the CT Dose Simulation Package was able to be compiled and used at a cluster server with 64 AMD 2.0 GHz processors. Depending the number of CPUs specified, the running time was reduced from tens of hours to be within an hour.

# Chapter 4 Peak Skin and Eye Lens Dose from Brain-Perfusion CT Examinations Based On Monte Carlo Simulations[†]

## 4.1 Introduction

With the increased z-axis coverage and improved temporal sampling rate of multi-detector CT (MDCT) scanners, brain-perfusion scanning has become a viable tool for evaluating cerebral perfusion defects in patients with a suspicion of stroke. CT perfusion plays an important role in determining the nature, age, mechanism and potential reversibility of a stroke rapidly and within the critical therapeutic time window[78]. Brain-perfusion examinations with MDCT are also an important tool in the evaluation of brain tumors. Applications include using differences in the intrinsic perfusion characteristics of brain neoplasms to determine their malignant potential, and assessing response to therapy by monitoring changes of the integrity of the blood-brain barrier[79].

CT perfusion imaging requires repeatedly exposing one location of the head in order to monitor the uptake and wash-out of iodinated contrast. These images are then used as an input for post-processing calculations that allow one to estimate functional cerebral perfusion parameters such as mean transit time, cerebral blood flow, tissue permeability, and cerebral

[†] This chapter is based on the following publication:

Zhang D, Cagnon CH, Villablanca PJ, Cody DD, Stevens DM, Zankl M, DeMarco JJ, McCollough CH, Turner AC, Khatonabadi M, McNitt-Gray MF. "Peak Skin and Eye Lens Dose from Neuro-Perfusion CT Examinations Based On Monte Carlo Simulations". AJR, 198:412-417, 2012.

blood volume[80]. To repeatedly scan the same volume of brain tissue, there is typically no table motion during the scan (some recent advances have enabled scan modes in which the table is moved rapidly back and forth to increase z-axis coverage, yet maintaining a sufficient temporal sampling.). In either approach, the accumulated radiation dose to the skin or eye lens can be high, leading to concerns about potential radiation injury from these scans. For example, high radiation doses to local tissues (skin, lens of eye) may be delivered that have the potential to cause deterministic effects such as erythema (skin reddening), epilation (hair loss) or cataractogenesis (if the eye lenses are exposed by the x-ray beam). According to some recent studies, the thresholds for these effects could be as low as 1 Gy or even lower[81-84]. Several approaches have been suggested to avoid direct exposure of the eye lens, such as tilting the gantry to avoid the lens or maximizing the distance between the scan volume and the eyes. However, the effectiveness of these techniques in reducing lens dose has not been clearly demonstrated using Monte Carlo simulations.

It is important for radiologists, medical physicists and CT technologists to understand local radiation dose to skin and eye lens from CT brain-perfusion examinations to avoid unnecessary radiation hazards. The purpose of this study is to: (a) use Monte Carlo simulation methods to accurately estimate the radiation dose to the eye lens and skin from CT brain-perfusion studies; (b) investigate how closely the dose metric reported on the scanner console ($CTDI_{vol}$) matches actual eye lens and skin doses estimated using Monte Carlo methods; and (c) investigate the efficacy of dose reduction techniques to exclude the eye lenses from the primary scan range.

## 4.2 Methods

### 4.2.1. CT Scanner Models

UCLA CT Dose Simulation Package was used to develop MDCT source models to simulate scanners from all major manufacturers, including the Siemens Sensation 64, GE LightSpeed VCT, Philips Brilliance 64, and Toshiba Aquilion 64. Each of these MDCT source models has been benchmarked against physical measurements made in phantoms under a variety of conditions, and each agreed to within 5%[75]. The simulations take into account various aspects of the individual CT scanner designs, and CT perfusion protocol parameters, such as x-ray beam spectra, bowtie filtration, x-ray collimation characteristics, scan location and other factors[41,85]. The user is able to specify acquisition parameters such as tube voltage (kVp), current-time product (mAs), and collimation, etc.

### 4.2.2. Patient Model

To estimate dose to the skin and eye lens, an adult female patient model, Irene, from the GSF (now: Helmholtz Zentrum München) family of voxelized models was used. This model was developed based on whole body CT images of a female patient 32 years of age by individually segmenting radiosensitive organs and tissues, including skin and eye lens[86]. The weight and the height of the patient model were 51 kg and 163cm, respectively. The voxels in the model were 1.875 mm x 1.875 mm x 5 mm, with a resolution of 5 mm in the longitudinal direction..

### 4.2.3. Peak Skin Dose and Eye Lens Dose Estimation

By defining the tally voxels at various locations, the radiation dose can be assessed anywhere in the patient models using MCNPX. In order to get the peak dose for skin, the mesh tally feature in MCNPX was used to get 3D dose distribution in the patient model within the scan range. Mesh tallies are composed of a 3D array of voxels in a high-resolution Cartesian-coordinate mesh structure. These mesh tally voxels were set to overlap perfectly with the voxels of the patient phantom. Since the mesh tally result is a 1D array representing the 3D dose distribution, they do not distinguish between different tissues. Therefore in order to localize the skin tissue and eye lens tissue, a MATLAB subroutine was created to map the original patient model matrix to the 3D dose distribution matrix from mesh tally. The peak skin dose and eye lens dose were then obtained as the maximum dose and the average dose of those voxels identified as belonging to the skin and eye lens, respectively. The dose results were first divided by the density of the skin or eye lens to convert the unit from MeV/cm$^3$/particle to MeV/g/particle, then it was multiplied by the normalization factors to get absolute dose.

### 4.2.4. Monte Carlo Simulation of Brain-perfusion CT Examinations

Simulations were performed using cerebral perfusion acquisition protocols posted on the website of The American Association of Physicists in Medicine (AAPM)[87]. These included protocols for three out of the four scanners modeled in this study and are summarized in Table 4.1. Since the published protocols do not include a protocol for the Toshiba Aquilion 64 (only Toshiba Aquilion One and Aquilion Premium), this scanner was excluded from this part of the study. It should be noted that all the protocols employed lower tube potential and relatively lower mAs as compared to non-cerebral perfusion protocols. That is because in brain-perfusion CT

examinations, the image quality is not as crucial as in other exams, e.g. a routine head exam. Since the pixels are routinely binned during post-processing, and hence smoothing of the images, the acquisition parameters need not resemble a routine head exam[88]. In all simulations, there was no table motion, and repeated axial scans were simulated.

**Table 4.1 AAPM-posted protocols for the range of scanners and modes that were modeled in this study[87]**

| Scanner/Mode | kVp | bowtie | Nominal collimation (total) in mm | mAs/rotation | No. of rotations | total mAs |
|---|---|---|---|---|---|---|
| Siemens Sensation 64 | 80 | general | 24 x 1.2 (28) | 270 | 40 | 10800 |
| GE VCT axial mode | 80 | head | 64 x 0.625 (40) | 150 | 22 | 3300 |
| GE VCT cine mode | 80 | head | 64 x 0.625 (40) | 150 | 45 | 6750 |
| Philips Brilliance 64 Non-Jog mode | 80 | general | 32 x 1.25(40) | 125 | 30 | 3750 |

Note. --- There is no table movement for all four protocols listed in the Table. For Siemens Sensation 64 and GE VCT cine mode, the x-ray beams are on continuously; For GE VCT axial mode and Philips Brilliance 64 Non-Jog mode, the x-ray beams alternate between on and off and the acquisitions are not continuous. kVp = kilovoltage, mAs = milliampere seconds.

Clinically, the locations of perfusion defects may vary, requiring different anatomy to be scanned. However, to represent the worst case dose scenario, all of the simulated brain-perfusion scans were performed at the location where the eye lenses were completely covered by the primary beam (Figure 4.1). $CTDI_{vol}$ is a standardized quantity that measures the radiation output of the scanners using a specific measurement phantom; $CTDI_{vol}$ is not a measure of patient dose[89]. It depends on the CT scanner model and the beam quality. The values of $CTDI_{vol}$ that correspond to each of these specific protocols were from the AAPM website. These values were

compared to the Monte Carlo method estimated doses to eye lens and peak skin dose from each protocol to determine the differences between estimated patient dose and the scanner output ($CTDI_{vol}$) associated with the protocol.

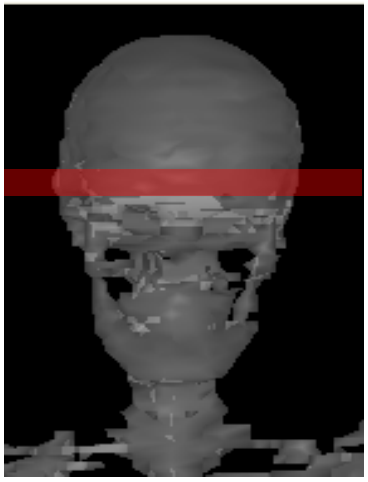

**Figure 4.1 An anterior-posterior view of the patient model (Irene) to illustrate the scan location. The shaded rectangular box indicates the beam coverage (24 x 1.2 mm), where the eye lenses are completely included.**

Although most manufacturers recommend the use of lower tube potential, in order to obtain more generalizable results that can be used for any acquisition protocol, simulations were also performed for all available tube potentials for each of the four scanners, including the Toshiba Aquilion 64. Again, repeated axial scans were simulated with no table movement, and the scan location was directly over the eyes of the patient. For the Toshiba Aquilion 64, the 64 x 0.5 mm collimation and a small bowtie were used. The peak skin dose and eye lens dose were reported on a normalized basis of milli-Gray (mGy) per 100 mAs.

### 4.2.5. Eye Lens Dose Reduction

In order to investigate the change in eye lens dose from tilting the gantry away from this structure, brain-perfusion axial scans were simulated using the AAPM posted protocol for an example scanner, the Siemens Sensation 64 CT, using a protocol of 24x1.2mm, 80 kVp, 270 mAs/rotation, and 40 total rotations, with the gantry tilted by 5, 10, 15, 20, 25 and 30 degrees. Figure 4.2a illustrates graphically that by tilting the gantry angle, the primary x-ray beam covers a smaller volume of eye lens tissue.

In order to investigate eye lens dose reduction when the location of the scan volume was moved further away (i.e. superior) from the eye lens, brain-perfusion axial scans were simulated with the Monte Carlo tool using the same AAPM posted protocol for a Siemens Sensation 64 CT scanner, with varying imaging volume positions centered from 5.5 cm above the eye lens to 5.5 cm below the eye lens at 0.5cm intervals. This is illustrated in Figure 4.2b.

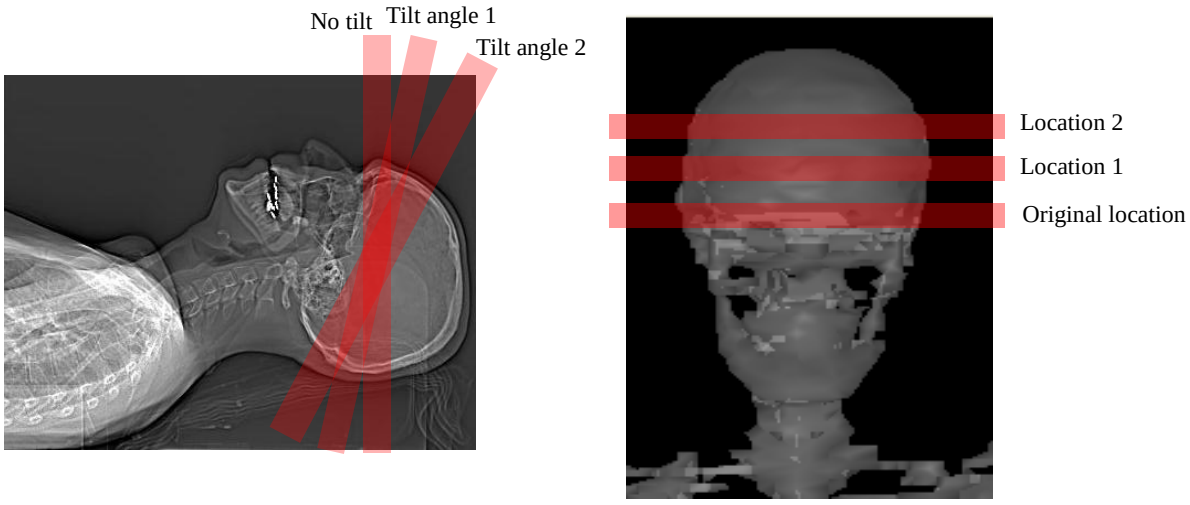


**Figure 4.2. a). Illustration of tilting CT scanner gantry angle to avoid direct exposure to eye lenses. Tilt angle 1 is non-ideal because the eye lens may still be partially irradiated directly. Tilt angle 2 is preferred, where eye lens are completely out of the x-ray beam. b). Illustration of moving the scan location further from the eye lens.**

## 4.3 Results

### 4.3.1. Peak Skin Dose and Eye Lens Dose Using AAPM Protocol

The peak skin dose and eye lens dose to the Irene model from a brain-perfusion examination using the AAPM protocols for three of the four scanners were calculated as absorbed dose in unit of mGy, as shown in Table 4.2. For peak skin dose, the values ranged from 87 mGy to 348 mGy; for eye lens dose the values range from 81 mGy to 279 mGy. There are significant dose differences between these scanners because the imaging protocols (mAs/rotation, temporal sampling interval, etc.) are very different. Therefore one cannot claim the superiority of one scanner over another only based on these dose information. $CTDI_{vol}$ values, which are a dose index and are often used to approximate patient dose, are also listed in Table 4.2. This table shows that peak skin dose and eye lens dose are estimated to be only 66%

to 79%, and 59% to 63% of the $CTDI_{vol}$ values , respectively under this worst case scenario (x-ray beam directly over the eye lens).

**Table 4.2 Monte Carlo Based Estimates of Peak Skin Dose and Eye Lens Dose to the Patient and Measured $CTDI_{vol}$ (mGy) From a Brain-Perfusion CT Examination For the AAPM-posted Acquisition Protocols For Four Scanners From Three Different Manufacturers**

| Scanner/Mode | $CTDI_{vol}$ (mGy) | skin | | eye lens | |
|---|---|---|---|---|---|
| | | dose (mGy) | % of CTDI | dose (mGy) | % of CTDI |
| Siemens Sensation 64 | 433 | 326 | 75% | 256 | 59% |
| GE VCT axial mode | 216 | 170 | 79% | 137 | 63% |
| GE VCT cine mode | 441 | 348 | 79% | 279 | 63% |
| Philips Brilliance 64 | 132 | 87 | 66% | 81 | 61% |

### 4.3.2. Peak Skin Dose and Eye Lens Dose at All Tube Potentials for Four scanners

The peak skin doses from brain-perfusion examinations estimated for all available tube potentials on all four scanners were normalized to mGy/100 mAs and are shown in Table 4.3. The similar information for the eye lens dose is shown in Table 4.4. Since organ dose at a given tube potential is proportional to total mAs, the dose from any arbitrary user-specific protocol using the collimation provided in Table 4.1 can be estimated using these tables. For example, in order to calculate the dose from the AAPM protocol (80 kVp) for the Siemens Sensation 64, the

user simply needs to multiply the mGy dose values from this table by the ratio of the total mAs ([(270 mAs/rotation x 40 rotations)] / [100 mAs]), which is 3 mGy x 270 x 40 / 100 = 324 mGy.

**Table 4.3 Estimated Peak Skin Dose to the Patient From a Brain-Perfusion Examination in the Unit of mGy/100mAs For all Tube Potentials For Scanners From Four Different Manufacturers**

| | Simulated peak skin dose (mGy/100mAs) | | | |
|---|---|---|---|---|
| kVp setting | 80 kVp | 100 kVp | 120 kVp | 140 kVp |
| Siemens Sensation 64 | 3.0 | 6.2 | 10.5 | 16.4 |
| GE VCT (axial or cine) | 5.2 | 8.8 | 13.2 | 18.2 |
| Philips Brilliance 64 | 2.3 | N/A | 7.2 | 11.1 |
| Toshiba Aquilion 64 | 5.4 | 9.5 | 14.1 | 18.1* |

Note. --- The peak skin dose is normalized to the unit of mGy/100 mAs.

*Toshiba Aquilion 64 provides a tube potential setting of 135 kVp instead of 140 kVp.

**Table 4.4 Estimated Eye Lens Dose to the Patient From a Brain-Perfusion CT Examination in the Unit of mGy/100mAs For all Tube Potentials For Scanners From Four Different Manufacturers**

| | Simulated eye lens dose (mGy/100mAs) | | | |
|---|---|---|---|---|
| Scanner | 80 kVp | 100 kVp | 120 kVp | 140 kVp |
| Siemens Sensation 64 | 2.4 | 5.2 | 8.9 | 14.5 |
| GE VCT | 4.1 | 7.1 | 10.7 | 14.7 |
| Philips Brilliance 64 | 2.2 | N/A | 6.7 | 10.4 |
| Toshiba Aquilion 64 | 4.4 | 7.7 | 11.5 | 14.7* |

Note. --- The eye lens dose is normalized to the unit of mGy/100 mAs.

*Toshiba Aquilion 64 provides a tube potential setting of 135 kVp instead of 140 kVp.

### 4.3.3. Eye Lens Dose Reduction by Tilting the Gantry Angle

Figure 4.3 shows the eye lens dose (in mGy) as a function of the tilted gantry angle from a brain-perfusion CT examination using the AAPM protocol parameters for a Siemens Sensation 64 scanner. When the eye lens is completely covered, the absorbed dose is about 256 mGy.

When the gantry was tilted by 15 degrees away from the eye lens, the dose to that structure was decreased by 87%.

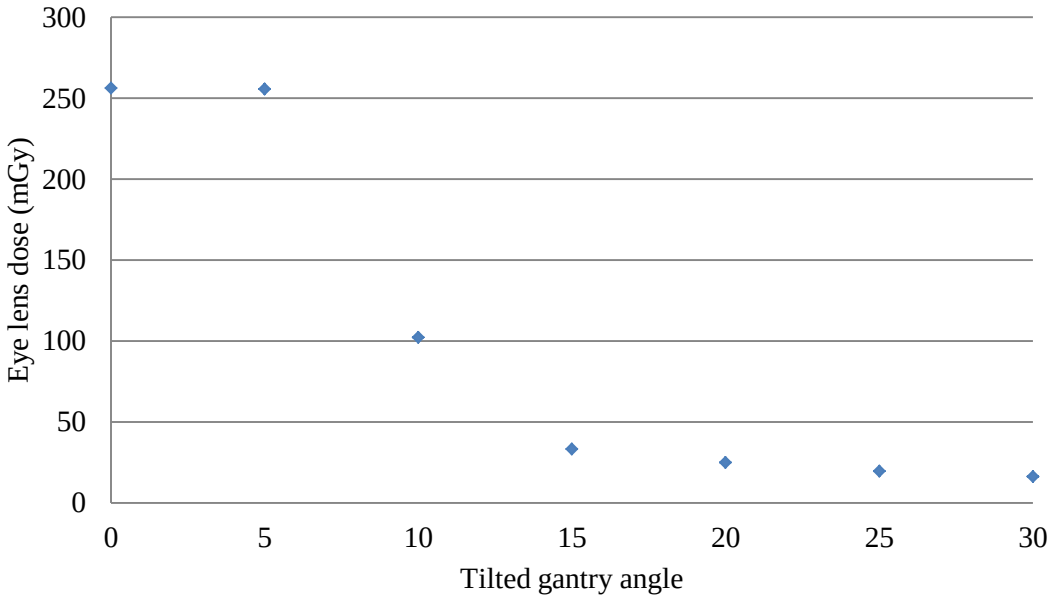


**Figure 4.3 Eye lens dose as function of tilted gantry angle from an AAPM protocol (80 kVp, 24 x 1.2 mm collimation, 270 mAs/rotation, 40 rotations) brain-perfusion examination for a Siemens Sensation 64 scanner.**

### 4.3.4. Eye Lens Dose reduction by Moving Scan Location away from the Eye Lens

Figure 4.4 shows the eye lens dose as a function of the scan location from a brain-perfusion CT examination for a Siemens Sensation 64 scanner. The eye lens dose was decreased by approximately 50% when the scan location was displaced just 1.5 cm away from the eye lens, and 86% when the scan location was displaced a full 2 cm away (superior or inferior) from the center of the eye lens. It should be noted that moving the scan location 2 cm resulted in a geometry in which the eye lenses are just out of the x-ray primary beam. This is a function of

both the simulated beam width for this scanner (24 x 1.2 mm = 28.8 mm nominal beam width, actual beam width is 32.2 mm) and the anatomy of the Irene patient model.

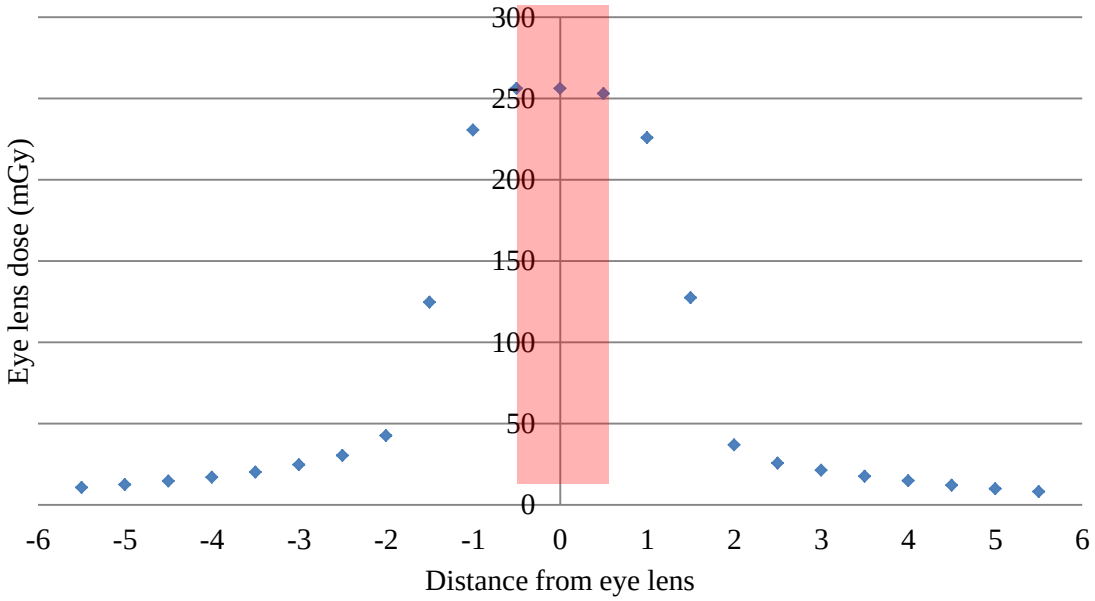


**Figure 4.4 Eye lens dose as function of scan location from an AAPM protocol (80 kVp, 24 x 1.2 mm collimation, 270 mAs/rotation, 40 rotations) brain-perfusion CT examination for a Siemens Sensation 64 scanner. The width of the eye lens in z direction for this patient model (Irene) is 1cm. The shaded box indicated the eye lens range in longitudinal direction. Therefore when the scan location is 2cm away from the center of the eyes, the eye lens are completely out of the x-ray beam (larger than half of the beam width plus half of the eye lens width).**

## 4.4 Discussion

This study used Monte Carlo based simulations to provide estimations of peak skin dose and eye lens dose from brain-perfusion CT examinations for specific acquisition protocols for scanners from the four major manufacturers. Depending on the scanners used in the examination, the peak skin and the eye lens dose ranged from 81 to 348 mGy for selected acquisition protocols posted on the AAPM website.

These results indicate that, while there are wide variations among scanners, the dose from brain-perfusion CT scans performed on these scanners is well below 1000 mGy. While ICRP guidelines suggest thresholds of 2000 mGy, 3000 mGy, and 2000 mGy for transient erythema, temporary epilation, and cataract formation, respectively[90,91] , some newer studies have proposed that the threshold for cataractogenesis is actually much lower if it exist at all[81-84,92]. Therefore, the radiation doses from CT brain-perfusion should be carefully monitored, and dose reduction schemes should be employed whenever feasible.

In a clinical environment, multiple brain-perfusion scans may be performed within a short period for various reasons, such as therapeutic repeat, change of the medical status of the patient, repeat scans due to technical inadequacies including motion artifacts, contrast bolus monitoring errors, or patient mis-positioning. Further, CT perfusion scan protocols are not regulated among different clinical sites; hence, some may use lower kVp and mAs protocols, while others may use higher kVp and mAs protocols. As described previously, since in brain-perfusion CT exams, the image quality can afford to be lower than routine head exams, it is important for each clinical site to optimize their scan protocols according to the characteristics of the CT scanner to ensure lower radiation dose delivery to the patients. For example, lower tube potential should be used, which is also appropriate for quantitative CT studies; mAs should be lower than diagnostic head exams; the number of acquisitions should be minimized to achieve lower total mAs without sacrificing the sampling rate. To assist clinicians in accounting for site to site variations in the applied protocols, Table 4.3 and Table 4.4 provide a tool for calculating the peak skin dose and the eye lens dose from any acquisition protocol. In some sites, only

processed perfusion map images are provided to the radiologists. In these cases, the acquisition and dose parameters (kVp, mAs, $CTDI_{vol}$) should still be monitored by the radiologists (e.g., through review of the patient protocol page or dose report summaries).

As an illustrative example, an arbitrary brain-perfusion scanning protocol using 100 kVp, 200 mAs/rotation, and 40 rotations at a GE VCT scanner is considered. The total mAs is 8000 (200 mAs/rotation * 40 rotations). This requires that the normalized dose value of 8.8 mGy/ 100 mAs (obtained from Table 3, GE VCT scanner at 100 kVp) has to be multiplied by a factor of 80 (total mAs of 8000 divided by 100) to obtain the peak skin dose. The result is an estimated peak skin dose of approximately 704 mGy. It should be noted that in these Tables the dose to eye lens represents the worst case scenario. Therefore, if the x-ray beam does not irradiate the eye lens directly (e.g., by controlling the longitudinal and angular positions of the images), the eye lens will receive lower radiation dose, as demonstrated in Figure 4.3 and Figure 4.4.

Although the $CTDI_{vol}$ is the value reported on the scanner console and in all dose reports on the scanner, it is not patient dose[89]. Rather, $CTDI_{vol}$ is defined as the average dose to a homogeneous 16 cm diameter acrylic phantom for a 100 mm-long scan. It is an index that describes the amount of radiation being emitted by the scanner. This study showed the overestimation of $CTDI_{vol}$ to both the skin dose and the eye lens dose. This is because in CTDI determinations, the scattered radiation generated in the 100mm long ion chamber is included, which represents contributions from adjacent scanning positions; while in brain-perfusion scans, there are no scatter from adjacent tube positions (or very little, if there are two adjacent

acquisitions). Overall, $CTDI_{vol}$ does provide a very conservative estimate (higher by at least 30%) of the peak skin and the eye lens doses, especially for the eye lens dose, since the numbers provided in Table 4.2 represent the worst-case scenario with direct irradiation of the eyes. This conservatism is recognized in international CT safety standards, which acknowledge that $CTDI_{vol}$ will overestimate surface dose for perfusion scans[93].

Radiation dose to the eye lens can be effectively reduced by avoiding direct exposure of this tissue. The reduction potential depends on the anatomy of the patient and the beam, so the absolute gantry tilt angle or scan location do not necessarily result in the percent dose reduction shown in Figure 4.3 and Figure 4.4. However, the dose drop off is obvious once the eye lens is outside the primary beam. This can be achieved by tilting the gantry angle, tilting the patient's head or adjusting the scan location. The sharp drop off in Figure 4.3 and Figure 4.4 suggests that the contribution from scattered radiation to the eye lens dose is small. This is probably because the eye lenses are located at the body surface, where there is less scatter build-up than at locations at depth within the patient. Although these two techniques (tilting the gantry angle and moving the scan location away from the eye lens) will not reduce the peak skin dose, they may be employed in clinical practice to ensure lower eye lens doses and presumably a lower risk of developing cataracts. Needless to say, the exact tilt gantry angle and scan location should be determined by a neuro-radiologist so that the region of interest (mid cerebral area including the basal ganglia nuclei for suspected stroke patients) is completely within the imaged volume so that the clinical objectives of the examination are not compromised in an effort to minimize dose to the lens of the eye.

It is a limitation of this study that only one scanner from each of the four major manufacturers was modeled. These did not include some new scanners (e.g. GE Discovery 750HD scanner, Siemens Definition Flash scanner), which have a scan acquisition mode (sometimes referred to as a shuttle mode or a short helical scan) to move the patient in and out of the gantry during the brain perfusion examination in order to image a greater volume of brain tissue. Some of these scanners do not support tilting of the gantry. Therefore, in the setup of the patient, the patient's chin should be tilted toward the chest (if possible) to better avoid the exposure of the eyes. In addition, some new scanners provide a coverage that is wide enough to include the whole brain anatomy (e.g. Toshiba Aquilion One scanner with 160 mm longitudinal coverage); for such scans, the eye lenses are inevitably within the beam during the whole examination, and therefore the possibility of dose reduction to the eye lens by moving the scan location or tilting the gantry does not exist. However, manufacturers offering whole brain imaging have introduced methods to assist in dealing with dose concerns by performing all required imaging functions in a reduced number of scans, such as an initial non-contrast scan, followed by a second contrast enhanced scan from which the arterial (CTA), venous (CTV) and brain perfusion (CTP) data are extracted.

Only one adult patient model was studied in this work and it may not represent the entire patient population. Usually patients with smaller size receive higher organ dose when the same scanning technique is used[50,94,95]. This will be investigated in Chapter 5. Pediatric patients will receive higher organ doses for the same scanning protocol, but brain perfusion examinations are performed primarily in adult patients and hence adult patients are more relevant. Additionally,

for very young pediatric patients in which the calvarium is less calcified than for adults, an even lower mAs can be used. Tube current modulation (TCM) was not simulated in this study because this approach is typically not used for brain-perfusion CT examination of the head. The size and the shape of the head do not vary sufficiently to justify the need for this application. Furthermore, the setting associated with TCM can easily be misunderstood in perfusion mode and potentially cause over-exposure to the patients[88].

In summary, the radiation dose from CT perfusion studies should be carefully controlled to minimize patient dose and maximize the benefit-to-risk ratio of the examination. Clinical institutions can use the results from this study to ensure that their brain-perfusion protocols (for any of the four scanners at any selected tube potential) operate below the limits where deterministic effects may be seen from radiation dose to eye lens and skin. In addition, it was demonstrated that the $CTDI_{vol}$ value reported on the scanner consoles overestimates the peak skin and eye lens doses from brain-perfusion studies. Therefore it should only serve as a conservative predictor. Tilting the gantry angle and moving the scan location further away from structures vulnerable to deterministic effects, such as the eye lens, could effectively reduce the dose to these structures. It is suggested that these dose reduction techniques be employed in clinical practices whenever possible.

# Chapter 5 Estimating Peak Skin and Eye Lens Dose from Neuro-Perfusion Examinations Using Monte Carlo Based Methods: Comparing the Monte Carlo Results with CTDIvol, TG111, and IMPACT Dosimetry Tool

## 5.1 Introduction

In order to investigate the radiation dose from neuro-perfusion CT scans, either retrospectively or prospectively, it is essential to have dose metrics that are easily measured and obtained. CTDI calculation assumes a contiguous set of scans over a relatively large region, and the measurements involve the use of a 100mm long ion chamber, which approximates multiple scan average dose (MSAD) for scans with table incrementations. While this metric applies to many clinical uses of CT, in neuro-perfusion scans however, there is no table incrementation and local peak doses to skin and eye lens are of more interest. Chapter 4 demonstrated that CTDI overestimates the peak skin dose. This is also shown in some other studies[96]. It may be more appropriate to use methods described in AAPM TaskGroup 111 report[97], where the measurements are performed at the 12:00 position of a 16cm diameter PMMA phantom using a small ion chamber with a shorter active length in longitudinal direction to estimate peak dose. Despite the fact that TG111 measurement could potentially provide more accurate dose estimation to peak skin and eye lens dose, it still does not take into account of the complexity of the heterogeneity of patient's anatomy. IMPACT CT patient dosimetry calculator, a commonly used tool for CT dose purposes, allows the users to select the scan range and reports simulated results based on Monte Carlo methods. However, it matches the modern CT scanners with the original modeled CT scanners using a specific technique instead of directly modeling the modern

CT scanners. Furthermore, it uses the MIRD mathematical patient model, in which all the organs are represented by highly approximated simple geometry and also does not appreciate the anatomical difference between patients. On the other hand, Monte Carlo based methods simulations using realistic voxelized patient models have been regarded and accepted as the most reliable method for the estimation of radiation dose to individual organs[41,50,85,94,95,98-101].

The local dose to skin tissue and eye lens from CT neuro-perfusion examinations should be well understood so that potential radiation safety issues could be avoided. Chapter 4 investigated the peak skin dose and eye lens dose delivered to a patient during CT neuro-perfusion scans for a range of scanning protocols. The purpose of this study is to: (a) extend the previous study and investigate dose to a variety of patients and (b) investigate how well these doses can be matched by some commonly used CT dose metrics or tools, such as CTDI, TG111 measurements, and IMPACT.

## 5.2 Methods

### 5.2.1. Patient Models

On GSF family of voxelized models, both skin and lens of the eye were explicitly represented in these patient models and so radiation dose could be tallied in these voxels. Because neuro-perfusion examinations are rarely performed on pediatric patients, only adult patients were considered in this study. Therefore two adult male and two adult female patient models (Irene, Donna, Golem, and Frank) were selected to represent a reasonable adult patient cohort. Although the results for Irene were reported already in Chapter 4, it is still included in

this chapter for comparison with other patient models. As shown in Table 5.1, although these four patient models have various body habitus, their head sizes are very similar. Since in neuro-perfusion scans the head is the only body part exposed to radiation, these four models represent the variation of patient anatomy, rather than the variation of patient body size.

**Table 5.1 Age, gender, and size descriptions of the 4 models used in this study.**

| Model | Age (yr) | Gender | Weight (kg) | Height (cm) | Head perimeter (mm) |
|---|---|---|---|---|---|
| Golem | 38 | Male | 69 | 176 | 61 |
| Frank | 48 | Male | 95 | 174 | 61 |
| Irene | 32 | Female | 51 | 163 | 57 |
| Donna | 40 | Female | 79 | 170 | 56 |

### 5.2.2. Scanning Protocols

For each combination of the four patient models and the four scanner models, all available kVps were simulated and the doses were reported on a per 100mAs basis. These results can be easily scalable by the actual mAs used for a given scanner and kVp setting. As in Chapter 4, the scan simulations were performed using repeated axial scans at the location where the primary beams cover the eye lens completely.

To summarize the scanning protocols, the widest collimation and typical bowtie filter for head scan was used for each scanner (24 x 1.2mm and general bowtie for Siemens Sensation 64; 64 x 0.5mm and small bowtie for Toshiba Aquilion 64; 64 x 0.625mm and general bowtie for Philips Brilliance 64; 64 x 0.625mm and medium bowtie for GE VCT).

### 5.2.3. Measurements and IMPACT Calculations

Although Chapter 4 provided the comparison of CTDI and actual patient dose, it was only for a limited set of scan protocols (only for the kVps used in AAPM protocols). Therefore, in order to investigate how well CTDI and TG111 measurements predict the peak dose of eye lens and skin under a variety of different kVps, these values were obtained by measurements on the scanners. To obtain CTDIvol values, standard CTDI head measurements (single axial scan with a 100mm long pencil ion chamber in a 16 cm diameter PMMA CTDI head phantom) were performed using the same collimation and bowtie settings for all four scanners investigated in this study under all available tube voltage. Then CTDIvol values under each condition were calculated by the weighted summation of CTDI at 12:00 position and CTDI at center position[20].

For TG 111 small chamber measurements, single axial scans were also performed on the 12:00 position of a CTDI head phantom using a Radcal Farmer chamber with the active length of 18mm. Due to limited access to all scanners, TG111 small chamber measurements were performed under all kVps only for the Siemens Sensation 64 scanner, the GE LightSpeed VCT scanner, and the Toshiba Aquilion 64 scanner.

Eye lens dose were obtained for each kVp setting for all four scanners from IMPACT (version 1.0.3) on a per 100 mAs basis. IMPACT only reports the average dose to skin instead of local peak skin dose therefore only eye lens doses were compared between Monte Carlo simulations and IMPACT. The scan range was selected so that the eye lens is fully covered by the primary beams, as the scenario in the simulations. This is shown by Figure 5.1.

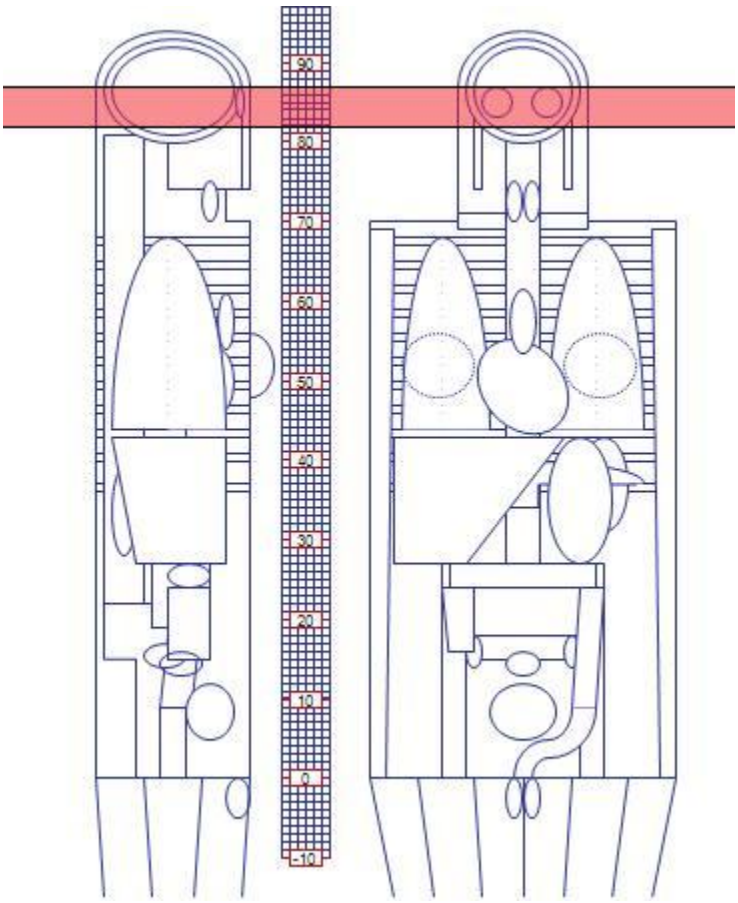


**Figure 5.1 The mathematical phantom in IMPACT for the calculation of eye lens dose. The shaded region shows a scan range from z=82 to z=87 which completely covers the eye lens.**

## 5.3 Results

### 5.3.1. Computation Time

All the simulations were performed on a parallel computing cluster server with 32 AMD 2.0 GHz processors. The number of particles (NPS) in MCNPX was set to 100 million to ensure good statistics. The mesh tally used in this study caused prolonged running time because all the photon interactions happened in each mesh tally voxel had to be tracked. The average running time for each simulation is about 5 hours. The error of all the results from mesh tally was within 1%.

### 5.3.2. Peak Skin Dose and Eye Lens Dose for Different Scanners and Patients

Peak skin dose and eye lens dose were calculated in the unit of milli-Gray (mGy) on a per 100 mAs basis for each kVp on all four scanners for all four patients, as shown in Table 5.2. It was also graphically plotted in Figure 5.2. The abscissa of Figure 5.2 is the combination of different scanners and patient models, while the ordinate is the radiation dose for different kVps. As shown in Figure 5.2, peak skin dose is almost always a little higher than eye lens dose under the same condition, but the behavior of peak skin dose and eye lens dose across different kVp, different scanners and different patient models are very similar. Depending on the scanner and patient model, the peak dose to skin from a single neuro-perfusion examination ranges from 2.3 mGy/100mAs to 18.2 mGy/100mAs. For example, skin peak dose for Irene at 140kVp from GE LightSpeed VCT is 18.2 mGy/100mAs. Meanwhile, the peak dose to eye lens ranges from 2.0 mGy/100mAs to 16.2 mGy/100mAs. For example, eye lens dose for Golem at 135kVp from Toshiba Aquilion is 16.2 mGy/100mAs. It should be noted that 140kVp is not usually used in clinics. Rather than providing clinical relevant dose values, these high kVp results serve as a reference for dose levels performed at lower kVps.

**Table 5.2 Peak skin dose and eye lens dose from Monte Carlo neuro-perfusion simulations for four patient models under all kVps on four CT scanners. The doses were normalized on a mGy per 100 mAs basis. a) Peak skin dose; b) Eye lens dose.**

a) Peak skin dose

| | Siemens Sensation 64 (mGy/100mAs) | | | | GE VCT (mGy/100mAs) | | | | Philips Brilliance 64 (mGy/100mAs) | | | | Toshiba Aquilion 64 (mGy/100mAs) | | | |
|---|---|---|---|---|---|---|---|---|---|---|---|---|---|---|---|---|
| kVp | Irene | Frank | Donna | Golem | Irene | Frank | Donna | Golem | Irene | Frank | Donna | Golem | Irene | Frank | Donna | Golem |
| 80kVp | 3.0 | 2.8 | 3.0 | 2.8 | 5.2 | 5.0 | 5.2 | 4.9 | 2.3 | 2.4 | 2.3 | 2.4 | 5.4 | 5.3 | 5.4 | 5.2 |
| 100kVp | 6.2 | 6.1 | 6.3 | 5.9 | 8.8 | 8.5 | 8.8 | 8.3 | NA | NA | NA | NA | 9.5 | 9.2 | 9.5 | 9.0 |
| 120kVp | 10.5 | 10.3 | 10.5 | 10.0 | 13.2 | 12.8 | 13.1 | 12.4 | 7.2 | 7.5 | 7.3 | 7.3 | 14.1 | 13.8 | 14.2 | 13.4 |
| 140kVp (135 for Acquilion) | 16.4 | 16.5 | 16.5 | 16.0 | 18.2 | 17.5 | 18.1 | 17.0 | 11.1 | 11.6 | 11.1 | 11.2 | 18.1 | 17.6 | 18.1 | 17.1 |

b) Eye lens dose

| | Siemens Sensation 64 (mGy/100mAs) | | | | GE VCT (mGy/100mAs) | | | | Philips Brilliance 64 (mGy/100mAs) | | | | Toshiba Aquilion 64 (mGy/100mAs) | | | |
|---|---|---|---|---|---|---|---|---|---|---|---|---|---|---|---|---|
| | Irene | Frank | Donna | Golem | Irene | Frank | Donna | Golem | Irene | Frank | Donna | Golem | Irene | Frank | Donna | Golem |
| 80kVp | 2.5 | 2.5 | 2.2 | 2.6 | 4.1 | 4.3 | 3.8 | 4.6 | 2.2 | 2.1 | 2.0 | 2.3 | 4.4 | 4.6 | 4.0 | 4.8 |
| 100kVp | 5.4 | 5.4 | 4.8 | 5.6 | 7.1 | 7.5 | 6.6 | 7.8 | NA | NA | NA | NA | 7.7 | 8.2 | 7.1 | 8.5 |
| 120kVp | 9.3 | 9.3 | 8.4 | 9.6 | 10.7 | 11.4 | 9.9 | 11.8 | 6.7 | 6.8 | 6.2 | 7.1 | 11.5 | 12.3 | 10.6 | 12.7 |
| 140kVp (135 for Acquilion) | 15.0 | 15.0 | 13.8 | 15.6 | 14.7 | 15.7 | 13.6 | 16.1 | 10.4 | 10.4 | 9.8 | 11.0 | 14.7 | 15.8 | 13.6 | 16.2 |

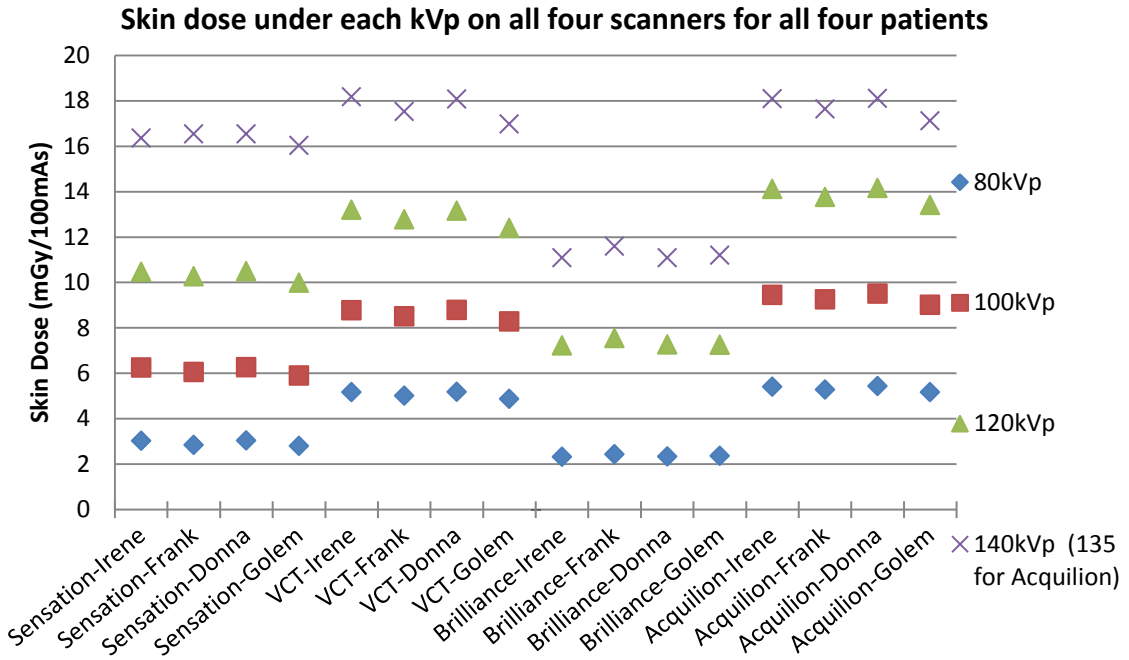


(a)

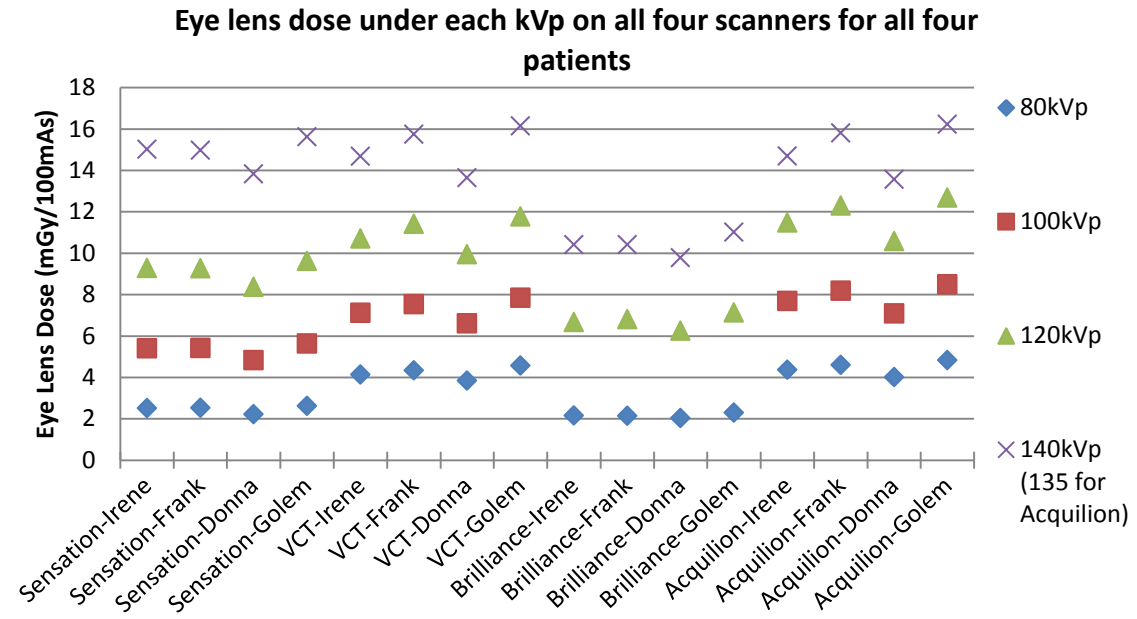


(b)

**Figure 5.2 Skin dose (a) and Eye lens dose (b) under each kVp on all four scanners for all four patient models on a 100mAs basis.**

Higher kVp always results in higher dose when the same mAs were used. For example, peak skin dose from 120kVp is always about 2 to 3 times higher than that from 80kVp across all the scanners and patient models. The dose difference from various scanners is large. For example, for patient Donna at 120 kVp, the peak skin dose from Toshiba Aquilion 64 is 14.2 mGy/100mAs, while it is 7.3 mGy/100mAs from Philips Brilliance 64. This shows that a factor of two differences can exist between two different scanners, even using the same imaging protocol. This is consistent with results found in a previous publication[102]. The dose difference from various patients is fairly small. For example, for Siemens Sensation at 80 kVp, the peak skin dose ranges from 2.8 mGy/100mAs to 3.0 mGy/100mAs among all four patient models investigated in this study.

### 5.3.3. Performance of CTDIvol Measurements to Predict Peak Skin and Eye Lens Dose

Table 5.3 shows the CTDIvol measurements that were obtained at corresponding bowtie filtration and collimation settings under all available kVps on the four scanners modeled in this study. Similar to the simulated organ dose, these values were also normalized on a mGy/100mAs basis. Figure 5.3a shows the ratio of CTDIvol to peak skin dose, while Figure 5.3b shows the ratio of CTDIvol to eye lens dose, for all kVps, all scanners and all patient models. The ratio values higher than one mean overestimation, while ratio values lower than one indicate underestimation.

**Table 5.3 CTDIvol measurements for all kVps on four scanners modeled in this study. The values were normalized on a mGy per 100 mAs basis.**

| | Siemens Sensation 64 | GE VCT | Philips Brilliance 64 | Toshiba Aquilion 64 |
|---|---|---|---|---|
| 80kVp | 4.0 | 7.5 | 3.3 | 6.9 |
| 100kVp | 8.3 | 13.3 | NA | 13.2 |
| 120kVp | 13.7 | 20.2 | 11.1 | 19.9 |
| 140kVp (135 for Acquilion) | 20.9 | 28.0 | 16.1 | 26.5 |

Figure 5.3 shows that CTDIvol generally overestimates peak dose to both skin and eye lens. Depending on kVp, the scanner and patient model, CTDIvol can overestimate peak skin dose by 26% to 65%, with the average overestimation of 44%, and it overestimates eye lens dose by 33% to 106%, with the average overestimation of 67%. CTDIvol overestimates eye lens dose more than peak skin dose because eye lens dose is usually a little lower than skin dose, as shown in Figure 5.2.

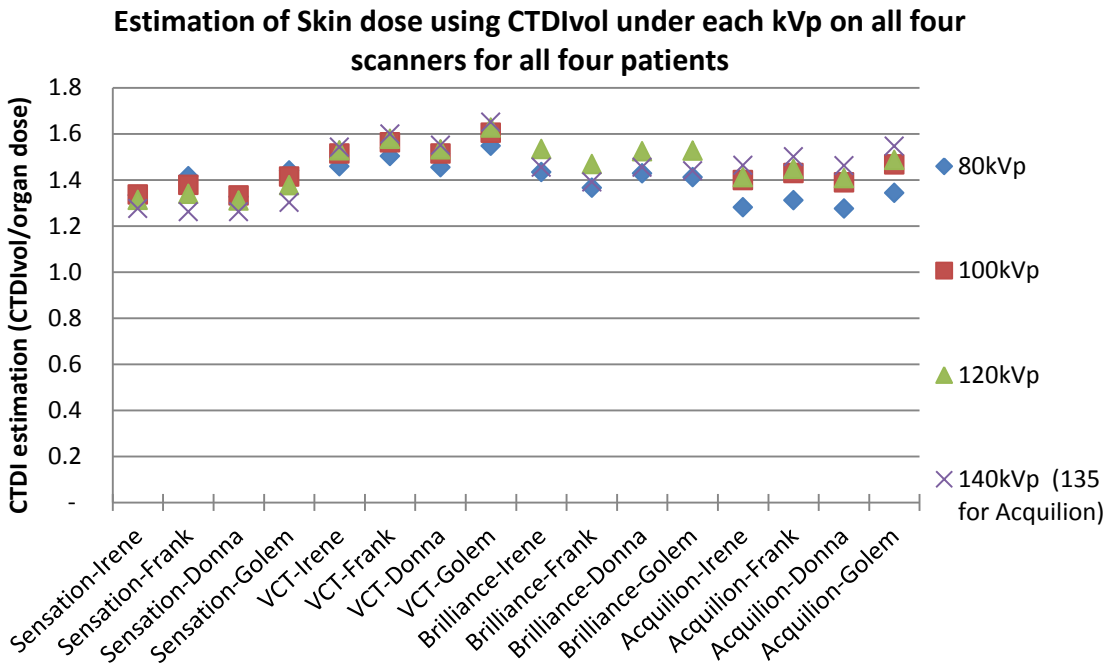


(a)

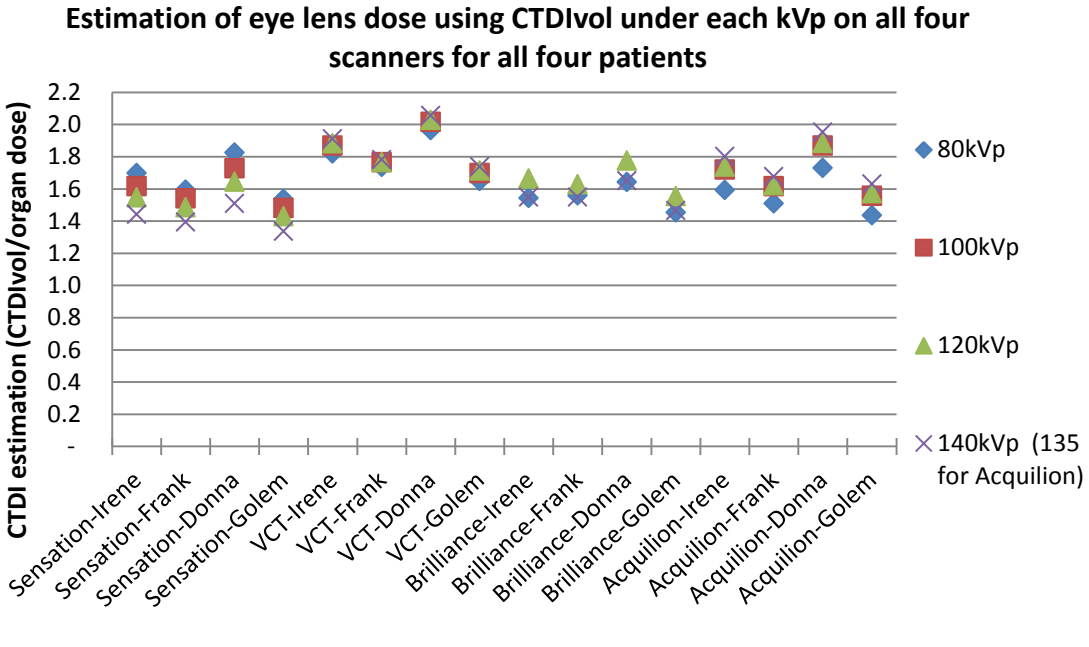


(b)

**Figure 5.3 CTDI estimation of skin dose (a) and eye lens dose (b) under each kVp on all four scanners for all four patient models.**

### 5.3.4. Performance of TG111 Measurements to Predict Peak Skin and Eye Lens Dose

Table 5.4 shows the TG111 measurements for all conditions. Figure 5.4a and Figure 5.4b show the ratio of TG111 measurements to peak skin dose and eye lens dose, respectively. As previously mentioned in 5.2.3, TG111 measurements were only performed for three of the four scanners so Figure 5.4 has less data points. Figure 5.4 shows that TG111 measurements provide a better prediction to both peak skin and eye lens dose than CTDIvol does. Depending on kVp, the scanner and patient model, TG111 measurements predict the skin dose from 14% underestimation to 33% overestimation, with the average prediction across all kVps, scanner and patient models of 7% overestimation. For eye lens dose, the TG 111 measured values predict the eye lens dose from 9% underestimation to 66% overestimation, with the average prediction of 27% overestimation.

**Table 5.4 TG111 measurements for all kVps on four scanners modeled in this study. The values were normalized on a mGy/100 mAs basis.**

| | Siemens Sensation 64 | GE VCT | Toshiba Aquilion 64 |
|---|---|---|---|
| 80kVp | 2.8 | 6.3 | 5.4 |
| 100kVp | 5.6 | 10.9 | 9.4 |
| 120kVp | 9.4 | 16.5 | 14.8 |
| 140kVp (135 for Acquilion) | 14.2 | 22.6 | 19.1 |

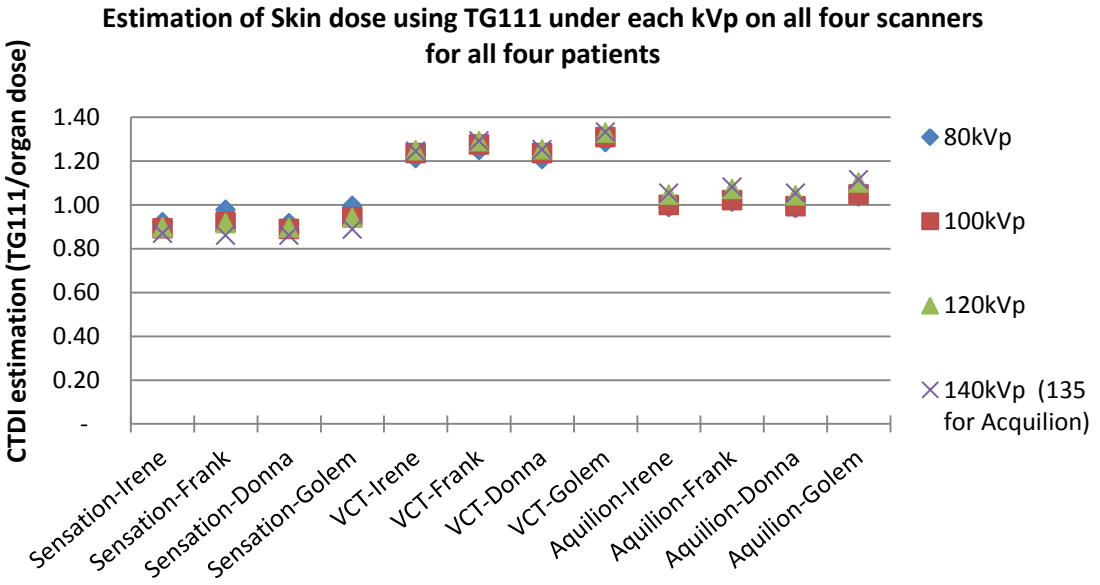


(a)

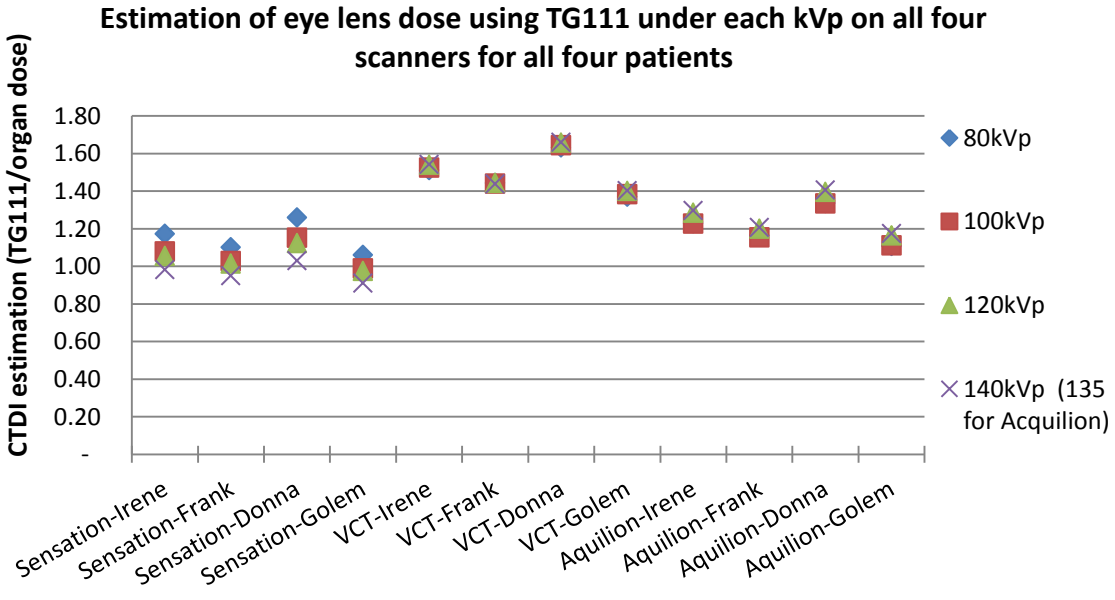


(b)

**Figure 5.4 TG111 estimation of skin dose (a) and eye lens dose (b) under each kVp on two scanners for all four patient models.**

### 5.3.5. Performance of IMPACT Calculations to Predict Eye Lens Dose

Table 5.5 shows the IMPACT calculations for eye lens dose under each condition. Figure 5.5 shows the ratio of IMPACT calculations of eye lens dose to the simulated eye lens dose using Monte Carlo methods. This figure demonstrates that IMPACT calculations also overestimate eye lens doses in most of the cases. Depending on the kVp, the scanner and patient model, the overestimation can vary from 2% to 82%. The average overestimation is 43%.

**Table 5.5 IMPACT eye lens dose calculations for all kVps on four scanners modeled in this study. The values were normalized on a mGy per 100 mAs basis.**

| | Siemens Sensation 64 | GE VCT | Philips Brilliance 64 | Toshiba Aquilion 64 |
|---|---|---|---|---|
| 80kVp | 3.3 | 6.7 | 3.2 | 5.7 |
| 100kVp | 6.6 | 12.0 | | 12.0 |
| 120kVp | 11.0 | 18.0 | 9.9 | 17.0 |
| 140kVp (135 for Acquilion) | 16.0 | 24.0 | 13.0 | 23.0 |

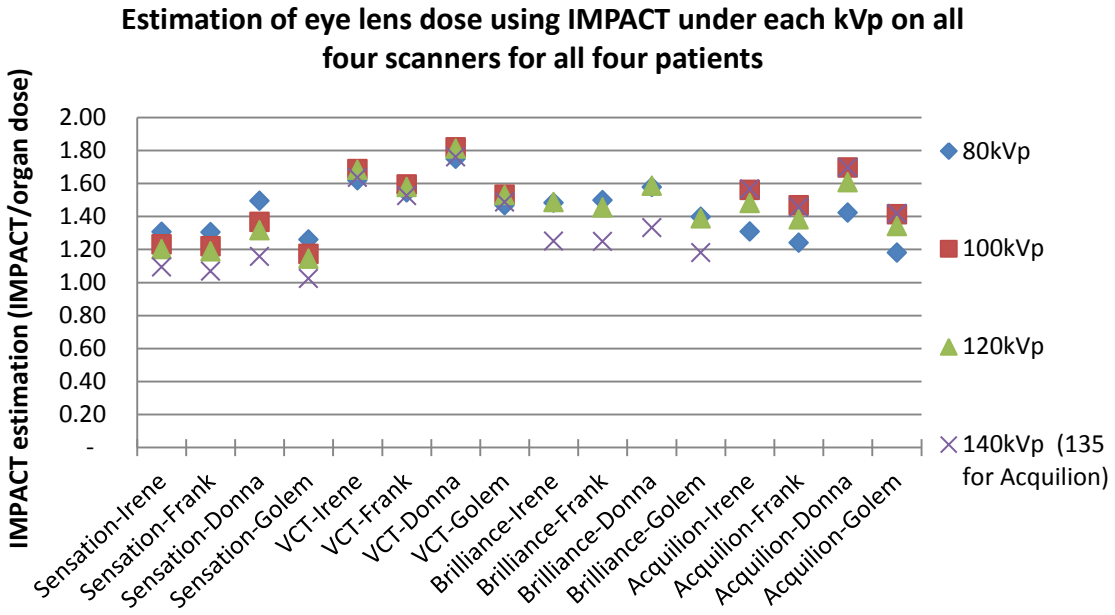


**Figure 5.5 IMPACT estimation of eye lens dose under each kVp on all four scanners for all four patient models.**

## 5.4 Discussion and Conclusion

This study used Monte Carlo method based simulations and provided estimations to peak skin dose and eye lens dose from CT neuro-perfusion scans for a range of adult patients under different tube voltage settings for four scanners from all major manufacturers. Several dose metrics, including the widely used CTDIvol and the newly proposed TG111 measurements, as well as IMPACT, a commonly used CT dose tool, were used in this study and their performance to match the actual peak skin and eye lens doses were evaluated.

Figure 5.2 provided dose to skin and eye lens at all kVps on different scanners for different patients. By comparing the dose difference across kVp (each column of data points), it was shown that at the same mAs, higher kVp always yields higher organ dose. This is because

the x-ray intensity is approximately proportional to the square of tube voltage, and there is larger amount of photons coming out of the x-ray tube at a higher kVp, even at the same mAs. By comparing the dose difference across patients, it was shown that the dose variation between patients is very small. This is not contradictive to other studies indicating higher doses for smaller patients[94], because the body part of interest in this study is head, where the size is relatively constant among adult patients. These results also indicate that the anatomical variation between adult patients is not very large. The morphologies of both skin and eye lens are reasonably constant across various patients: they are both organs located at surface and have little shielding effect from surrounding organs. On the other hand, by comparing the dose difference across scanners, it was shown that there is substantial dose variation between the scanners. This is consistent with previous work which studied the doses to different organs in abdominal region and also showed large dose differences[103]. This is primarily because of differences in filtration (including bowtie composition, thickness and shape) between various CT scanners. However, one cannot assert the superiority of one scanner over another solely based on the dose information because the image quality from these scanners can be different and is not considered here.

The results of this study showed that CTDIvol overestimate peak skin dose by 26% to 65%, and it overestimate eye lens dose by 33% to 106%. This is because of the integration effect of the 100cm long ion chamber. It captures the scatter tails of the longitudinal radiation profile within the length of the 100 cm ion chamber and estimates the average dose to the active volume in the chamber, while the peak dose obviously refers to a concept of local dose and does not

account for the integration effect. TG111 measurement on the other hand, uses a small chamber and it is closer to a peak dose measurement. Therefore it provides closer estimate to both eye lens and peak skin dose. For example, TG111 predicts the skin dose from 14% underestimation to 33% overestimation, and it predicts the eye lens dose from 9% underestimation to 66% overestimation. However, it should be noted that when the collimation is narrower than the active length of the small chamber (approximately 18 mm), partial volume correction would be needed. Overall, CTDI does provide a very conservative estimate (high by at least 30%) of peak skin and eye lens dose. Though there is underestimation in some scenarios, predictions using TG 111 measurements provide values that are closer to the simulated for both eye lens and skin dose. However, physicists and physicians should be aware that it still does not equal to patient dose. On the other hand, IMPACT CT dosimetry tool overestimate the eye lens dose by 2% to 82%. This may due to the reason that IMPACT used a technique to match the old scanner CT models to the modern CT scanner. The calculations did not take into account the sophistications of the beam spectra and bowtie filtration designs of the newest scanners.

The fact that the data points in Figure 5.3 and Figure 5.4 are much closer to each other than that in Figure 5.2 (both across different kVp within one scanner and across different scanners) demonstrate that both CTDI and TG111 measurements reasonably take into account of both the spectra variations across different kVp and across different scanners. It is meaningful to compare these results in three different aspects. First, for a specific scanner and patient model combination, the estimation differences between different kVps are small. For example, the points representing different kVps in Figure 5.3 and Figure 5.4 almost perfectly overlap with

each other. This fact indicates that both CTDI and TG111 dose metric take into account the changes of the photon energy spectra: when a different kVp is used, the behaviors of these two metrics are consistent with the behavior of the actual organ doses. Therefore the ratios are almost the same at different kVps. Second, for one specific scanner but different patient models, the estimation values do not vary much because the organ doses do not vary much across patient, as analyzed previously. Third, there is some difference of the estimation values between different scanners. For example, for Donna at 80 kVp, the CTDI overestimation of skin dose is 33% on Siemens Sensation 64 scanner, 45% on GE LightSpeed VCT scanner, 43% on Philips Brilliance 64 scanner, and 28% on Toshiba Aquilion  64 scanner. This result seems to be inconsistent with another previously published work where organ dose from helical scans on different scanners were normalized by their CTDIvol and the normalized results were very close, thus suggesting the feasibility to use the same coefficients to convert CTDIvol to organ dose even for different scanners[103]. The context is a little different in these two studies. In that study helical scans were used, therefore each organ not only receives dose from the primary beam, but also receive scatters from adjacent tube rotations. This is naturally equivalent to the intrinsic property of CTDI measurement, where both primary beam and scatter tails were included in the measured dose. In this study however, axial scans with no table motion were used and peak dose was of interest, where there is no scatter from adjacent rotations. Since the results at different kVps already shown that the photon spectra differences are well taken into account by CTDIvol, the differences of CTDIvol performances among these four scanners could be from different bowtie design, geometry and collimations.

Although TG111 measurements were only performed for three scanners, Figure 5.4 showed that its performance is also not very consistent across these three scanners. For example, for Siemens Sensation 64 scanner and Toshiba Aquilion 64 scanner, TG111 measurements are very close to peak skin dose while for GE LightSpeed VCT scanner, TG111 measurements give about 30% overestimation. Since there is no additional scatter from adjacent rotations in TG111 measurements, this dose metric should theoretically provide a more accurate estimate to point dose. The fact that it overestimates peak dose for GE LightSpeed VCT scanner is probably because of the scanner geometry and the shape of the bowtie filter.

The limitations of this study were already addressed in Chapter 4. For example, it did not model a recently developed technique (volume shuttle mode) utilized in some new scanner models during neuro-perfusion examinations. While this new technique may spread the total dose to a larger volume of the patient's anatomy, it may not necessarily reduce the peak dose, if that there is still some overlap between the two beams at extremity positions, so that certain part of the anatomy is always irradiated.

In summary, radiation dose from CT neuro-perfusion examinations should be closely managed. These include the accurate estimation of radiation dose (including the prospective prediction of dose and the retrospective evaluation of dose), the reduction of dose, the optimization of scan protocol, the enforcement of optimized scan protocol and the elimination of operation errors. This study could facilitate the optimization of scan protocol by providing very detailed dose perspectives across different patient and scanner models. In addition, it was

demonstrated that TG111 measurements estimates peak skin and eye lens dose closer than both CTDIvol and IMPACT CT dosimetry tool. While TaskGroup Report 111 was just published and these measurements are still not widely accepted, CTDIvol which is reported on the scanner can still serve as a conservative estimation of the peak doses. However, one should be aware that both TG111 peak dose metric and CTDIvol dose metric are still only indexes, instead of actual patient dose. IMPACT CT dosimetry tool meant to report the actual patient dose, but its approximations of both the CT scanner characteristics and the patient model limit itself to be used as an accurate estimator of organ doses.

## Chapter 6 Variability of surface and center position radiation dose in MDCT[†]

### 6.1 Introduction

Estimating patient dose, and especially organ dose from Multidetector CT (MDCT), continues to be of interest to the imaging community due to the continued growth in CT utilization. Currently, the standard method of measuring CT radiation output, the CT dose index (CTDI), requires the use of a standardized homogeneous cylindrical phantom, known as a CTDI phantom, a 100 mm long pencil ionization chamber and a single axial scan to obtain values used to compute $CTDI_{100}$, $CTDI_w$ and several other dose descriptors[104-108]. To account for parameters that are related to a specific imaging protocol, especially for helical acquisitions, $CTDI_{vol}$ was introduced[109].

Due to the larger beam collimations of MDCT systems and cone-beam CT systems, revisions of this methodology have been suggested and are under consideration for wider adoption by the medical physics community. For example, Dixon investigated the limitations of $CTDI_{100}$ in MDCT and proposed a new method to perform calculations to estimate typical

---

[†] This chapter is based on the following publication:

Zhang D, Savandi AS, Demarco JJ, Cagnon CH, Angel E, Turner AC, Cody DD, Stevens DM, Primak AN, McCollough CH, McNitt-Gray MF. "Variability of surface and center position radiation dose in MDCT: Monte Carlo simulations using CTDI and anthropomorphic phantoms",Medical Physics, 36(3):1025-38, 2009.

clinical CT doses, as opposed to CT scanner radiation output, with the use of a small volume detector and a helical scan[23,110].

Small detectors have also been used with anthropomorphic phantoms to obtain measurements that provide estimates of radiation dose to specific organs. Hurwitz et al[111] estimated radiation dose to the female breast from 16-slice MDCT helical examinations using metal-oxide-semiconductor field-effect transistors (MOSFETs) in an anthropomorphic phantom. In separate efforts, Hurwitz et al[112] and Jaffe et al[113] developed methods to determine fetal radiation doses resulting from 16-slice MDCT, using direct measurements of radiation-absorbed dose in an anthropomorphic phantom designed to simulate a gravid woman. More recently, Deak et al[114] estimated typical doses by calculating the energy deposition in a CTDI and anthropomorphic phantom using a collection of TLDs.

DeMarco et al[115] developed a Monte Carlo-based method to estimate radiation dose from MDCT using cylindrical and physical anthropomorphic phantoms. As part of their model verification, physical measurements were made using a collection of 20 MOSFET detectors placed nearly contiguously on the surface of the thorax of the anthropomorphic phantom. In a separate effort, DeMarco et al[116] used Monte Carlo simulation methods applied to cylindrical and physical anthropomorphic phantoms, where a film dosimeter was placed on the surface of CTDI phantoms to observe and measure the magnitude of the surface dose variation in MDCT. Both studies found that the larger cone angles from MDCT systems yield greater beam divergence and

resulted in surface dose variations, with the peak value twice as high as the valley; these variations were observed for both helical and contiguous axial scans.

These surface dose variations have potential implications for investigators who perform surface dose measurements using small detectors on either homogeneous (e.g. CTDI) or heterogeneous (e.g. anthropomorphic) phantoms. The purpose of this paper is to more completely evaluate the variability of absorbed radiation dose in both cylindrical and anthropomorphic phantoms at surface and central (or depth) positions when performing helical or contiguous axial scans. Variability will be assessed using computational models of both types of phantoms for a variety of z-axis beam profile (or simulated beam collimation) and pitch conditions. Although previous work has demonstrated that there is some variability at the surface of phantoms, this work will serve to further investigate and quantify this variability and the factors that influence it.

## 6.2 Methods

### 6.2.1. Scanner Model

In this study, a 64-slice CT scanner system (Sensation 64, Siemens Medical Solutions, Forcheim, Germany) was modeled for all simulations using Monte Carlo-based methods. The models were based on previous work[117] and take into account the x-ray source spectra, beam filtration (including bowtie filter) and scanner geometry (focal spot to isocenter distance, fan angle, etc.) as provided by the manufacturer. For this scanner, the widest available beam collimation is 24x1.2mm (nominal beam width of 28.8mm). The actual radiation profile was

measured using Optically Stimulated Luminescences (OSLs, CT Dosimeter, Landauer, Inc. Glenwood, Illinois) that were exposed in air at isocenter during a single axial scan using the 24x1.2mm nominal collimation. The OSL dosimeter was then sent to Landauer for reading. From the normalized radiation dose profile that resulted (a table of relative dose values as a function of z-axis location), the full width at half maximum (FWHM) of the dose profile was calculated to be 34.1 mm. This value was used as the measured beam width in the remainder of this study.

### 6.2.2. Phantoms

The cylindrical homogeneous phantoms used for CTDI measurements are well defined by U.S. and international regulatory agencies[104]. The polymethylmethacrylate (PMMA) phantom, PMMA rods and CTDI ion chamber were modeled, as described previously[118]. For all simulations in this manuscript, the 32cm diameter body CTDI phantom model was used.

A voxelized model of a heterogeneous anthropomorphic phantom, the ATOM family adult male (CIRS, Norfolk VA), was also used in the simulations. This physical phantom is comprised of the head and torso that represents a standard man who would have a height of 173 cm and weight of 73 kg. The voxelized model of the phantom is comprised of three different materials: bone, soft tissue, lungs. The model also includes the air around the phantom. The information about the density and composition of each simulated tissue type used in the Monte Carlo simulations was provided by the phantom manufacturer (Table 6.1). The voxelized phantom was created using an approach developed previously[116,119]. In this approach, spinal cord, spinal disk

and soft tissues are consolidated into one equivalent material. At the level of the chest, the lateral width of the phantom is 32cm, and the anterior-posterior (AP) thickness of the phantom is 22cm. At the level of the neck, the phantom is approximately circular with diameter 14 cm.

**Table 6.1 Description of Anthropomorphic Phantom Materials – Adult Male (ATOM, CIRS, Norfolk, VA)[120]**

| Materials | Physical density ($g \cdot cm^{-3}$) | $Z_{eff}$ | Electron Density ($cc^{-1}$) |
|---|---|---|---|
| Bones | 1.60 | 11.5 | $5.03 \times 10^{23}$ |
| Soft Tissue | 1.055 | 7.15 | $3.43 \times 10^{23}$ |
| Lungs | 0.21 | 7.10 | $0.681 \times 10^{23}$ |

### 6.2.3 Monte Carlo Method

UCLA CT Dose Simulation Package was used to estimate dose distributions along the z-axis at both surface and central positions for each phantom. By defining the tally points at various locations, the radiation dose can be assessed anywhere in the model using the Monte Carlo method. The mesh tally feature was used extensively in this study in order to efficiently tally the dose distribution in a high-resolution Cartesian-coordinate mesh structure. Mesh tallies are composed of a 3D array of voxels. A set of longitudinal mesh tallies was used to measure a 1D dose distribution for the CTDI phantom simulation, and a set of rectangular mesh tallies was used to measure a 2D dose distribution for anthropomorphic phantom simulation.

### 6.2.4. Simulation Experiments Under Different Beam Width, Pitch and Phantom Conditions

#### 6.2.4.1. Peripheral and Center Dose Profile for the CTDI Body Phantom

The purpose of these experiments was to investigate the nature and magnitude of the dose variation at surface and center locations of the CTDI body phantom under a variety of pitch and simulated beam width conditions. Pitch 0.75, 1.0 and 1.5 for helical scans, as well as contiguous axial scans were simulated for CT scan range over the full length of the CTDI body phantom (from -7.5cm to 7.5 cm) using 120kVp, 100mAs, 24 x 1.2mm wide detector configuration (28.8 mm nominal beam width). For each condition, both surface and center radiation profiles were obtained from the simulation results.

To investigate the effect of radiation beam width, three different beam widths were simulated for each experiment: (1) the nominal beam width of 28.8mm, which would be an ideal beam width; (2) the measured radiation beam width of 34.1mm, which is a realistic condition, and (3) a 41mm beam width which is 20% greater than the measured beam width and represents an extremely exaggerated condition.

For each simulation, one-dimensional mesh tallies were obtained in the (simulated) ion chamber at a peripheral position 1 cm below the surface and at the central location of the phantom, corresponding to the locations of physical measurements. Thus, the distance to isocenter was 15 cm for the peripheral location of the 32 cm phantom. The voxel size for each element in the mesh tally was 4mm x 4mm x 1mm, with a resolution of 1mm along the z-axis.

For each condition, the resulting z-axis profiles were determined from the mesh tally and converted to absolute dose normalized to tube current (in mGy/mAs). From these profiles, the magnitude of variation was estimated using percent ripple, which was calculated based on the difference from values at the peak to those in the valley.

#### 6.2.4.2. Surface and Center Dose Profiles in an Anthropomorphic Phantom

For the anthropomorphic phantom, we simulated helical scan pitch values of 0.75, 1.0, and 1.5, as well as contiguous axial scans. The simulated scans started at the superior edge of the phantom and continued until the inferior edge of the phantom, which covered the whole phantom completely. Tube voltage of 120kVp and tube-current-time-product of 100mAs were used as with CTDI phantom, but instead of various beam width settings, only the measured beam width of 34.1mm was utilized for the anthropomorphic phantom. Since mAs was held constant, mean dose decreased as pitch was increased, and vice versa.

To obtain the surface dose profile along the sagittal plane at the center of the phantom, two steps were performed. First, since MCNPX does not allow specifying mesh tallies along a non-straight line (e.g. the phantom surface locations along the sagittal plane), a set of rectangular mesh tally elements were used on the whole sagittal plane at the center of the phantom. Each mesh tally element has an x/y size of 2.968 mm x 2.968 mm and with a length of 2.5mm along the z-axis. The positions and sizes of mesh tallies were carefully selected so that only one material was included in each mesh tally. This two-dimensional mesh tally gave a dose distribution map of the central sagittal plane of the phantom, including all the air voxels. Second,

surface coordinates of the voxelized phantom were extracted along the interface between the air and the tissue and surface dose profiles were generated. As before, the resulting profiles were determined for each condition from the mesh tally and converted to absolute dose normalized to tube current (in mGy/mAs). From these profiles, the magnitude of variation was estimated based on the percent ripple.

#### 6.2.4.3. The Effect of Tube Start Angle

Because each simulation demonstrated a periodic behavior, the effect of source phase angle (or start angle of x-ray tube at the time the x-ray beam switches on) was investigated. In all previously described experiments, a tube starting angle of 0 degrees (corresponding to 12 o'clock in the gantry) was used. To further explore possible sources of variation due to start angle, the x-ray tube start angles were changed to be 90, 180 and 270 degrees for a clockwise rotation. Since the angular position of the x-ray tube at a specific table location would be different for various tube starting angles, the dose profile will shift according to different tube angular positions when x-ray is turned on. These experiments were performed with pitch =1.5 and the measured beam width (34.1mm).

#### 6.2.4.4. Varying Pitch to Obtain a Smooth Surface Dose Profile

The effectiveness of minimizing surface dose variation by adjusting pitch values was investigated. Previous published work proposed that a smooth surface dose can be produced by using a pitch value of

$$P = \frac{S\text{-}R}{S} \qquad \text{Equation 6.1}$$

where S is the source to isocenter distance and R is the distance from isocenter to the point of surface dose measurement.[110] If the measured beam width is taken into account, then this pitch value would be adjusted to be

$$P' = \frac{A}{N} * \frac{S\text{-}R}{S} \qquad \text{Equation 6.2}$$

where A is the measured beam width, and N is the nominal beam width. This is similar to the approach of Vrieze et al [121] who did this work with measurements. This pitch can be called the Completely Smoothed Profile Pitch (CSPP). For the Siemens Sensation 64 CT scanner, S=57cm. For the 32 cm CTDI phantom, phantom radius R=15cm (measurement is at 1cm below surface for CTDI body phantom); for the 24 x 1.2 nominal collimation, N=28.8mm and A=34.1mm. The pitch value using the ideal approach for a CTDI body phantom is 0.74, while the CSPP value, where the measured beam width is taken into account, is 0.87.

Therefore, two separate experiments were performed to obtain the surface dose profiles for the CTDI phantom using the measured beam width (34.1mm), but different pitch values of 0.74 and 0.87.

Similar experiments were also performed on the anthropomorphic phantom. However, R is not uniform along the z direction in this case. R at the neck region (from isocenter to the anterior surface of the neck) is approximately 7cm, and R at chest region (from isocenter to the anterior surface of the chest) is about 11cm. Therefore, two CSPP values, 1.04 and 0.96, were calculated separately for these two radii using equation (2) with measured beam width taken into

account. They are referred to as neck pitch and chest pitch, respectively. In addition, one more pitch value was evaluated which was the midpoint of these two pitch values (1.0) to investigate if one pitch could smooth the dose variation for both neck and chest regions. Simulations were performed using the measured beam width (34.1mm) and these three pitch values. Again, the surface dose profiles were determined for each condition from the mesh tally and converted to absolute dose normalized to tube current (in mGy/mAs). The percent ripple was calculated from these profiles.

#### 6.2.4.5. Evaluation of Peripheral Dose Curve on CTDI Phantom Using a Virtual Farmer Chamber

To investigate the peripheral dose variation behavior in practical measurements, an additional peripheral dose distribution was generated using a virtual dosimeter with size larger than the size used in simulation (1 mm). The size of the dosimeter will determine the pattern of the surface dose variation because of the integration that it performs along the z direction. A 24 mm long virtual Farmer Chamber, which is a typical size, was chosen to evaluate the effect of dosimeter size. The dose distribution curve for this dosimeter was obtained by convolving the 1 mm resolution peripheral dose distribution with a 24 mm long region. This will be illustrated by simulating an acquisition with pitch 1.5.

#### 6.2.4.6. Varying Pitch to Obtain a Uniform Dosimeter Output Based on the Dosimeter Length

Since the general shape of surface dose variation has a periodic distribution, if the length of the dosimeter roughly equals the period observed in the dose variation curve, the dosimeter

reading will be the average dose variation over one complete cycle. Because the period of the dose variation curve is basically the table feed per rotation, (i.e. the product of nominal beam width and pitch), a specific pitch value can be determined to obtain that average value; this pitch is the detector length divided by the nominal beam width and can be called the Functionally Smoothed Profile Pitch (FSPP). For scans using this pitch, although the surface dose profile itself still has variations, the period of this variation matches the size of the dosimeter so that the average dose is measured, regardless of where this detector is located along the z-axis. FSPP is a function of detector length in the z-direction and nominal beam width. For a 24 mm long Farmer Chamber and the nominal beam width used here (28.8mm), the FSPP pitch would be 0.83. To demonstrate this, an acquisition was simulated with pitch 0.83 for the CTDI phantom and surface dose profile was obtained as before; it should be noted that the actual beam width of 34.1mm was used for this simulation. The dose distribution curve using this pitch value for the virtual dosimeter was obtained by the same convolution method described above.

### 6.2.5. Measurements on the Scanner for Confirmation of the Simulations

To confirm that the peripheral dose profile would have the same behavior as in the simulations, OSLs were used for a contiguous axial scan on Siemens Sensation 64 MDCT with nominal beam width of 28.8mm. 32cm CTDI phantom was used and OSLs were put in a specific holder which can fit in the peripheral cavity at 12 o'clock of the phantom. OSL results were obtained similar to the methods described in section 6.2.2.

## 6.3 Results

The MCNPX run time for the CTDI body phantom geometry was approximately two hours for 100 million source photons using an AMD Athlon 64 Processor running at 2.00 GHz. Simulations took approximately 48 hours for the anthropomorphic model for 400 million source photons. The number of histories used for the simulations where the pitch value was varied to smooth the surface dose variation was set to be 800 million for better statistics. The relative errors of the Monte Carlo simulations were within 3% for CTDI phantom and within 2% for anthropomorphic phantom for most voxels in the mesh tally. A few mesh tally voxels (less than 1%) had relative errors as high as 6%. This may due to the limited number of entrance photons for that specific mesh tally voxel in the simulation. Overall, these statistics were considered acceptable.

### 6.3.1. Peripheral and Center Dose Profile for the CTDI Body Phantom

For the CTDI phantom, the central dose profile for pitch = 1 is shown in Figure 6.1, which is representative of all the center dose profiles because they have similar uniform distributions. This is because of the smoothing effect of scattered radiation within the phantom. The results of the peripheral dose profiles for all combinations of pitch and simulated radiation beam width are shown in Figure 6.2. This figure demonstrates that although radiation dose profiles at the center position of a CTDI phantom are relatively constant, the increased beam divergence with wider beams results in peripheral dose variations, generating pronounced peaks and valleys instead of uniform distributions. Even for the contiguous axial scan (second row), there are dramatic peaks and valleys in the peripheral dose distribution. For the case where the simulated beam width is equal to the nominal beam width, the percent ripple can be as high as

50%. For the case where the simulated beam width is equal to the measured beam width, though the valleys are not as deep or as wide, the percent ripple is still nearly 50%. The contiguous axial scans (second row of Figure 6.2) also show that when the radiation beam width is increased (for this same nominal collimation), not only do the valleys fill in, but new peaks are created at the locations where the valleys used to be and reach values nearly 50% higher than the previous peaks.

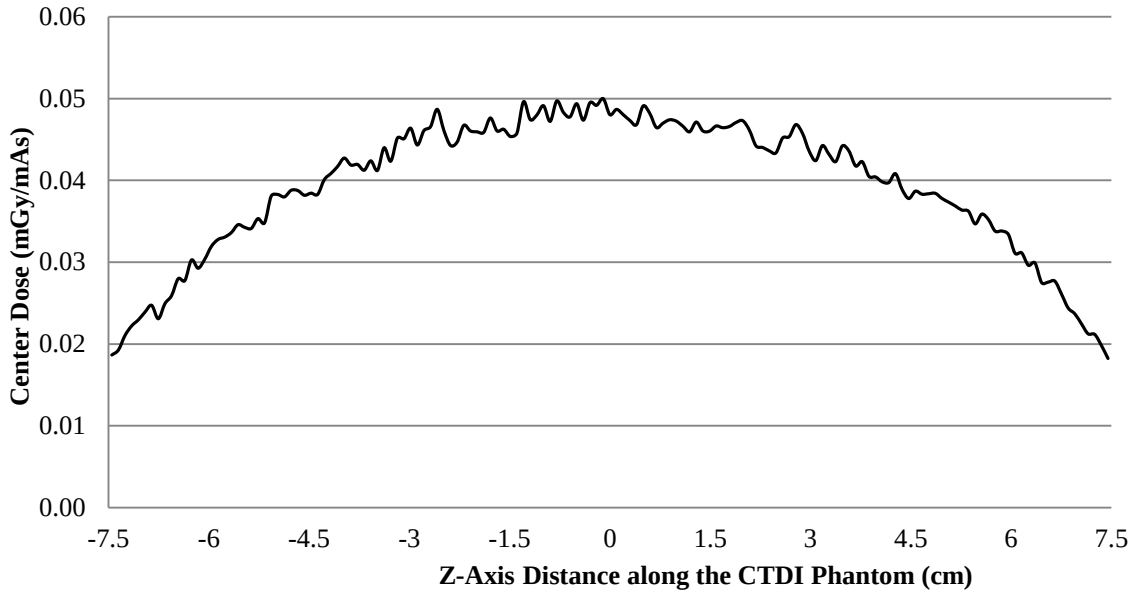


**Figure 6.1 Center dose profile for 32cm CTDI phantom, pitch 1.0 helical scan, measured beam width 34.1mm. All central profiles were similar due to the smoothing effect of the large scatter contribution in the center of a large phantom.**

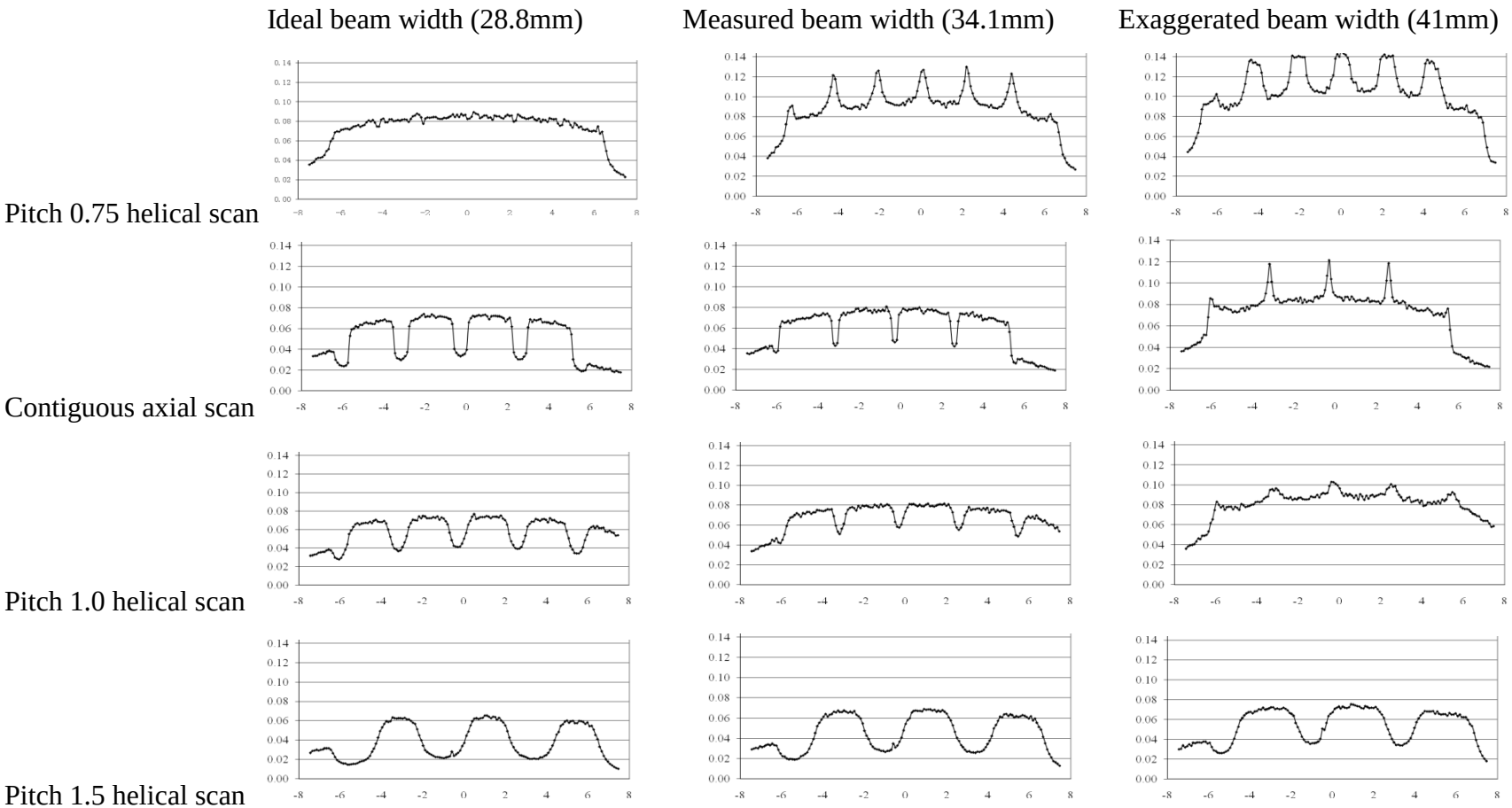


**Figure 6.2 Peripheral CTDI dose profiles for all radiation profile widths and pitch values used in this study.**

Figure 6.2 also demonstrates that pitch 1.0 helical scans show similar behavior to the contiguous axial scans, although the valleys are shallower and wider than the axial scans. Additionally, the new peaks created by the exaggerated beam width case are not as high (only increasing approximately 20%). The pitch 1.5 helical scans show wider and deeper valleys (as expected), with the percent ripple being as high as 70%. The results from an overlapping pitch (pitch = 0.75) provide a smooth peripheral dose profile in the case where the simulated beam width is equal to the nominal beam width (ideal case) , but when the simulated beam width is equal to the measured beam width (34.1 mm), then peaks are created that can be 40% higher than the previous peak values.

Figure 6.3 is a schematic figure to demonstrate the role of beam divergence, even for a contiguous axial scan. This figure shows that for a contiguous axial scan with a radiation beam width at isocenter equal to the nominal beam collimation (e.g. Figure 6.2, second row, first column), the central region is contiguously covered by the primary beam but the surface of the CTDI phantom is not.

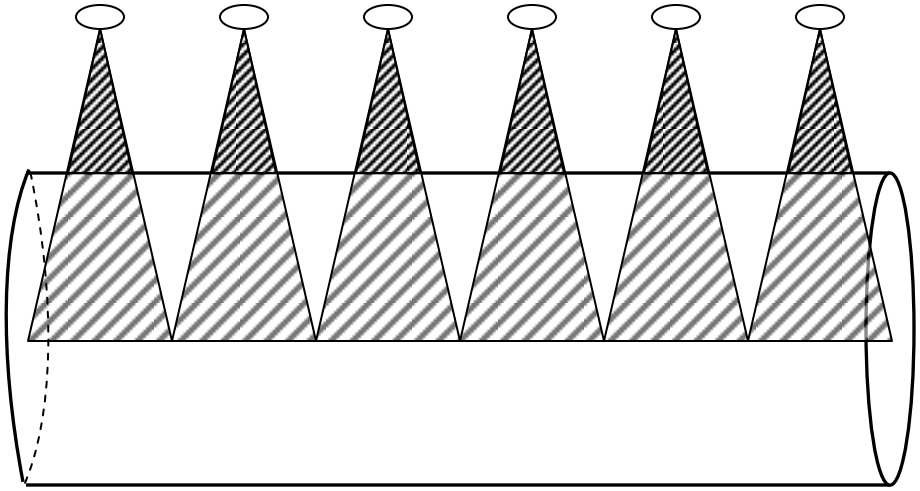

**Figure 6.3 Lateral view of cylindrical phantom and divergent x-ray beam to illustrate the effect of cone angle. An ideal beam width is assumed (FWHM = nominal beam collimation) for the condition of a contiguous series of axial scans. The surface is not completely covered by the primary entrance beam. The small ellipses represent tube positions.**

Figure 6.4 demonstrates the effects of varying only the pitch using measured beam width (34.1mm) condition. A helical scan of pitch 1 shows that the percent ripple is 30%. For a contiguous axial scan the percent ripple increases to 45%. For extended pitch 1.5, it can be as high as 62%. For pitch 0.75, the edges of the subsequent cone beams overlap and a new peak is created which results in a 40% increase.

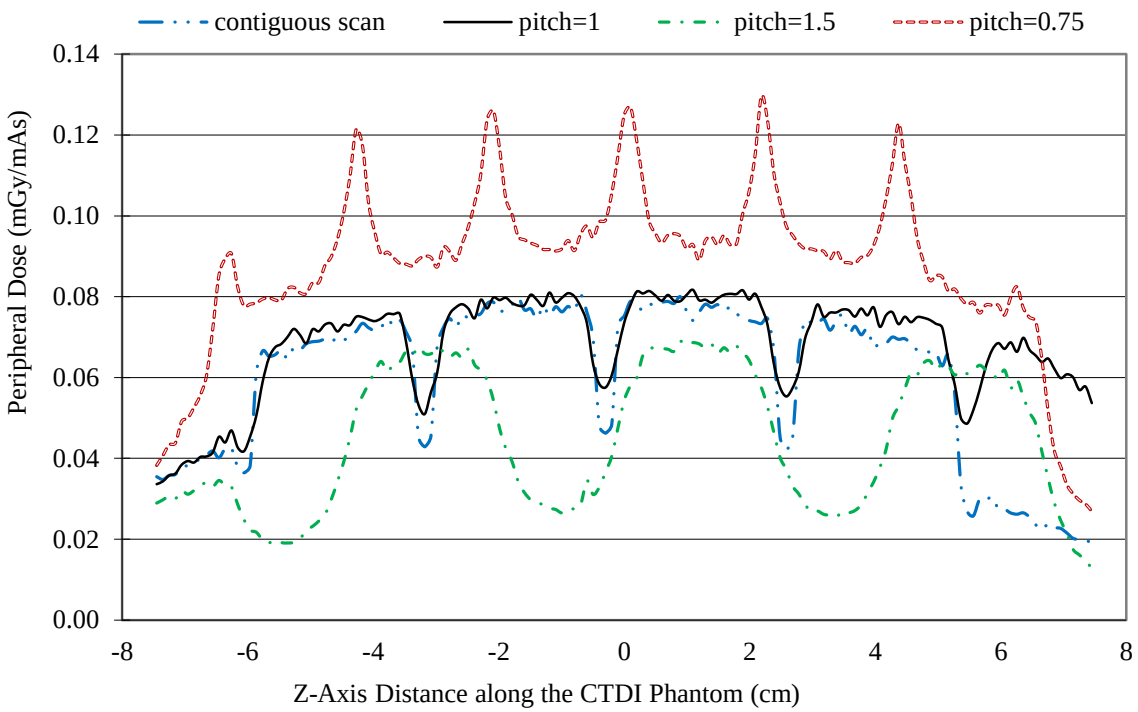


**Figure 6.4 Peripheral dose profile on 32cm CTDI phantom for different pitch values,(a contiguous axial scan and helical scans with pitch values of 0.75, 1, and 1.5) for a constant beam width (here using actual measured beam width of 34.1 mm).**

The effect of different radiation beam widths is shown in Figure 6.5 for a given nominal beam width. This is best illustrated for pitch 1.5 helical scans where no overlap of the primary beam exists. As beams width increases, there is more exposure (both primary beam and secondary scatter), and hence the height of both peaks and valleys increases. Also, as the beam width increases, the valleys between every two beams are filled in due to the decreasing distance between the edges of the beams. Thus, amplitude variations (from peak to valley) for larger beam widths are less dramatic than for narrower beam widths. For example, the percent ripple is as high as 70% for a beam width of 28.8mm and decreases to 53% for a beam width of 41mm. The peripheral dose distribution at various beam widths for pitch 1.0 is shown in Figure 6.5b.

This Figure demonstrates that with wider radiation beams widths, complete filling in of the valleys can occur and result in new peaks being formed where the edges of the radiation beam overlap in adjacent rotations, even for pitch 1.

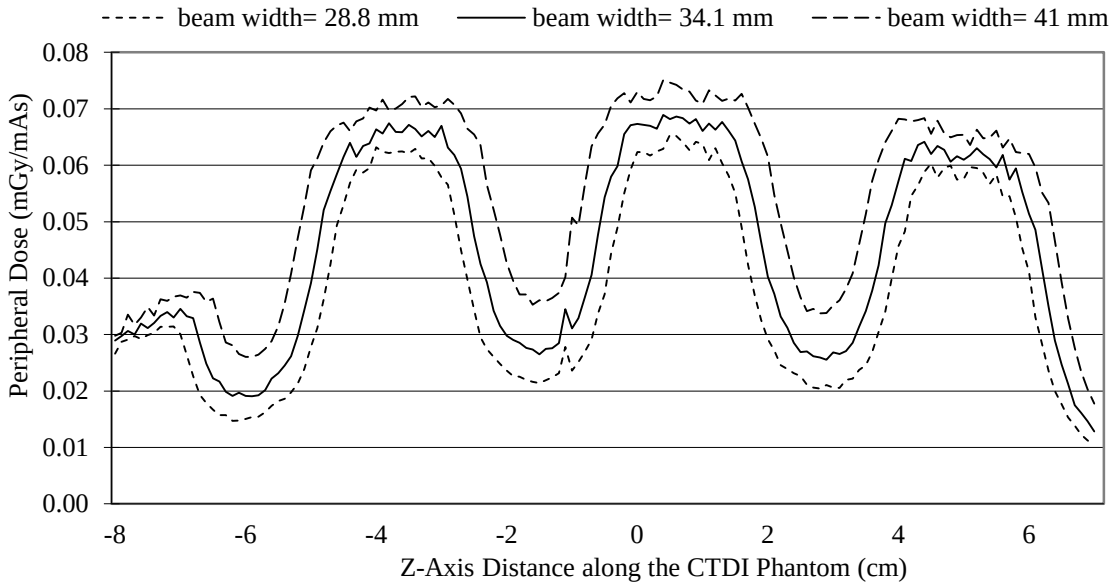


a.

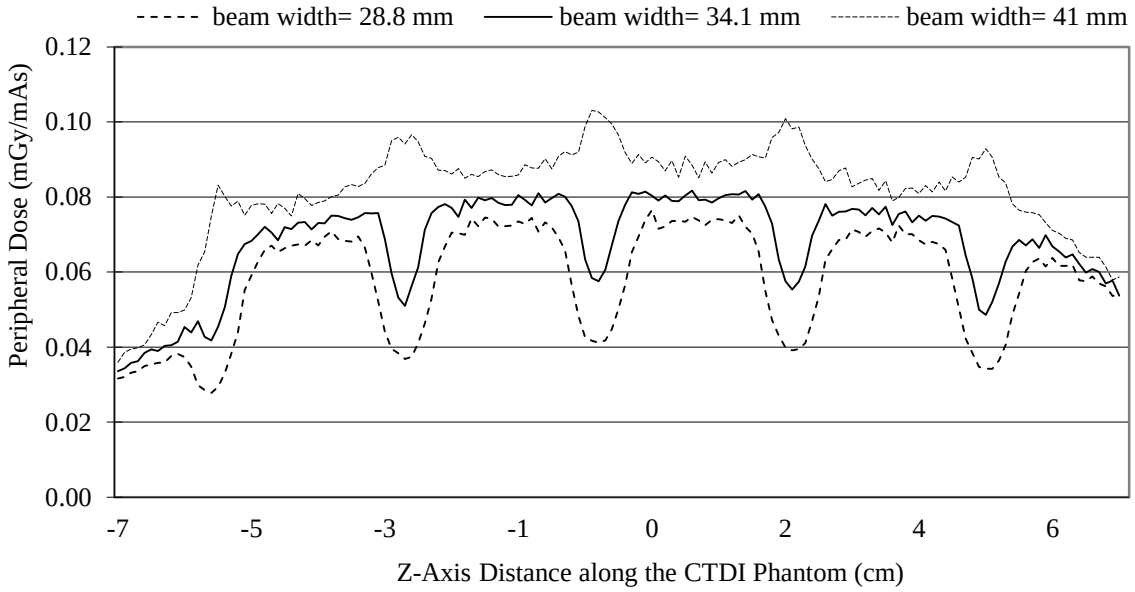


b.

**Figure 6.5 a) Peripheral dose profiles on 32cm CTDI phantom for three different radiation beam widths using the same nominal (28.8mm) collimation and the same helical pitch (1.5). b) Same as a) but with pitch 1.0. As beam width increases, new peaks occur where there is overlap of primary beams.**

### 6.3.2. Surface and Center Dose Profile on Anthropomorphic Phantom

The radiation dose profiles at the anterior surface position of the anthropomorphic phantom were examined for both helical and contiguous axial scans. These simulations gave similar results to CTDI phantoms in terms of surface dose variation. Figure 6.6a shows the anterior skin dose profile for helical pitch 0.75, pitch 1.0, and pitch 1.5 as well as contiguous axial scan with the measured beam width of 34.1mm. The surface dose (skin) is higher close to the neck region where the A-P phantom thickness is around 14cm, and it decreases at thoracic and abdominal locations where the thickness is about 22cm. Figure 6.6b is a sagittal view of the anthropomorphic phantom for reference. Helical scans of pitch 1.0 provide a more uniform dose profile through the chest and abdomen regions, where the percent ripple is 5%. For pitch 1.5, the percent ripple can be as high as 40%. For pitch 0.75, a peak is created which results in a 37% increase in surface dose.

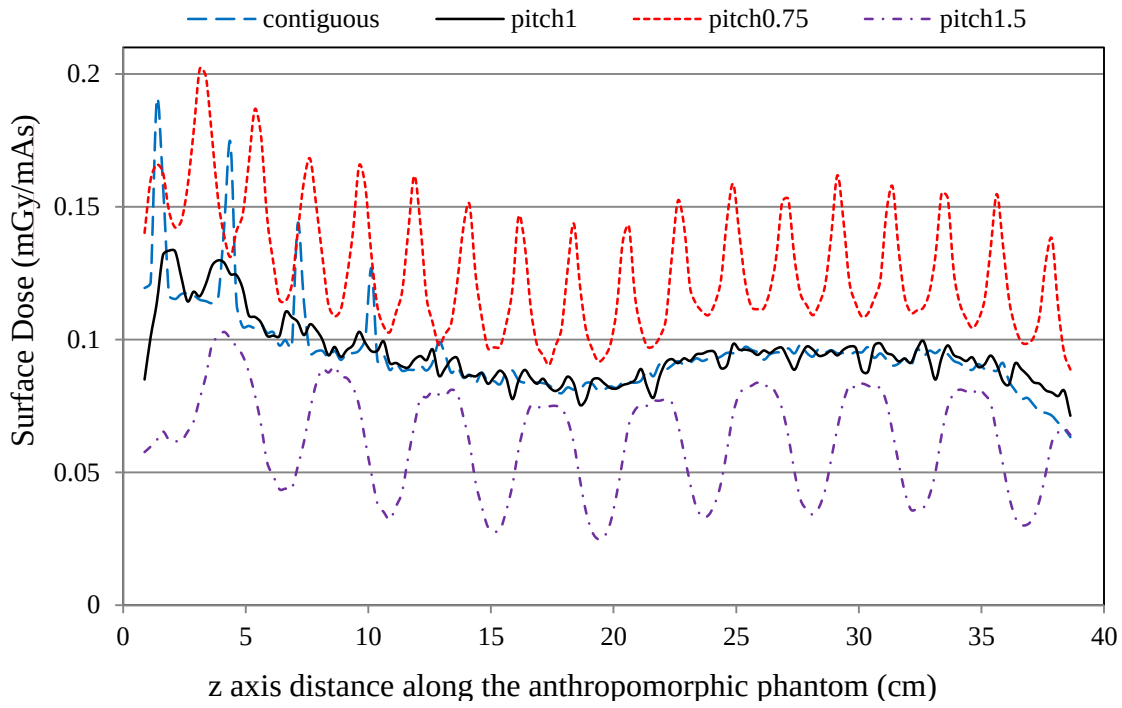


a.

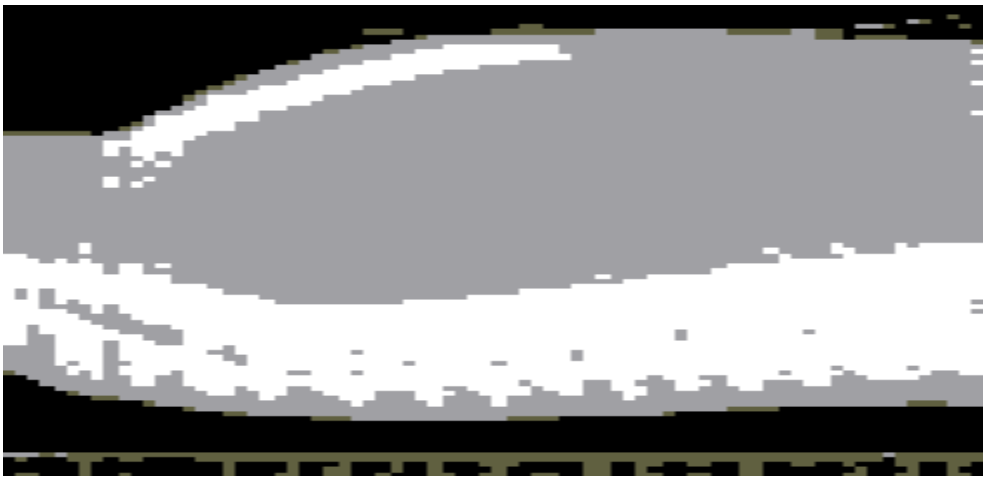

b.

**Figure 6.6 a) Surface dose profile for anthropomorphic phantom at pitch 0.75, pitch 1, pitch 1.5 as well as a contiguous axial scan. b) The bottom illustration shows the central sagittal plane of the phantom. The Anterior-Posterior thickness of the neck and thoracic regions is approximately 14cm and 22cm, respectively.**

### 6.3.3. The Effect of Tube Start Angle

Figure 6.7 shows the peripheral dose profiles at various tube start angles. This effect is best illustrated for a pitch 1.5 helical scan. As expected, different tube start angles create a phase shift in the peripheral dose profile, resulting in dramatic variation in dose at a given z-axis location. For a given location (z-axis position), the peripheral dose can vary by more than a factor of two depending on the tube start angles. For example, at the center location (0cm), the peripheral dose values range from 0.027 to 0.068 mGy/mAs depending on the tube start angle. Only the dose profiles for pitch 1.5 and measured beam width of 34.1mm are presented here, but the other simulation results were similar.

These surface dose variations would have significant implications for measurement of standard dose indices such as CTDIw. Though the current definition of CTDI is that it is measured with a single axial scan, there are active discussions to perform these standard measurements with helical protocols. In the above example, the CTDI value measured at the center position from a helical scan would be 0.035mGy/mAs. Adapting the current definition of $CTDI_w$ ( = (1/3)* $CTDI_{center}$ + (2/3)*$CTDI_{periphery}$) to these measurements, this would lead to $CTDI_w$ values which would range from 0.036mGy/mAs (when measured at the valley) to 0.055mGy/mAs (when measured at the peak), which leads to a difference as high as 50% between measurements. Note that this difference would be *only* due to differences in start angle (or essentially table position of the dosimeter). As will be shown in the sections below, there are strategies to reduce these variations using different pitch values and taking into account the length of the dosimeter.

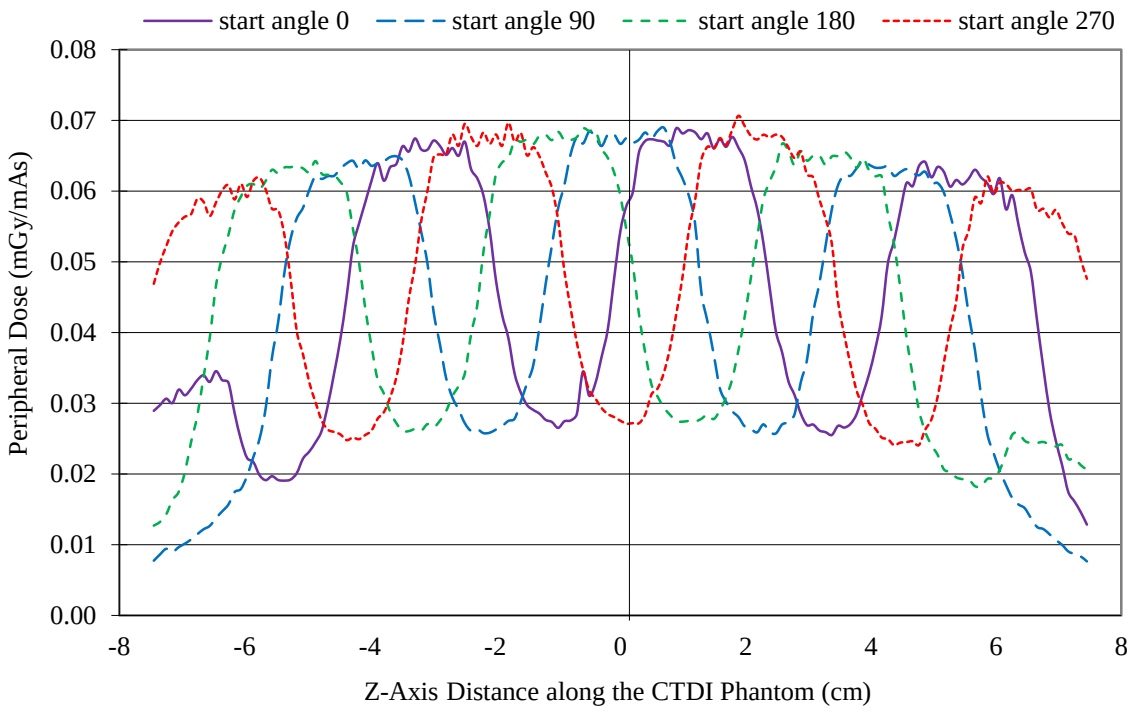


**Figure 6.7 Peripheral dose profile on 32cm CTDI phantom for different start tube start angles using a constant pitch 1.5 and measured beam width (34.1mm).**

### 6.3.4. Varying pitch to obtain a smooth surface dose profile

The effectiveness of CSPP for the CTDI phantom is shown in Figure 6.8, which shows that, with the measured beam width taken into account, the peripheral dose variation can be minimized. For this specific collimation setting, the CSPP value is 0.87. However, if the measured radiation beam width is not taken into account during the pitch calculation (pitch=0.74), then the peaks and valleys are still substantial. As discussed earlier, a pitch value that is too low causes beam overlap of primary radiation and creates new peaks. So it is important to take the measured beam width into account to arrive at a pitch value (described in equation 2) that minimizes peripheral dose variation. However, such an exact pitch value is not necessarily achievable in practice using commercial CT scanners. Figure 6.8 also shows the

peripheral dose profile for CTDI body phantom at the closest available pitch value 0.9 (comparing to 0.87). The difference between peaks and valleys is not trivial, with variations reaching 20%. This demonstrates that even when CSPP is selected based on the measured radiation profile, practical limitations may prevent a smooth surface profile from being obtained, and it may not be possible to obtain a completely smoothed profile when using a single small detector due to these variations.

The results from simulated scans using CSPP for the anthropomorphic phantom are shown in Figure 6.9, where neck pitch (1.04), chest pitch (0.96) and average pitch (1.0) were used. This shows that for the neck pitch value, the variation at the neck region can be reduced to about 9% (valley is 91% of the peak) but the variation at the chest region when using the neck pitch is still as large as 20%. It also shows that for the chest pitch value, the variation at the chest region is reduced below 8% but at the neck region the variation can still be as high as 16%. Choosing a midpoint pitch is a compromise rather than minimizing variations at both regions; resulting in variations that are nearly 20% in both the chest and neck regions. Therefore, for an anthropomorphic phantom where the distance between the surface to isocenter is not constant, there is no CSPP value which can perfectly smooth the surface dose curve. In addition, the heterogeneous nature of anthropomorphic phantoms also contributes to surface dose variation and cannot be controlled by the choice of pitch values.

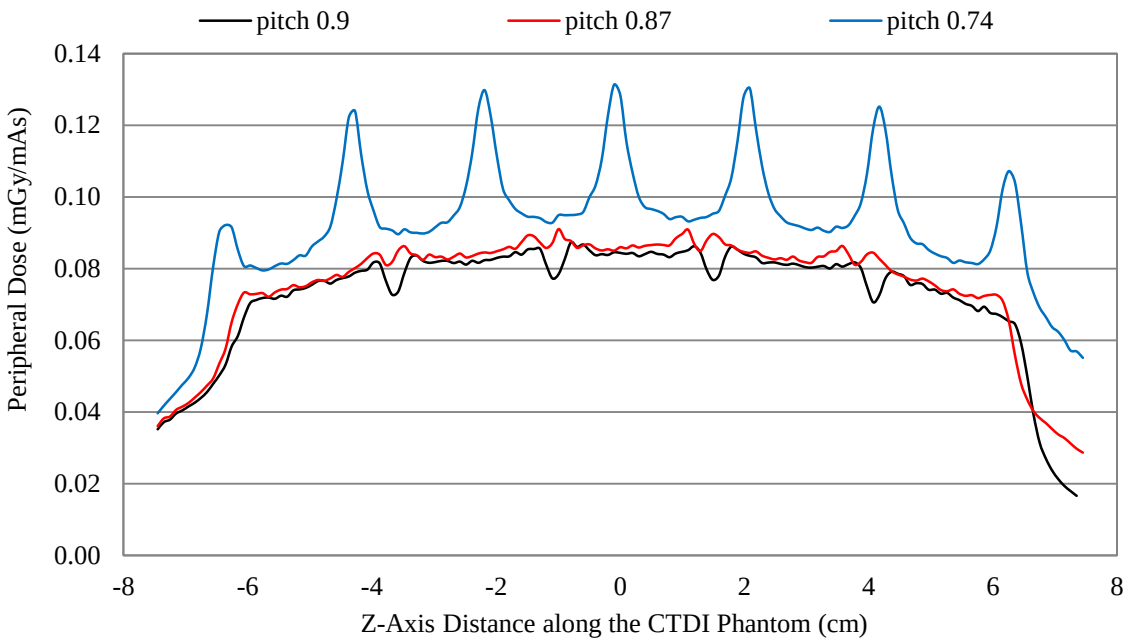


**Figure 6.8 Peripheral dose profile in CTDI body phantom for measured beam width 34.1mm, pitch 0.87, pitch 0.74 and pitch 0.9 helical scans. Pitch 0.87 is the desired pitch value predicted to produce the most uniform dose profile. Knowledge of the FWHM of the actual beam width is required to determine this value, as in equation 2. Pitch 0.74 is the calculated pitch value to smooth peripheral dose variations when the measured beam width is *not* taken into account. (i.e. the pitch calculated from equation 1.) Pitch 0.9 is the pitch value available on this scanner that is closest to the desired pitch value.**

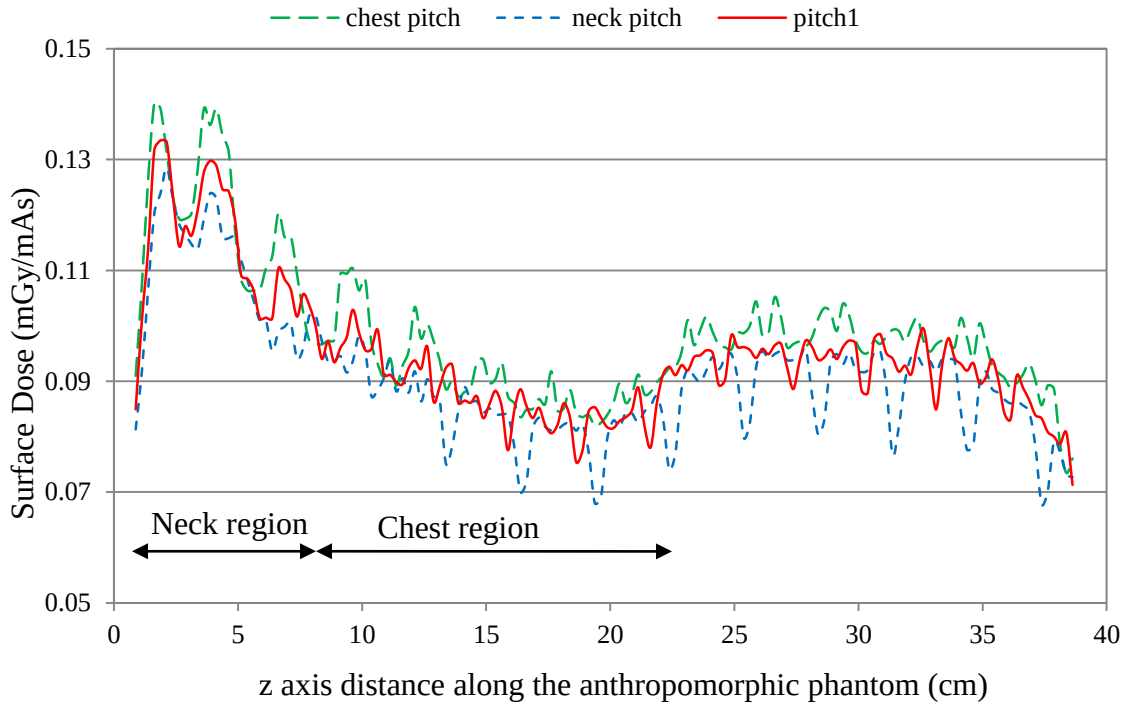


**Figure 6.9 Anterior surface dose profile on anthropomorphic phantom at chest pitch (0.96) to smooth the dose profile along the chest, neck pitch (1.04) to smooth the dose profile along the neck, as well as average pitch (1.0).**

These results show that the anthropomorphic phantom creates more complex patterns of surface dose than does the CTDI body phantom because of the heterogeneous composition and shape of the anthropomorphic phantom. Figure 6.10a shows the 2D dose distribution of the central sagittal plane for pitch 1.5 helical scan, with the same orientation in Figure 6.6b. This figure was generated using a temperature color map and indicates that the absorbed dose in the simulated bone materials (sternum and spine) is very high, because of the higher energy absorption coefficient. It also illustrates the heterogeneous nature of the dose distribution within the anthropomorphic phantom on the central sagittal plane. The periodic variation is clearly

observed in this figure and is most obvious at the peripheral positions (e.g. the anterior surface of the chest). Therefore, even the center dose profile (taken at depth as shown in Figure 6.10b) is not as uniform along the z-direction as in the cylindrical CTDI phantom (Figure 6.1).

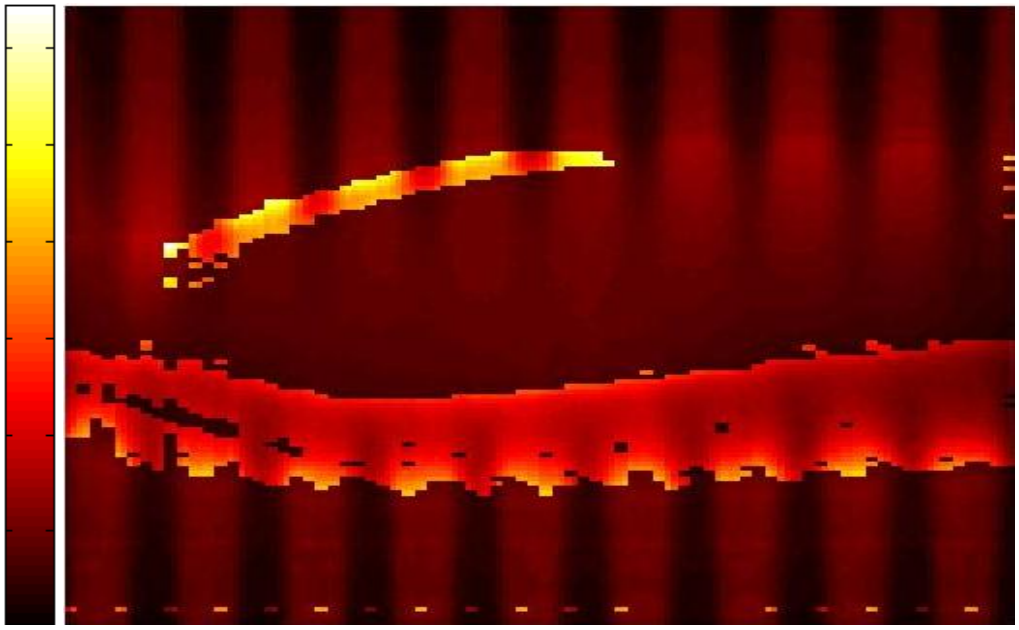

10a.

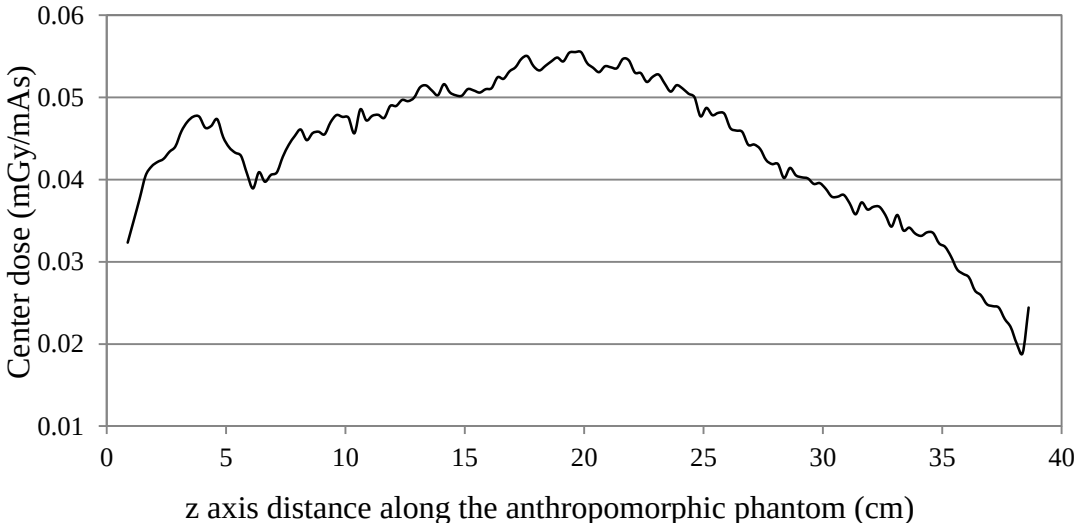


10b.

**Figure 6.10 a) The 2D dose distribution is displayed on the central sagittal plane of the anthropomorphic phantom, shown in Fig. 6b, for a pitch 1.5 helical scan. This is a temperature color map scale dose distribution, where white represents high dose and black represents low dose. b) The z-axis dose profile obtained at approximately the central depth of the phantom within this plane.**

### 6.3.5. Peripheral Dose Curve in CTDI Phantom Using a Virtual Farmer Chamber

In all of the results shown above for CTDI phantom, the voxel size along the z-axis direction was 1mm, providing a good representation of the dose as measured using small dosimeters such as TLDs or MOSFETs. However, when the dosimeter size is larger, the surface dose profile is altered due to the integration along the z-axis. This is illustrated in Figure 6.11, which shows the peripheral dose distribution for a 32 cm CTDI phantom that would be obtained using both 1 mm voxel tallies and a 24 mm long virtual dosimeter (e.g. Farmer Chamber) for a scan performed with the measured beam width (34.1mm) and pitch of 1.5. The curve for the 24 mm virtual dosimeter was obtained by convolving the original surface dose distribution with a 24 mm long square function centered at each point along the z-axis. This illustrates that the integration effect of the Farmer Chamber slightly averages out the dose variation. However, there are still substantial dose variations for pitch 1.5; the percent ripple is as high as 58%.

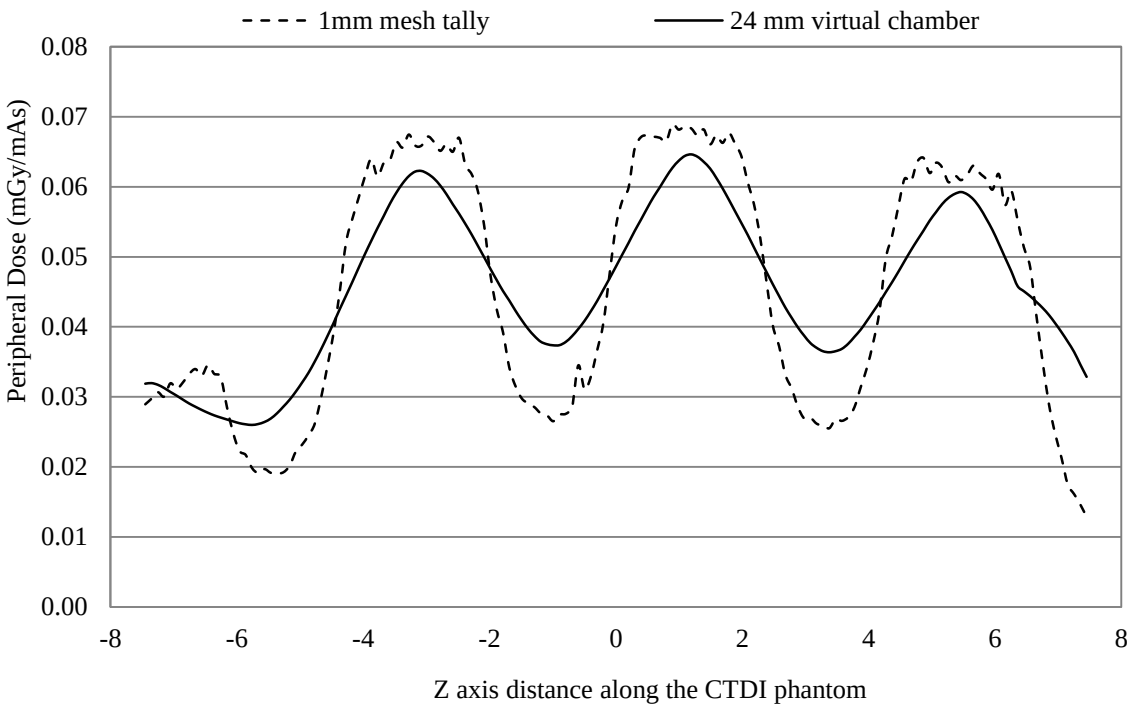


**Figure 6.11 The comparison of peripheral dose distribution from 1mm mesh tally and from a virtual 24mm long (z-direction) Farmer Chamber using a scan of a 32 cm CTDI phantom, measured beam width of 34.1mm and pitch of 1.5.**

### 6.3.6. Varying Pitch to Obtain a Uniform Dosimeter Output Based on the Dosimeter Length

Figure 6.12 shows the simulated surface dose profile using FSPP value 0.83 for 1 mm mesh tallies. It also shows the output of the 24 mm virtual Farmer Chamber. The results show that with this pitch, the surface dose profile measured with a 24 mm virtual dosimeter is very smooth. Simulations were also performed for pitch values close to FSPP and it was shown that the variation of the output of the chamber is within 5% when the pitch value is within FSPP ±0.17 (0.66 to 1.0). So FSPP is not as sensitive as CSPP in terms of the effectiveness to smooth

the surface dose variation. Unlike CSPP, a pitch value that is close to FSPP could also generate an output profile without too much variation.

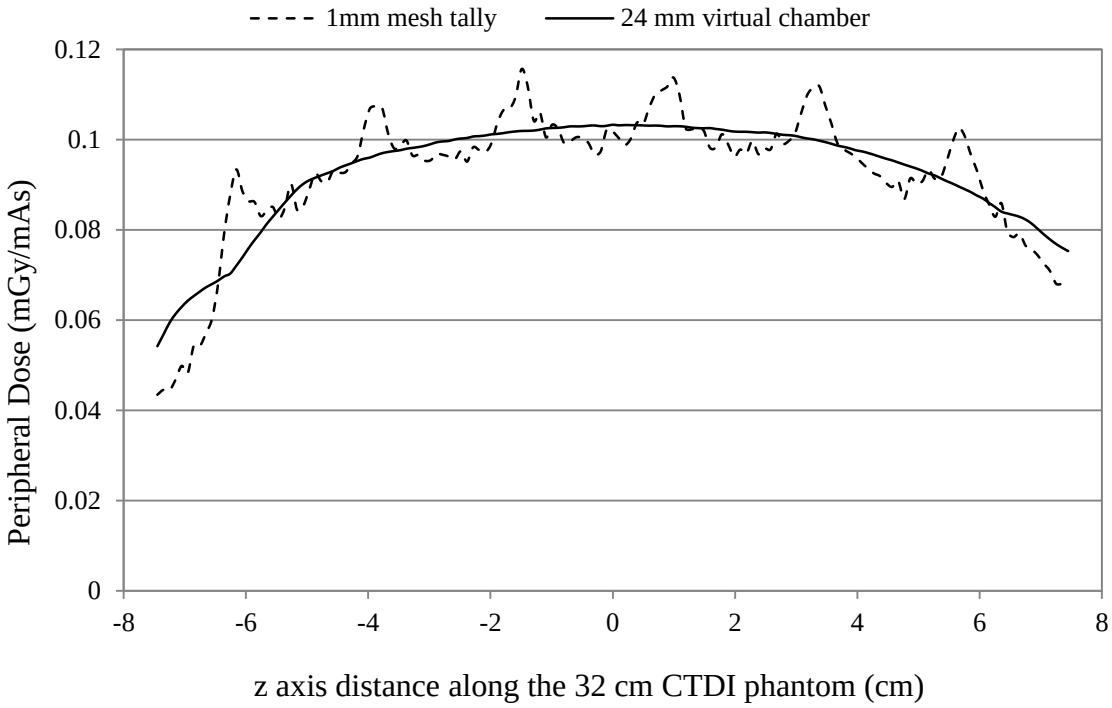


**Figure 6.12Surface dose profiles from the 1 mm voxel dose tallies and from the virtual 24 mm Farmer chamber for a pitch value of 0.83, which was the FSPP pitch value used to average out variations for the 24 mm long dosimeter.**

### 6.3.7. Measurements on the Scanner for Confirmation of the Simulations

The peripheral dose distribution at 12 o'clock position of a 32cm CTDI phantom from OSL measurements for a contiguous axial scan with 28.8mm nominal beam width is shown in Figure 6.13. The shape of this dose profile is very similar to the simulated one (Figure 6.2, row 2, column 2) in that both show peaks and valleys of approximately the same amplitude, width and frequency. They are not identical; possibly because an air filled ion chamber was modeled

in the simulation, rather than the OSL. These results are similar to those obtained in a previous publication[13], where good agreement was achieved for the peripheral dose profiles between simulations and measurements using MOSFETs.

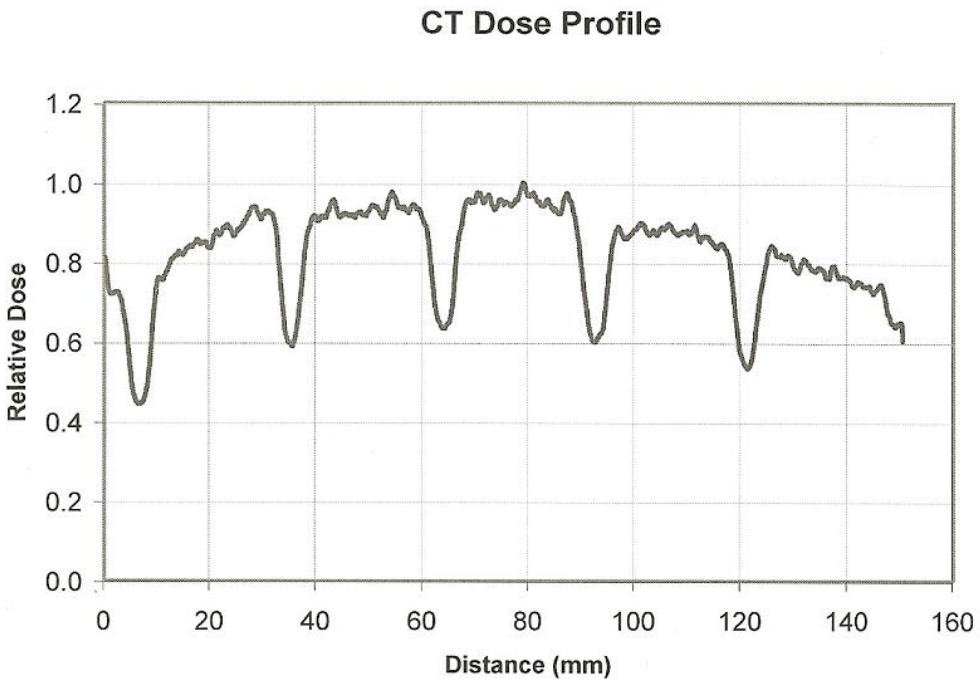


**Figure 6.13 Peirpheral dose profile on a 32cm CTDI phantom from OSL measurements for a contiguous axial scan with 28.8mm nominal beam width. Variation is clearly demonstrated as that in simulations.**

## 6.4 Discussion

In this work, Monte Carlo techniques were used to simulate the radiation dose distributions from a MDCT scanner. These profiles demonstrate a range of dose variability at peripheral positions, for both a homogeneous cylindrical phantom and a heterogeneous anthropomorphic phantom. These variations can have a significant impact on standard dosimetry

measurements (including those proposed) when helical scans are being used with small dosimeters. For CTDI measurements using a helical scan and small (24 mm long chamber), results from section 6.3.3 demonstrated differences in CTDIw values of up to 50% between measurements where only the tube start angle (an uncontrolled variable) was varied.

Peripheral dose profiles for the body CTDI phantom varied with pitch and beam width. In general, for both contiguous axial and helical scans, the entrance radiation dose was not always uniform along the z direction. Depending on the positions of the x-ray tube, some points along the surface at a given z-axis location are exposed to entrance, exit and scattered radiation, while points on the same surface at other z-axis locations are exposed only to exit and scattered radiation. The difference between the maximum and the minimum values of a surface dose profile depended on several factors, but was essentially determined by how uniformly the surface was irradiated by the primary entrance beams.

Generally, the variation of the surface dose distribution becomes larger when the pitch is higher, the simulated beam width is narrower, or the point of interest is more distal from isocenter. However, there are also conditions that can result in a uniform surface dose distribution such as that caused by a wider beam width, shown by the 41mm beam width with pitch 1 scan in Figure 6.2; or as caused by a lower pitch value, as the 28.8mm beam width with pitch 0.75 scan in Figure 6.2. There are also conditions in which wider beam widths and lower pitch values result in overlap of subsequent beams which then result in higher peak values as shown first in Figure 6.2 and specifically illustrated in Figure 6.4 (constant beam width and

varying pitch values) and Figure 6.6 (constant pitch, varying beam widths). These newly formed overlap regions can have doses as much as 40% higher than in areas where the primary radiation is not overlapped at the phantom surface.

The tube start angle is significant when determining the dose at a certain surface point because of the phase shift effect. In clinical applications using commercial CT scanners however, tube start angle is typically unknown and not under the user's control. As shown in Figure 6.7, the dose at a certain point can vary by a factor of more than two across different tube start angles. This can be a large source of error when determining surface dose on a patient or an anthropomorphic phantom, especially when the surface is farther from isocenter and especially when single measurements are made. Because the tube start angle is not under the user's control, it is generally not possible to reproduce multiple scans using the exact same start angle. Even if repeat measurements are made, there is no assurance that the range of possible start angles (and therefore the range of surface doses) has been adequately represented.

In all, for a homogeneous CTDI body phantom, the 'frequency' of the peripheral dose distribution decreases as the nominal beam collimation and pitch increase. The 'phase' depends on the tube start angle. The 'amplitude' increases with distance from isocenter. The shape of the distribution depends on the simulated beam width and pitch. These factors together determine the pattern of the surface dose variation. The results from this study also reveal the complexity of estimating surface dose in a complex heterogeneous anthropomorphic phantom or even in simple geometries such as a CTDI phantom. The limitation of this study is that only 32cm PMMA

phantom and only one set of collimation (28.8mm) were investigated. Therefore the results shown in this study are likely to be one of the worst case scenarios. However, since larger cone beam angle and higher pitch values may be used for fast CT scanning, and since very wide nominal beam width (>40mm) MDCT scan systems are being introduced, careful consideration should be made before the determination of surface dose.

Despite these significant variations, there may be several approaches to obtain reasonably accurate and reproducible surface dose measurements from helical scans. One appropriate approach when small (approximately 1 mm along z-axis) dosimeters are used is to increase the sampling frequency, which requires a large number of small detectors placed close enough to each other along the z-axis direction to adequately sample both the peaks and the valleys of the surface profile. A second approach is to manipulate pitch to be CSPP values so that the resulting surface dose will be more uniform. Dixon proposed a method to minimize the surface dose variation by using a pitch value less than or equal to the value described in equation 1[110]. Equation 1 was modified in this study to use the measured beam widths rather than nominal beam width, resulting in equation 2. Scanning with this CSPP value created a nearly smooth surface dose distribution. However, in practice this approach may be limited; the exact pitch value desired may not be available on a commercial scanner. In addition, for an anthropomorphic phantom, a single pitch value will not produce a constant surface dose value because the thickness of the phantom is not uniform and the materials are heterogeneous.

These findings have potential implications for point dose measurements in cylindrical or anthropomorphic phantoms, such as TLDs, MOSFETs, or small Farmer chamber measurements, including those being proposed as new dose metrics (such as those being developed by AAPM TG111). Depending on the size and type of the dosimeter, the pattern of the surface dose distribution variation can be affected by both dosimeter size and spacing. Furthermore, if the dosimeter has such a length in z direction that the sample length equals to the period of the surface dose distribution curve (or an integer multiple of the period), the output of the dosimeter is still uniform. This can be expressed using the following:

$$\text{Dosimeter length} = i * \text{period} = i * \text{table feed per rotation} = i * N * \text{pitch} \quad \text{Equation 6.3}$$

Where N is the nominal beam width, and i is an integer number starting with 1. Therefore, a pitch value can be chosen that will result in a smooth surface dose profile:

$$\text{FSPP} = \text{dosimeter length} / (i * N) \quad \text{Equation 6.4}$$

Figure 6.12 showed the dosimeter output for this desired pitch value when i is 1 (FSPP). Although the actual distribution of surface dose was not uniform, FSPP created a sampling interval where the 24 mm long virtual dosimeter was able to integrate over one full period of the dose distribution. The detector output is uniform and it represents an average of the surface dose.

This can be a third method to reduce surface dose variations in terms of practical measurements. In addition, since the pitch is not required to be the exact FSPP value to generate relatively smooth chamber output profile, this method has less limitation from the availability of the pitch on commercial scanners. However, this method is limited by the fact that FSPP is

related to the dosimeter length in z-direction and the nominal collimation used. For example, if a 3mm TLD and 28.8mm nominal beam width are used, the FSPP is 0.1, which is too small to be practical.

The second and third approaches proposed above involve the adjustment of pitch, which could reduce the variability of surface dose. In practical measurement, the dose from scans using other pitch can be obtained based on the ratio of pitch values, because the average dose is inversely proportional to pitch values.

This work is not only relevant to measuring doses in homogeneous and heterogeneous (anthropomorphic) phantoms, but it may be exploited to investigate methods to reduce organ dose without compromising image quality, especially for radiation sensitive organs at or near the surface such as the breast, thyroid and lens of eye. This leads to the investigation of the effects of surface dose variations from larger cone angles and helical scans on individual organ doses using voxelized patient models, such as the GSF models[122]. This will be discussed in Chapter 7.

# Chapter 7 Reducing radiation dose to selected organs by selecting the tube start angle in MDCT helical scans: a Monte Carlo based study[†]

## 7.1 Introduction

Radiation dose to patients continues to be a significant concern to medical physicists and to the broader medical community as well. Radiation dose from CT exams has been identified as the largsest source of medical radiation exposure[123]. Specifically for CT scans, various approaches have been developed to reduce radiation dose, including tube current modulation[124], adjusting/lowering mAs for patient size[125,126] and lowering kVp (especially for studies using iodinated contrast[127]), while maintaining diagnostic image quality.

One commonly used metric to evaluate risk from radiation is the effective dose, calculated from a weighted average of absorbed dose to individual radiosensitive organs as defined by ICRP[128]. While effective dose is very useful, it has been suggested that a better method to estimate risk would be to estimate the radiation dose to specific radiosensitive organs, which can be used in biological models to estimate the probability of radiation induced carcinogenesis and genetic effects[1,3,4,128,129].

[†] This chapter is based on the following publication:

Zhang D, Zankl M, DeMarco JJ, Cagnon CH, Angel E, Turner AC, McNitt-Gray MF. "Reducing radiation dose to selected organs by selecting the tube start angle in MDCT helical scans: a Monte Carlo based study", Medical Physics, 36(12), 5654-64, 2009.

Chapter 6 has shown that the surface dose distribution resulting from helical scanning of either a standard dosimetry phantom, (32 cm CTDI phantom), or an anthropomorphic phantom,

is periodic[130,131]. It was also shown[130] that the period is influenced by the actual radiation beam width and table movement. This work also demonstrated that the magnitude of the variation could be large, with maximum values greater than twice the minimum values under some conditions (e.g. pitch =1.5). This magnitude of variation has been shown in both homogenous cylindrical phantoms as well as heterogeneous anthropomorphic phantoms.

Because of the periodic nature of this dose pattern, the effect of the tube start angle (essentially determining a phase shift of the dose distribution) was investigated and it was shown that the tube start angle determined the locations of the high dose and low dose regions. For example, for a scan using pitch 1.5 and nominal beam width of 24 x 1.2mm, the simulated longitudinal dose distribution at the surface of a 32 cm diameter CTDI phantom along the z-axis is shown in Figure 7.1. This figure also describes the region where the X-ray beam turns on and off and the beginning and end of image data collection. The shape of the dose variation usually appears as a sinusoidal function because of the rotation of the CT tube. This creates “cold spots” (locations where the dose is minimum) along the z-axis. As the tube start angle changes, the distribution of these cold spots will “move” along the z-axis.

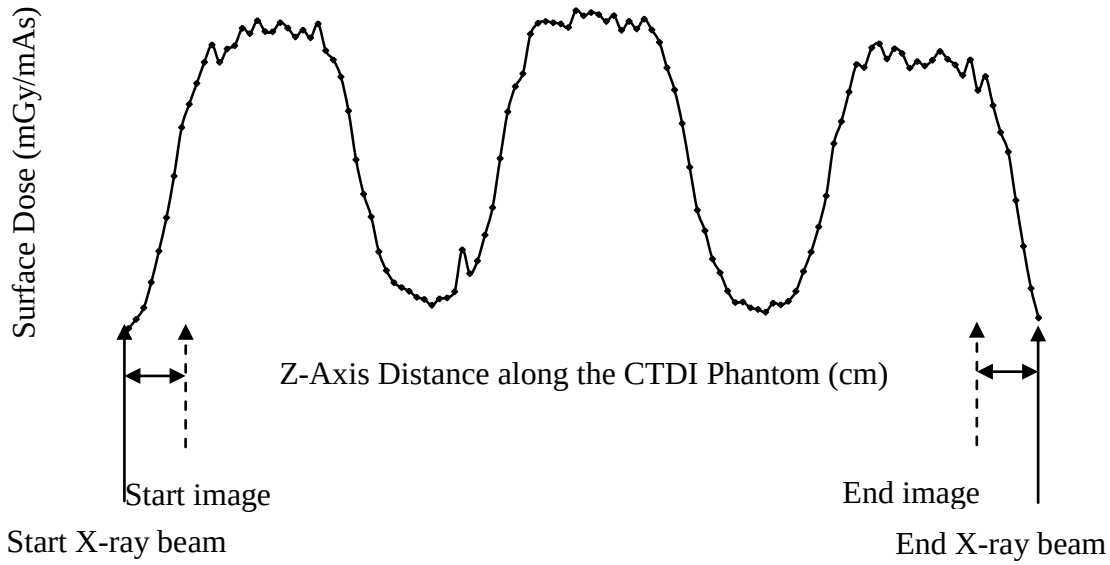


**Figure 7.1 The dose distribution along the z-axis on the surface of a CTDI 32 phantom undergoing a CT scan with nominal beam width of 28.8mm and pitch 1.5. The locations of X-ray beam on, X-ray beam off, start image data and end image data are also shown. Double headed arrows indicate regions of overscan.**

This concept is illustrated in Figure 7.2, which shows a divergent x-ray beam and the corresponding surface dose distribution along the z-axis under two scenarios with different tube start angles. An illustrative patient with a schematic indication of the location of the breasts is shown in the bottom of the figure as well. In the upper scenario, the cold spots occur at the location of the breasts, so the breast would receive lower dose, as opposed to the lower scenario, where the breasts would receive higher dose.

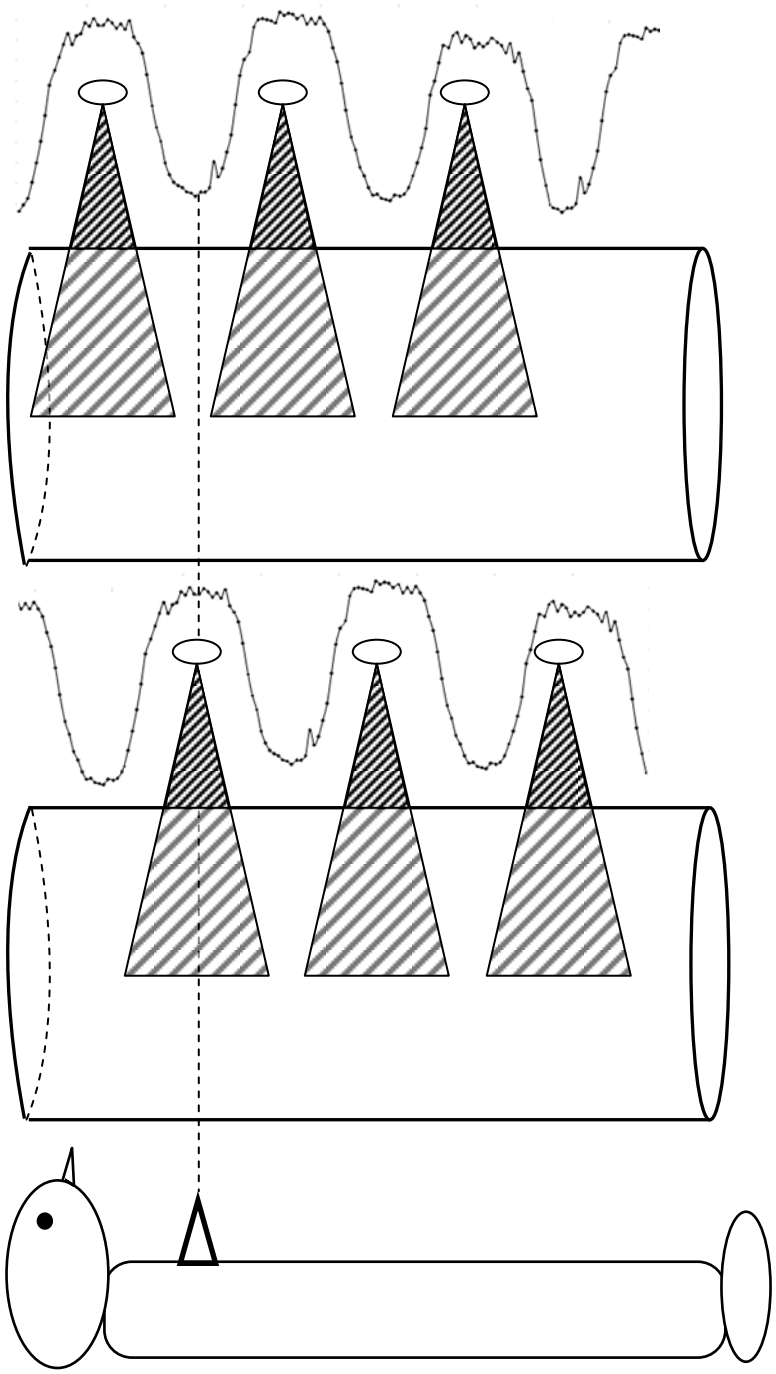

**Figure 7.2 Diagram illustrating the tube position and corresponding surface dose distribution along z-axis under two scenarios with different tube start angles at pitch 1.5. An illustrative patient with schematic indication of the location of the breasts is shown in the bottom as well. This figure shows that the dose to the breasts of the patient can be affected by selecting different tube start angles.**

Therefore, the purpose of this work was to extend the previous simulation work to investigate the effects these phase shifts, caused by different start angles, on organ doses in patients. While current MDCT systems do not allow the user to control the start angle, this study investigates the feasibility of exploiting this sinusoidal behavior to reduce the dose to a specific organ by varying the tube start angle, especially for a small peripheral organ on small patients. To do this, we simulated CT scans under different conditions (pitch, collimation, etc.) for different patient models (infant, small child, adult female and pregnant patient) under different start angle conditions to determine the effects on organ dose and to determine how much organ dose reduction was possible.

## 7.2 Methods

### 7.2.1. Patient Models

Several different patient models were evaluated and are described below. They are the Baby, Child and Irene models from the GSF (now: Helmholtz Zentrum München) family of computational, voxelized models[86,99] as well as a limited sample of the pregnant patient models described in Angel et al 2008[100]. For the GSF models, this included all radiosensitive organs, though only 6 are explicitly studied in this work; for the pregnant patient models, only the uterus, gestational sac and fetus were explicitly studied; all other voxels were assigned to one of six tissue categories (air, lung, fat, water, muscle or bone) based on Hounsfield Unit as described in Table 1 from DeMarco et al[98].

**Table 7.1 Age, gender, size and voxel descriptions of the 3 models used in this study.**

| Model | Age | Gender | Weight (kg) | Height (cm) | Voxel size (mm) |
|---|---|---|---|---|---|
| Baby | 8 weeks | Female | 4.2 | 57 | 0.85 x 0.85 x 4 |
| Child | 7 years | Female | 21.7 | 115 | 1.54 x 1.54 x 8 |
| Irene | 32 years | Female | 51 | 163 | 1.876 x 1.876 x 5 |

#### 7.2.1.1 GSF Phantoms

For this study, Baby, Child and Irene were selected from the GSF family to represent small patients with different body habitus. Some basic parameters of these three models are summarized in Table 7.1. The selected organs used for evaluating dose variation were the testes, ovaries, breasts, thyroid, uterus and eye lenses, whenever they are available in the phantom. These organs were selected because they are all relatively small in size and so higher dose reduction is expected for these small organs. It should be noted that although Baby and Child are female phantoms, testes were added into the gonads by GSF in order to calculate average gonads doses. Also, despite the fact that Child is a female phantom, no breast voxels were identified.

#### 7.2.1.2 Pregnant Patient Phantoms

In addition to GSF whole body phantoms with various age and size, a series of previously developed pregnant female models[100] with various gestational stages were used in this study to investigate the dose to fetus. The CT images of pregnant females were gathered from CT examinations performed under clinically indicated scans, such as trauma. The uterus, gestational

sac and fetus from these CT images were contoured by radiologists whenever they were visible. These three types of tissues were assigned as separate individual organs in the phantom and they were used to evaluate the dose variation caused by tube start angle in CT scans. There were in total 24 pregnant female models in this series of phantoms, from which 4 of them were selected for this study to represent different gestational stages, with emphasis on the early gestational stages because the size of the fetus is smaller. These four models are referred as F26, F10, F7, and F31 in this study, using the same nomenclature as in Angel 2008. The voxel size for each model is 2.4mm x 2.4mm x 5mm. The fetal age, size of the uterus in longitudinal direction and the studied regions for each model are summarized in Table 7.2. The uterine length in the longitudinal direction for each model was estimated from the original voxel data.

**Table 7.2 The size, gestational age and related information for studied pregnant female phantoms in this work (model refers to the patient model from Angel 2008).**

| Model | Gestational Age | Uterine Length | Studied regions | | |
|---|---|---|---|---|---|
| | (week) | (cm) | Uterus | Gestational sac | Fetus |
| F26 | 5 | 7 | √ | √ | - |
| F10 | 7 | 6 | √ | √ | - |
| F7 | 12 | 7.5 | √ | √ | √ |
| F31 | 19 | 18.25 | √ | √ | √ |

### 7.2 2. Organ Dose Estimation

UCLA CT Dose Simulation Package was used to estimate organ dose. As described in Chapter 3, Under charged particle equilibrium condition the absorbed dose to each voxel is

equivalent to the collision kerma in this voxel, which was calculated by multiplying the mass energy-absorption coefficients with the energy fluence evaluated by MCNPX based on track-length estimation. Then the mean dose to an organ was estimated by averaging the dose to each voxel across all the voxels belonging to the organ. All the organ dose results were converted from MCNPX raw output to absolute dose normalized to tube current (in mGy/mAs) using normalization factors calculated from scan measurements in air and corresponding simulations in air, described in a previous publication[85].

### 7.2 3. Simulation Experiments

For all the experiments in this study, simulated whole-body scans were performed for each phantom using 120kVp and 300mAs. Whole-body scan here refers to the full coverage of all the voxels in every phantom. For GSF phantoms, the scan limits extend from the top of the head to the bottom of the feet; for pregnant patient models, they extend from the lower thorax to the pubic symphysis.

To investigate the dose variation from different tube start angles, various tube start angles ranging from 0 degrees to 340 degrees with an interval of 20 degrees were used for each set of simulations, which means 18 simulations were performed on each patient model using different tube start angles while keeping all the other scanning parameters constant. In the simulations, 0 degrees means the tube is at the top of the gantry (12:00 position). To make the results more intuitive, the angle that is reported is not the start angle, but rather the angle of the x-ray source as it crosses the longitudinal center of the organ being investigated; which we will call the Organ

Crossing Tube Angle (OCTA). For example, for the Baby GSF phantom, when using a pitch of 1.5 and a nominal beam collimation of 28.8 mm, a start angle of 0 degrees (the angle of the source is at 12:00 position at the start of the x-ray beam on), the angle of the x-ray source as it crosses over the center of the eye lenses is 107 degrees (OCTA=107 degrees). When the OCTA that results in the minimum dose for a particular organ is known, then the appropriate start angle can be calculated easily, as described below in 7.2.4.

To explore the correlation between the magnitude of organ dose reduction and the scanning parameters, pitch and collimation values were varied for each set of patient models. For the GSF models, three clinically relevant pitch values of 0.75, 1, and 1.5 were tested; for the pregnant patient models, only the pitch values of 0.75 and 1.5 were tested. For all patient models, two sets of collimation settings were simulated: one is the nominal beam width of 28.8mm with the actual beam width of 32.2mm; the other one is a case where the nominal beam width is 40mm and the actual beam width is 44.7mm, calculated based on the ratio of the actual/nominal beam width for the 24x1.2mm collimation. While 40mm beam width is not currently available in the modeled scanner, many other manufacturers have scanners with the same or even larger beam widths.

For each patient model, organ of interest and set of scanning parameters (pitch and nominal collimation pair), the OCTA that results in the highest dose is used as the worst case reference. Based on this worst case reference value, the dose reduction from the worst case is calculated for each OCTA value. This value demonstrates how much savings is possible

compared to the worst case. In currently available MDCT scanners available, there is no specific ability to control the start angle, therefore, the OCTA is similar to a random variable, with some patients receiving the highest dose to a specific organ and some the lowest dose to that same organ. For each experiment shown below, all results are presented as dose reduction compared to the worst case.

### 7.2.4. The Calculations of OCTA

MATLAB subroutines were created to compute the OCTA at a given tube start angle, as well as to obtain the location, size and centroid for each organ in each patient model. Given an organ's location and size information, the centroid along the longitudinal (z) axis is determined by averaging the longitudinal location of all the voxels assigned to the organ. When that centoid location is known as well as the scan start location (start of x-ray beam on as described in Figure 7.1) and the table feed per rotation (the product of pitch and nominal beam collimation), then the number of gantry rotations that will occur from the scan start location to the centroid of the organ was obtained by the following equation.

$$R = (OLoc - SLoc)/(pitch \times N) \qquad \text{Equation 7.1}$$

,where R is the number of rotations of the tube from the scan start location to the organ centroid, OLoc is the location of organ centroid along the longitudinal axis (z-axis), SLoc is the longitudinal axis scan start location (where the X-ray beam first turns on), N is the nominal beam collimation and pitch is conventionally defined (Note that Pitch x N = table feed in mm/rotation). After the calculation of R using equation 1, the OCTA is obtained by equation 2.

$$\text{OCTA} = \text{tube start angle} + 360 \times (\text{R} - \text{floor}(\text{R}))$$ Equation 7.2

,where floor(R) is the integer part of R. It should be noted that the tube start angle that yields a particular value of OCTA for each organ is patient specific and organ specific. For example an OCTA of 180 degrees for the lens of the eye may have a different start angle from the one required to yield an OCTA of 180 degrees for the thyroid. Similarly, OCTA of 180 degrees for the lens of the eyes may correspond to different start angles for the Baby phantom and for the Child phantom.

## 7.3 Results

### 7.3.1. GSF models

For each patient model, organ, pitch and collimation combination, a set of 18 simulations were performed, each with at different tube start angles. The organ dose reductions (compared to the worst case OCTA) are presented graphically by plotting the percent reduction of organ dose (on the y axis) as a function of the OCTA (on the x axis). Since three pitch values (0.75, 1, 1.5) and two collimation settings (28.8mm, 40mm) were simulated, there are 6 such graphs possible for each patient model. As an example, the dose reduction curves for all the studied organs in Baby phantom with all pitch values and nominal collimations are shown in Figure 7.3a through 7.3f, with each figure demonstrating a different pitch/collimation combination. The organ dose reduction as a function of OCTA can be observed from these figures. For example, as shown in Figure 7.3d, the dose reduction compared to the worst case scenario for breasts for a scan with 1.5 pitch and 40 mm nominal beam width is almost 35%. For testes dose from the

same scan, the dose reduction is 28%. It should be noted that the magnitude of dose variation is caused by solely changing the tube start angle while keeping all the other scan parameters constant.

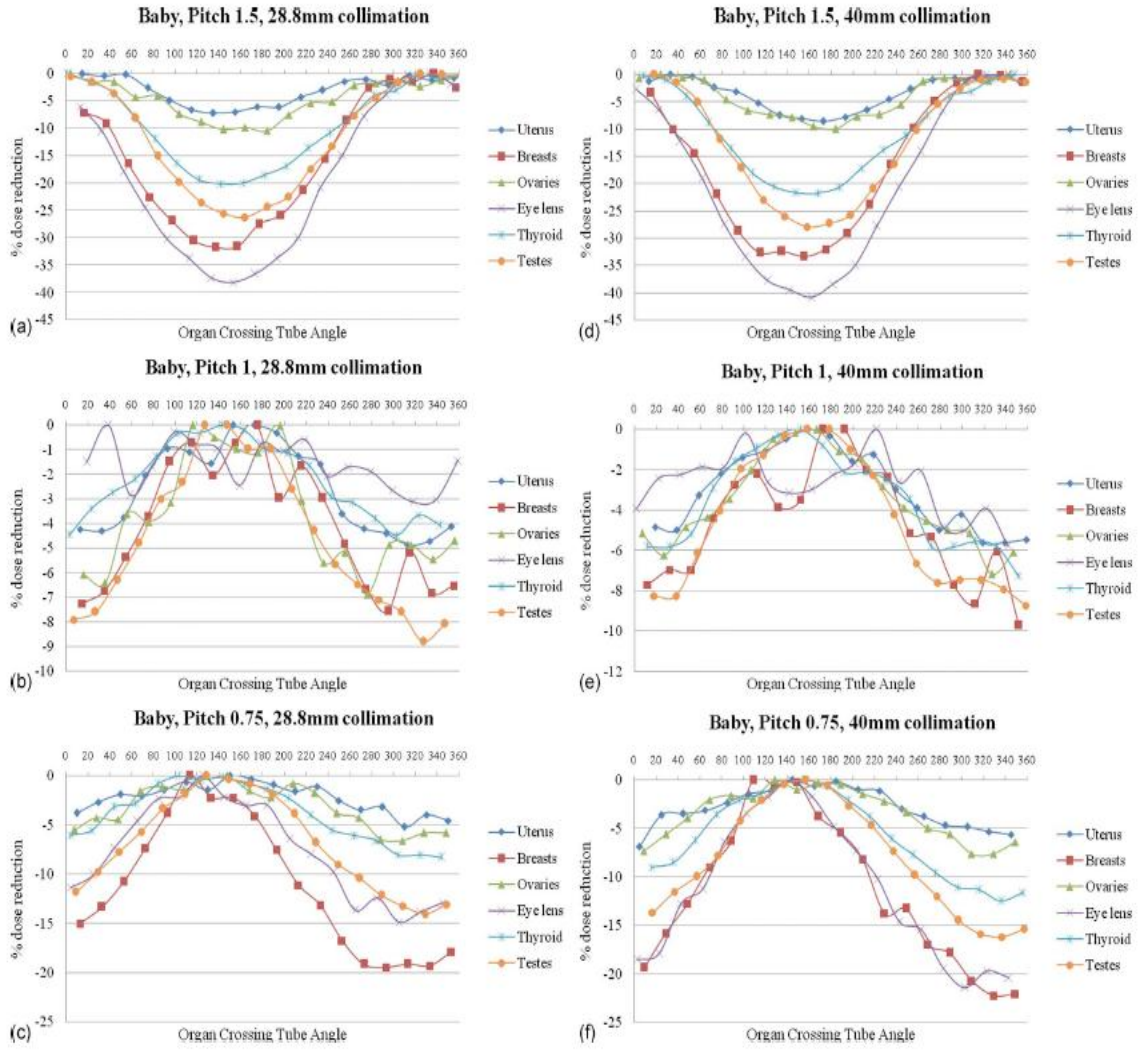


**Figure 7.3 the organ dose variation curves for Baby phantom from a simulated CT scan with various pitch and collimation settings. a). pitch 1.5 and 28.8mm nominal collimation; b). pitch 1 and 28.8mm nominal collimation; c). pitch 0.75 and 28.8mm nominal collimation; d). pitch 1.5 and 40mm nominal collimation; e). pitch 1 and 40mm nominal collimation; f). pitch 0.75 and 40mm nominal collimation. It should be noted that the same OCTA may correspond to different tube start angle for different organs.**

These results indicate that for Baby, the largest dose reductions occur for eye lens, thyroid, breasts and testes – all of which are at or near the surface of the patient and all of which have at least 20% dose reduction for pitch 1.5. These results also show that the largest dose reductions occur for pitch 1.5 and pitch 0.75. Pitch 1 does not show large dose reductions, regardless of OCTA. This is not surprising because the magnitudes of the surface dose variations are much smaller when using pitch 1.0 than with pitch 1.5 or pitch 0.75, which is consistent with the results in phantoms as shown in Chapter 6. These figures also show that the OCTA is different for different pitch values: it is approximately 180 degrees for pitch 1.5 and approximately 0 degrees for pitch 0.75. Finally, they also show slightly larger dose reduction for a wider beam collimation setting (40 mm compared to 28.8 mm).

Similar figures of organ dose reduction as a function of OCTA could be made for Child and Irene patient models. The behavior is similar and so they are not shown here; rather the maximum organ dose reductions for each patient model are summarized in Table 7.3 for all three GSF phantoms.

**Table 7.3 The maximum dose reduction for all the studied organs for GSF phantoms, under all simulated pitch values and collimation settings.**

| | Collimation 28.8mm | | | Collimation 40mm | | |
|---|---|---|---|---|---|---|
| Organ | Pitch 1.5 | Pitch 1.0 | Pitch0.75 | Pitch 1.5 | Pitch 1.0 | Pitch 0.75 |
| Baby breast | **32%** | 8% | **20%** | **33%** | 10% | **22%** |
| Baby ovaries | 11% | 7% | 7% | 10% | 7% | 8% |
| Baby testes | **26%** | 9% | 14% | **28%** | 9% | 16% |
| Baby thyroid | **20%** | 4% | 8% | **22%** | 7% | 12% |
| Baby uterus | 8% | 5% | 5% | 9% | 6% | 7% |
| Baby eye lens | **38%** | 3% | 15% | **41%** | 6% | **21%** |
| Child ovaries | 8% | 3% | 3% | 10% | 3% | 3% |
| Child testes | **33%** | 6% | 11% | **36%** | 9% | 16% |
| Child thyroid | **20%** | 3% | 4% | **25%** | 6% | 8% |
| Child uterus | 11% | 3% | 4% | 13% | 4% | 5% |
| Child eye lens | **49%** | 7% | **20%** | **51%** | 8% | **23%** |
| Irene breasts | 4% | 3% | 3% | 8% | 3% | 5% |
| Irene ovaries | 4% | 3% | 3% | 6% | 2% | 3% |
| Irene thyroid | 4% | 3% | 3% | 17% | 1% | 6% |
| Irene uterus | 4% | 2% | 2% | 8% | 2% | 2% |
| Irene eye lens | **52%** | 11% | 17% | **54%** | 13% | **22%** |

It can be shown from Table 7.3 that for the adult patient model (Irene), the dose reduction is not quite as large as the pediatric models except for the lens of the eyes. But for the pediatric models (Child and Baby), the dose reduction to the breast, testes, thyroid, and eye lenses are all considerable (on the magnitude of 20% or more). Ovaries and uterus on pediatric patients have lower dose reduction (on the magnitude of 10%), because these two organs are located at depth (rather than at the surface) than the other four organs.

By comparing the results across different pitch values (different columns in Table 7.3) it can be seen that the magnitude of dose reduction for pitch 1.5 is the largest, with the dose reduction up to 54% for Irene eye lens at 40 mm nominal beam width. For pitch 0.75 the magnitude of dose reduction is not as high as that for pitch 1.5, but it is still considerable, for example, 23% for Child eye lens at 40 mm nominal beam width. The dose reduction is not large for pitch 1, where it is below 10% for most of the organs in all GSF models.

By comparing the results across different collimations (28.8 mm and 40 mm in Table 7.3) it can be seen that the magnitude of dose reduction for the 40 mm nominal beam width is slightly larger than that for the 28.8 mm nominal beam width for almost all of the cases. For example, for Child testes, the maximum dose reduction values at 28.8 mm nominal beam width for pitch 1.5, pitch 1.0 and pitch 0.75 are 33%, 6%, 11%, respectively, while at 40 mm nominal beam width they are 36%, 9%, and 16%.

The comparison of the results across different organs on different patient models (different rows in Table 7.3) is not as straightforward. In general, larger dose reduction occurs

for smaller, peripheral organs in smaller patients. For example, the maximum dose reduction values of the eye lenses for all three phantoms are relatively large because the eye lenses is a small surface organ. The maximum dose reduction for 40 mm collimation at pitch 1.5 (the fourth column in Table 7.3) was plotted in a three dimensional space as a function of both organ length in the longitudinal dimension and the distance from the center of the organ to the isocenter. It is shown in Figure 7.4, from which it can be observed that there is a general trend: as the organ size decreases and the distance to isocenter increases, the dose reduction will increase.

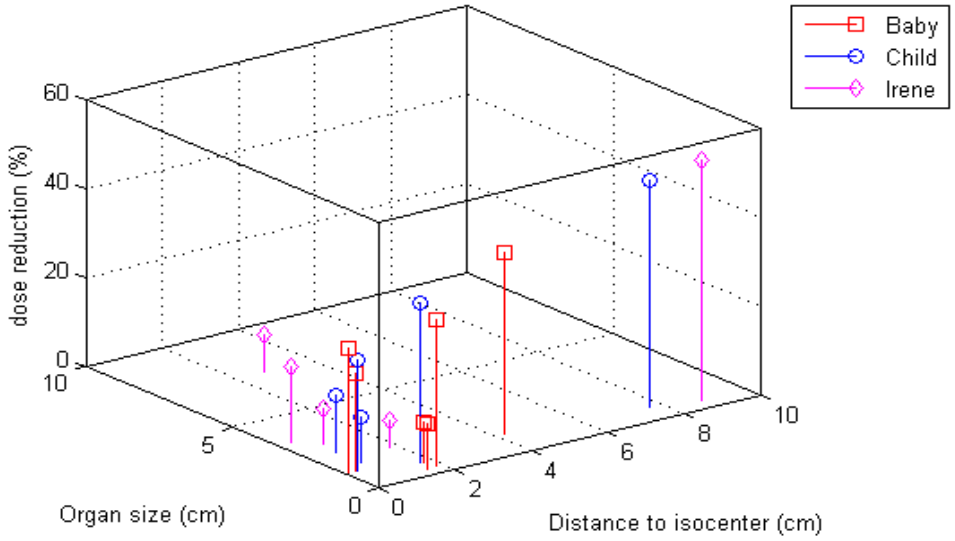


**Figure 7.4 The maximum dose reduction for individual organs from 3 GSF phantoms for a 40 mm collimation pitch 1.5 simulated CT scan as a function of both organ size in longitudinal dimension and its distance to isocenter in AP dimension.**

### 7.3.2. Pregnant female models

The organ dose variation curves for pregnant female models were plotted in the same way as for GSF phantoms. The organ dose variation can again be clearly observed. As an

example, the percent dose reduction curves as a function of OCTA from simulated scans with 40 mm nominal collimation, pitch 1.5 and pitch 0.75 for F7 phantom are shown in Figure 7.5. The maximum dose reduction for pregnant model organs from the combinations of all the pitch and collimation settings is shown in Table 7.4.

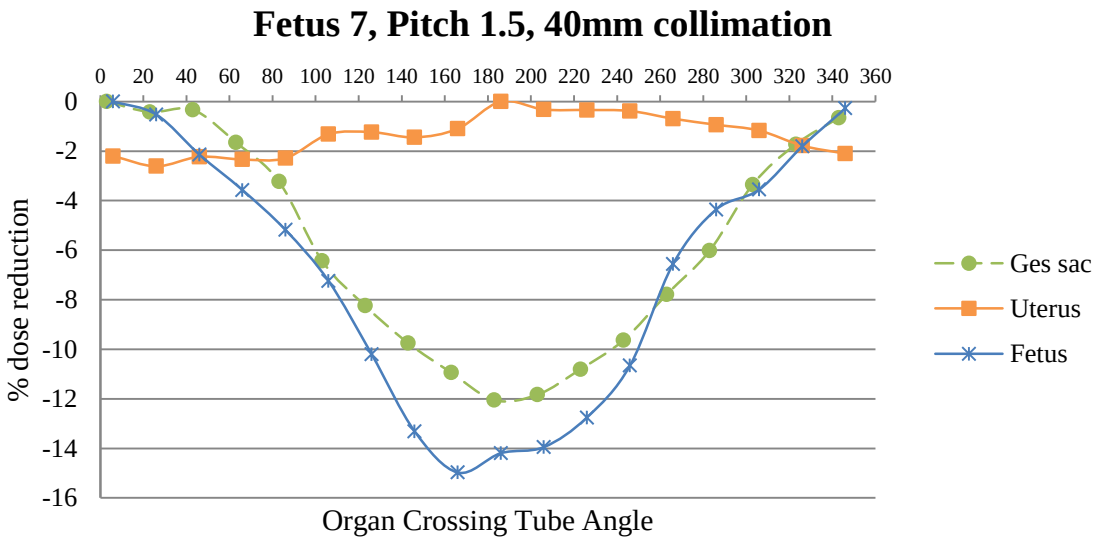


(a)

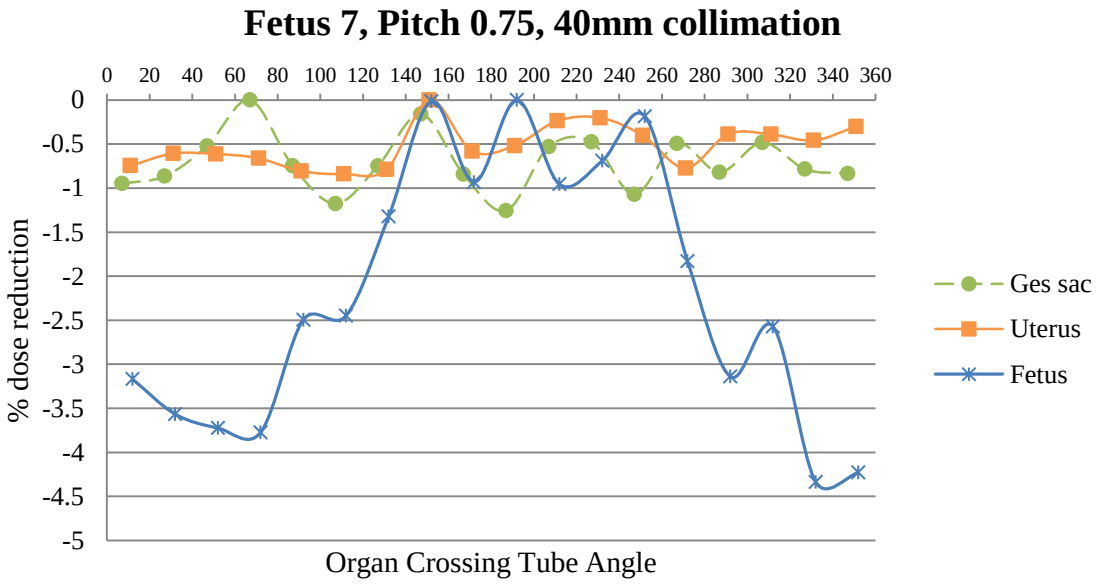


(b)

**Figure 7.5 The organ dose variation curves for F7 phantom from a simulated CT scan with 40mm nominal collimation and various pitch values. a). pitch 1.5; b). pitch 0.75.**

**Table 7.4 The maximum organ dose reduction for several pregnant female phantoms, under all the simulated pitch values and collimation settings.**

| | Collimation 28.8mm | | Collimation 40mm | |
|---|---|---|---|---|
| Organ | Pitch 1.5 | Pitch0.75 | Pitch 1.5 | Pitch0.75 |
| F24 (5 weeks) Ges sac | 12% | 5% | 17% | 8% |
| F10 (7 weeks) Gas Sac | 12% | 5% | 18% | 6% |
| F7 (12 weeks) fetus | 11% | 2% | 18% | 5% |
| F31 (19 weeks) fetus | 1% | 1% | 3% | 3% |

This table shows that the magnitude of dose reduction to the fetus for pitch 1.5 can exceed 10% for the early gestational age models (≤ 12 weeks) for 28.8 mm collimation setting and increases to approximately 18% for 40 mm collimation setting. Results from pitch 0.75 yield smaller dose reductions with the earliest gestational age model yielding only an 8% dose reduction for the 40 mm collimation setting. Results from the later gestational model (19 weeks) used in this study show very small dose reduction regardless of pitch, collimation or start angle, which is to be expected for larger objects or organs.

This table also indicates that dose reductions are not as large as those observed in Baby and Child phantoms. This is understandable because the early gestational age fetus, while small, is located somewhat centrally in the body. This table does show some similar general trends between the dose reduction and length in longitudinal dimension as in the GSF models in that a smaller size fetus has higher dose reductions. For example, at pitch 1.5, the maximum dose reduction is above 10% for F24, F10 and F7. But for the pregnant patient model with a later

gestational age (19 weeks) the fetus is larger and the dose reduction is nearly negligible (F31). These results are also similar to that for GSF phantoms in terms of pitch and collimations: pitch 1.5 and wider collimation yield larger organ dose reductions.

It should be noted that for the two phantoms with the earliest gestational age (F24, F10), dose to fetus is not directly simulated in this study because the fetus tissue was too small to be identified by the radiologists from CT images; in the original study[100], the radiologist identified the gestational sac and we estimated dose to that tissue to serve as an indirect estimate of the dose to the fetus. This does not mean that there is no fetus dose; in fact they may have a very high magnitude of dose variation from varying tube start angle because of their extremely small size. Furthermore, the development of fetus is very active in the initial few weeks so they are even more sensitive to radiation[132].

### 7.3.3. Computational Time

The computational time for each MCNPX simulation (fixed pitch, collimation and tube start angle) was about 5 minutes on a parallel computing cluster server with 64 AMD 2.0GHz processers. Because for this study the requirement of the relative errors of the output results is very high, a total of 100 million photon histories were used for each simulation. The standard deviation of all the results from MCNPX was within 1.2%, with most of them below 0.5%. The scenarios where the error is higher than 0.5% happens when the size of the organ is very small, for example, eye lenses, because for such cases the number of photons that enters the organ can be small.

## 7.4 Discussion

In this work, Monte Carlo simulations were used to investigate the effect of the tube start angle on organ dose in several patient models. While current MDCT systems do not allow the user to control the start angle, this study investigated the feasibility of exploiting this sinusoidal behavior to reduce the dose to a specific organ by varying the tube start angle, especially for a small peripheral organ on small patients. Results were presented showing the magnitude of organ dose reduction possible if the ability to choose the tube start angle were to be provided.

The results demonstrate a range of dose reduction for various organs in various phantoms undergoing a full body scan. This dose reduction can be large, for example, for Baby phantom the maximum reduction of the breast dose could be as high as 33%. For pediatric patients, the dose reduction to breast, testes, thyroid and eye lenses is considerable (20% or more) while the dose reduction to ovaries and uterus is lower (10%). For adult patients, the dose reduction is only considerable for the eye lenses. For pregnant patients at early gestational stage (<10 weeks), the dose reduction to fetus can be up to 17-18%.

The organ dose variation resulting from varying the tube start angle depends on the scan parameters, especially pitch and nominal collimation. Chapter 6 showed that if the scanned object is a large (32 cm diameter) cylindrical homogeneous phantom, the dose distribution at the isocenter would be uniform, no matter what the pitch and nominal collimation are. However, if the region of interest is at a peripheral or surface position (for example, breasts), instead of the isocenter, the longitudinal dose distribution could have large variations. This is because at

peripheral positions, some areas are exposed to entrance, exit and scattered radiation, while other areas may be exposed to either only exit and scatted radiation (e.g. pitch 1.5) or they may be exposed to an overlap region where they receive entrance radiation from two successive rotations (e.g. pitch 0.75).

The magnitude of organ dose reduction resulting from varying tube start angle is highly related to the location of the organ, size of the organ and anatomy in the vicinity of the organ in question. If the organ is perfectly at the isocenter, the organ would have very minor dose variation from varying tube start angle because the dose distribution at isocenter is nearly uniform. If the organ is relatively large, such as lung or liver, it also will not have significant variation because its dimension in longitudinal direction is much larger than the period of the dose distribution (which is basically table feed per rotation), and the organ dose integrated over several periods will not be able to reflect the peaks and the valleys. For example, the organ dose of F31 pregnant patient phantom does not have considerable variations depending on the tube start angles because the organ (fetus) is relatively large. The anatomy in the vicinity of the organ in question is also an important factor. For example, the eye lens is surrounded by more bone than the breasts, so it has a higher magnitude of dose variation. In addition, although fetus is almost at the isocenter, it may be surrounded and protected from radiation by pelvis, except for the anterior direction. This will also result in some dose variation as a function of tube angle.

Since the table feed per rotation is the product of pitch and nominal collimation, these two parameters determine how ‘continuous’ the surface (or peripheral position) is covered by the

primary beam. For example, if the table feed per rotation is much larger than the actual beam width (as in pitch larger than 1.0), there may be considerable area on the surface that is not covered by the primary entrance beam and hence the longitudinal dose distribution will have higher variation. So theoretically, as the pitch and nominal collimation increase, the organ dose would have larger dose reduction. This was illustrated in Table 7.3 where the maximum dose reduction is higher for pitch 1.5 than that for pitch 1 for all cases, and it is slightly higher for 40mm nominal beam width than that for 28.8mm nominal beam width.

However, the dose reduction of pitch 1 is not higher than that for pitch 0.75. This is because as the pitch decreases to a certain value, the overlap of the adjacent radiation beams occurs, resulting in an overlap peak. As illustrated in Figure 7.6, this scenario creates a new mechanism of organ dose variation, where inside the overlap region the organ receives higher dose and outside the overlap region the organ receives lower dose. Therefore, there is a "threshold" pitch for each organ in each phantom, such that the larger the difference between the pitch used in scan and the threshold pitch is, the higher the achievable dose reduction could be. It is expressed in equation 3.

$$P_{threshold} = (1 - \frac{d}{iso}) \times \frac{A}{N} \qquad \text{Equation 7.3}$$

,where d is the distance between organ centroid to the isocenter in the A-P dimension, A is the actual beam width, N is the nominal beam width, and iso is the distance between the x-ray tube anode to the isocenter. Typically d (less than 10 cm for most of the organs) is much smaller than

iso (usually 50 cm to 60 cm), so the threshold pitch can be approximated by A/N, which is about 1.1 in this study.

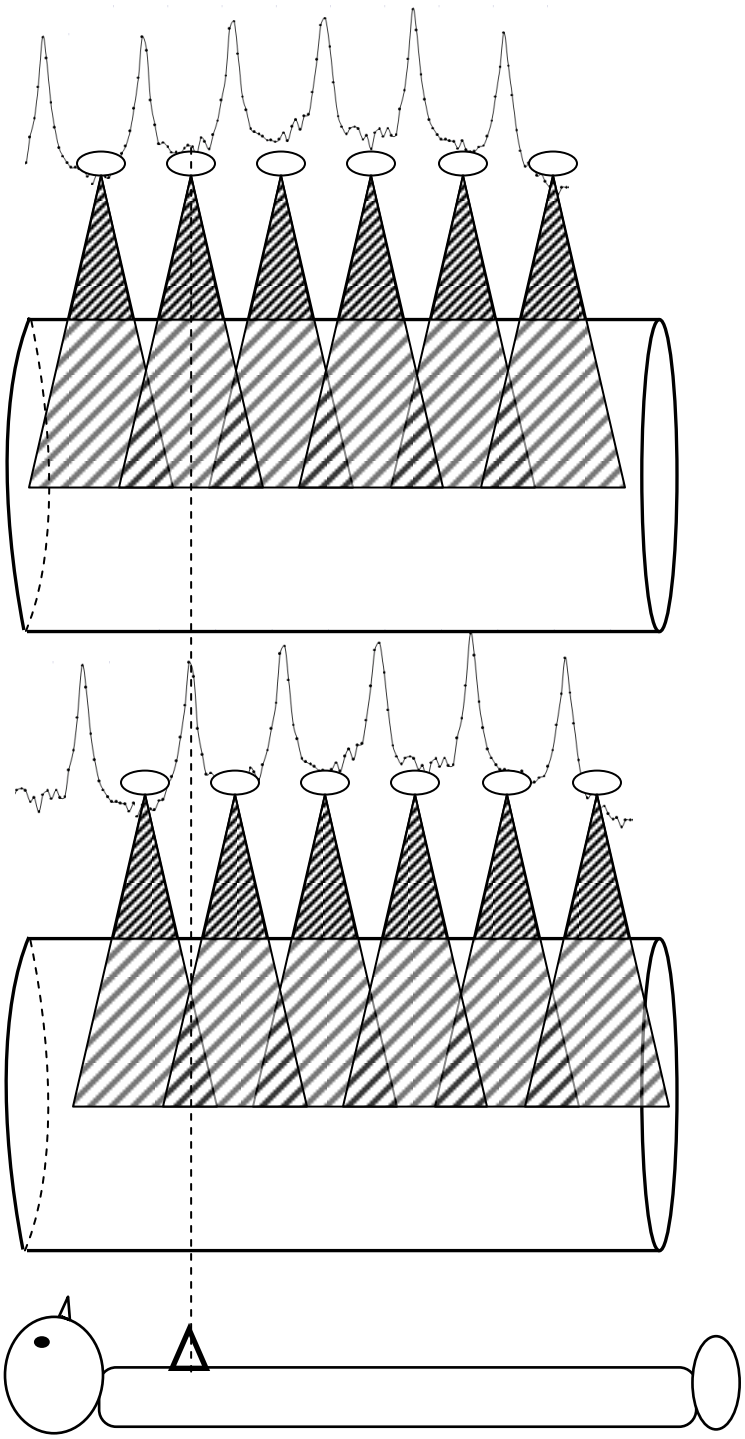

**Figure 7.6 Diagram illustrating the tube position, corresponding surface dose distribution along z-axis under two scenarios with different tube start angles, and a patient, at pitch 0.75. It's shown that the dose to the breasts of the patient can be affected by selecting different tube start angles.**

When the pitch used in the scan is higher than threshold pitch, "cold spots" are created along the longitudinal direction of the organ (as illustrated in Figure 7.1). In comparison, when the pitch used in the scan is lower than threshold pitch, then overlap peaks result and "hot spots" are created as demonstrated in Figure 7.6. If an organ has a relatively small extent in the longitudinal direction, its dose may be affected by these hot or cold spots, the location of which can be affected by the tube start angle. Thus two organ dose reduction strategies can be applied for these two different scenarios. For the first scenario (pitch $P > P_{threshold}$), the dose to an organ in question can be minimized if the tube start angle were to be selected in such a way that when the tube passes the organ, it is at posterior side of the patient (assuming the organ is on the anterior side of the patient); this corresponds to OCTA of 180 degrees. For the second scenario (pitch $P < P_{threshold}$), the organ dose can be minimized by selecting a tube start angle such that when the tube passes the organ, it is at the anterior side of the patient, which corresponds to an OCTA of 0 degrees. Of course, the effectiveness of both techniques also depends on the anatomy in the vicinity of the organ in question. From Figure 7.3 it is seen that the optimal angles are slightly off by about 20 degrees. One reason may be that the Baby model used in this study is in supine position slightly rolled to its left.

As the cone angle increases, the area of these cold or hot spots will also increase for helical scans, which causes larger variation of organ dose depending on tube start angle. Since very wide nominal beam width (>40mm) MDCT scan systems are being introduced, this method could potentially serve as an important dose reduction technique.

Most of the investigated organs in this study are relatively small in size and easy to be anatomically located (e.g. lymph nodes are difficult to locate). These organs happen to be located close to the anterior surface of the patient body. The dose reduction strategies would have been different if these small organs were located at the back or at the side of the body. However, all the posterior and lateral organs have larger size in longitudinal direction comparing to the nominal collimation and hence the dose strategies being proposed in this study cannot be applied anyway.

The voxel sizes of all phantoms are considered small enough to accurately represent the selected organs, with the possible exception of eye lenses. For GSF Baby and Irene, there are 69 voxels and 84 voxels identified as eye lenses, respectively. However, for GSF Child model, there are only 28 voxels identified as eye lenses. Given the voxel size for GSF Child (1.54x1.54x8mm), there are not a large number of voxels to represent the eye lenses, which may make it difficult to estimate the dose reduction accurately. However, because the beam width used here has a width of 28.8 mm (or 40 mm) and when pitch is great than one, there are large gaps between adjacent rotations; therefore, we would still expect significant dose reduction for the eye lenses.

There are several limitations in this study. First, the sample size of the patient models is relatively small. While the three GSF phantoms and the four pregnant female phantoms do represent a distribution of the patient size, they cannot represent the whole patient population. Since the magnitude of the dose reduction depends on the size of the organ, the dose reduction

should have larger magnitude for smaller sized patients. But GSF Baby (8 weeks) is very small, so larger magnitude dose reductions would not be expected. For a larger size patient, the dose reduction may be lower that observed in GSF model Irene, but perhaps not much lower, because larger patients do not necessarily have much larger organs, e.g., eye lenses.

Second, this technique to reduce organ dose by selecting a specific tube start angle can only ensure that one organ gets the minimum dose while not controlling the dose to other organs. But this doesn't impair this technique to be a useful organ dose reduction strategy because it does not put other organs at any higher risk than they are currently experiencing under uncontrolled (i.e. random start angle) helical scans. In addition, the simulations in this study considered constant tube current only. The effect from tube current modulation (TCM) is not simulated. This study did not specifically address any issues of image quality, though the impact would be expected to be insignificant because there is no change in acquisition parameters such as tube current, rotation time, beam collimation or pitch. Also in order to apply the technique of reducing dose to certain organ by controlling the tube start angle in practice, there may be some other practical considerations to take into account. For example, it requires the knowledge of the location of the organ prior to the CT scan (which could be available from the scan projection radiograph or planning view); the localization of the organ position should be very accurate; the organ must not move during the examination, etc.

In currently available commercial CT scanners, the tube start angle is not controlled by the user and is either a completely random variable (any start angle is possible) or a limited

random variable (only certain start angles are allowed, but are still not controlled by the user). So the dose received by the organs investigated in this study using current MDCT scanners would be randomly distributed on the dose reduction curves shown. The purpose of this study was to investigate the magnitude of organ dose reduction that might be achieved if the capability to control the tube start angle were to be provided. This technique may be applied to a small organ on small patients, fetus on pregnant patients with early gestational stage, or eye lenses on adult patients. Since tube current modulation (TCM) techniques do not perform very well for pediatric patients (because they are more circular than elliptical for example), this method could also serve as a complementary approach to TCM. The clinical realization of this methodology might not be trivial and would require implementation by scanner manufacturers; however, there are some current products which do at least take the tube start angle into consideration such as: (a) a dose reduction method which turns the x-ray beam off over the anterior portion of the patient (X-care, Siemens Medical Solutions, Forcheim, Germany) and (b) a method not used for radiation dose reduction but for synchronizing helical source paths between pre- and post-contrast scans (typically within the head) for the purposes of minimizing artifacts when subtracting the two scans (Sure Subtraction, Toshiba Medical Systems, Inc., Otawara-shi, Japan). These two products provide at least some indication that controlling the start angle may be feasible in some MDCT scanners in the future.

# Chapter 8 Reducing Organ Dose from CT by controlling both Tube Start angle and Table Height

## 8.1 Background and overview

The table height during a CT scan has drawn some attention in recent years and it has implications for both radiation dose and image quality[133,134]. There are primarily two concerns regarding the vertical position of the table during CT scans. One is its interference with tube current modulation; the other concern is that it may cause additional image noise and possible artifacts. These concerns are explained below.

In modern CT scanners, tube current modulation is used for almost all clinical protocols, such as thorax and abdomen scans. Its purpose is to deliver only necessary radiation across patients with different sizes, and across different projection angles for each patient based on the attenuation. The Topogram (or Scout image, Scanogram), which is basically a radiograph image of the patient, is usually obtained before the actual scan for the prescription of scan location, and more importantly, for gathering information about the attenuation of the patient, which will be used as input to determine the appropriate exposure level at different anatomical locations. Some topograms are performed in the AP/PA direction, while some other are performed in the lateral direction. When it's performed at AP/PA direction, the table height could yield incorrect information about the size of the patient to the algorithm for the calculation of tube current modulation schema. For example, in an AP topogram, if the table is raised above the center, the projected radiograph would be larger than it is supposed to be due to the magnification. This is

shown in Figure 8.1. Therefore, the algorithm would process the attenuation data as if it was a larger patient and hence generate incorrect higher tube current[133].

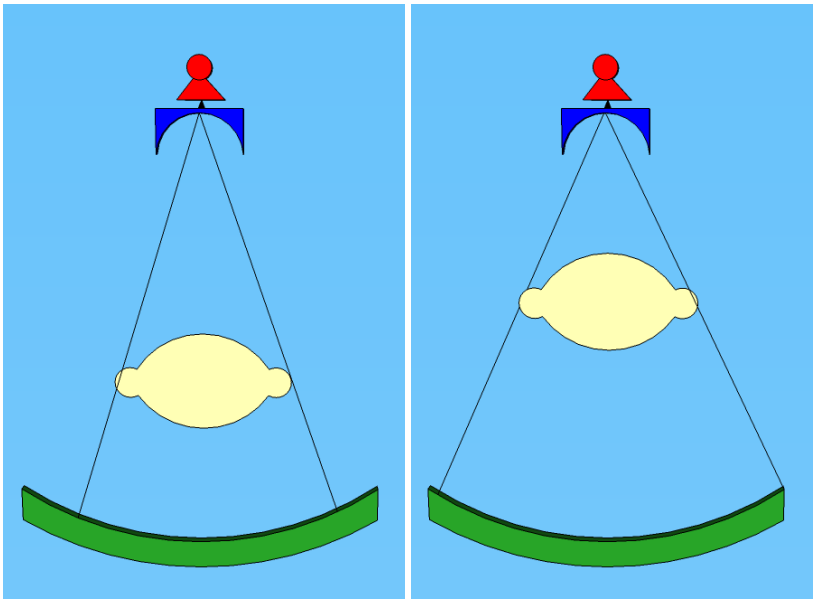

(a) (b)

**Figure 8.1 The illustration of the magnification of topogram image when the table is raised. a). Table is at regular height. b). Table is raised.**

Changing the table height may also introduce some potential degradation of image quality, including the effect on noise and CT number. Because the shape of the bowtie is designed to compensate for the in-homogeneity of x-ray intensity at detector when the patient is positioned at center (shown in Figure 8.2a), the x-ray intensity can differ significantly across the detector when the patient is off-center (shown in Figure 8.2b). At the location where the x-ray intensity is lower and with less number of photons, the noise would be inevitably higher due to the Poisson statistical distribution of the photons[134]. In addition, the beam may be more hardened

for the rays that travel through more bowtie filtration. Therefore the CT number may also be not accurate.

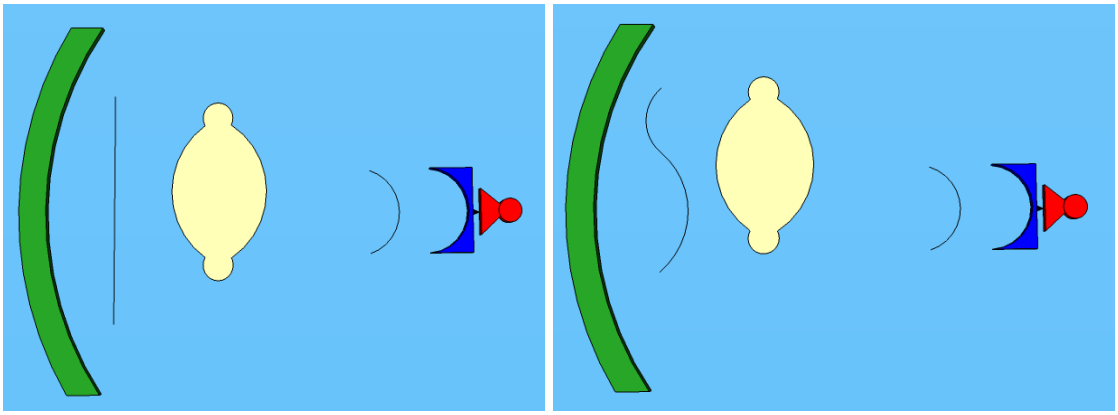

a) b)

**Figure 8.2 The x-ray intensity when the patient is centered (a) and off-center (b). The lines illustrates the relative intensity of x-ray beam.**

Although the adjustment of table height in CT scans could potentially have some adverse effect on image quality, it could also potentially help reducing the radiation dose to the peripheral organs. The aim of this chapter is to investigate the reduction of organ dose in CT scans by combining the adjustments of both tube start angle and table height. This technique is proposed in this dissertation to reduce dose while maintaining image quality. As discussed above, since the adjustment of table height may have complications for scans with TCM, the dose reduction for using fixed tube current and using TCM were investigated separated. First, the mechanism of dose reduction by adjusting table height is discussed. Then, the dose reduction from the combination of adjusting tube start angle and table height was investigated for constant tube current scenario using measurements on phantoms, as well as simulations on voxelized patient models. Subsequently, the dose reduction was studied for TCM scans using both phantom

measurements and Monte Carlo simulations. Next, since a lot of simulations were conducted for the simulation of controlling tube start angle and table height, the Monte Carlo model was validated by benchmarking simulated results and measurements at various tube start angles and table heights. Finally, the effect to image quality from adjusting tube start angle and table height was studied. The overview of this Chapter is illustrated in Figure 8.3.

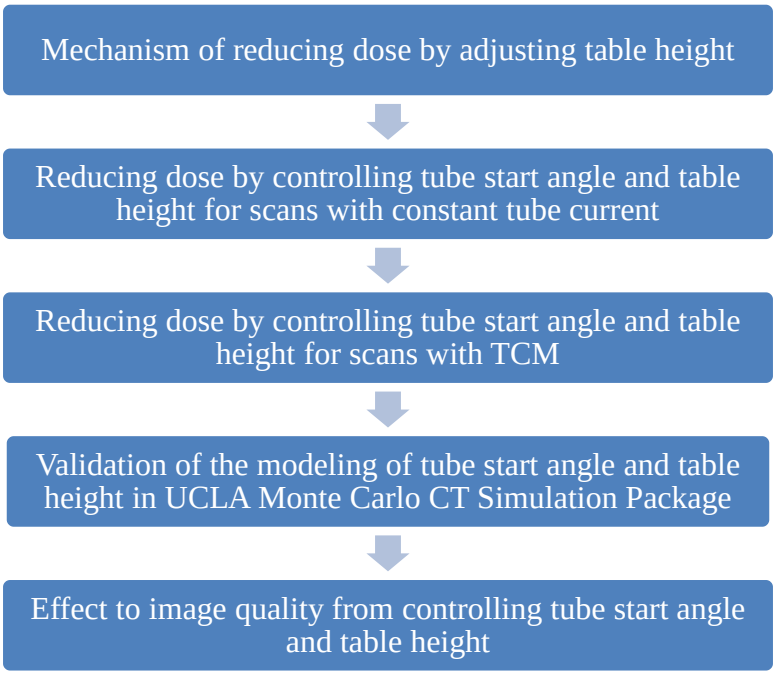


**Figure 8.3 Overview of Chapter 8.**

## 8.2 The mechanism of dose reduction by adjusting table height

In order to investigate the effect of table height on the dose delivered to the patient, especially to the peripheral or surface dose of the patient, a series of simulations for single axial scans were performed to monitor the exposure to the 12:00 position (very close to the suface) of a 32 cm CTDI phantom using Monte Carlo simulations. The simulated CTDI 12:00 was plotted

as a function of tube start angle at a variety of table heights, as shown in Figure 8.4. It should be noted that the bump around tube start angle of 0 degree is due to a small over-scan when the single axial scan start because of the ramp up of the tube potential. Since the location of the ion chamber (12:00 position) corresponds to the tube angle 0, this effect is only perceivable when the tube start angle is 0. The reason that the bump is more prominent when the table is higher is that the ion chamber is closer to the x-ray source.

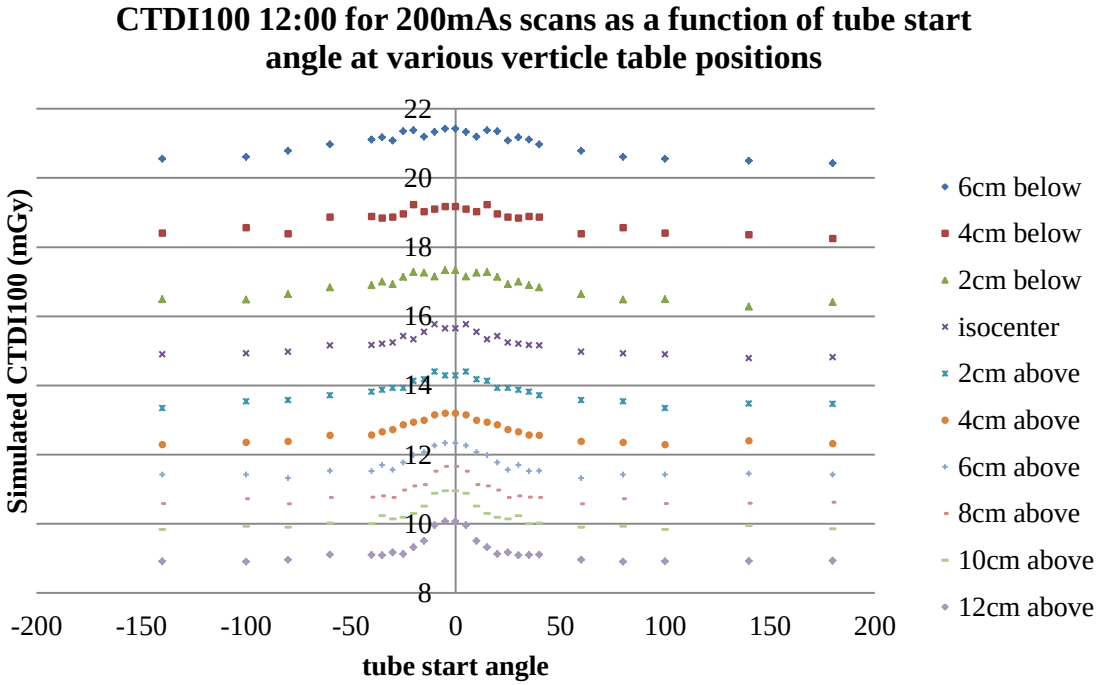


**Figure 8.4 Simulated CTDI 12:00 as a function of tube start angle at a variety of table heights.**

Figure 8.4 showed that as the table is raised, the CTDI 12:00 decreased, while as the table is lowered, the CTDI 12:00 increased. This fact seems counter-intuitive because as the table is raised, the ion chamber is closer to the source at 12:00 position, however, the exposure is lower

for a single axial scan. In order to investigate the mechanism of this effect, mesh tally in MCNPX was used to study the 3D radiation dose distribution within the CTDI phantom for a single axial scan. Figure 8.5 shows the dose distribution at two different table heights: at isocenter and 12 cm above the isocenter. Difference images between dose maps at each these two table heights were also shown. In these figures black color corresponds to lower dose, while white color corresponds to higher dose. It showed that when the table was raised (at 12 cm above isocenter), the upper part of the phantom received lower dose comparing to when it's at isocenter (black on the upper part of the difference image), and the lower part of the phantom received higher dose (white on the lower part of the difference image).

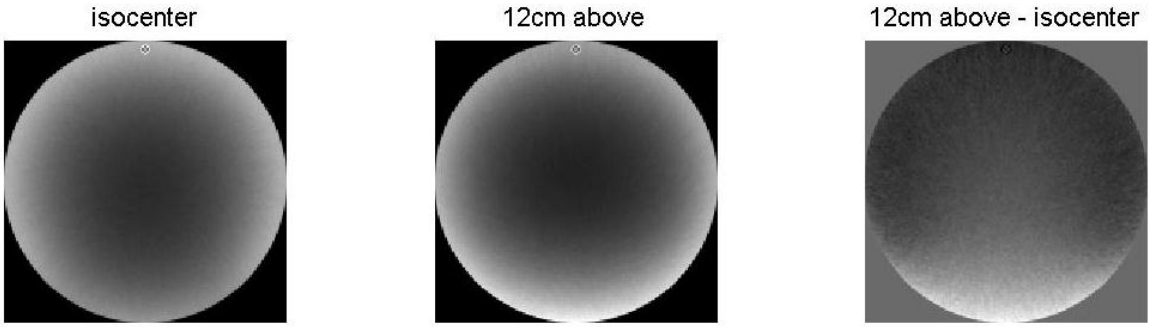


**Figure 8.5 Dose distribution maps within a 32 cm CTDI phantom for single axial scans at two different table heights (isocenter and 12 cm above isocenter), as well as the difference image between dose distribution maps.**

To investigate the physics behind this fact, a separate set of simulations were performed with the bowtie filter taken out. The results are shown in Figure 8.6, which showed that the change of dose distribution when the table is raised is the opposite of the scenario where the bowtie filter was in. In other words, the upper part of the phantom received higher dose, and the lower part of the phantom received lower dose when the table is raised. Therefore, it was

demonstrated that the non-intuitive behavior of the dose change at different table heights was caused by the bowtie filter. Because of the shape of the bowtie filter, when the area of interest is pushed closer to the isocenter in the CT gantry, it always receives lower filtration from the bowtie filter from each projection and hence has higher intensity (shown in Figure 8.7a), while when the area is moved away from the isocenter, it receives more filtration caused by the bowtie filter and hence has lower intensity (show in Figure 8.7b).

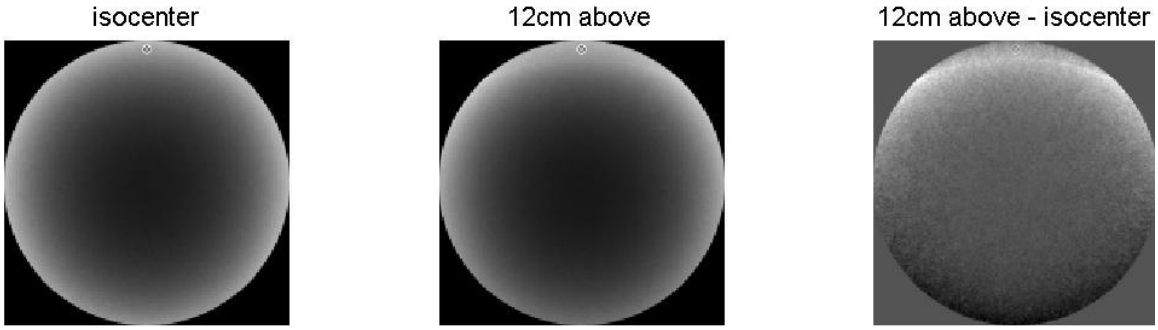


**Figure 8.6 Dose distribution maps within a 32 cm CTDI phantom for single axial scans at two different table heights (isocenter and 12 cm above isocenter), as well as the difference image between dose distribution maps. Bowtie filtrations were deliberately taken out for these simulations.**

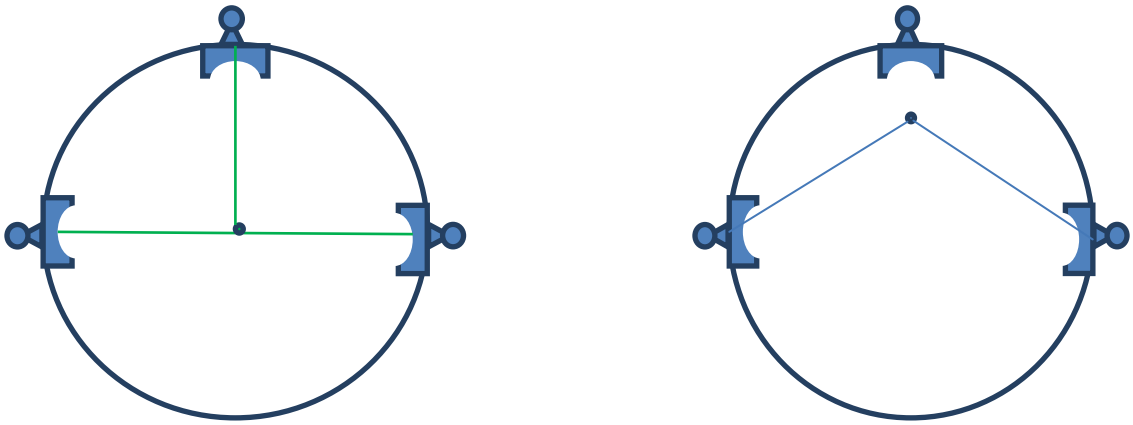

**a)** **b)**

**Figure 8.7 Illustration of the additional attenuation from bowtie filtration when for a point further away from the isocenter.**

Therefore, the shape of the bowtie filtration and the nature of the circular moving pattern of the x-ray source in CT have determined that a part of the object being scanned would receive lower radiation dose if it is moved away from the isocenter. Meanwhile, another part of the object which is moved closer to the isocenter would receive higher radiation dose. In other words, the dose distribution within an object could be manipulated by raising or lowering the table during CT scans. This phenomenon may be applied to patients to alleviate radiation dose to organs that are more radio-sensitive in clinical CT scans. Furthermore, the effect of adjusting table height could be combined with the control of tube start angle discussed in Chpater 7 to achieve even larger dose reduction to critical organs. In order to achieve this goal, a series of measurements and simulations were performed to study the potential use for dose reduction from these techniques and their potential impact on image quality.

## 8.3 Reducing Radiation Dose by Controlling Table Height and Tube Start Angle Under Constant Tube Current

The effects from both techniques were first investigated for scans with constant tube current. Although TCM is used for most of the scan protocols to deliver less radiation dose to patients, a few protocols still use constant tube current, such as some head scan protocols, since the shape of head is rather round and there is very little difference of attenuation across projections. Furthermore, it is crucial to start with relatively simple to explore the physics mechanism by leaving out TCM, which could be a complicating factor.

### 8.3.1. Methods (Constant tube current)

#### 8.3.1.1 Methods - Exposure Measurements on a Thorax Phantom at Various Table Heights and Tube Start Angles (TCM off)

A Radcal 0.6 cc ionization chamber was placed on the surface of the chest of an anthropomorphic phantom developed by Radiology Support Device Inc[135] to study the effect of both tube start angle and table height on the radiation dose to a small volume at the patient surface, shown in Figure 8.8. Helical CT scans using clinically routine chest protocols were performed for a Siemens Sensation 64 scanner using 28.8mm collimation, 120kVp, 150 mAs, and pitch 1.5. The table was set to a variety of heights to investigate the effect of table height on dose. Since the tube start angle is random and it is not under the user's control for helical scans, 24 helical scans were performed under each table height to yield a variety of tube start angles. The exposure of the ionization chamber and the tube start angle were recorded for each scan. In order to obtain the tube start angle for each scan, the raw projection data was extracted from the scanner console and was read in with a MATLAB subroutine which calls several proprietary dynamic link library provided by Siemens.

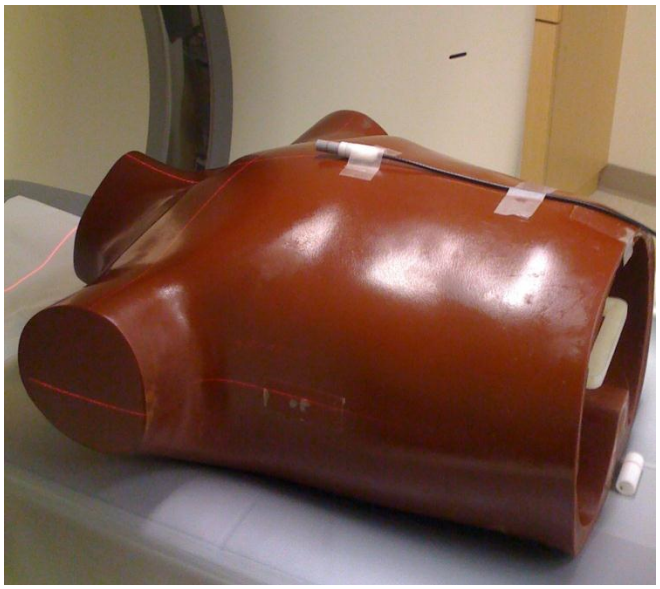

**Figure 8.8 The setup of the experiment: a Radcal small ionization chamber was placed on the anterior surface of an anthropomorphic thorax phantom.**

### 8.3.1.2. Methods - Organ Dose Reduction to GSF Patient Models by Adjusting Tube Start and Angle Table Height (TCM off)

In order to investigate the magnitude of the reduction of radiation dose to individual organs, Monte Carlo simulations were performed using the GSF family patient models. In addition to Baby, Child, Irene, Donna, Frank, and Golem that were used in the previous chapters, the remaining four models Helga, Visible Human, Rex and Regina were also include in the simulations to represent a reasonable cohort of patient population with a distribution in age, gender and size[136,137]. The information for each model in the GSF family is shown in Table 8.1.

**Table 8.1 Age, gender, and size descriptions of GSF models used in this study.**

| Model | Age | Gender | Weight (kg) | Height (cm) |
|---|---|---|---|---|
| Baby | 8 weeks | Female | 4.2 | 57 |
| Child | 7 years | Female | 21.7 | 115 |
| Irene | 32 years | Female | 51 | 163 |
| Donna | 40 years | Female | 79 | 170 |
| Helga | 26 years | Female | 81 | 170 |
| Golem | 38 years | Male | 69 | 176 |
| Frank | 48 years | Male | 95 | 174 |
| Visible Human | 39 years | Male | 103 | 180 |
| Rex | 38 years | Male | 70 | 176 |
| Regina | 43 years | Female | 59 | 167 |

In the light of the potential larger dose reduction from wider beam width and higher pitch, a Siemens Definition Flash scanner was modeled, which has a Flash Mode of dual source, with the widest collimation of 38.4 mm and the largest pitch of 3.2. With the wider collimation and higher pitch, the table travels very fast in the Flash Mode, which yields very quick scans with more advantages in terms of cardiac imaging and the tolerance of patient motion. In the same time, the high pitch (effectively 1.6) and wide collimation result in much wider gaps between adjacent x-ray beams. Therefore, the dose reduction brought by controlling the tube start angle would potentially be more significant.

For each GSF model, the radiation dose to each radiosensitive organs with the weighting factor higher than 0.01 (including gonads, breast glandular tissue, lung, thyroid, colon, stomach, bladder, esophagus, and liver) were estimated at 18 tube start angles with 20 degrees apart at each specific table height[11]. Dose to eye lens and kidneys were also included although they have lower weighting factors, because there has been concerns about dose to eye lens, as discussed in Chapter 4. Kidneys are included because they are located towards the posterior side of the body which could be used to demonstrate the concept in the results that will follow. These simulations were performed for five different table heights (center, 6cm above center, 12cm above center, 6cm below center, and 12cm below center). It should be noted that although in practical environment the gantry is usually not large enough for positioning the center of the patient to be 12cm above the isocenter, this table height was still included in the study to illustrate the concept.

The equivalent source method was used to obtain spectra and bowtie filtration information for both x-ray tubes with 95 degree apart from each other. Instead of simulating two sources in the same MCNPX run, 2 separated runs with each corresponding to one source were performed, and the results were combined in the end. The results were reported on a per 100mAs basis, so that radiation dose to each organ for scans with other mAs values can be obtained by scaling since dose is proportional to mAs. The simulations were performed using Flash mode on the Definition Flash CT scanner with dual source, 120 kVp, 64 x 0.6mm (38.4mm) nominal collimation, 43mm actual beam width, and a pitch of 3.2.

### 8.3.2. Results (Constant tube current)

#### 8.3.2.1. Results - Exposure Measurements on a Thorax Phantom at Various Tube Start Angels and Table Heights

The exposure measurements were plotted as a function of tube start angle for various table heights in Figure 8.9. The selection of tube start angle and table height results in significant changes in radiation dose at the patient surface. At each table height, the sinusoidal behavior as a function of tube start angle can be observed, same as the simulation results shown in Chapter 7. As the table is raised (dosimeter closer to the top of gantry), the exposure decreases, while as the table is lowered (dosimeter closer to the bottom of the gantry), the exposure increases. Compared to the worst case start angle (dose is the highest) when the patient is centered, the radiation dose can be 36% higher or 65% lower by adjusting the table height and the tube start angle while keeping all other scanning parameters (kVp, mAs, pitch) the same for the Sensation 64 scanner.

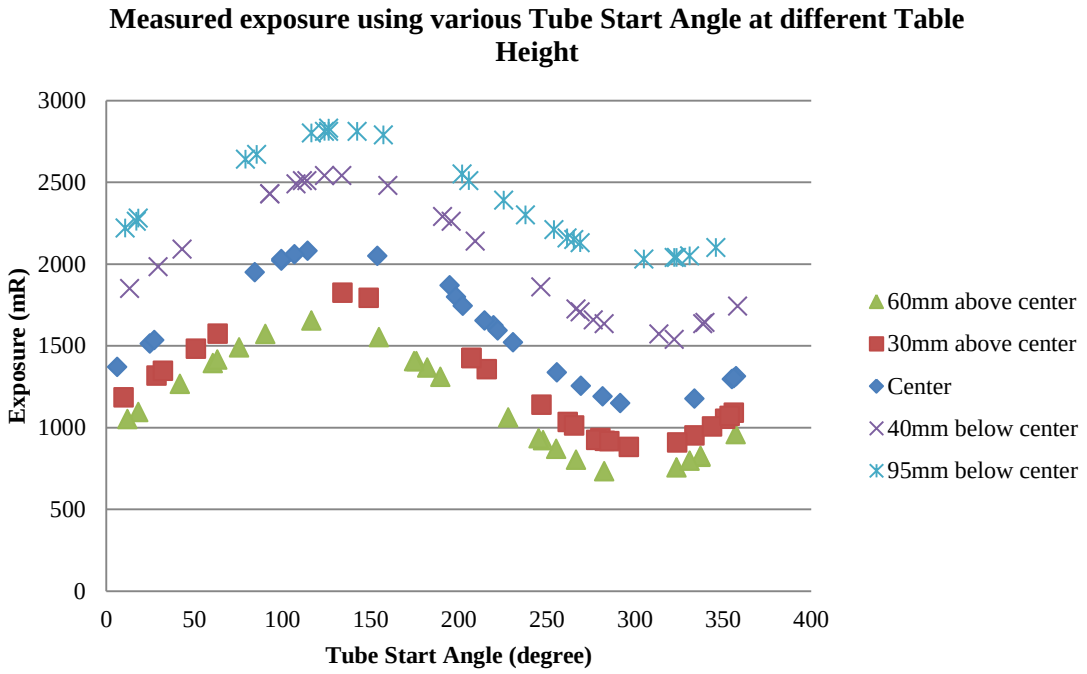


**Figure 8.9 Exposure measured at the surface of an anthropomorphic phantom versus tube start angle at a variety of table heights for the chest protocols of a Siemens Sensation 64 CT scanner under constant tube current.**

### 8.3.2.2. Results - Organ Dose Reduction to GSF Models by Adjusting Tube Start Angle and Table Height

The organ doses were plotted as a function of tube start angle for different table heights. Since there are in total 10 GSF models, and the dose to 11 organs, whenever available, were reported for each model, there are in total more than 100 plots. They are too many to be included in the dissertation. Therefore only a series of examples are shown. Specifically, the breast dose reduction for Irene, the eye lens dose reduction for Frank, the liver dose reduction for Donna, and the kidney dose reduction for Rex are shown here in Figure 8.10(a) – 8.10(d). Comparing to a small volume ion chamber on the surface of an anthropomorphic phantom used in the measurements, an organ sits in a much more complex radiation attenuation environment with

varying sizes. Even though, Figure 8.10 shows similar dose variation pattern as it is in Figure 8.9.

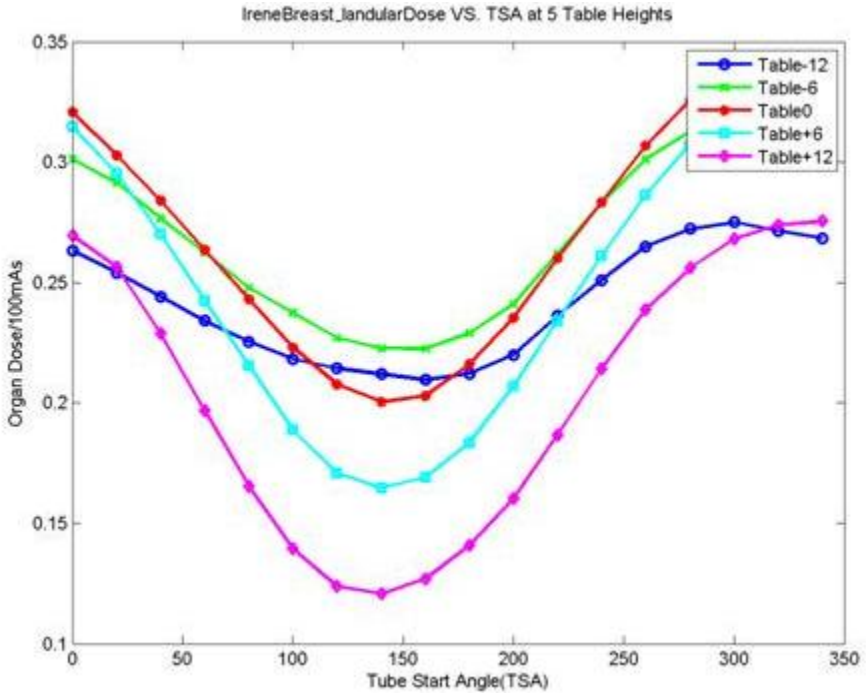


(a)

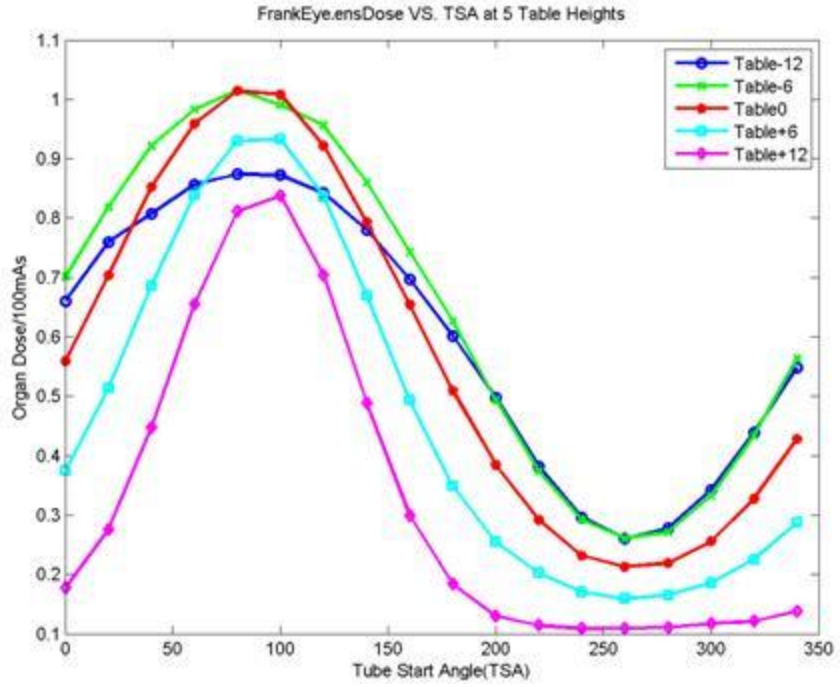
FrankEye.ensDose VS. TSA at 5 Table Heights
Table-12
Table-6
Table0
Table+6
Table+12
Organ Dose/100mAs
Tube Start Angle(TSA)
1.1
1
0.9
0.8
0.7
0.6
0.5
0.4
0.3
0.2
0.1
0
50
100
150
200
250
300
350

(b)

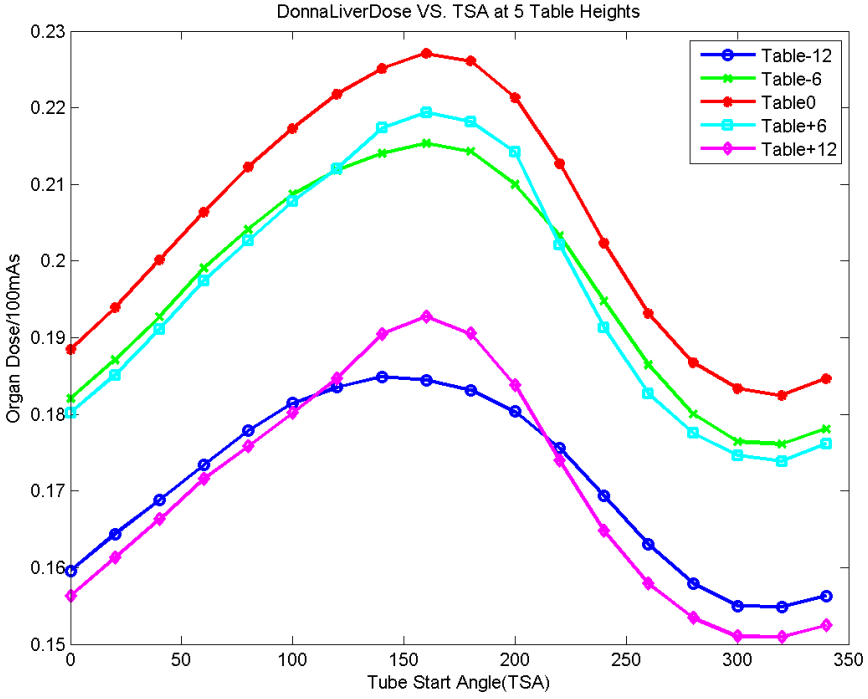
DonnaLiverDose VS. TSA at 5 Table Heights
Table-12
Table-6
Table0
Table+6
Table+12
Organ Dose/100mAs
Tube Start Angle(TSA)
0.23
0.22
0.21
0.2
0.19
0.18
0.17
0.16
0.15
0
50
100
150
200
250
300
350

(c)

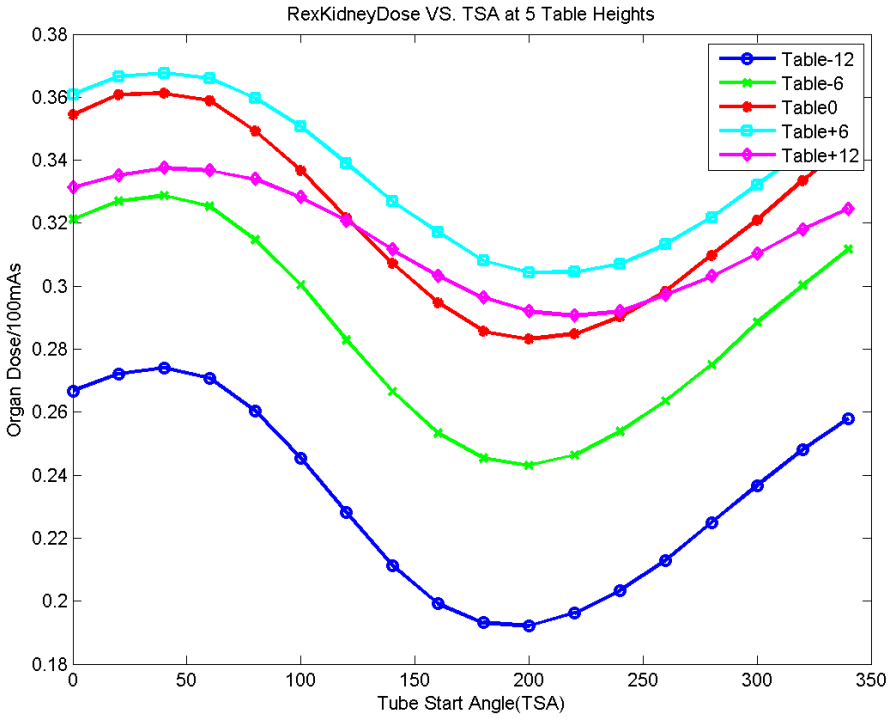


(d)

**Figure 8.10. Exemple organ dose as a function of tube start angle at various table heights: isocenter (Table0), 6cm above isocenter (Table+6), 12cm above isocenter (Table+12) , 6cm below isocenter (Table-6), 12cm below isocenter (Table-12). (a) the breast dose for Irene, (b) the eye lens dose reduction for Frank, (c) the liver dose reduction for Donna, and (d) the kidney dose reduction for Rex.**

### 8.3.3. Discussion (Constant tube current)

The effect of tube start angle remains the same as what was discussed in Chapter 7: as the tube start angle changes, there is significant organ dose variation. The magnitude of dose variation, however, is larger than that from a Siemens Sensation 64 scanner. Previously it was concluded that the technique to control the tube start angle to reduce organ dose only works for pediatric patients, or very small organs for adults patients, such as eye lens. However, with the much larger beam width and higher pitch on Siemens Definition Flash CT scanner, the technique

can essentially be applied to any organ, regardless of the patient and organ size. For example, Table 7.3 showed that the potential dose reduction from adjusting the tube start angle on a Sensation 64 CT scan for Irene is only 4%, while Figure 8.10a showed that the dose reduction can be as high as 45% (when the patient is centered) if the scan is performed under Flash mode on Definition Flash CT scanner. Even for organs as large of liver, the dose reduction from adjusting the tube start angle can be 20%, as shown in Figure 8.10c when table is centered. For small organs such as eye lens, the dose reduction is dramatic: 80% as shown in Figure 8.8b when table is centered.

Raising or lowering the table changes the radiation dose to individual organs. For example, Figure 8.10a shows that the breast dose to Irene is reduced by about 40% when the table is raised by 12cm. Compared to the measurement results shown in Figure 8.9, the results for organ doses are not as self-explanatory. For example, it is very clear in Figure 8.9 that as the table is raised, the radiation dose to the small ion chamber decreases. However, Figure 8.10c shows that the dose to liver decreases no matter if the table is raised or lowered. By reviewing all the results for all the organs and all the patients, it could be concluded as follows: **for organs that are in the anterior side of the patient, such as eye lens and breast, the organ dose decreases as the table is raised. For organs that are in the posterior side of the patient, such as kidneys, the organ dose decreases as the table is lowered. For organs that are in the middle, such as gonads, lungs, thyroid, colon, stomach, bladder, esophagus, and liver, the organ dose decreases as the table moves either up or down.**

The rule of the thumb is that as the table moves up and down, the further away an organ of interest is from isocenter, the lower radiation dose it would receive. This explains why in some cases such as what is shown in Figure 8.10a for breast glandular tissue, that lowering the table would sometimes also reduce the radiation dose. While lowering the table first make the breast glandular tissue closer to isocenter and therefore increase the radiation dose to it, if the table is lowered so much that the breast glandular tissue is past the isocenter, the radiation dose will start decreasing again. In order to demonstrate this in a clearer fashion, another set of simulations with finer samples of table heights were performed just for Irene at a single tube start angle. The relative differences of radiation dose to several organs were plotted as a function of table height and shown in Figure 8.11. For anterior organs such as breast glandular tissue and eye lens, the radiation dose always decreases as the table is raised (higher table height value); while when the table is lowered (lower table height value), the radiation dose first increases and then decreases when the organ passes the isocenter. Similarly, for posterior organs such as kidneys and rectum, the radiation dose always decreases as the table is lowered; while when the table is raised, the radiation dose first increase and then decreases. For organs in the middle, such as liver, the radiation dose decreases no matter the table is raised or lowered. This is a general rule, although the absolute “turning point” still depends on the specific organ size and patient anatomy.

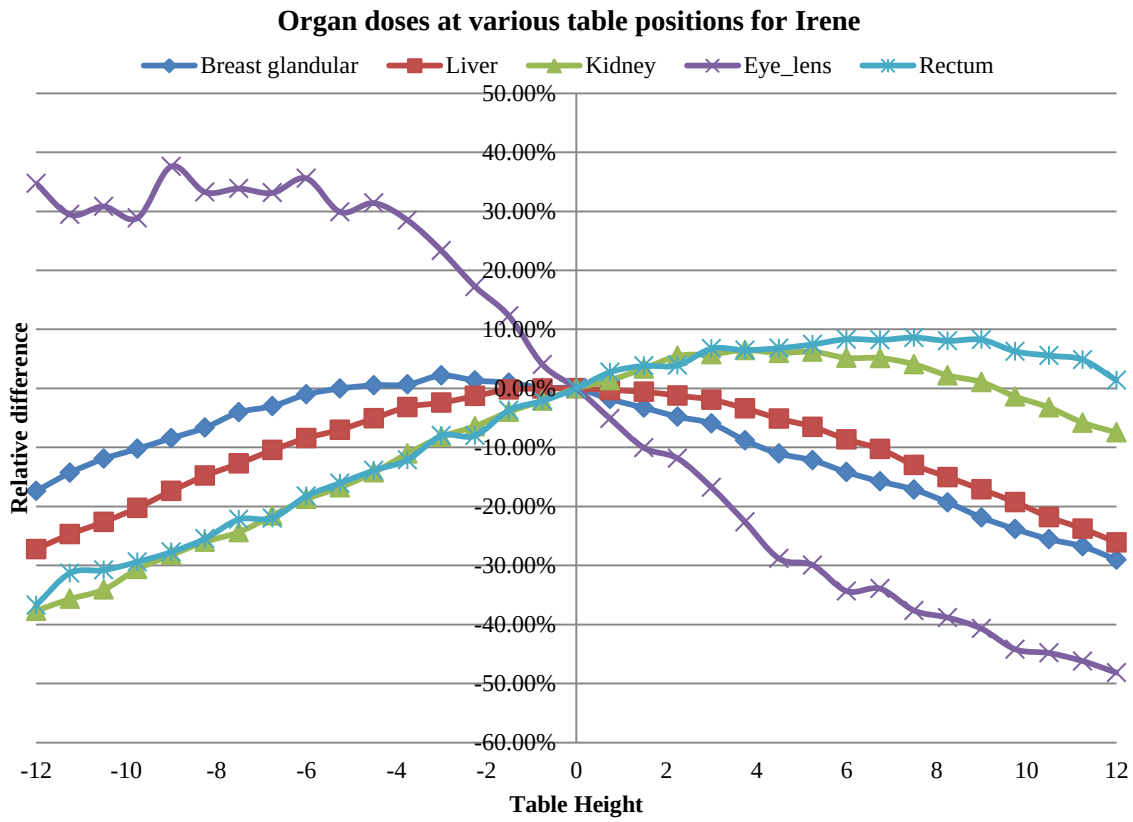


**Figure 8.11 The relative difference of radiation dose to several organs for Irene at different table heights.**

## 8.4 Reducing Radiation Dose by Controlling Table Height and Tube Start Angle Under Tube Current Modulation

After investigating the effects under constant tube current, it is necessary to study these effects when tube current modulation is used. Since when the tube current is modulated, the photon fluence would be different when the x-ray tube is irradiating the patient across projections. This may cause the behavior or the magnitude of the dose reduction from adjusting tube start angle and table height to be different.

### 8.4.1. Methods (TCM on)

#### 8.4.1.1 Methods - Exposure Measurements on a Thorax Phantom at Various Table Heights and Tube Start Angles (TCM on)

Using the same methods as described in 8.3.1.1,exposure measurements were performed on the surface of a chest anthropomorphic phantom at different tube start angles and table heights, except that in this set of measurements the tube current modulation was turned on, as what's routinely prescribed in clinics. As discussed in 8.1, when TCM is used, the mis-positioning of a patient during the topogram can cause the magnification of the projection image and therefore influence the calculation of the attenuation of the patient during the TCM planning. **In order to circumvent this, the topograms were performed at the center position, and then the table was moved to different heights while every scan uses the same topogram for the TCM planning.** To demonstrate the larger dose savings from the Flash mode, another set of measurements were performed using a Definition Flash CT scanner (120kVp, 140 Quality Reference mAs, 38.4mm collimation, dual source, 3.2 pitch).

#### 8.4.1.2 Methods - Validation of the TCM Schema When Topogram is Performed at a Different Table Heights

In the previous section, in order to get rid of the magnification effect on TCM scheme, it was proposed to adjust the table height after the topogram is performed at center. However, it is unclear if changing the table height after topogram would still affect the TCM schemes. In order to verify that it would not interfere with the TCM schemes, a MATLAB subroutine was used to plot the TCM schemes (tube current versus table position) for each scan performed in the

previous session, including both scans on Sensation 64 scanner and scans on Definition Flash scanner, and compared to the TCM scheme with the table positioned at the center to study differences.

#### 8.4.1.3 Methods - Organ Dose Reduction to Clinical Patient Models by Controlling Tube Start Angle and Table Height (TCM on)

Section 8.3.2.2 showed the organ dose reduction by adjusting table heights and tube start angles under constant tube current. However, this is not the case for the majority of clinical practices. Therefore it is necessary to study the behavior, as well as the magnitude of organ dose reduction when tube current modulation is used. Since TCM scheme depends on attenuation information for each specific patient, it is necessary to use clinical patient models with known tube current functions, which is not the case for the GSF Family of voxelized models. As a result, new patient models were generated based on images obtained from actual exams performed at UCLA. Since smaller patients could potentially receive more dose reduction from adjusting tube start angle, 2 pediatric patient models were created. The first patient is a 15 year old female, while the second patient is a 4 year old female. These two patients both underwent a CT chest exam acquired on a Siemens Definition Flash CT scanner with CareDose 4D turned on. Flash thorax protocol was used for both patients with 120kVp, 128 x 0.6 collimation, dual source, and pitch of 3.0. Patient-specific and exam-specific tube current scheme functions were then extracted from raw projection files of each patient, and they were used as input in the Monte Carlo simulations to obtain organ dose estimates.

For each patient, a voxelized model was created from image data using the methods developed previously[48,50]. This process for a particular organ (glandular breast tissue) is illustrated in Figure 8.12. First, the contours of a region that fully encompass breast glandular tissue were explicitly drawn on each slice using manual and semi-automatic contouring techniques. Then a threshold technique was used to identify true glandular breast tissue within the region. The density and material composition for this organ was defined based on the corresponding description in the ICRU Report 44 composition of body tissue tables[76]. In addition to glandular breast tissue, lungs were also segmented in a similar approach. For regions on the images that were not explicitly contoured, they were assigned to one of six tissue types (lung, fat, water, muscle, bone or air) and one of 17 density levels based on their Hounsfield Unit (HU) value on a per voxel basis, as described in DeMarco et al[119].

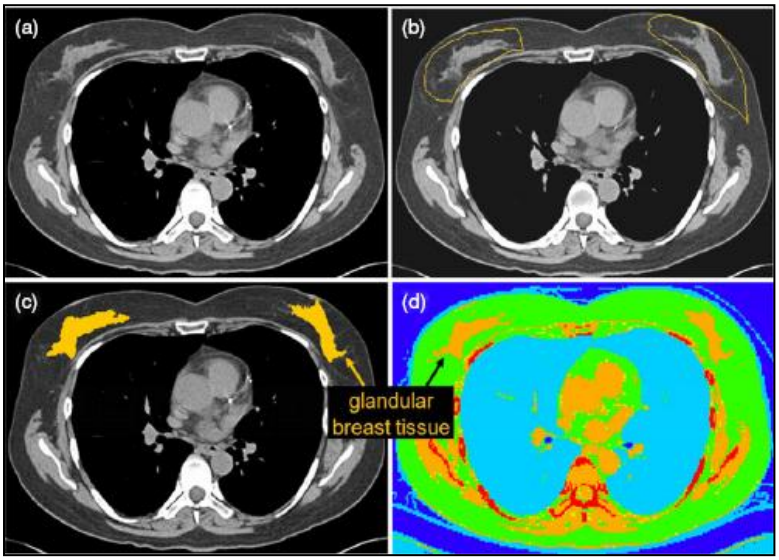


**Figure 8.12 Generation of a voxelized model: (a) original patient image, (b) contour of the breast region, (c) threshold image to identify glandular breast tissue and (d) the resulting voxelized model. Reprinted from Angel, et al[48].**

For each of these two patient models, dose to glandular breast tissue and lungs were estimated using Monte Carlo simulations under a variety of combinations of table heights and tube start angles for a Definition Flash CT scanner. The table was set to be at center, 5cm above center, 10 cm above center, 5cm below center, and 10cm below center. Similar to 8.2.2, at each specific table height, 18 simulations were performed with different tube start angles, and the results from tube A and tube B were combined to yield total radiation dose to organs. Since TCM scheme was used as input in Monte Carlo simulations, and the scheme obtained from the raw projection data has one specific tube start angle, different TCM schemes were generated by shifting the original scheme in the angular domain (e.g., a shift in the x-axis if tube current is plotted as a function of tube angle). It should be noted that the relationship between tube current and table position is kept unchanged in this process.

#### 8.4.1.4. Methods - Validation of the TSA Change on TCM

In the previous section, the tube current modulation schema for different tube start angles were generated by adding angular 'phase shift' onto existing tube current modulation scheme obtained from raw projection data. However, it is unclear that if tube current modulation scheme with different tube start angles can be approximated using this approach. In order to validate this methodology, a thorax anthropomorphic phantom was scanned for 10 times with TCM turned on to yield a number of different tube start angles. The tube current modulation schemas for each of these scans were obtained using the MATLAB subroutine, and they were compared to each other.

### 8.4.2. Results and Discussions (TCM on)

#### 8.4.2.1. Results - Exposure Measurements on a Thorax Phantom at Various Table Heights and Tube Start Angles (TCM on)

The measured exposure was plotted as a function of tube start angle for a number of table heights and it is shown in Figure 8.13 for the Sensation 64 CT scanner. The results are shown in Figure 8.14 for the Definition Flash CT scanner.

Similar to the cases where the tube current was kept constant, the selection of tube start angle and table height results in significant changes in radiation dose at the patient surface. Compared to the worst case start angle when the patient is centered, the radiation dose can be 35% higher or 70% lower by adjusting the table height and the tube start angle while keeping all other scanning parameters (kVp, mAs, pitch) the same for the Sensation 64 scanner; for the Definition Flash scanner with a wider nominal beam width and higher pitch, this range increases to 72% higher or 79% lower. Generally, as the table moves higher (dosimeter closer to top of gantry), the exposure decreases. However, there is one exception where when the table is moved from 100mm to 145mm below isocenter for the Definition Flash scanner, the radiation dose decreased, as opposed to increase. This is because the ion chamber was moved down far enough to pass isocenter, and therefore the measured exposure started to climb up again because of the attenuation from the bowtie filtration edges. This was also explained in 8.3.3.

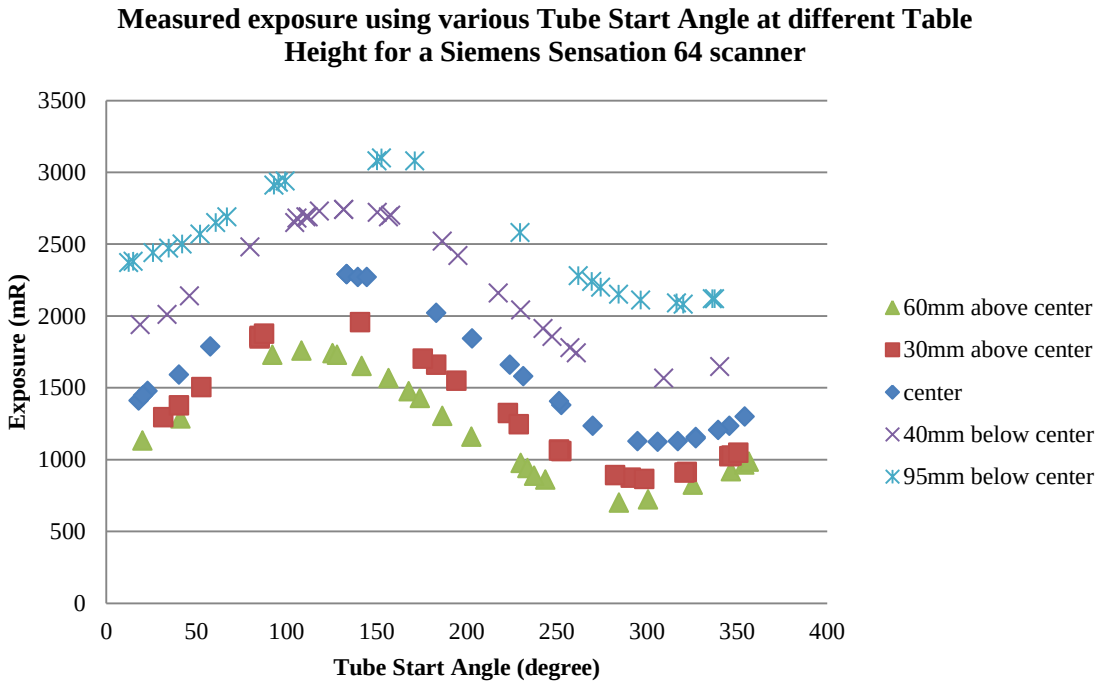


**Figure 8.13 Exposure measured at the surface of an anthropomorphic phantom versus tube start angle at a variety of table heights for the chest protocols of a Siemens Sensation 64 CT scanner.**

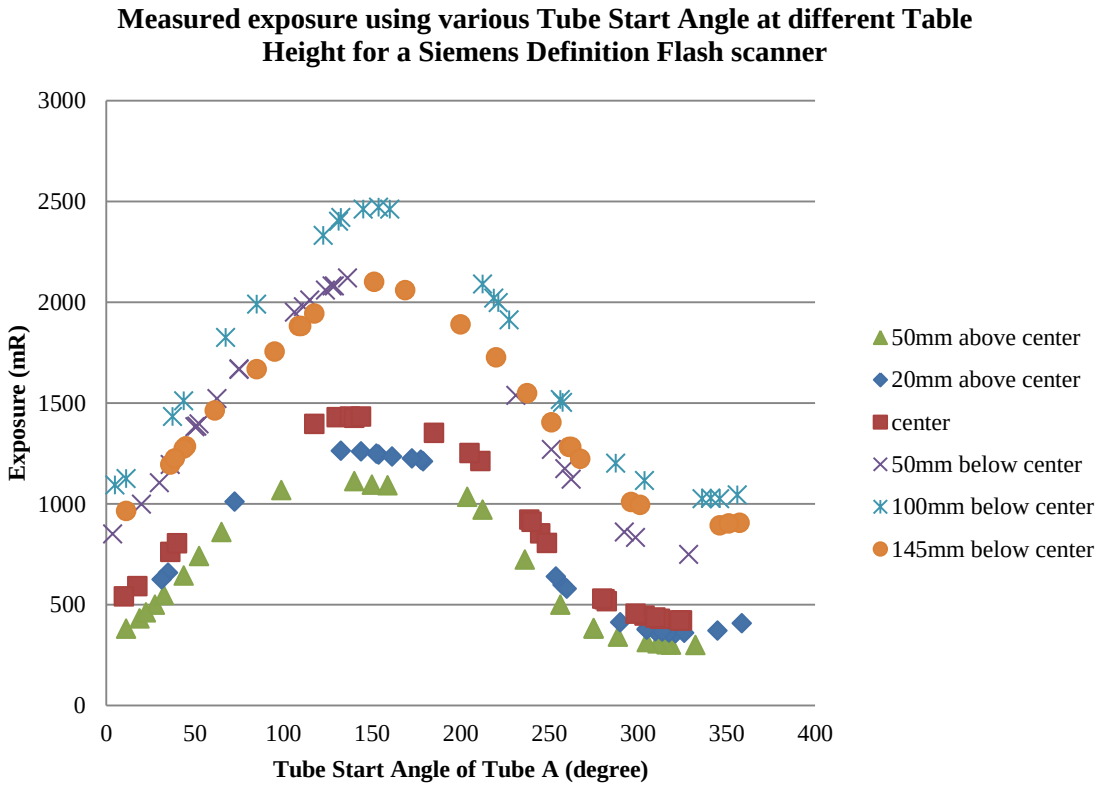


**Figure 8.14 Exposure measured at the surface of an anthropomorphic phantom versus tube start angle at a variety of table heights for the chest protocol of a Siemens Definition Flash CT scanner.**

### 8.4.2.2. Results - Validation of the TCM Schema When Topogram is Performed at a Different Table Heights

The results for Sensation 64 scanner for validation are shown in Figure 8.15, while the results for Definition Flash scanner are shown in Figure 8.16. For Sensation 64 scanner, there are tube current modulations both in xy plane (in plane) and in z direction (along the table movement). Figure 8.15 shows that all TCM scheme curves more or less overlap with each other along table position. Therefore it demonstrates that there is no significant difference in the

modulation in z direction. In xy plane, there are some slight off-phase behaviors between different curves. This can be explained by the differences in the tube start angle for each scan, since tube start angle is random. For the Flash mode of Definition Flash scanner, there is only z direction tube current modulation. Figure 8.16 shows that the scans at center and at 20mm above center have almost the same TCM schemes, while scans at other four table heights have almost the same TCM schemes. However, the tube current of the latter group is about 5% higher than the former group. It is suspected that this 5% difference comes from experiment setup differences such as accidental movement of the phantom between scans.

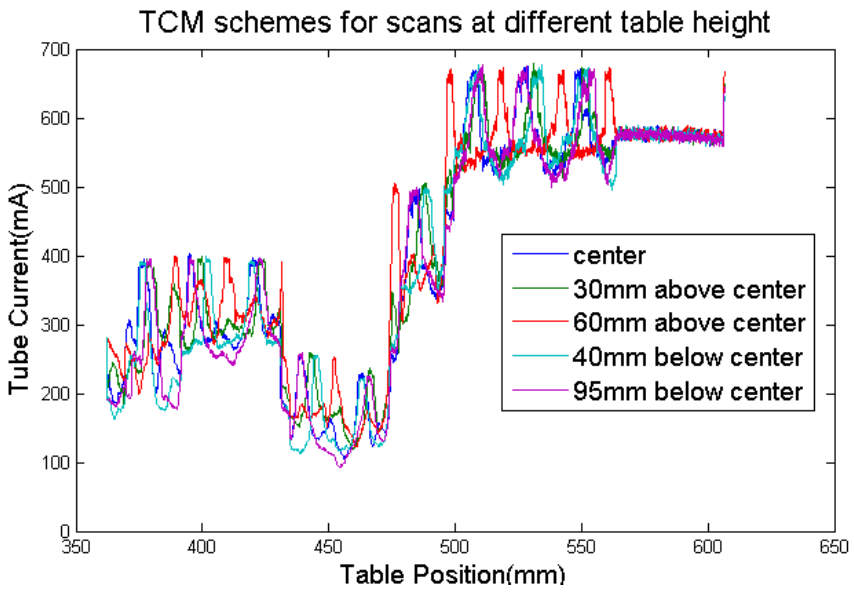


**Figure 8.15 TCM schemes for a chest anthropomorphic phantom under scans at different table height after the topogram at center for Siemens Sensation 64 CT scanner.**

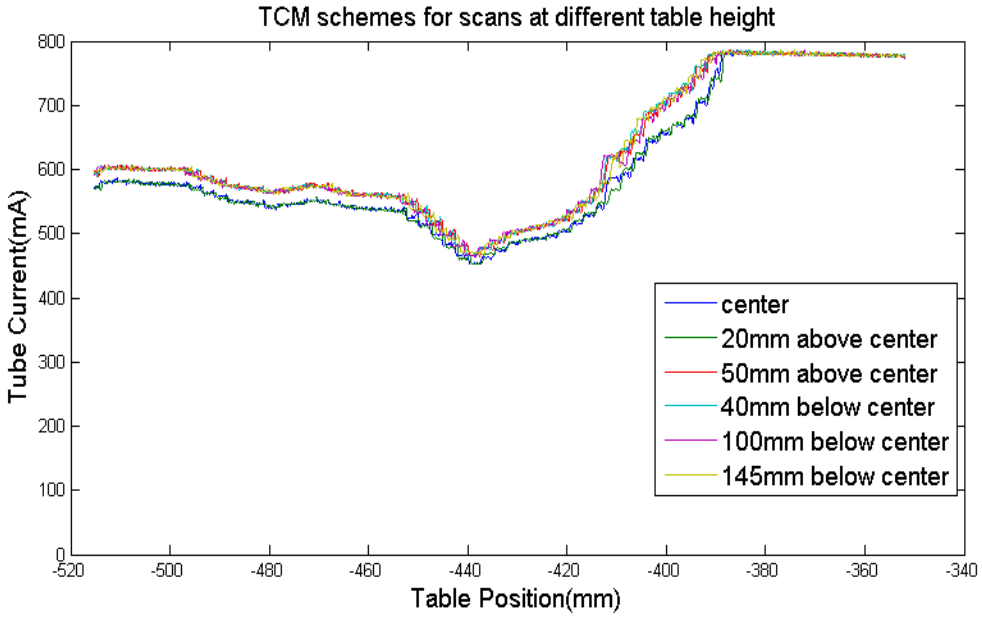


**Figure 8.16 TCM schemes for a chest anthropomorphic phantom under scans at different table height after the topogram at center for Siemens Definition Flash CT scanner.**

### 8.4.2.3. Results - Organ Dose Reduction to Clinical Patient Models by Controlling Tube Start Angle and Table Height (TCM on)

Dose to the lungs and glandular breast tissue for both patients is shown in Figure 8.17. The results were reported on a per 100mAs basis. It is shown that the tube start angle does not have much of an effect to dose to lungs, even to patient 2 with the age of 4 years. However, raising or lowering the table could reduce dose to lungs by up to 30%, as shown in Figure 8.17a and Figure 8.17c. This is consistent with the results shown previously in Chapter 7 and 8.3.2.2: large organs do not benefit from adjusting tube start angles, but they benefit from adjusting table height. For small organs such as glandular breast tissue, there is significant dose reduction from controlling both tube start angle and table height. For example, for larger patients such as patient

1, the dose reduction is on the order of 30% from tube start angle. For smaller patients such as patient 2, who has only very small amount of glandular breast tissue, the dose reduction is on the order of 50%. For both patients, the dose reduction is about 25% when the table is raised by 10cm. Overall, when the TCM is used, the behavior of dose reduction to organs is very similar to that without TCM.

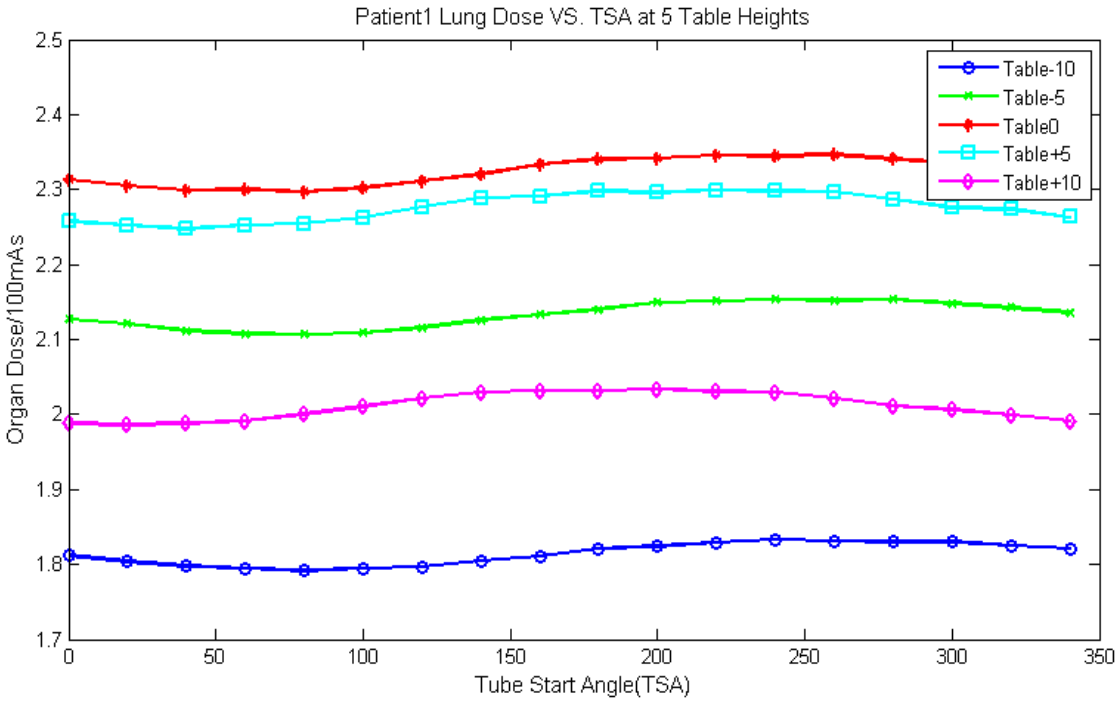


(a)

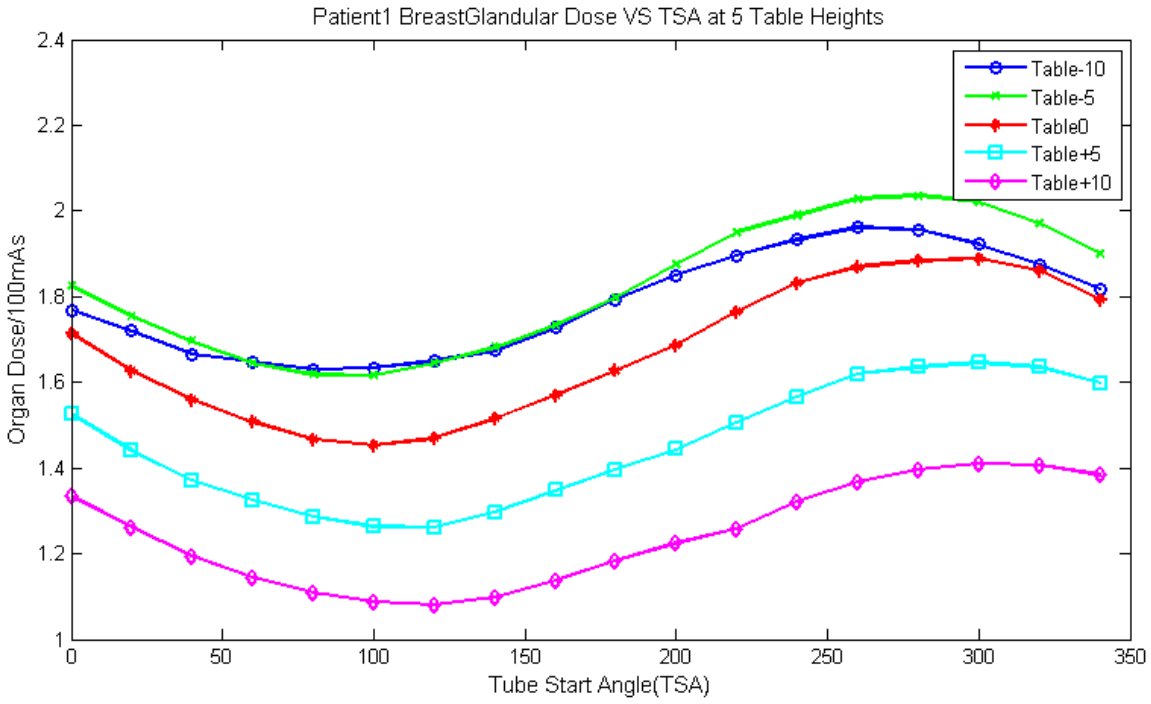
Patient1 BreastGlandular Dose VS TSA at 5 Table Heights
Organ Dose/100mAs
Tube Start Angle(TSA)
Table-10
Table-5
Table0
Table+5
Table+10
2.4
2.2
2
1.8
1.6
1.4
1.2
1
0
50
100
150
200
250
300
350

(b)

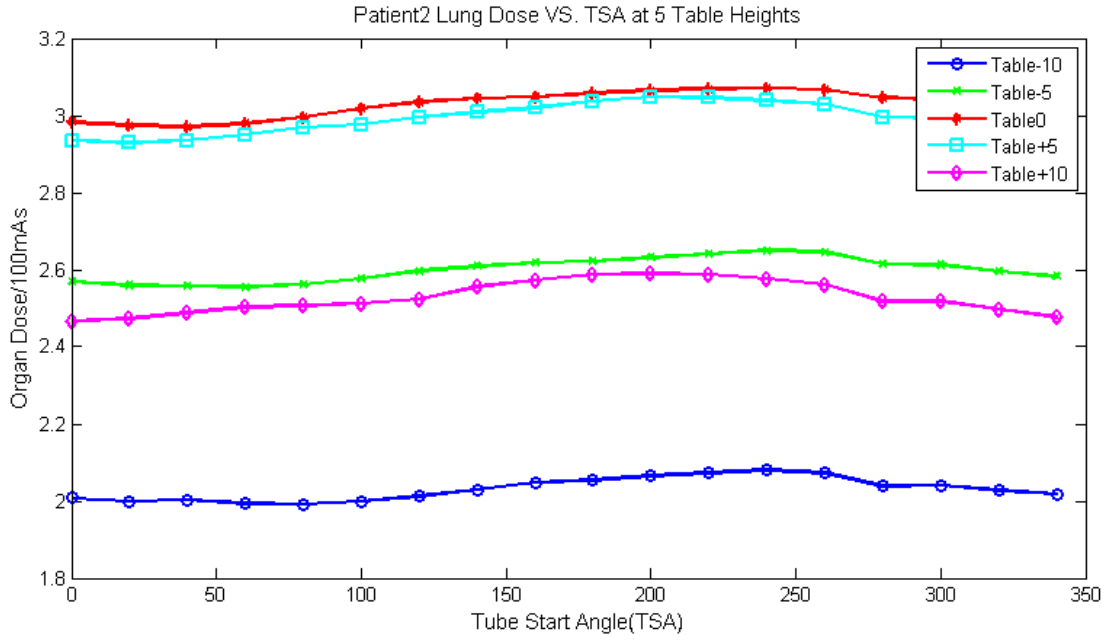
Patient2 Lung Dose VS. TSA at 5 Table Heights
Organ Dose/100mAs
Tube Start Angle(TSA)
Table-10
Table-5
Table0
Table+5
Table+10
3.2
3
2.8
2.6
2.4
2.2
2
1.8
0
50
100
150
200
250
300
350

(c)

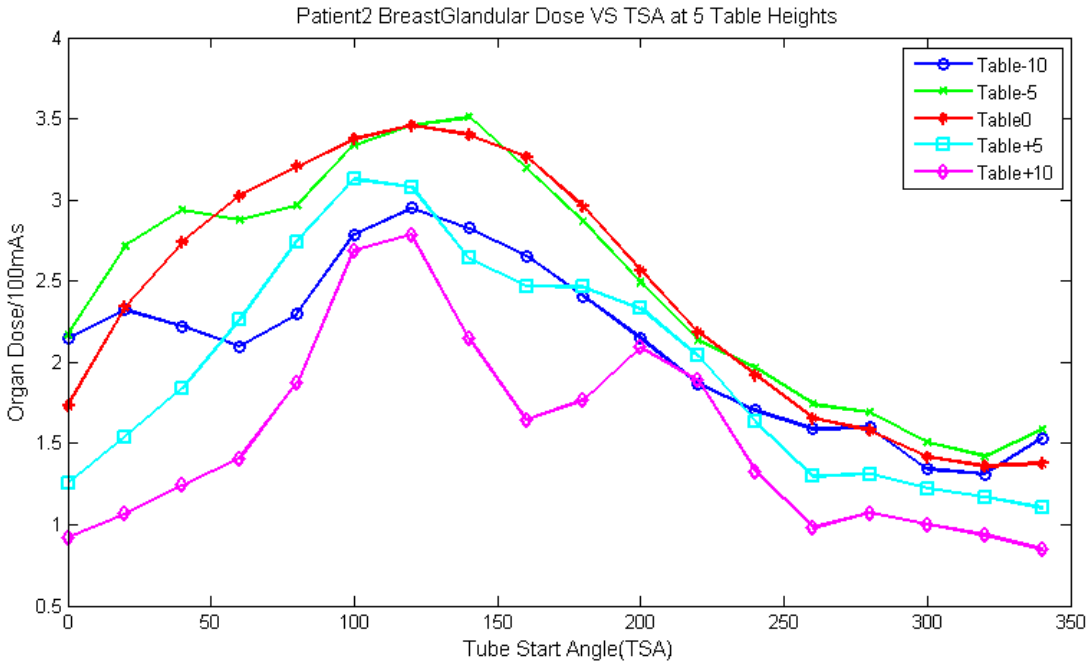


(d)

**Figure 8.17 Lung and breasts dose as a function of tube start angle at various table heights: isocenter (Table0), 5cm above isocenter (Table+10), 10cm above isocenter (Table+10) , 5cm below isocenter (Table-5), 10cm below isocenter (Table-10). (a) the lung dose reduction for patient 1, (b) the breast dose reduction for patient 1, (c) the lung dose reduction for patient 2, and (d) the breast dose reduction for patient 2.**

### 8.4.2.4. Results - Validation of the TSA Change on TCM

Figure 8.18 shows the tube current as a function of tube angle for each of the 10 scans. Since the tube start angle is random and it is not under control, the modulation schemes start with different angle. However, the shape and the magnitude of the schemes barely change for scans with different tube start angles. Therefore, it could be concluded that the method used in 8.4.1.3 to generate tube current modulation scheme at different tube start angles is valid.

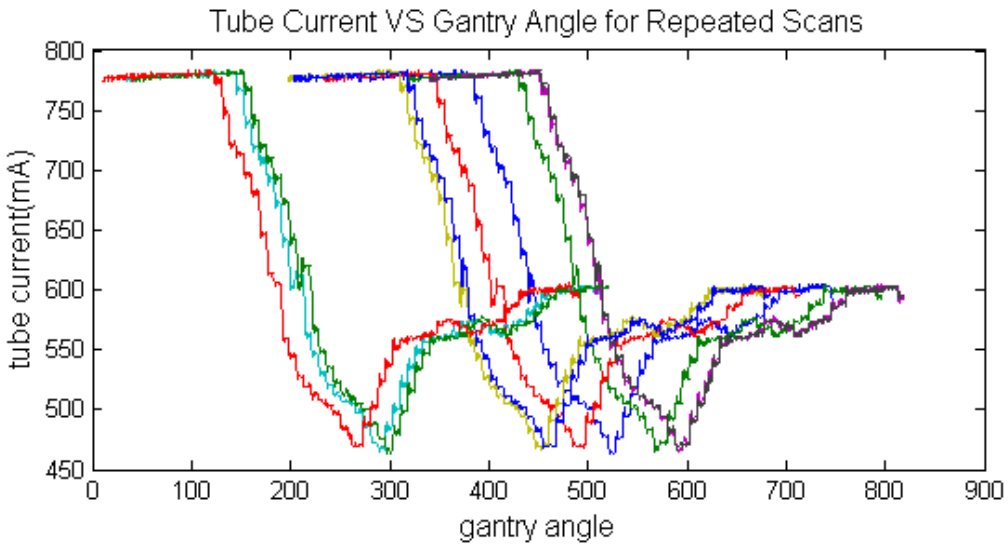


**Figure 8.18 Tube current as a function of gantry angle for scans with different tube start angles. It could be concluded that the differences in tube start angle do not cause effect to the modulation schema.**

## 8.5 The Validation of The Modeling of Tube Start Angle and Table Height in MCNPX

In the UCLA CT Dose Simulation Package, tube start angle and table height were specifically modeled as input parameters which the users can specify. These were used in the simulations description throughout this chapter. Since the validation methods described in Chapter 3 compares the measured and simulated CTDI, which does not take the tube start angle and table height into account, it is necessary to validate the model in a more complex radiation transport environment where tube start angle and table height play critical roles. The small ion chamber measurement on the surface of an anthropomorphic phantom is a perfect candidate for such set of validation experiments. Therefore, Monte Carlo simulations were performed for the measurement series using Sensation 64 CT scanner for every single scan at each table height, and the simulated results were compared to the measurements.

### 8.5.1. Methods

A voxelized model of the thorax phantom was created from the image data from one of the scans using the methods described in 8.4.1.3. The wall of the ionization chamber and the air inside the ionization chamber were manually contoured. Since the ion chamber has very small volume (0.6cc), the original resolution (512 x 512) of the CT images was retained in order to obtain sufficient resolution to tally within the air portion of the ionization chamber. Since the purpose of this set of simulations is to validate the tube start angles, and from Chapter 6 it was learned that any displacement of scan start location along z-axis would have significant effect on the distribution of the dose profile on surface, the over-scan range was carefully selected by examining the tube current scheme in the raw data in order to assure that the x-ray beam on starts at the exact correct location and the exact correct tube start angle. Simulations for each scan were performed and post-processed to be in the unit of mGy, and they were compared to the measurements. At each table height, the percent error of the simulated dose was calculated for each tube start angle relative to the dose measured with the ionization chamber.

### 8.5.2. Results and Discussions

Table 8.2 shows the measured dose, simulated dose, as well as their relative difference for each table height. Figure 8.19 shows the doses as function of tube start angle for each table height.

**Table 8.2 Measured dose, simulated dose, as well as their difference in the unit of mGy for experiments of helical scans on a Sensation 64 CT scanner irradiating a small ion chamber on the surface of a thorax phantom.**

| Center (mGy) | | | 30mm above center (mGy) | | | 60mm above center (mGy) | | |
|---|---|---|---|---|---|---|---|---|
| Measured | Simulated | Difference | Measured | Simulated | Difference | Measured | Simulated | Difference |
| 10.07 | 9.09 | -9.7% | 8.05 | 7.17 | -10.9% | 7.61 | 6.95 | -8.7% |
| 11.36 | 11.51 | 1.3% | 15.98 | 15.87 | -0.7% | 6.63 | 5.97 | -10.0% |
| 17.70 | 18.04 | 1.9% | 7.73 | 6.97 | -9.8% | 11.48 | 11.19 | -2.5% |
| 12.01 | 12.59 | 4.8% | 9.56 | 9.51 | -0.5% | 9.58 | 9.27 | -3.2% |
| 10.42 | 9.26 | -11.2% | 8.21 | 7.31 | -11.0% | 9.21 | 9.04 | -1.8% |
| 14.24 | 12.90 | -9.4% | 9.22 | 9.09 | -1.5% | 7.19 | 6.82 | -5.2% |
| 11.72 | 10.25 | -12.5% | 11.54 | 11.69 | 1.4% | 14.50 | 14.78 | 1.9% |
| 17.07 | 17.42 | 2.0% | 9.98 | 8.98 | -10.0% | 8.08 | 7.42 | -8.2% |
| 14.50 | 12.99 | -10.4% | 10.37 | 10.53 | 1.5% | 7.24 | 6.82 | -5.8% |
| 16.38 | 14.74 | -10.0% | 12.49 | 11.51 | -7.9% | 8.19 | 7.64 | -6.7% |
| 10.30 | 10.01 | -2.8% | 8.33 | 7.98 | -4.2% | 6.41 | 5.63 | -12.1% |
| 17.96 | 17.33 | -3.5% | 11.80 | 12.04 | 2.1% | 7.04 | 6.19 | -12.1% |
| 11.51 | 11.76 | 2.2% | 8.82 | 8.75 | -0.9% | 12.21 | 12.06 | -1.3% |
| 18.22 | 18.55 | 1.8% | 7.96 | 7.63 | -4.2% | 12.31 | 12.04 | -2.2% |
| 17.78 | 18.04 | 1.4% | 8.09 | 7.11 | -12.1% | 13.60 | 13.51 | -0.6% |
| 15.77 | 14.11 | -10.5% | 9.39 | 9.40 | 0.1% | 8.40 | 8.17 | -2.7% |
| 15.28 | 14.22 | -6.9% | 8.03 | 7.08 | -11.9% | 11.09 | 10.86 | -2.1% |
| 11.41 | 11.67 | 2.3% | 11.89 | 10.92 | -8.1% | 11.97 | 11.72 | -2.1% |
| 13.96 | 12.55 | -10.1% | 13.80 | 14.04 | 1.8% | 13.78 | 14.04 | 1.9% |
| 13.32 | 12.07 | -9.4% | 12.99 | 13.43 | 3.4% | 6.98 | 6.40 | -8.3% |
| 18.05 | 18.36 | 1.7% | 9.07 | 8.09 | -10.8% | 12.32 | 12.07 | -2.0% |
| 11.00 | 9.53 | -13.4% | 15.71 | 15.33 | -2.4% | 13.05 | 13.01 | -0.4% |
| 13.26 | 13.42 | 1.2% | 12.48 | 11.51 | -7.8% | 9.30 | 8.61 | -7.5% |
| 13.44 | 13.71 | 2.0% | 8.87 | 7.84 | -11.6% | 12.40 | 12.84 | 3.5% |

(Continue Table 8.2)

| 40mm below center (mGy) | | | 95mm below center (mGy) | | |
|---|---|---|---|---|---|
| Measured | Simulated | Difference | Measured | Simulated | Difference |
| 21.72 | 21.07 | -3.0% | 17.78 | 17.56 | -1.3% |
| 15.10 | 13.73 | -9.1% | 17.87 | 18.00 | 0.7% |
| 17.37 | 17.72 | 2.0% | 24.62 | 25.19 | 2.3% |
| 14.31 | 14.20 | -0.8% | 18.83 | 18.04 | -4.2% |
| 14.32 | 12.97 | -9.4% | 20.15 | 19.50 | -3.2% |
| 21.81 | 22.20 | 1.8% | 23.13 | 24.32 | 5.2% |
| 22.25 | 22.60 | 1.6% | 19.45 | 20.59 | 5.9% |
| 21.29 | 22.09 | 3.8% | 24.62 | 25.40 | 3.2% |
| 16.29 | 14.92 | -8.4% | 18.92 | 18.19 | -3.9% |
| 13.78 | 13.07 | -5.2% | 19.80 | 21.05 | 6.3% |
| 21.29 | 22.09 | 3.8% | 23.39 | 24.81 | 6.1% |
| 16.21 | 16.54 | 2.1% | 24.62 | 25.40 | 3.2% |
| 21.99 | 22.36 | 1.7% | 17.87 | 18.07 | 1.1% |
| 14.38 | 14.45 | 0.5% | 18.66 | 18.11 | -3.0% |
| 15.27 | 15.79 | 3.4% | 21.99 | 21.28 | -3.2% |
| 18.75 | 17.34 | -7.5% | 18.40 | 18.81 | 2.2% |
| 14.96 | 13.47 | -10.0% | 24.53 | 25.77 | 5.0% |
| 22.25 | 22.23 | -0.1% | 19.36 | 18.50 | -4.4% |
| 13.47 | 13.33 | -1.1% | 19.97 | 21.08 | 5.6% |
| 14.53 | 13.24 | -8.9% | 24.44 | 24.56 | 0.5% |
| 20.06 | 18.74 | -6.6% | 20.94 | 20.60 | -1.6% |
| 21.99 | 22.16 | 0.8% | 22.34 | 21.78 | -2.5% |
| 18.31 | 18.85 | 3.0% | 24.79 | 25.40 | 2.5% |
| 19.80 | 18.50 | -6.6% | 17.96 | 18.48 | 2.9% |

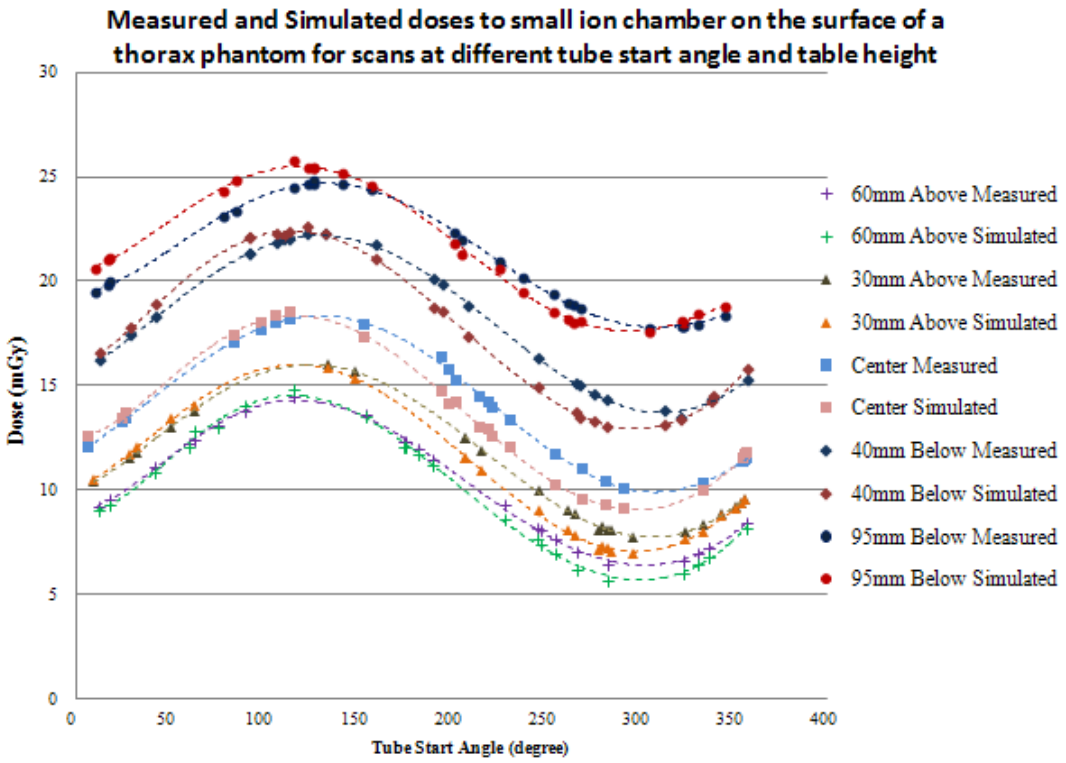


**Figure 8.19 Measured and simulated doses versus tube start angles at different table heights for scans using a Siemens Sensation 64 scanner for the validation of the modeling of tube start angle and table heigh.**

These results illustrated that, putting apart other factors such as spectra, bowtie filtration, particle transport, patient modeling, etc., it is possible to obtain simulation accuracies with a root mean square error of less than 10% even by taking into account the delicate details of tube start angle and table height. It has been suggested that for simulations as complex as CT dose, which include a large number of parameters that could influence the results, simulation with errors of up to 20% can be considered accurate[39]. The maximum absolute error reported in Table 8.2 was 13.4%, which is well below 20%. Figure 8.19 shows that there is a consistent a phase shift between the simulated and measured values as a function of tube start angle. This may attribute

to a lateral displacement between the geometry in measurements and that in simulations. This in another way illustrates the importance of exactly matching all the intricate and detailed conditions for a validation study.

## 8.6 Effects on Image Quality

It has been demonstrated in the previous sessions that organ dose can be significantly reduced by adjusting the tube start angle and table height in helical CT scans, especially when the collimation is wide, and when the pitch used is high. Before these two techniques are proposed to be used in practice, however, it is crucial to investigate how much the image quality would be compromised. The purpose of this session is to study how the change of tube start angle and table height may influence the image quality. Measurements on different phantoms under a variety of scanning protocols are proposed using a Siemens Sensation 64 MDCT scanner.

### 8.6.1. Effect from Tube Start Angle

The change of tube start angle has no influence to image quality of CT images because in all clinical MDCT systems, the tube start angle is a random variable. If tube start angle had any effect on image quality, the quality assurance of CT scanners has to take it into account. The fact that it is random in current clinical practice proved that it does not have any effect on image quality.

### 8.6.2. Effect from Table Height

#### 8.6.2.1. Methods

The effect to image quality from changing table height was investigated both under constant tube current and under tube current modulation.

For constant tube current, the ACR accreditation physics testing procedures[138] were performed at various table heights. These include the assessments of CT number accuracy, low contrast resolution, homogeneity and high contrast resolution. Scans were performed at different table heights (3cm above isocenter, 6cm above isocenter, 4cm below isocenter, and 9.5cm below isocenter) using 120kVp, 200mAs, 24 x 1.2 mm collimation, and pitch of 1. For the assessments of CT Number accuracy, ROIs were drawn for each of the four inserts with different materials (bone, polyethelyene, acrylic, and air), as well as for water at the CT Number module of the phantom. This was performed on 3 consecutive slices and it is illustrated in Figure 8.20. For the assessment of low contrast resolution, two ROIs were drawn at the insert and the background at the low contrast resolution module of the phantom. Contrast to Noise Ratio (CNR) was calculated as ($Mean_{Signal}$ - $Mean_{Background}$)/Standard $Deviation_{Background}$. CNR was calculated for 3 consecutive slices on the low contrast module and this process is illustrated in Figure 8.21. For the assessment of homogeneity, 5 ROIs were drawn at the homogeneity module of the ACR phantom at 3 o'clock, 6 o'clock, 9 o'clock, 12 o'clock and center position, respectively. The maximum difference between the mean CT number of the four peripheral positions and that of the center position was computed. This process was performed for 2 consecutive slices and it is illustrated in Figure 8.22. Finally, for the assessment of high contrast resolution, a slice with the highest spatial resolution was chosen to represent the spatial resolution for images obtain at each table height. This is illustrated in Figure 8.23.

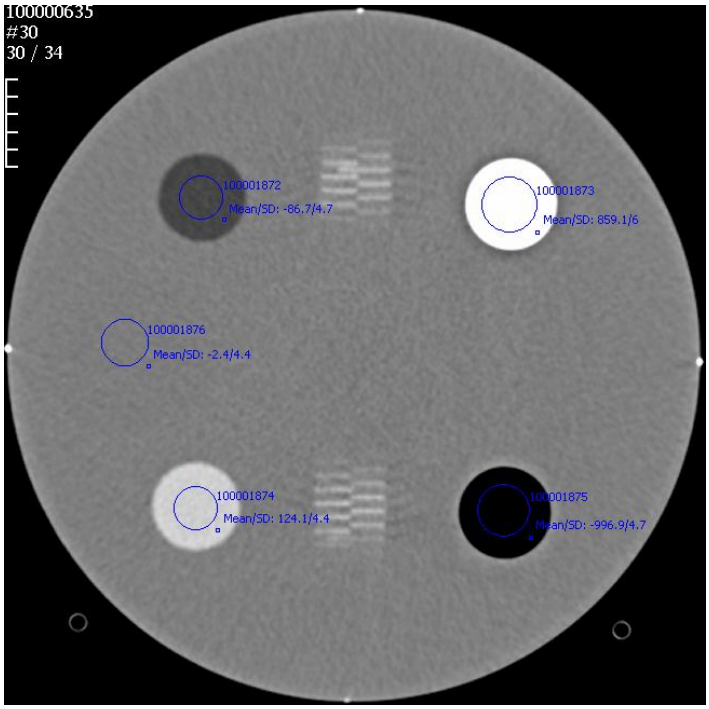


**Figure 8.20 ROIs were drawn for each of the four inserts with different materials, as well as for water. Upper left: Polyethelyne; Upper right: Bone; Lower left: Acrylic; Lower Right: Air; Middle left: Water.**

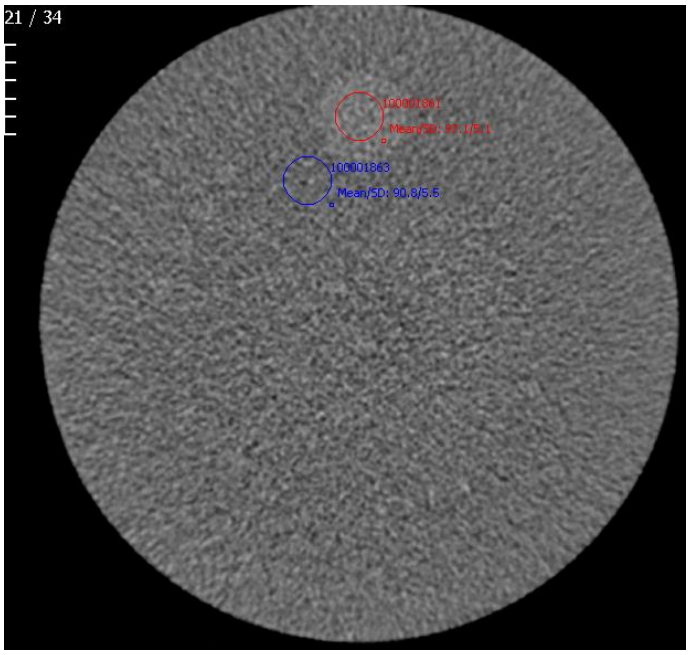


**Figure 8.21 ROIs were drawn at the low contrast signal and the background at each slice of the low contrast module.**

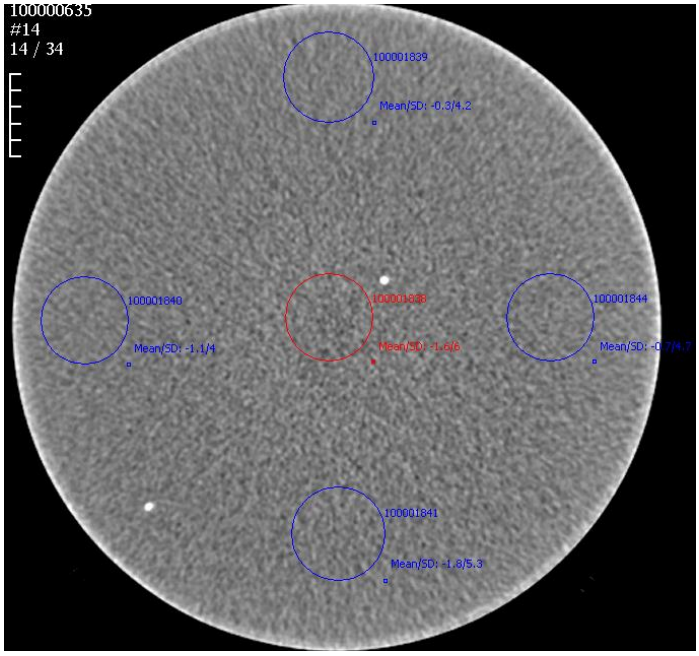


**Figure 8.22 Five ROIs were drawn at the homogeneity module of the ACR phantom to calculate the maximum difference between the CT mean number of any of the four peripheral position to that of the center position.**

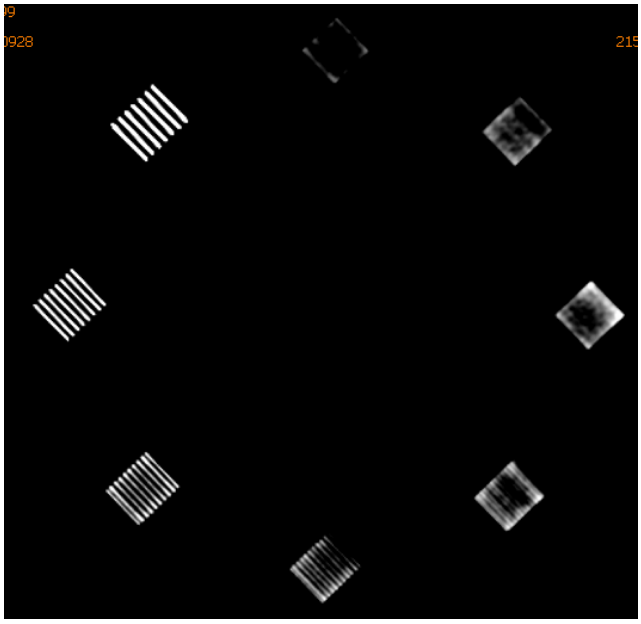

**Figure 8.23 One slice with the highest spatial resolution was selected to represent the spatial resolution for image sets obtained at different table heights.**

For tube current modulation, the thorax phantom was scanned at different table heights (as previously, 3cm and 6cm above isocenter, as well as 4cm and 9.5cm below isocenter) using 120 kVp, 200 Quality Reference mAs, 24 x 1.2 mm collimation, and pitch of 1. CT number and noise were measured in the heart region, which is a relative uniform area of the on images obtained at different table height. This is illustrated in Figure 8.24.

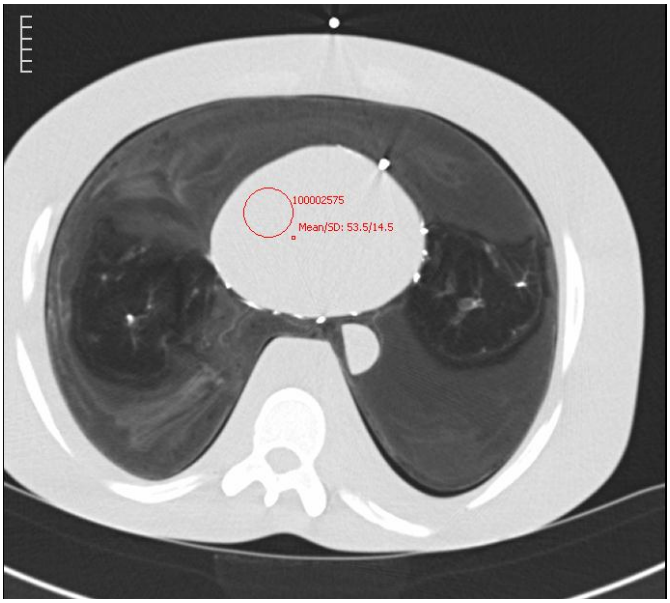


**Figure 8.24 CT number and noise were measured in the heart region of an anthropomorphic chest phantom for images at each table height.**

### 8.6.2.2. Results and Discussion

Table 8.3 shows the results for CT Number measurements of five different materials, as well as CNR measurements at all five table heights. Both the values for three individual slices and the average are reported. Comparing to the center location, the CT Numbers at four different table heights for all five materials are within ±5 HU, except for bone at 3cm above isocenter, and air at 9.5cm below isocenter. This may due to the variation of beam hardening effect when the

table is raised or lowered, which have a larger effect on materials that have extreme CT numbers, such as bone (very large) and air (very small). Nonetheless, the CT number change for materials in soft tissue region is very minor when the table is located at different vertical positions within the gantry, from the very bottom to the very top. For bone and air, since the contrast on a CT image around these two materials is usually large, it is suspected that the appearance of the image details would not change even when the CT numbers differ by 20HU. As for CNR, there is merely any degradation between center and various table heights, except for the table height of 9.5cm below isocenter. At this table height the entire ACR phantom is below the isocenter. In addition, there are some artifacts around the top of the phantom which caused the inconsistency of CNR, shown in Figure 8.25.

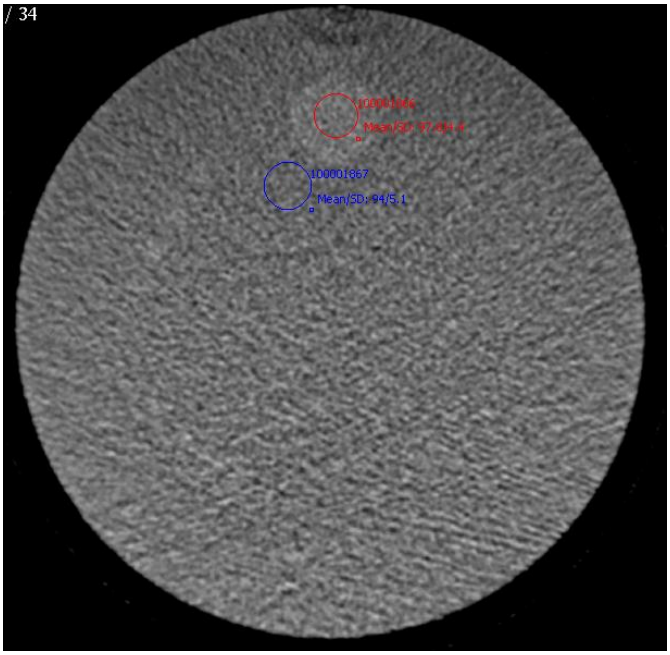


**Figure 8.25 When the table is moved to the very bottom in the gantry, the entire ACR phantom is below isocenter. There are some artifacts at the top of the phantom.**

**Table 8.3 CT Numbers for five different materials on the ACR phantom for scans performed at five different table heights. Measurements were made on 3 consecutive slices and the average number is reported as well.**

| | CT Numbers | | | | | CNR |
|---|---|---|---|---|---|---|
| | Bone | Polyethlyene | Acrylic | Air | Water | |
| 6cm above | 854.8 | -82.5 | 128.4 | -993.0 | -0.5 | 1.30 |
| | 853.1 | -81.9 | 128.8 | -996.0 | 1.0 | 1.29 |
| | 854.8 | -82.5 | 128.4 | -993.0 | -0.5 | 1.33 |
| Mean | **854.2** | **-82.3** | **128.5** | **-994.0** | **0.0** | **1.31** |
| 3cm above | 831.6 | -82.3 | 125.2 | -997.2 | -1.2 | 1.258 |
| | 829.3 | -82.3 | 124.4 | -995.5 | -2.2 | 1.426 |
| | 834.0 | -81.8 | 124.9 | -995.6 | -1.8 | 1.357 |
| Mean | **831.6** | **-82.1** | **124.8** | **-996.1** | **-1.7** | **1.35** |
| center | 855.9 | -86.4 | 122.7 | -997.7 | -2.2 | 1.155 |
| | 859.1 | -86.7 | 124.1 | -996.9 | -2.4 | 1.145 |
| | 857.6 | -85.6 | 125.8 | -996.6 | -2.4 | 1.117 |
| Mean | **857.5** | **-86.2** | **124.2** | **-997.1** | **-2.3** | **1.14** |
| 4cm below | 863.5 | -88.4 | 126.9 | -997.0 | -2.2 | 1.016 |
| | 862.1 | -90.1 | 124.4 | -994.9 | -2.9 | 1.211 |
| | 861.6 | -88.9 | 124.4 | -993.9 | -4.0 | 1.140 |
| Mean | **862.4** | **-89.1** | **125.2** | **-995.3** | **-3.0** | **1.12** |
| 9.5cm below | 859.2 | -83.8 | 128.7 | -985.7 | 1.5 | 0.97 |
| | 859.2 | -83.7 | 130.7 | -986.3 | 2.1 | 0.75 |
| | 856.7 | -83.4 | 129.5 | -982.6 | 1.1 | 0.75 |
| Mean | **858.4** | **-83.6** | **129.6** | **-984.9** | **1.6** | **0.82** |

Table 8.4 shows the results for homogeneity assessments. This table reports mean CT number for ROIs at all five different locations and the maximum difference of CT numbers between peripheral position and center position for five different table heights. Values for 2 individual slices and the mean value are reported. The maximum difference is used to assess the homogeneity performance of the scan. According to these results, the maximum difference at any of these 5 table heights is within 4HU. Therefore the homogeneity is within tolerable range

for images at all table heights. Finally, the spatial resolution for each of the 5 table heights are all 6 lp/cm. Raising or lowering the table does not have any effect on the spatial resolution of the images.

**Table 8.4 The mean CT number for ROIs at all five different locations as well as the maximum difference between peripheral position and center position for five different table heights. Values for 2 individual slices and the mean value are reported. The maximum difference is used to assess the homogeneity performance of the scan.**

| | 3 o'clock | 6 o'clock | 9 o'clock | 12 o'clock | center | Maximum Difference |
|---|---|---|---|---|---|---|
| 6cm above | 2.7 | 1.9 | 1.5 | 1.1 | 1.6 | 1.1 |
| | 2.4 | 1.3 | 1.9 | 2.2 | 1.8 | 0.6 |
| Mean | **2.6** | **1.6** | **1.7** | **1.7** | **1.7** | **0.9** |
| 3cm above | -0.1 | 0.1 | -2.7 | -0.7 | -1.4 | 1.5 |
| | -0.5 | -0.5 | -1.5 | -0.3 | -1.5 | 1.2 |
| Mean | **-0.3** | **-0.2** | **-2.1** | **-0.5** | **-1.5** | **1.4** |
| center | -0.3 | -1.1 | -1.8 | -0.7 | -1.6 | 1.3 |
| | -1.2 | -2.3 | -2.6 | -2.5 | -2.7 | 1.5 |
| Mean | **-0.8** | **-1.7** | **-2.2** | **-1.6** | **-2.2** | **1.4** |
| 4cm below | -3.1 | -1.9 | -1 | -2.2 | -2.9 | 1.9 |
| | -4.3 | -2.5 | -3.1 | -3.4 | -3.8 | 1.3 |
| Mean | **-3.7** | **-2.2** | **-2.1** | **-2.8** | **-3.4** | **1.6** |
| 9.5cm below | 0.2 | 2.2 | 2.7 | 2.4 | 3.4 | 3.2 |
| | -0.2 | 1.9 | 1.5 | 2.7 | 3.1 | 3.3 |
| Mean | **0.0** | **2.1** | **2.1** | **2.6** | **3.3** | **3.3** |

Table 8.5 shows the mean CT number and noise for a homogeneous region on the thorax anthropomorphic phantom at all 5 table heights. Both mean CT number and noise remain about the same when the table is raised by 3cm, 6cm, or lowered by 4cm. However, when the table is lowered by 9.5cm, the image noise increased dramatically. For example, the standard deviation of the ROI changed from 14.5 when the phantom is centered to 70.2 when the phantom is at the

lowest position in the gantry. Figure 8.26 shows that there is significant artifact and deterioration of the image quality when the table is lowered by 9.5cm. Figure 8.26 also shows that when the table is so low, the entire phantom is below the isocenter, and there are some severe artifacts around the upper part of the phantom, where the isocenter is located. This is consistent to the decreased CNR values when the table is lowered to the very bottom position in the gantry. The reason may due to the large imbalance of the detector response within a row: at certain projections, half of the detectors receive very large amount of photons since there is no attenuation at all from the object being scanned, and the other half row of the detectors receive relatively low amount of photons. This imbalance might trigger some compensation algorithm in the raw data process flow and therefore resulted in degraded image quality.

**Table 8.5 The mean CT number and noise for a homogeneous region on the thorax anthropomorphic phantom at all 5 table heights.**

| | Mean CT number | Noise |
|---|---|---|
| 6cm above | 50.6 | 14.1 |
| 3cm above | 54.7 | 13.6 |
| isocenter | 53.5 | 14.5 |
| 4cm below | 54.9 | 16.2 |
| 9.5cm below | 59.3 | 70.2 |

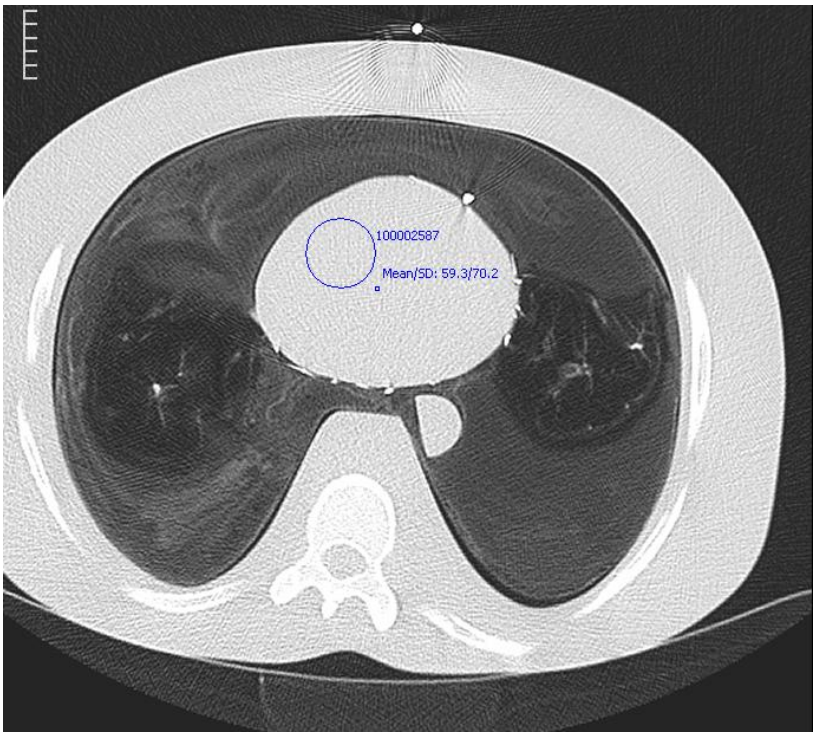


**Figure 8.26 The image quality decreased dramatically when the table is positioned at the very bottom position in the gantry.**

## 8.7 Conclusion and Discussion

With the results from both physical measurements and computational simulations, this study demonstrated that organ dose can be reduced significantly by adjusting tube start angle and table heights in CT scans, whether TCM is turned off or on. Depending on the acquisition parameters of the scan, including collimation width, pitch, and the table height, radiation dose can be reduced by up to 80%. Currently, the control of tube start angle is not enabled in commercial CT scanners. However, the adjustment of table height is easily accessible.

Due to the fundamental principle of dose reduction from controlling tube start angle, this technique aims for reducing radiation dose to only one specific radiosensitive organ. This organ

has to be identified by the user before the CT scan, so that the distance between the scan start location and organ location could be used as input to calculate necessary tube start angle that would yield lowest radiation dose to the organ. Therefore, in clinical practice, the potential paradigm could be as follows. After topogram is performed, and before the CT scan is acquired, the technologist needs to identify the organ of interest on the radiograph, such as eye lens or breasts for pediatric patients. It should be noted that only this organ of interest is assured to receive minimum dose. The radiation dose to other organs would remain uncertain within its dose range, which means the dose can be anywhere in that range, depending on the scan acquisition parameters (collimation, pitch) and patient anatomy. However, this is just the same as current clinical practice, where tube start angle and the exact organ dose in the range are random.

Unlike controlling tube start angle, adjusting the table height could achieve dose reduction to multiple organs. However, it still does not universally reduce radiation dose to all the organs. Instead, dose to anterior organs decreases as the table is raised, while dose to posterior organs decreases as the table is lowered. Since most of the radiosensitive organs are located more or less toward the anterior side of a patient, it is recommended to raise the table to achieve overall dose benefits. At a higher table height, since the distance between an anterior organ (such as glandular breast tissue) to the isocenter is further, the dose benefit from controlling tube start angle is even larger, as discussed in 7.3.1. In other words, raising the table ‘magnifies’ the dose reduction effect from controlling the tube start angle for anterior organs. This was demonstrated in Figure 8.10a, where the magnitude of dose variation from changing tube start angle is the largest for the table height of 12cm above isocenter. In clinical practice, in

order to avoid the effect of magnified radiograph to the TCM planning, the paradigm could be as follows. The table height is adjusted so that the patient is center in the gantry before the topogram. After the topogram is obtained, the technologist then identifies the location of the organ of interest that would receive minimum dose from controlling tube start angle. Then the table is raised to a higher location in the gantry, followed by the CT scan.

Controlling the tube start angle does not have any effect on image quality. Adjusting the table height does increase image noise and cause some artifacts when the object being scanned is pushed completely to be within the lower half of the gantry. However, since all the CT manufacturers have limitations for the highest location of the table to accommodate patients with large size, the table cannot be raised so high that the entire patient is above the isocenter. Since in this dissertation it was suggested to raise the table for dose reduction purpose, the image quality would not be seriously affected. It was demonstrated in 8.6.2.2 that the assessments of CT numbers, noise, homogeneity and spatial resolution were all within the range of acceptance when the table is raised by 6cm. In fact, this is the highest allowed location of the table for this particular CT scanner model (Siemens Sensation 64 scanner). At this range of table raise, the resulting dose reduction to glandular breast tissue can still be about 20% according to Figure 8.13, Figure 8.14, and Figure 8.17.

To conclude, controlling the tube start angle (not currently available but may be available in future) and raising the table height (available today) within the allowable table range are two viable tools to reduce individual organ dose. Depending on the location and size of the organ, the

dose reduction could be up to 60% to 70%. For CT scanners other than the ones investigated in this dissertation (Siemens Sensation 64 and Siemens Definition Flash), the exact dose reduction numbers may not agree with the numbers reported here. But the general principle should apply to all CT scanners.

Rather than changing the overall radiation output (such as changing kVp or mAs), these two technique ‘customize’ the distribution of the radiation within patient body to minimize the risks from CT scans by taking the radio-sensitivity of different organs into account. They serve as two new methods to reduce patient radiation dose while maintaining image quality. In the next Chapter, method to reduce dose that affects image quality, but preserves diagnostic performance will be investigated.

## Chapter 9 Observer Performances at Reduced Dose Levels for a Challenging Clinical Task

In previous chapters, dose reduction techniques that do not require the change of x-ray tube output have been investigated, such as adjusting the scan location (Chapter 4), controlling tube start angle and table height (Chapter 7 and 8). These techniques minimize radiation dose to target organs and do not reduce dose universally to all organs. This chapter instead, focuses on reducing dose by directly decreasing tube output, specifically the mAs value. Radiation dose decreases proportionally to mAs, since mAs is proportional to the number of photons, which determines the radiation dose. Unlike the previous techniques, which do not directly affect image noise, reducing mAs results in an increase of the image noise. This will degrade image quality. However, the degradation of image quality does not always lead to the degradation of diagnostic outcome. Therefore, it is necessary to consider radiation dose in the context of image quality, and eventually in the context of the ultimate endpoint of medical images – diagnostic performance.

### 9.1 Introduction

The tradeoff between image quality and radiation dose is a long standing dilemma. Numerous studies have been performed to assess either image quality, or radiation dose, or both, for various clinical indications and CT scanners. Simple image quality metrics such as noise or contrast-to-noise ratio (CNR) have been used to assess the performance of CT scanners. However, these metrics obtained in phantoms are too simple to predict the actual diagnostic outcome from CT images, considering the variety of the nature of the clinical tasks (e.g., high contrast task versus low contrast task) and the clinical subtleties involved in each task. Therefore,

it is imperative to investigate image quality in the context of a specific clinical task, by investigating the actual end point of the use of CT images – diagnostic performance.

As for radiation dose, CTDI or DLP has been used widely as metrics for dose assessments. However, as discussed in Chapter 1, these metrics only quantify the output of the CT scanners, and they do not represent the radiation dose actually delivered to patients, which varies based on factors such as patient size and anatomical characteristics. Therefore, it is essential to use organ dose, which is a more meaningful and useful dose metric that could even be used to assess risk, as radiation biological models continue to evolve. This study investigates the tradeoff between diagnostic performance for a specific clinic task and radiation dose to the patients by seeking the answers to the following questions: 1) How does mAs level affect the relative diagnostic performance level? 2) How much absolute organ dose is needed for an absolute diagnostic performance? Figure 9.1 summarizes the innovation of this study by advancing simple image quality metric to diagnostic performance, and advancing simple CT dose metric to organ dose.

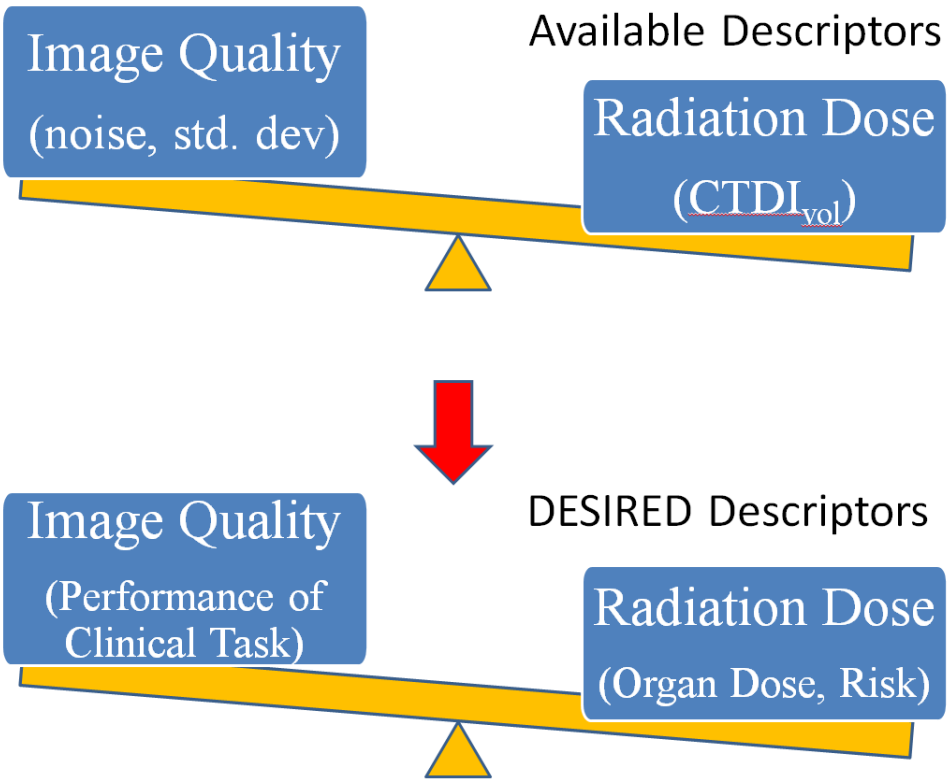


**Figure 9.1 Advancing from basic image quality metrics to diagnostic performance, and advancing from CTDI to organ dose are the innovations of this study.**

### 9.1.1. Diagnostic Performance

The fundamental difference of the nature of various diagnostic tasks determines that their tolerances of image noise are different. For example, a task to seek lung nodule could endure much higher noise than a task to identify liver lesion, since the difference in attenuation (and therefore contrast) between soft tissue (nodule) and air (lung) is high, as shown in Figure 9.2. The tradeoff between image quality and radiation dose refers to the determination of the minimum dose level which still ensures the required diagnostic performance for each specific diagnostic task. On one hand, image quality cannot be sacrificed so much that the benefit of the exam is negated. On the other hand, target image quality should be appropriately defined for

each specific diagnostic task, so that no radiation higher than necessary is delivered to patients for diagnostic purposes. This optimization process is very challenging due to the complexity of the clinical indications for CT and the variations in observer preferences. The gold standard for determining the target image quality that just yields an acceptable diagnostic outcome is to perform trained human observer studies for a clinically relevant diagnostic task. For the purpose of this study, this diagnostic task was determined to be CT diagnosis of appendicitis, which will be introduced in 9.1.4.

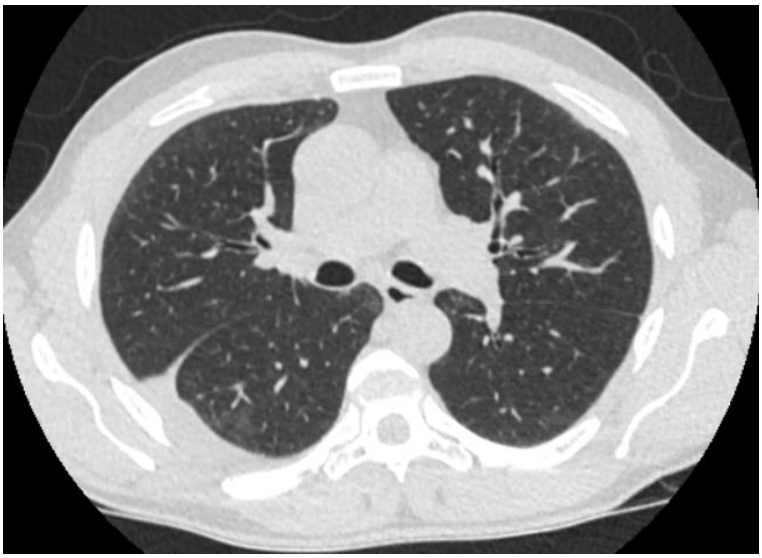

**Figure 9.2 Example CT image of a high contrast task for the detection of lung nodules.**

Depending on the resource and available data, different strategies to evaluate the lowest acceptable dose can be used. For example, in some studies, the evaluation of "image quality" or "diagnostic acceptability" was used as the criteria for the determination of the diagnostic performance[139], without considering the correct diagnosis as the "diagnostic truth", based on which diagnostic accuracy could be calculated. In the design of these studies, the images were

rated, or determined to be clinically acceptable or not at each dose level. However, this is not the same as, and may not even correlate with diagnostic performance (whether the radiologist detects the condition accurately and reproducibly). The results of this process are heavily dependent on the experience level and preference of the interpreting physicians, and limited in validity due to the lack of "diagnostic truth" for each case. This dissertation, however, adopts the other type of evaluation which uses the "truth" of the diagnoses (medical diagnosis including surgical or pathological results) as an end point in analysis[140-143]. Using this approach, the diagnostic accuracy could be calculated; therefore the actual diagnostic performance could be analyzed at different dose levels. Based on the relationship between the diagnostic outcome (in terms of sensitivity and specificity) and the radiation dose level, the lowest acceptable dose level that can yield acceptable diagnostic performance could be determined. This approach is closer to clinical reality for investigating the tradeoff between diagnostic outcome and radiation dose.

### 9.1.2. Simulating Lower Dose Images

Some studies used images at different dose levels from different patient cohort and investigated the diagnostic performances[143]. This approach is limited by the potential patient-specific variables between different patient cohorts, such as age, size, area, and so on. In contrast, a number of studies have investigated the diagnostic performance at difference dose levels by scanning the patients multiple times[141,142,144]. This approach eliminates the variations from different patient cohorts. However, it has several limitations. First, the study may not be reproducible since patients were exposed to radiation multiple times, which may add to their potential risks. Second, due to the same reason, the number of scans is usually limited to two (a

regular scan and a low technique scan), which limits the studies to investigate the performance across a larger dose range. Finally, since there are intervals between scans, the patient may move and therefore the anatomy may be slightly different, which adds another factor to the performance difference between the scans.

To overcome these limitations, a very valuable approach has been proposed which simulate images at various reduced dose levels based on existing clinical data. This approach allows several datasets at multiple radiation dose levels without patient variation or movements. After generating a number of image sets at lower dose levels, the investigators can compare the diagnostic quality between these images using the same patient data by removing patient-specific variables. This approach also makes it possible to determine the lowest acceptable dose level without additional patient scans[139,145-148].

Studies have been done to simulate low dose images by directly adding uniform noise images in image domain[149]. However, due to the nature of CT reconstruction process, in order to accurately simulate lower dose images, the artificial noise should be directly added to the raw projection data. This is one of the biggest obstacles for widespread use of this approach due to two reasons. First, the raw projection data used for reconstruction is not usually accessible, although it exists on CT scanners. Second, it would be ideal to insert artificial noise on the data which represents the original output of the detectors. However, a number of processing steps, which are highly proprietary, are applied and represent pre-processing to this data to generate the 'raw' projection data for reconstruction. Therefore even when the raw data is obtained, it is very

challenging, if not impossible, to recover the unprocessed raw data. Due to these reasons, most noise-insertion tools were developed by manufacturers[150]. These tools are only available for a few scanner models. In addition, they are only distributed to a few users under research agreements. Several reverse engineering efforts have also been made to develop noise-insertion tools[151]. This dissertation uses a combination of manufacturer provided codes and self-developed methods to generate a noise insertion package. This will be discussed in detail in 9.2.2.

### 9.1.3. Assessment of Image Quality

Performing observer studies under different combinations of scan technique parameters is the gold standard to investigate the tradeoff between radiation dose and image quality. However, this approach is also very time consuming and expensive. Although these types of studies are essential to the field and will always be required to establish estimates of actual human performance, they are simply too expensive to perform routinely for optimization purposes.

Alternatively, a more efficient method is to develop image quality metrics that can be quantitatively measured and are highly correlated with human performance for a specific diagnostic task. These image quality metrics can potentially be developed based on the measurements on patient images, or on phantoms, or on both. The lowest acceptable dose level which still provides sufficient diagnostic information could be determined with the help of such metrics. However, this is an extremely challenging task due to the complexity and variation of the clinical indications in CT imaging, as well as the intricacy of the interpretations of these indications by human. Some metrics are currently being explored to quantify various aspects of

CT image quality. These include noise, Contrast to Noise Ratio (CNR), Modulation Transfer Function (MTF), Noise Power Spectrum (NPS), and Slice-Sensitivity Profile (SSP)[152-154]. However, these metrics still cannot provide comprehensive description of CT image quality and do not perfectly correlate with diagnostic performance. An example is that the low contrast detectability is not improved as CNR increases by using different reconstruction kernels[155].

### 9.1.4. Appendicitis

Abdominal pain is the most common reason for Emergency Room (ER) visits, with up to 8 million visits per year for this complaint in the USA. Right lower quadrant (RLQ) pain accounts for a large percentage of these cases. RLQ is one of the most challenging clinical presentations, with a vast list of different diagnoses. Differential diagnosis for RLQ pain includes conditions affecting multiple anatomic structures in the region, including ileum, cecum, appendix, ascending colon, mesentery, omentum, and adnexal region. Among these diagnoses, appendicitis is the most common condition (14%) which requires surgery in patients with RLQ pain[156]. Appendicitis is caused by the inflammation due to obstruction of the lumen. It usually happens to people in their second and third decade of life. Pathologically, appendicitis starts with luminal obstruction, followed by bacterial infiltration and white cell diapedesis. Vascular compromise leads to ischemia and perforation, which may progress to phlegmon (inflammatory mass) and abscess (fluid collection) formation.

MDCT has emerged as the modality of choice for evaluation of patients with right lower quadrant pain, with sensitivity and specificity for diagnosing appendicitis around 90% to 100%[157,158]. It is used in up to 90% of patients before appendectomy. Various protocols are used

for evaluation of RLQ pain and possible appendicitis, with comparable accuracies. Most institutions perform abdominal and pelvis CT following administration of intravenous and oral contrast, although recent literature supports the use of intravenous contrast only with similar accuracy[156]. IV contrast highlights inflammation in the wall of the appendix, while oral contrast helps differentiate the appendix from adjacent bowel and anatomical structures. Contrast administration is especially helpful in thin patients who lack sufficient mesenteric fat, which makes identification of the appendix and periappendiceal fat stranding more difficult. Diagnosis may also be difficult in elderly and female patients, in the latter population due to significant prevalence of gynecologic etiologies for right lower quadrant pain. Because acute appendicitis commonly affects young adults, the high amount of radiation dose delivered by abdominal CT raises concerns regarding its use as a first-line examination tool in this patient population. Furthermore, some patients present to the ER with recurrent abdominal pain, and receive multiple CT scans of the abdomen and pelvis. In summary, appendicitis is a common disease, with significant radiation exposure for the general population given the incidence of RLQ pain and increasing use of CT for diagnosis.

### 9.1.5. The Focus and Scope of This Study

The general purpose of this study is to study diagnostic performance in a challenging CT clinical task (appendicitis) by investigating its tradeoff with radiation dose. As discussed in 9.1.1, a well-designed observer study, which is the gold standard, was used to approach this problem. Due to the expensive nature of a human observer study, it was proposed to perform a pilot study

using a relative small number of patient cases in order to demonstrate the mechanism of the study, as well as to get some preliminary results about the diagnostic performance of different observers at various dose levels. This dissertation focuses on the pilot study.

In order to perform observer studies which are necessary to obtain comprehensive information about diagnostic performance, a noise-insertion tool to simulated images with lower radiation dose was developed and validated. For radiation dose, the UCLA CT Dose Simulation Package (described in Chapter 3) was used to estimate patient specific organ dose to the patients undergone these CT scans. The diagnostic performances at different radiation dose levels were compared to determine the radiation dose that is enough for the diagnosis of appendicitis. The results of the study seek to answer the following questions. 1) For the diagnosis of appendicitis, what mAs level could yield the same diagnostic performance as the original dose level? 2) For the diagnosis of appendicitis, how much liver dose can be reduced in order to achieve the same diagnostic performance as original acquisition? In addition, in order to explore image quality metric, the relationships between diagnostic performances and a simple objective image quality metric (noise), as well as subjective image quality rating were investigated. Another purpose of this pilot study is to find out any potential limitations of the design of the experiments by going through the mechanism of the data collection, observer study and data analysis.

## 9.2 Methods

### 9.2.1. Case Collection and Selection

The raw projection data of CT examinations performed for suspected appendicitis cases (i.e. patients who presented with RLQ pain and clinical suspicion of appendicitus) were collected from a collaborating clinical site. These exams were performed on a Siemens Sensation 64 CT scanner, using the same imaging protocol: 120kVp, 24 x 1.2mm collimation, pitch of 1; Siemens TCM (CareDose4D with 250 Qual. Ref mAs, corresponding to $CTDI_{vol}$ of 16 mGy) was employed for each scan. Either intra-venous contrast alone or intra-venous and oral contrast was used for these patients. About 100 patient cases have been collected.

A clinical review committee consisting of two experienced senior radiologists was formed to be consultants for the general design of this study. They were excluded from being observers in this study. For the pilot study, 20 patient cases were selected, representing 10 positive and 10 negative cases of appendicitis. The selected cases demonstrate a range of distribution of CT appearance relative to suspected diagnosis of appendicitis. Accordingly, the selection criteria for the 20 patient cases was to include obvious positive cases, subtle positive cases, obvious negative cases, and subtle negative cases, resulting in a mix of obvious and subtle cases for each category. Several cases with alternative diagnosis causing abdominal pain were also included, in order to represent clinical practice. For example, cases of diverticulitis (which are negative for appendicitis) were included. Since locating the appendix itself is a challenging task in abdominal CT, one case where the appendix is not visible at the baseline dose level was also included as a negative case.

Medical records were reviewed by the reviewing committee for presence or absence of appendicitis to establish diagnostic truth. This allowed the estimates of diagnostic accuracy, sensitivity, and specificity for statistical analysis. The processes of case selection and medical records reviews were performed by a radiologist from the reviewing committee who is a major contributor to the study.

### 9.2.2. Noise Insertion Tool and Its Validation

A previously published methodology was utilized for the development of a software package which takes the raw projection data of a CT scan and inserts a specified amount of noise, in order to simulate raw projection data at lower mAs level[151]. In this method, air scans at various mAs levels were performed first to obtain the fluence of the x-rays at different mAs levels. Look up tables of mAs versus fluence were then created, which also included the attenuation information of the bowtie filter along the fan-angle dimension. Based on the original mAs and the desired lower mAs values, the look up table is used to obtain the desired fluence level. In addition, phantom scan was performed to create intensive attenuation to estimate the electronic noise of the CT system. Finally, a noise model which assumes an inverse relationship between noise and the square root of photon fluence was used to guide the amount of Gaussian noise to be added to the raw projection data based on the look up table, the original and the desired lower mAs, and information about the electronic noise. This process is illustrated in Figure 9.3.

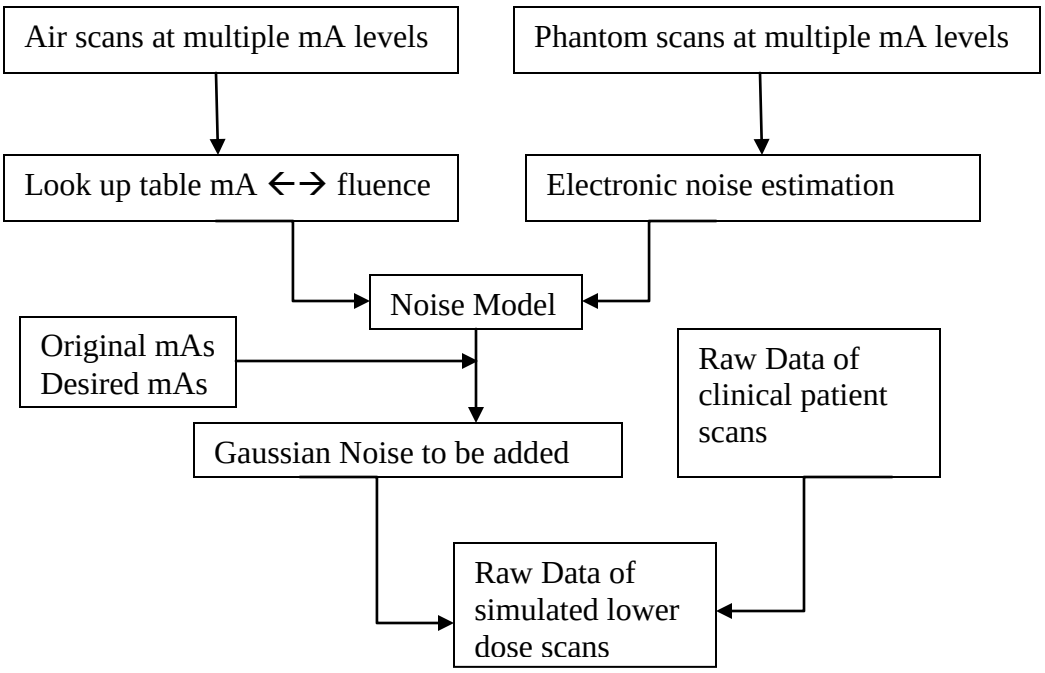


**Figure 9.3 The workflow of the noise insertion tool.**

Using this method, a MATLAB subroutine was developed based on some proprietary dynamic function (.dll) files containing information about the proprietary data structure of Siemens raw projection data. These files were obtained from Siemens under research agreement. A series of validation efforts were made in the original publication from Whiting, including noise measurement, analysis of NPS, as well as an observer study[151]. Although that same fundamental method was used, in the realm of this dissertation, some additional validation were performed to ensure the performance of this noise-insertion tool under both constant tube current and tube current modulation mode. A homogeneous elliptical phantom and a thorax anthropomorphic phantom were used to validate the algorithm. Baseline scans at 250mAs/Qualify Reference 250mAs (with CareDose4D) were obtained for both phantoms under both constant tube current and tube current modulation mode. Simulated and actual images at

200mAs, 150mAs, and 100mAs were generated. For the elliptical phantom, a ROI was placed at the position shown in Figure 9.4, and then the standard deviation (noise) was compared under each scenario with the results summarized in Table 9.1. For the thorax phantom, a ROI was placed at a homogeneous area shown in Figure 9.5, and the noise was compared in a similar fashion, with the results summarized in Table 9.2.

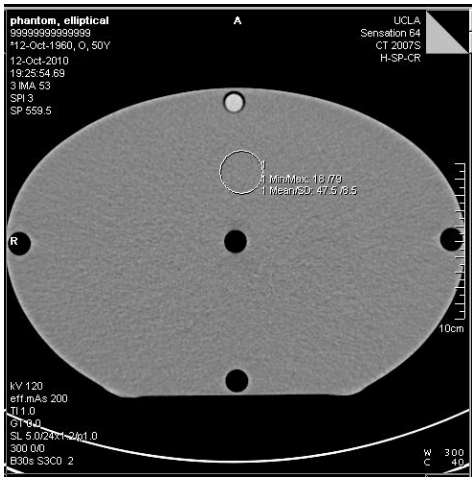


**Figure 9.4 ROI in the elliptical phantom for the benchmark between simulated images and actual images.**

**Table 9.1 Comparisons of the standard deviation of ROI between simulated and actual images for three mAs levels under both no TCM and TCM mode for the homogeneous elliptical phantom.**

| | | 200mAs | | | 150mAs | | | 100mAs | | |
|---|---|---|---|---|---|---|---|---|---|---|
| | | Sim | actual | %diff | Sim | actual | %diff | Sim | actual | %diff |
| no TCM | slice 1 | 8.5 | 8.5 | 0.0% | 9.7 | 10.2 | -4.9% | 12.4 | 12.1 | 2.5% |
| | slice 2 | 8.7 | 8.7 | 0.0% | 9.9 | 9.7 | 2.1% | 11.5 | 11.8 | -2.5% |
| | slice 3 | 8.8 | 8.9 | -1.1% | 10.1 | 9.6 | 5.20% | 12.5 | 12.1 | 3.3% |
| TCM | slice 1 | 11.7 | 11.6 | 0.9% | 13.8 | 13 | 6.2% | 16.9 | 16.4 | 3.0% |
| | slice 2 | 11.8 | 11.3 | 4.4% | 13.7 | 13.4 | 2.2% | 16 | 16.6 | -3.6% |
| | slice 3 | 10.9 | 11.2 | -2.7% | 13.5 | 13.7 | -1.5% | 16.2 | 16 | 1.3% |

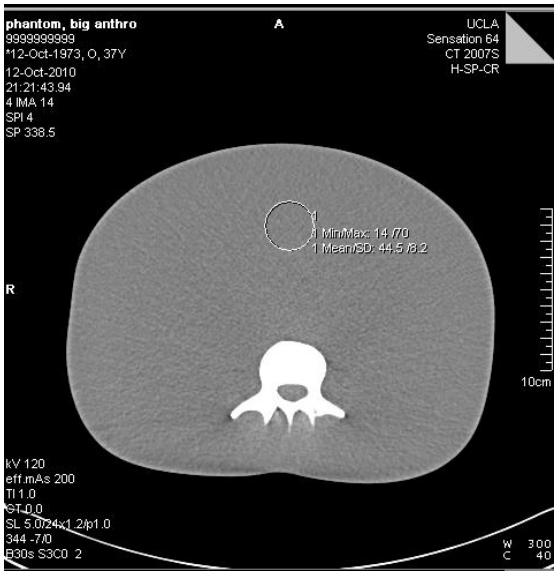


**Figure 9.5 ROI in a homogeneous area in thorax phantom for the benchmark between simulated images and actual images.**

**Table 9.2 Comparisons of the standard deviation of ROI between simulated and actual images for three mAs levels under both no TCM and TCM mode for the anthropomorphic thorax phantom.**

| | | 200mAs | | | 150mAs | | | 100mAs | | |
|---|---|---|---|---|---|---|---|---|---|---|
| | | Sim | actual | %diff | Sim | actual | %diff | Sim | actual | %diff |
| no TCM | slice 1 | 8.6 | 8.2 | 4.9% | 9.3 | 9.6 | -3.1% | 11.5 | 11.6 | -0.9% |
| | slice 2 | 8.5 | 8.6 | -1.2% | 9.2 | 9.3 | -1.1% | 11.5 | 11.9 | -3.4% |
| | slice 3 | 8.7 | 8.8 | -1.1% | 9.5 | 9.4 | 1.1% | 11.3 | 11.7 | -3.4% |
| TCM | slice 1 | 13.4 | 13.4 | 0.0% | 15.6 | 15.3 | 2.0% | 18.8 | 19.6 | -4.1% |
| | slice 2 | 13.8 | 13 | 6.2% | 15.6 | 15.6 | 0.0% | 18.4 | 18.7 | -1.6% |
| | slice 3 | 13 | 12.9 | 0.8% | 15.6 | 15.6 | 0.0% | 18 | 17.8 | 1.1% |

As shown in Table 9.1 and Table 9.2, most of the percent difference values of the noise between simulated and actual images are within 4%, with the maximum of 6.2%. 14 out of 18 data points are less than 4% for the elliptical phantom, and 15 out of 18 data points are less than

4% for the thorax phantom. Considering the random nature of the measurement of noise, this level of agreement is well within the range of acceptance.

In a separate effort, a 20cm water phantom was scanned at baseline dose of 120mAs. Simulated and actual images at 100mAs, 80mAs, 60mAs, 40mAs, and 25mAs were obtained. Two ROIs were placed in the phantom image, with one at center and the other at peripheral position. The standard deviation (noise) was compared under each scenario with the results summarized in Table 9.3. Again, the differences between actual scanned and simulated low dose images were very small, even down at 25mAs level. This indicates the robustness of the algorithm even at very low dose level range.

**Table 9.3 Comparisons of the standard deviation of ROI between simulated and actual images for 5 mAs levels for the water phantom.**

| | | actual | simulated | difference |
|---|---|---|---|---|
| Center | 100mAs | 16.5 | 16.4 | -1% |
| | 80mAs | 18.1 | 17.9 | -1% |
| | 60mAs | 19.3 | 20.5 | 6% |
| | 40mAs | 27.7 | 26.7 | -4% |
| | 25mAs | 32.5 | 32.7 | 1% |
| | | | | |
| Peripheral | 100mAs | 14.3 | 14.5 | 1% |
| | 80mAs | 15.8 | 16.3 | 3% |
| | 60mAs | 16.9 | 17.8 | 5% |
| | 40mAs | 22.9 | 22.9 | 0% |
| | 25mAs | 27.8 | 28.9 | 4% |

Figure 9.6 shows an example case of images in axial view at 100%, 70%, 50%, 30%, and 20% dose levels, respectively.

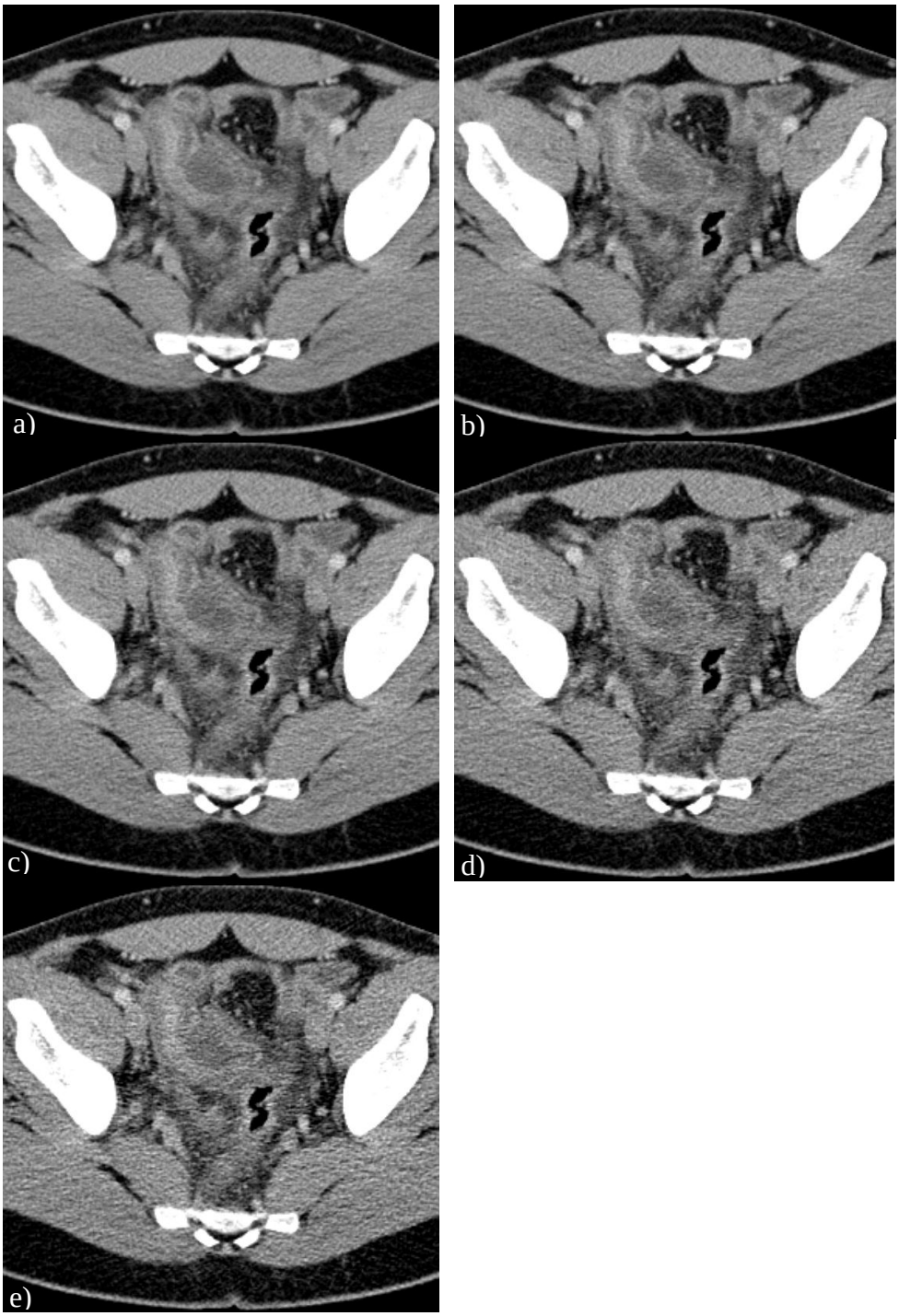


**Figure 9.6 A series of exemple images. a) original 100% dose; b) 70% dose; c) 50% dose; d) 30% dose; e) 20% dose.**

### 9.2.3. Case Processing

Preliminary review for 2 cases at 100%, 90%, 80%, 70%, 60%, 50%, 40%, 30%, 20%, and 10% dose levels were performed within the reviewing committee to investigate the number and the magnitude of dose levels for the study. After careful discussion and reviewing of these example images, the proposed simulated reduced dose levels were chosen to be 70%, 50%, 30%, and 20% of the original dose. A total of 5 dose levels were selected, allowing sufficient discrimination of change in diagnostic performance for this pilot study. In addition, it was determined that 20% dose level was sufficiently low to yield unacceptable image quality for diagnosis. The selection of low dose levels (70%, 50%, 30 % and 20% of the original dose) was intended to generate a sharp change in reader diagnostic performance in diagnosing appendicitis so that the lowest possible dose level that maintains diagnostic performance could be identified.

The noise-insertion tool which accounts for TCM was used to add noise to the raw projection data of each of the selected 20 cases to simulate new raw data files as if they were scanned at lower dose levels (70%, 50%, 30%, and 20% of the original mAs). These generated raw data files were then taken to the CT scanner console for the reconstruction of images in both axial and coronal views at 5 mm intervals. This resulted in 100 image sets (20 patient cases x 5 dose level for each case). The slice thickness of 5mm reflects the clinical practice at the site where the patient cases were collected. All the image sets were anonymized, so that all the patient-specific and exam-specific information was removed from the images.

### 9.2.4. Observer Study

Six observers with a range of levels of experience in interpreting abdominal CT images were recruited to participate in this study. All of the observers are attending physicians in their institute and they all have experience reading CT images for appendicitis. Each observer had 5 reading sessions with 20 image sets for each session, which results in 100 image sets per reader. Each reading session comprised 20 image sets from non-repeating patients, so that 1 data set from each patient was included in each session. Since the same patient data (at different dose levels) were seen by the observers multiple times, in order to minimize the potential observer bias from remembering the individual patient cases, at least a 2 week wash out interval was required between sessions for each reader.

Another effort to minimize the bias from the observers was randomization of the order of the patient case and the order of the dose level presented to the observer. For the same patient, the observers would be less likely to remember the case if they saw the lower dose level images (noisier) prior to the higher dose level images (less noisy), since it would allow less recognition of anatomical details to facilitate case recollection. However, putting the lowest dose images (noisiest images) for all the patients in the first several sessions might make the reading frustrating due to the increased noise in the images. Therefore, the general randomization strategy was to present the lower dose images more often in the earlier sessions (but some will appear in later sessions), while presenting higher dose images for interpretation more often in the later session (but some also appeared in earlier sessions).

In order to further minimize observer bias, very limited information was given to the observers before all the reading sessions were finished. Specifically, the observers were only told the following information: 1) This was a study about reading abdominal CT images for appendicitis. 2) It concerns radiation dose and the ability to detect and diagnose appendicitis. 3) The overall effort would entail 5 sessions of 1 to 2 hours duration for each session. The observers were not told about any of the following information: 1) The number of patient cases, number of dose levels, or randomization of the cases. 2) That we even had the ability to simulate different levels of mAs for each case. Although there was a wash out period, as the experiment carried on, the observers were able to discover that they had seen the same patient at different dose levels. However, hiding some information from them helped to keep the bias to a minimum.

In order to obtain the diagnostic confidence, observer's subjective assessment of image quality, as well as some understanding of what are the different individual findings that guided them to their ultimate diagnosis, each observer was required to make a complete diagnosis of each image set in each session by rating their confidence for each image set (e.g., each patient case at each specific dose level). The answer to each question was based on a 5 point scale (unless otherwise indicated):

1 - Definitely not,
2 - Probably not,
3 - Indeterminate,
4 - Probably yes, and
5 - Definitely yes.

These questions are listed as follows:

1) Is the Appendix Visualized from origin to tip? (Yes or No)

2) Is the appendix pathologically dilated (over 6 mm)?

3) Is there fat stranding?

4) Is there increased enhancement/hyperemia?

5) Is there periappendicial fluid in the RLQ?

6) Is there bowel wall thickening?

7) Is there Phlegmon and/or Abscess?

8) Is there free air?

9) Is there an alternative diagnosis? (The choices are: No alternative diagnosis, Colitis, Diverticulitis, Ovarian cyst, Others)

10) Is there Appendicitis?

11) Rate Image Quality. The choices are:

- Poor, not diagnostically acceptable for interpretation;

- Suboptimal, worse than routine images with excessive image noise;

- Acceptable, diagnostic interpretation possible but noiser than routine images;

- Good, noise similar to routine dose images;

- Excellent, no image noise.

These questions were determined to be critical and appropriate clinical relevant questions during the diagnosis of appendicitis by the reviewing committee.

### 9.2.5. Viewing Platform Implementation

An experiment was developed on a java based software package called QIWS (Quantitative Imaging Work Station)[159] to implement the functions for viewing the images and

selecting the answers to each of the questions for the observers. It incorporates basic DICOM viewer functions such as the ability to adjust the window/level, scroll through images, and so on, so that the observers can imitate their routine clinical practice. In addition, it provides a marking tool for the observer to identify the diameter of the appendix, and a worksheet which contains all the questions and answers in the format of multiple choices. Both axial and coronal views of each image set were displayed for all the sessions using a two monitor system, although the software does not "link" coronal images with axial images (automatically changing slice location in one view according to the selected location in the other view). Before each observer's first session, he/she received a training session to help them get familiar with the platform. Figure 9.7a shows a screenshot of the platform, and Figure 9.7b shows the worksheet the observers used to provide the answer to each question.


a)

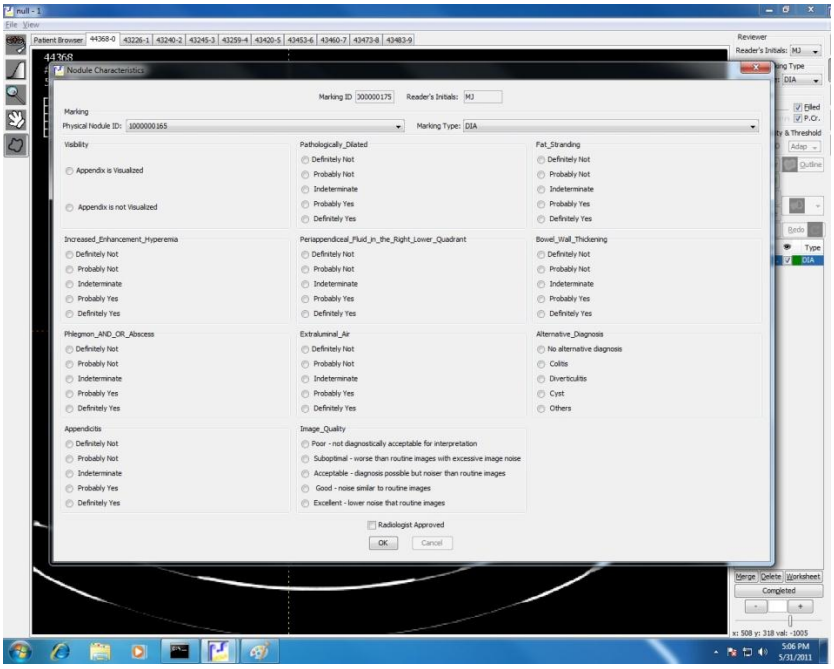


b)

**Figure 9.7 a) The viewing platform; b) the worksheet for observers to answer questions.**

### 9.2.6. Simple Image Quality Measurements

In order to investigate how the image quality changes with radiation dose, and how the diagnostic performance changes with image quality, for each patient's images at each dose level, simple ROIs were placed in relative uniform regions of the anatomy. From these ROIs, the standard deviation was extracted and served as a first order estimate of the noise. Three different locations were chosen for the estimation of noise: liver, bladder, and body fat. Figure 9.8 shows an example of a measurement of ROI noise in the liver.

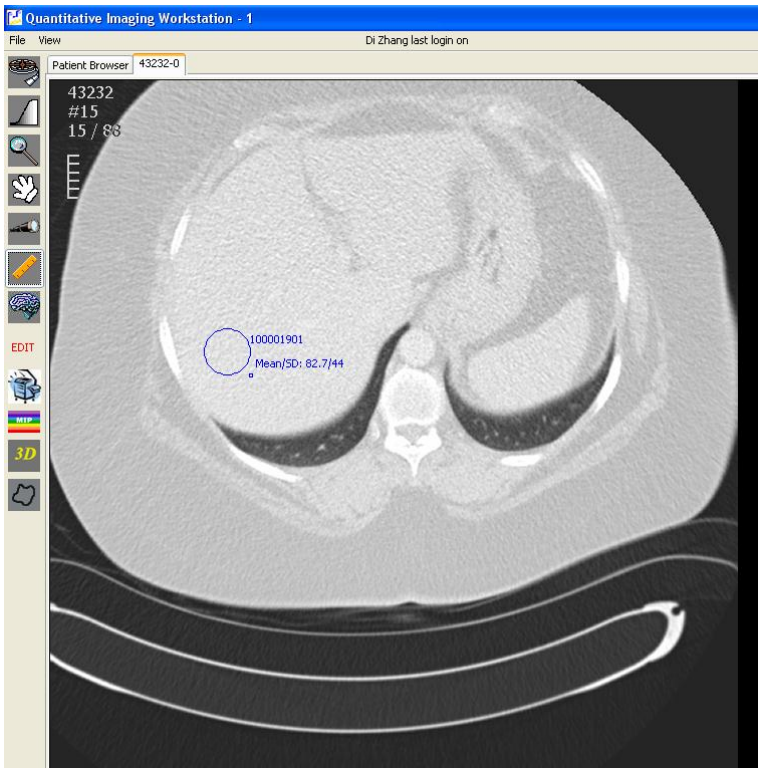


**Figure 9.8 The measurement of ROI noise in the liver.**

### 9.2.7. Monte Carlo Simulation for Organ Doses

The approach described in 8.4.1.3 was used to accurately estimate organ dose for this group of patients as well. Three organs, including liver, kidneys and spleen, were contoured for each of the 20 patients for organ dose estimations. TCM schema for each patient was extracted from the raw projection data and used as input for Monte Carlo simulations. Using this method, the dose to liver, kidneys and spleen was obtained for the original 100% dose level. Since organ dose is proportional to mAs, the organ dose at 70%, 50%, 30%, and 20% were obtained by scaling by the factor of mAs. Therefore, organ dose was obtained for 100 CT scans in total, including 20 original scans and 80 simulated virtual CT scans.

### 9.2.8. ROC methodology

Receiver Operating Characteristics (ROC) analysis methodology has been used in the field of medical imaging successfully to evaluate observer performance in terms of their abilities to use image data to classify patients as "positive" or "negative" for a particular disease[160-163]. If a case is correctly diagnosed as positive, it is defined as a true positive case. If a case is incorrectly diagnosed as positive, it is defined as a false positive case. If a case is correctly diagnosed as negative, it is defined as a true negative case. If a case is incorrectly diagnosed as negative, it is defined as a false negative case. The basic concepts to evaluate the assessment of a binary diagnostic test (disease or non-disease) or an imaging system are sensitivity and specificity. Sensitivity refers to true positive fraction (TPF) which stands for the percent of the diseased population that is correctly diagnosed. Therefore, sensitivity can be calculated by:

$$Sensitivity = \frac{number\ of\ true\ positive}{number\ of\ true\ positive + number\ of\ false\ negative}$$

Specificity refers to true negative fraction (TNF) which stands for the percent of non-diseased population that is correctly diagnosed. Therefore, specificity can be calculated by:

$$Sensitivity = \frac{number\ of\ true\ negative}{number\ of\ true\ negative + number\ of\ false\ positve}$$

Sensitivity and specificity defines the performance of an observer on a specific diagnostic task using a specific modality. Ideally sensitivity and specificity shall all be 1. In this case every single case would be correctly diagnosed. In reality however, there is a tradeoff between sensitivity and specificity. During the diagnosis to make a binary decision (positive or negative), as the 'decision criteria' (confidence threshold) changes, both sensitivity and specificity changes accordingly. For example, when the decision criterion is the least aggressive, all the cases are called negative. In this case the sensitivity is 0, and the specificity is 1; when the decision criterion is most aggressive, all the cases are called positive. In this case the sensitivity is 1, and the specificity is 0. Therefore, there is a tradeoff between sensitivity and specificity as the criteria gradually changes. This is shown in Figure 9.9. The bell-shaped curves represent probability density distribution of a radiologist's confidence in a positive diagnosis for a particular diagnostic task. A confidence threshold, represented by the vertical line, separates "positive" decision from "negative" decisions. As the location of the confidence threshold changes, the TPF and FPF changes accordingly, resulting in a tradeoff between sensitivity and specificity.

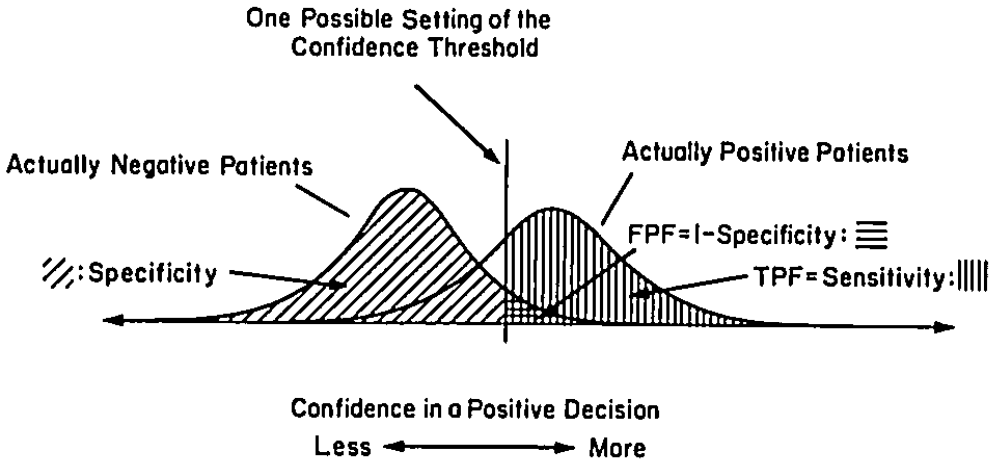


**Figure 9.9 The tradeoff between sensitivity and specificity as the confidence threshold gradually changes. Reprinted from Metz 1986[163].**

ROC curve is a plot of sensitivity versus 1-specificity as the confidence threshold varies. In other words, it is a plot of true positive fraction (TPF) as a function of false positive fraction (FPF). Therefore it always starts at (0,0) and ends at (1,1). ROC analysis takes into account the false positive and the false negative cases and it gives an overall spectrum of diagnostic performance as the decision criteria changes. It is also independent of disease prevalence, overcoming the limitations of other performance metrics such as diagnostic accuracy. In addition, Readers adjust their mind-set or level of aggressiveness as a function of the imaging context and available information; thus, the entire ROC curve (or a large region of it) is necessary to characterize diagnostic performance. Therefore, ROC analysis is widely used in medical imaging field in the applications of comparing one modality against another[160,162,163] or evaluating the value of Computed Aided Diagnosis (CAD)[161,164].

Various figures of merit of ROC performance, including the partial area under the curve in a particular region of interest or the area under the entire ROC curve (AUC), are commonly used in studies to assess overall diagnostic performance. AUC also offers a statistical power advantage compared with using a single sensitivity-specificity pair, because these summary measures effectively average over multiple "noisy" estimates of the sensitivity-specificity pairs that result from finite data sets.[161]

Since ROC shows TPF as a function of FPF, if a reader were to random guess, the probability between diagnosing a positive case correctly and incorrectly would be approximately the same. Therefore TPF would be more or less equal to FPF. That translates to a unity ROC curve with the AUC value of 0.5. On the other hand, if the reader performs perfectly, TPF would be high (with the value of 1) for all FPF values. That translates to a square ROC curve with the AUC value of 1. A regular ROC curve usually falls in between these two extreme conditions, with the AUC value from 0.5 to 1. A higher AUC value generally indicates a better performance. Figure 9.10a shows the examples of a regular ROC curve, as well as the two ROC curves with the worst (AUC value of 0.5) and the best (AUC value of 1) performance. Figure 9.10b shows the corresponding AUC value for each of these three ROC curves.

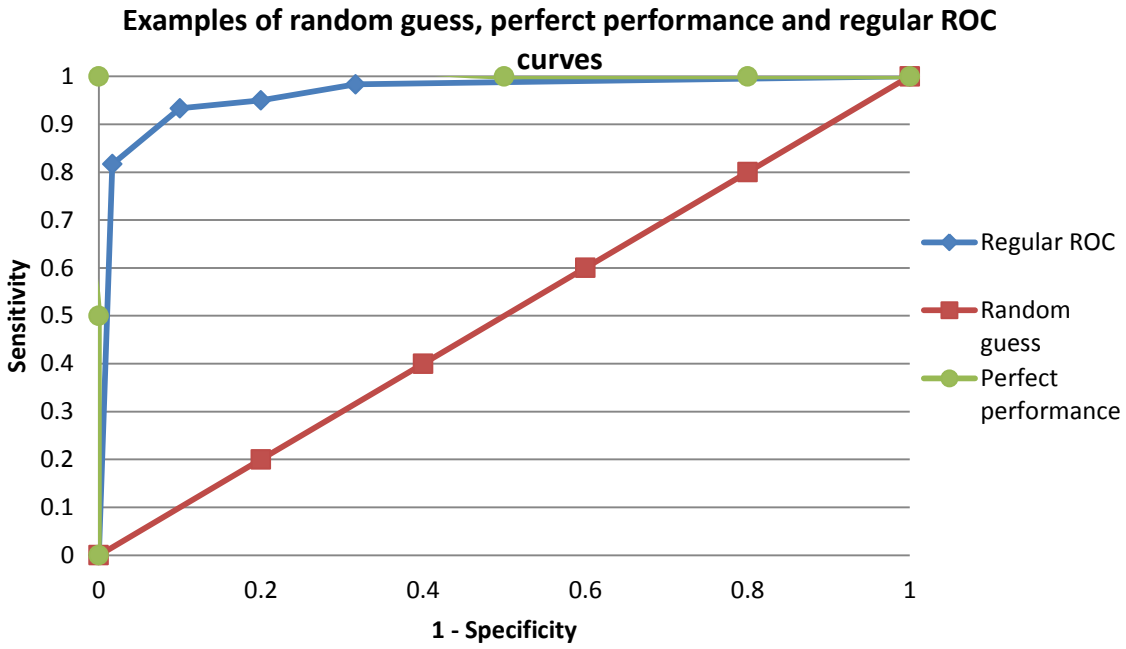


(a)

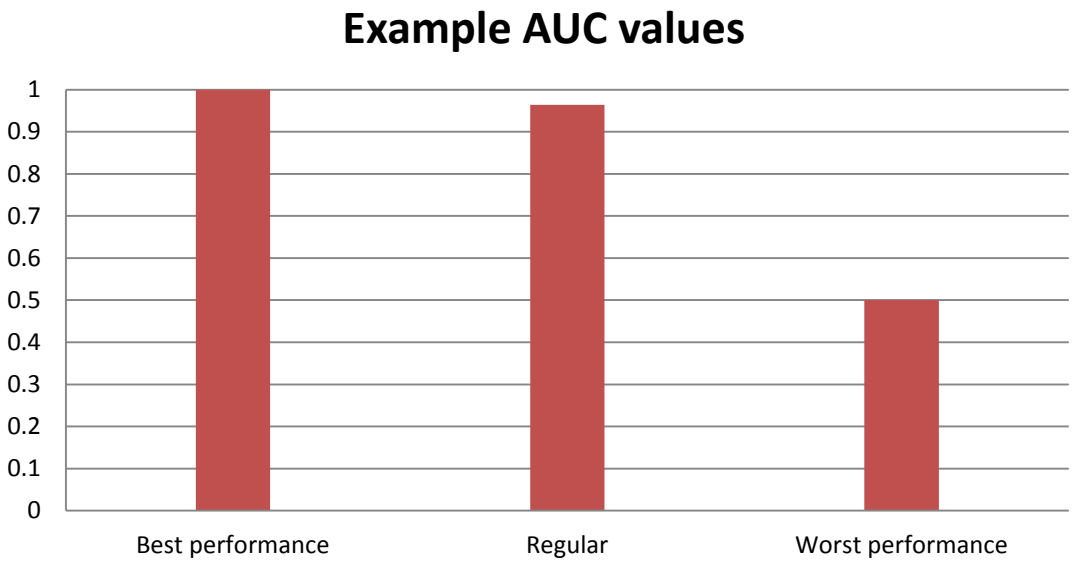


(b)

**Figure 9.10 a) Example ROC curves for regular condition, random guessing condition, and perfect performance condition. b) The AUC value for a regular ROC curve is between 0.5 and 1.**

AUC as a figure of merit has several advantages. In addition to the stronger statistic power described above, it also provides a more comprehensive representation of the overall performance of the modality to be investigated. When comparing two modalities, there is often ambiguity if only one single sensitivity-specificity pair is available, since the 'decision criteria' is a variable. For example, if two modalities has the (sensitivity, 1-specificity) points shown in Figure 9.11a, there is not enough information to conclude which modality is superior, since modality B represent a higher TPF, but at the cost of a higher FPF. Figure 9.11b illustrates one possible scenario, where modality B is superior to modality A at all FPF values. Figure 9.11c however, illustrates another possible scenario, where the ROC curves for the two modalities coincide. Therefore, the information provided by sensitivity-specificity pairs is not sufficient to evaluate the overall system performance. On the other hand, AUC value provides the capabilities for overall system performance evaluation.

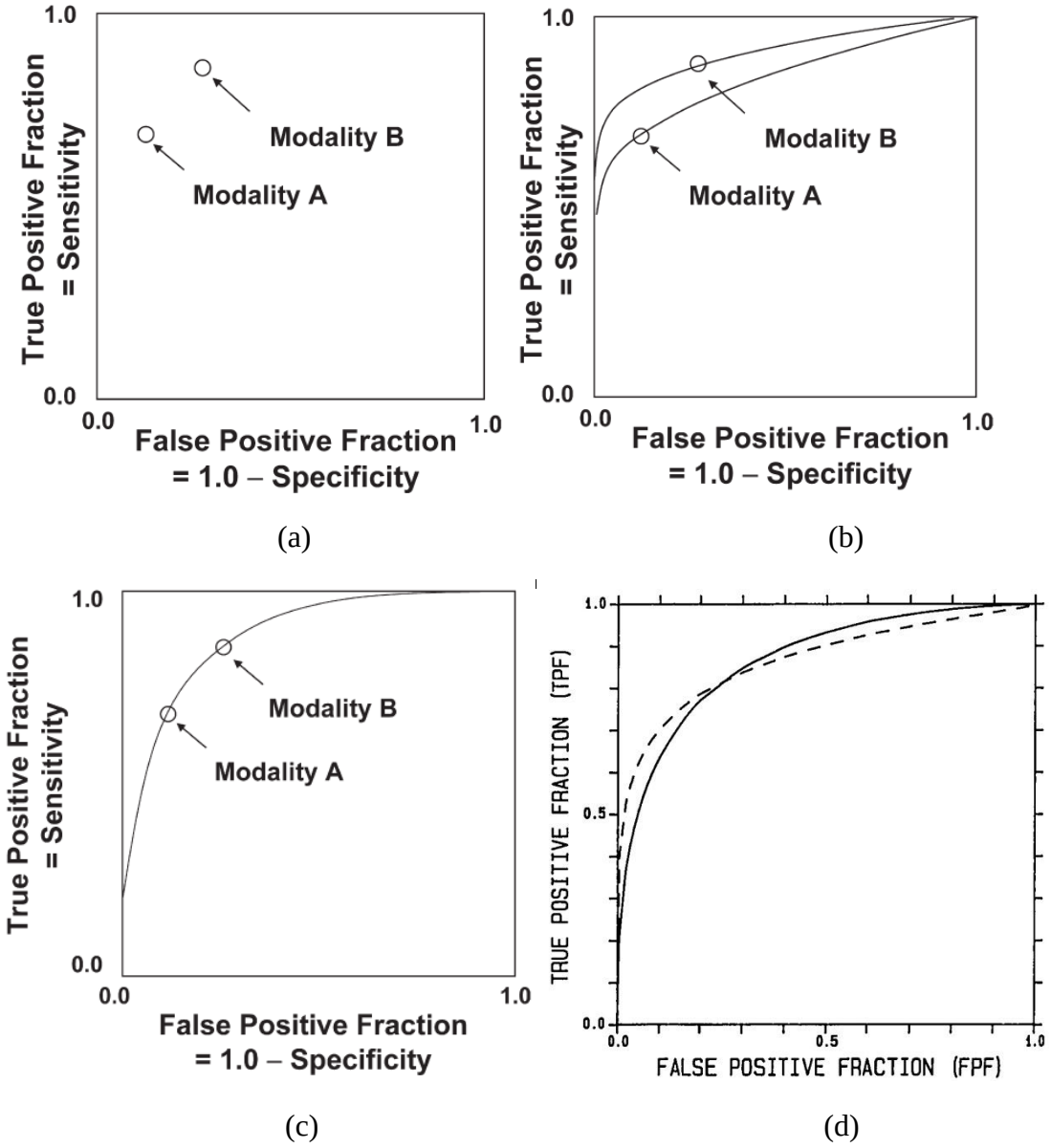


**Figure 9.11 Examples to show the advantages and disadvantages of AUC metric. Reprinted from Wagner[164] and Metz[165].**

Although AUC is a great figure of merit to assess the overall performance of a modality, it is only a single value, which obviously does not offer all the information contained in a complete ROC curve. Figure 9.11d showed an example where two different ROC curves have

the same AUC value. In this case, the AUC metric fails to provide comprehensive comparison between these two modalities. Nonetheless, with this limitation keeping in mind, AUC will be used as the figure of merit to compare systems in this dissertation.

### 9.2.9. ROC Analyses

In the context of this dissertation, the answer of the question about the final diagnosis of appendicitis has a five point scale. Assume "definitely not" corresponds to 1, "probably not" corresponds to 2, "indeterminate" corresponds to 3, "probably yes" corresponds to 4, and "definitely yes" corresponds to 5. Therefore using different decision criteria by changing the threshold of calling a case positive (>=1, >=2, >=3, >=4, >=5, >5), there was in total 6 data points on the ROC curves, including the anchor points of (0,0) and (1,1).

Using the procedures to generate ROC curves described above, the ROC curves were created for each observer at all dose levels (6 plots with each showing 5 ROC curves, one for each dose level). These ROC curves were averaged over all 6 observers to generate the averaged diagnostic performance across all the observers as a first step. Corresponding AUC values were calculated to evaluate the changes of diagnostic performance as a function of radiation dose. Furthermore, due to the fact that the six observers have different levels of experience in interpreting abdominal images, additional analysis was performed by separating the six observers into three different groups. Out of the six observers, two of them were abdominal trained radiologists who routinely read abdominal CT images (referred to as "abdominal trained, routine CT readers" in this dissertation). Two of them were non-abdominal trained radiologists who routinely read abdominal CT (referred to as "non-abdominal trained routine CT readers" in this

dissertation), and two of them were non-abdominal trained radiologists who occasionally read abdominal CT (referred to as "non-abdominal trained occasional CT readers" in this dissertation). For each of these subgroups, there were 20 patients x 5 dose levels x 2 observers = 200 observation events. And for each dose level, there were 40 observation events. In order to investigate the difference of diagnostic performance for observers with different levels of experience, the 2 ROC curves within each of these three sub reader groups were averaged to yield the average diagnostic performances for each sub reader group, and corresponding AUC values were calculated.

In this dissertation, ROC analyses were performed in order to answer several fundamental questions: 1). As the mAs level is decreased, at what mAs level is there no significant difference in terms of relative diagnostic outcome between dose levels? 2). How much can the organ dose be reduced before compromising diagnostic performance? 3). How much noise is allowed before diagnostic performance is compromised?

For the first question (diagnostic performance versus dose level), in order to find out how diagnostic performance is affected by relative mAs level, ROC curves were generated for each of the dose levels. AUC for each mAs level was calculated and compared. For the second question (diagnostic performance versus organ dose), in order to find out how much absolute organ dose is needed for an absolute diagnostic performance, the organ dose (e.g. dose to liver) was calculated first for each patient at each specific dose level. Although TCM, which intends to compensate for the patient size, was used in all scans, the organ dose will be different among

patients scanned at the same nominal Quality Reference mAs level because of the complexity of the TCM schemes (for example, the tube current may be maxed out for some really large patients). Second, the image sets were stratified based on the organ dose into several groups. ROC analysis was performed for each of these groups to compare their diagnostic performance. For the third question (diagnostic performance versus image noise), the image sets were stratified based on the image noise followed by similar ROC analysis to investigate the differences in diagnostic performance.

### 9.2.10. Standard error estimation using Bootstrapping method

There is, of course, uncertainly in estimating the AUC from a small sample size. In order to obtain the estimations of standard error of AUC for each scenario (dose level, reader combination, etc.), a bootstrapping method was used. This method was implemented by constructing a large number of resamples of the patient cases with an equal size to the original dataset. For example, for each resample, 20 patient cases were randomly selected from the original 20 patient cases (which possibly repeats cases). And the AUC was calculated based on the current 20 patient cases. This process was repeated for 2000 times to obtain a distribution of AUC, so that the standard error of AUC could be estimated.

In addition to the estimation of standard error, a statistical test was used to analyze if reader performance at 20% mAs level, 30% mAs level, 50% mAs level, and 70% mAs level are statistically significant different than the performance at the original 100% mAs level. A p value of less than 0.05 was considered to be statistically significant, and the tolerance for AUC difference was determined to be 0.05.

Due to the relatively small sample size of the patient, the power calculation was performed in order to obtain an estimated sample size for a large study that would achieve statistical significance for an AUC difference of 0.05.

## 9.3 Results

### 9.3.1. ROC Based on Dose Levels

On all patients, Tube Current Modulation was performed (Siemens CareDose4D) using a standard setting of Quality Reference mAs =250. The original and corresponding simulated lower dose settings are shown in Table 9.4.

**Table 9.4 Quality Reference mAs and $CTDI_{vol}$ of 32 cm phantom for original and corresponding simulated lower dose settings.**

| Percent of Original | Qual Ref mAs | $CTDI_{vol}$ |
|---|---|---|
| 100% | 250 | 16.0 mGy |
| 70% | 175 | 11.2 mGy |
| 50% | 125 | 8.0 mGy |
| 30% | 75 | 4.8 mGy |
| 20% | 50 | 3.2 mGy |

ROC analysis provides a complete description of the effects on sensitivity and specificity as the decision criteria changes. The ROC curves averaged over all 6 observers are shown in Figure 9.12a for all five different dose levels with each curve representing a dose level. Figure 9.12b shows the corresponding AUC values for each dose level, with the error bars showing the standard deviation of the AUC values at each dose level obtained from the bootstrapping method. There is only a very small difference between the AUC values across 100%, 70%, and

50% dose levels. Although the 30% dose level has a slightly lower AUC compared to the three higher dose levels, the AUC at 20% dose level actually increased compared to 30% dose level.

At 20%, 30%, 50%, 70% dose levels, the p values for an AUC difference of 0.05 compared to the original 100% dose level are all higher than 0.5. Therefore AUC differences between each these four lower dose levels and the original dose level are not statistically significant.

The power calculation indicated that 332 samples of appendicitis subjects (161 positive cases and 161 negative cases) is needed in order to detect a difference of 0.05 between a diagnostic test with an AUC of 0.96 and another diagnostic test with an AUC of 0.91 using a two-sided z-test at a significance level of 0.05.

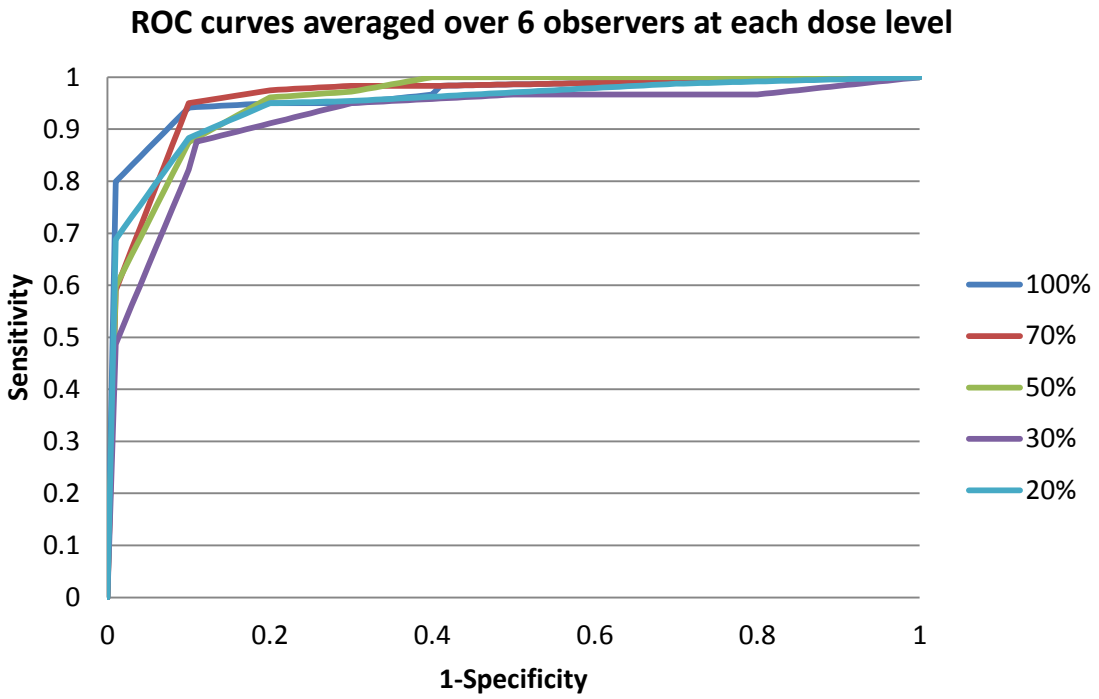


(a)

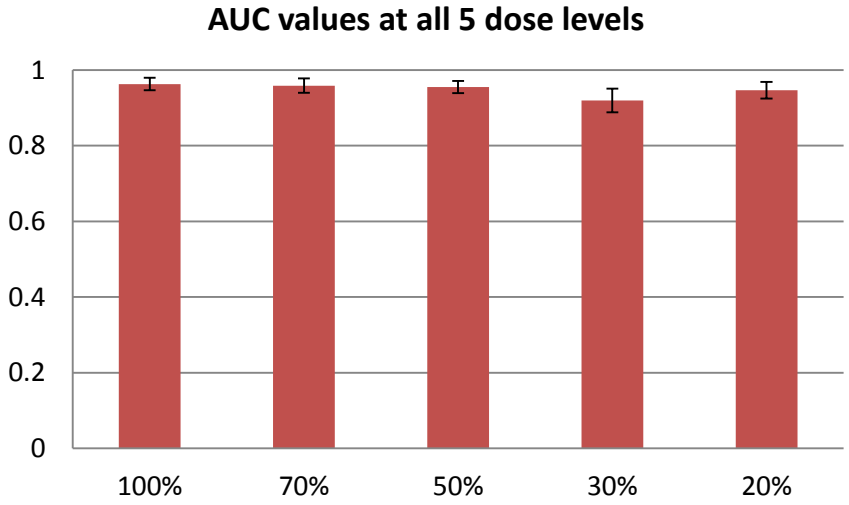


(b)

**Figure 9.12 a) ROC curves averaged over 6 observers for all five dose levels. b) AUC averaged over 6 observers for all five dose levels.**

Figure 9.13 shows the ROC curves at different dose levels for the 2 abdominal trained routine CT readers and the corresponding AUC values. For this group of 2 readers, the AUC at 100% dose level is 1. This corresponds to ideal performance, e.g., at any operating point, either sensitivity or specificity is 1. As the dose level decreases, the diagnostic performance degraded a little. However, the AUC is still as high as 0.986 even at 20% dose level. This corresponds to a sensitivity of 90% at a specificity of 95% on the ROC curve.

Figure 9.14 shows the averaged ROC curves at different dose levels for the 2 non-abdominal trained routine CT readers and the corresponding AUC values. For this sub group of 2 readers, the AUC value is 0.995 at 100% original dose level, which includes an operation point on the ROC curve at sensitivity of 99.5% with a specificity of 91%. As the dose level decreases, the diagnostic performance does not decrease dramatically. For example, at 70% and 50% dose level, the AUC values 0.987 and 0.989 compared to that of 0.995 at 100% dose level. There is some degradation of diagnostic performance at 30% dose level and further degradation at 20% dose level.

Figure 9.15 shows the averaged ROC curves at different dose levels for the 2 non-abdominal trained occasional CT readers and the corresponding AUC values. For this sub group of 2 readers, as the dose level decreases from 100% to 70% and 50%, the performance does not change much. There was an obvious drop of AUC value at 30% dose level, but there was a large increase of AUC value at 20% dose level.

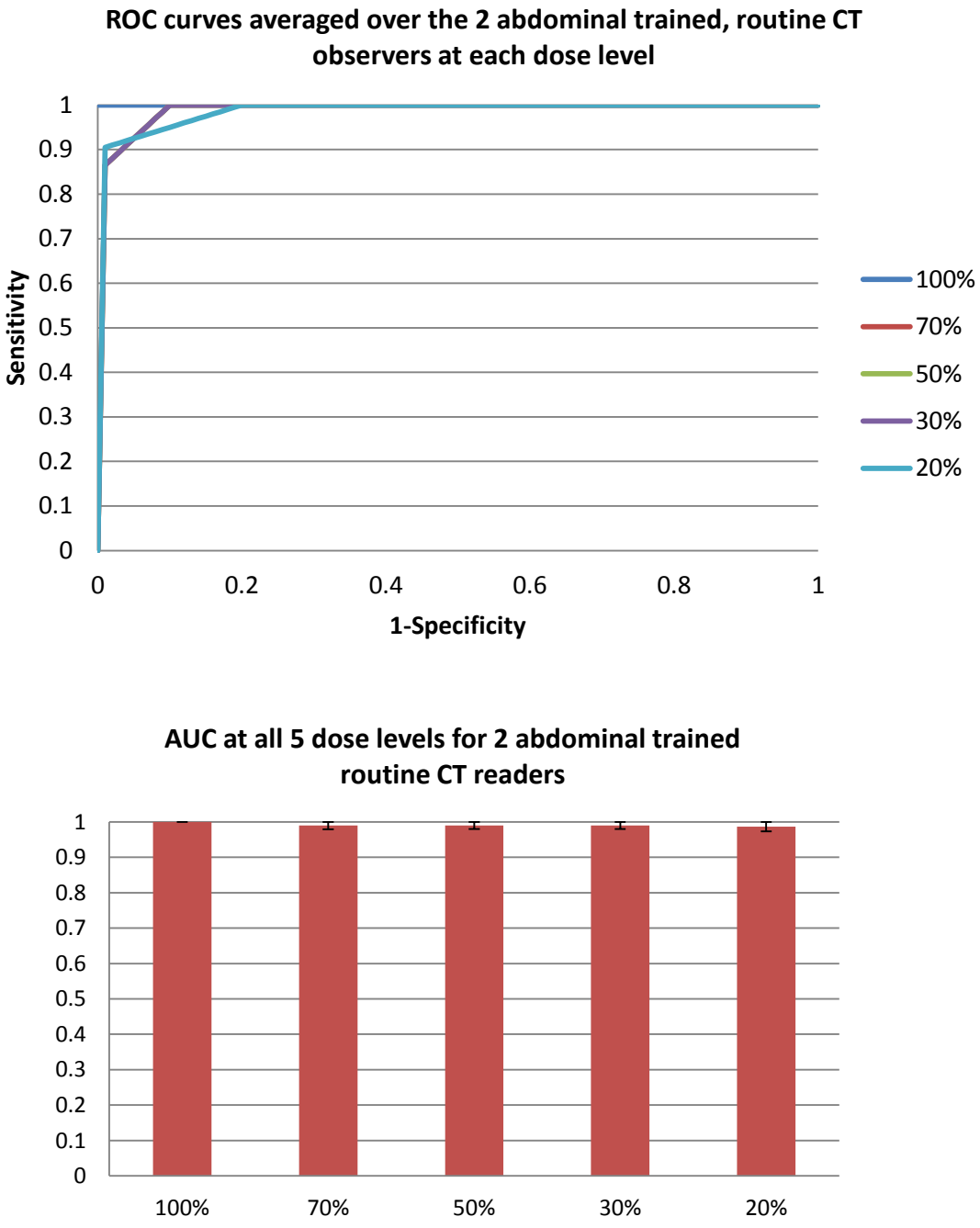


**Figure 9.13 ROC curves and AUC values for all five dose levels for the 2 abdominal trained routine CT readers.**

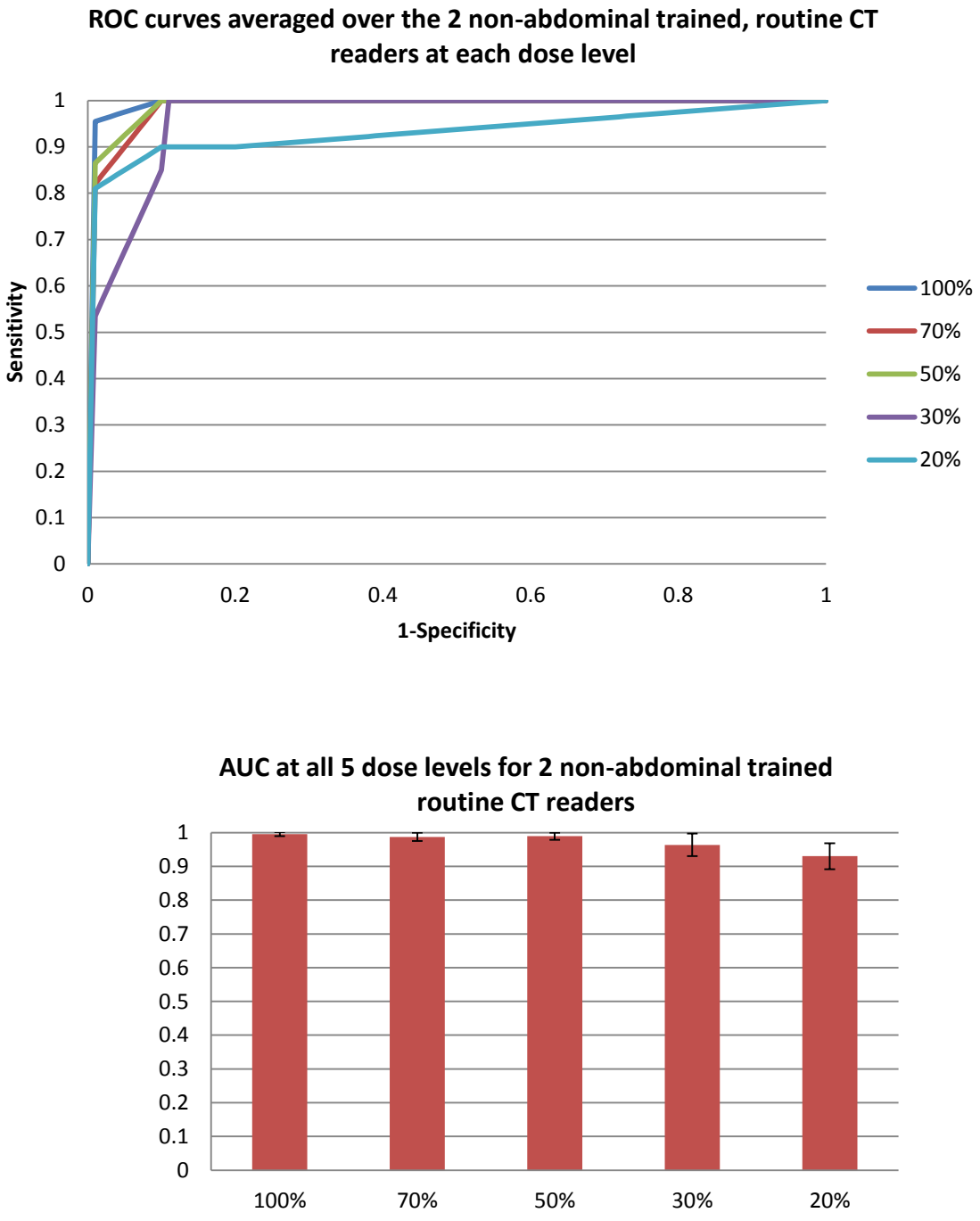


**Figure 9.14 ROC curves and AUC values for all five dose levels for the 2 non-abdominal trained routine CT readers.**

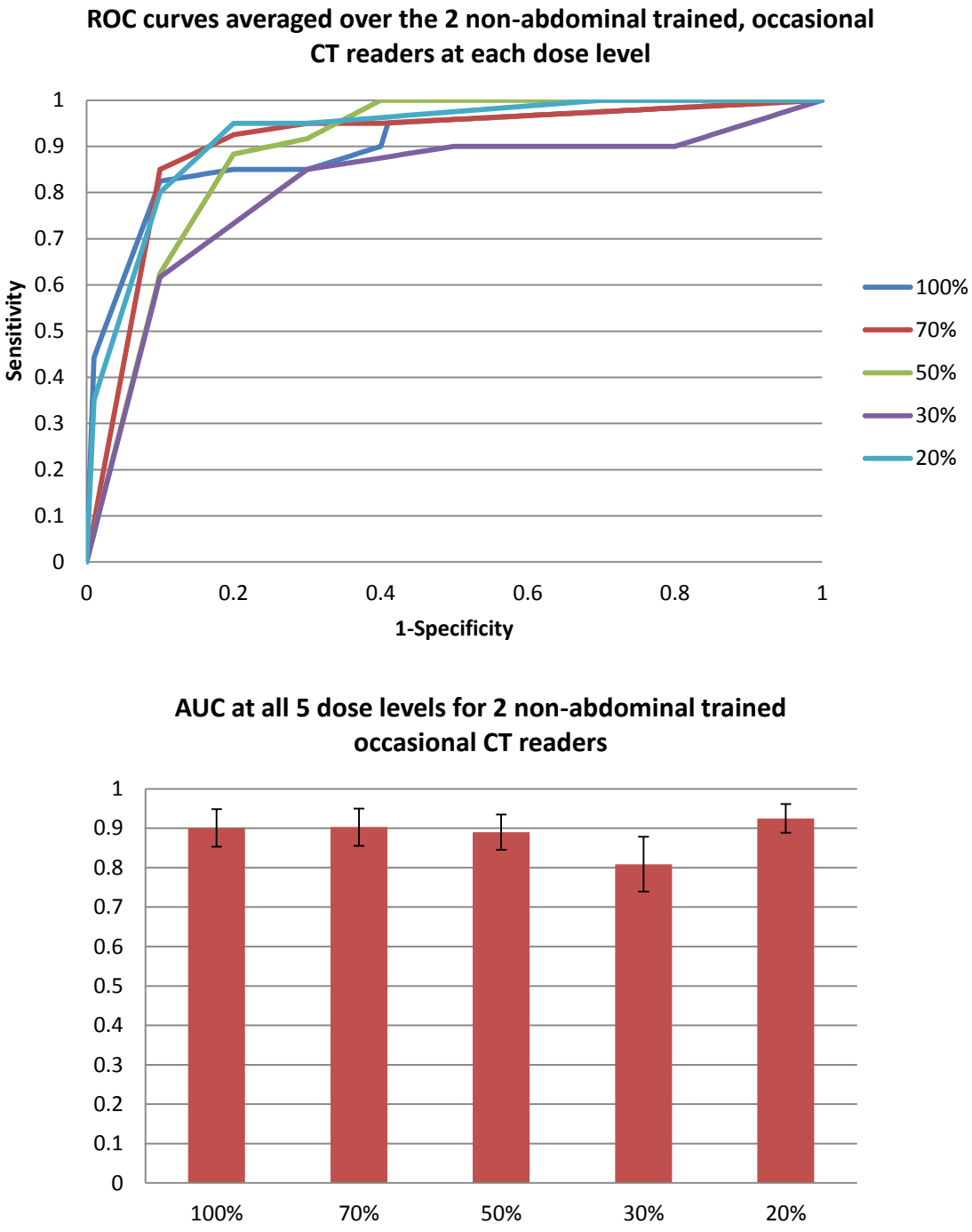


**Figure 9.15 ROC curves and AUC values for all five dose levels for the 2 non-abdominal trained occasional CT readers.**

### 9.3.2. ROC Based on Organ Doses

In order to investigate the change of diagnostic performance when actual organ dose changes, Monte Carlo simulation was used to accurately estimate the organ dose from these CT examinations, including the simulated lower dose virtual CT scans. Out of the three organs (liver, spleen, kidneys), liver was selected to represent the radiation dose to an organ since liver is the largest organ, which makes it less susceptible to geometric factors such as tube start angle during CT scans, as discussed in Chapter 7.

Estimated liver dose values ranged from 10.2 to 22 mGy for patients scanned under the original (100%) conditions which reflect our current clinical techniques. Simulated lower doses ranged from 2 mGy (smallest patient, 20% of original) to 15.4 mGy. Therefore, the radiation dose to liver to all 100 scans (including 20 original patient scans and 80 simulated virtual scans at lower dose levels) ranges from 2.04mGy to 22mGy. Table 9.5 shows the dose settings and the range of estimated liver doses for the original and the simulated dose levels. It should be noted that the $CTDI_{vol}$ shown in Table 9.5 corresponds to the $CTDI_{vol}$ at the Quality Reference mAs, instead of the effective mAs reported for each patient after each scan. The $CTDI_{vol}$ after the scans have a range of values and depend on the size of the patient, just like the liver doses shown in Table 9.5. More results regarding the relationship between patient size and radiation dose when TCM is used will be shown in 9.3.5.

**Table 9.5 Quality Reference mAs , $CTDI_{vol}$ and range of estimated liver doses for original and corresponding simulated lower dose settings.**

| Percent of Original | Qual Ref mAs | $CTDI_{vol}$ | Range of Liver Doses |
|---|---|---|---|
| 100% | 250 | 16.0 mGy | 10.2 to 22 mGy |
| 70% | 175 | 11.2 mGy | 7.1 to 15.4 mGy |
| 50% | 125 | 8.0 mGy | 5.1 to 11.0 mGy |
| 30% | 75 | 4.8 mGy | 3.1 to 6.6 mGy |
| 20% | 50 | 3.2 mGy | 2.0 to 4.2 mGy |

Based on liver dose values, the 100 scans were stratified into five groups in a manner that the number of scans in each group is the same, so that the comparison of diagnostic performance between these groups can be statistically meaningful. Therefore each group has 20 scans. These ranges are: 2.0 to 4.0mGy, 4.0 to 6.3mGy, 6.3 to 9.6mGy, 9.6 to 13.4mGy and 13.4 to 22.0mGy. Since there are six observers, the number of observations in each group is 20 x 6 = 120. It should be noted that by using this stratification strategy, each liver dose range may have repeated cases at different dose levels. For example, for the 2.0 to 4.0mGy liver dose range, one patient case appears twice, with once at 20% dose level (2.0mGy), and once at 30% dose level (3.1mGy). This is because for each specific dose level, the patient size variation causes a range of liver dose, as shown in Table 9.5.

ROC curves averaged over all 6 readers for all five different liver dose ranges and corresponding AUC values are shown in Figure 9.16, with each curve representing a liver dose range. The AUC values are the same between 13.4-22.0mGy and 9.6-13.4mGy dose groups. When the liver dose is further decreased, the performance is slightly degraded but similar to the

results observed in section 9.3.1, as the liver dose is decreased to the lowest liver dose range (2.0-4.0mGy), the performance slightly increased again.

Figure 9.17 shows the ROC curves averaged over the 2 abdominal trained routine CT readers at different liver dose ranges and the corresponding AUC values. For this group of 2 readers, the AUC values at both 13.4-22.0mGy liver dose range and 9.6-13.4mGy liver dose range are 1, meaning ideal performance. As the liver dose decreases, the diagnostic performance is only slightly degraded. The AUC value remains as high as 0.986 even at 2.0-4.0mGy liver dose range. This corresponds to a performance point with a sensitivity of 95% at a specificity of 90% on the ROC curve.

Figure 9.18 shows the ROC curves averaged over the 2 non-abdominal trained routine CT readers at different liver dose ranges for and the corresponding AUC values. For this group of 2 readers, when the liver dose is above 9.6mGy, the AUC values are very close to, if not equal to 1 (0.995 for the first liver dose range and 1.0 for the second liver dose range). As the dose level continues to decreases, the diagnostic performance gradually decreased, too. For example, the AUC value decreased to 0.984 and 0.962 at the next two liver dose ranges. At 2.0-4.0mGy range, the AUC value is 0.929. This includes an operation point on the ROC curve with a sensitivity of 90% at a specificity of 90%.

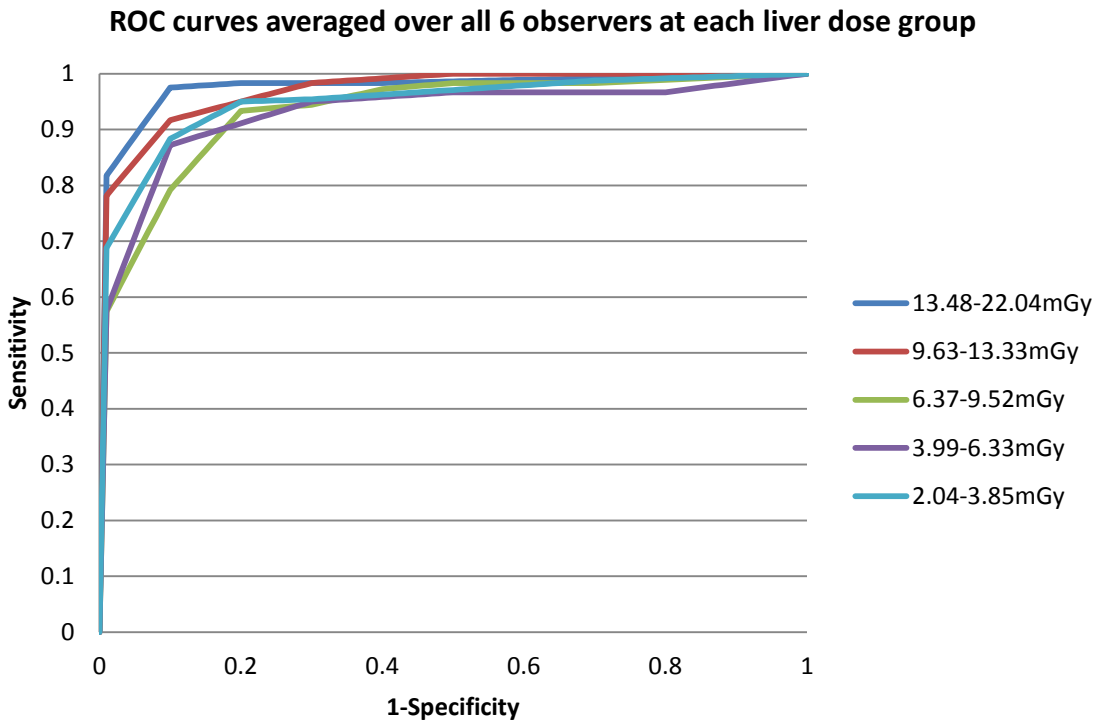


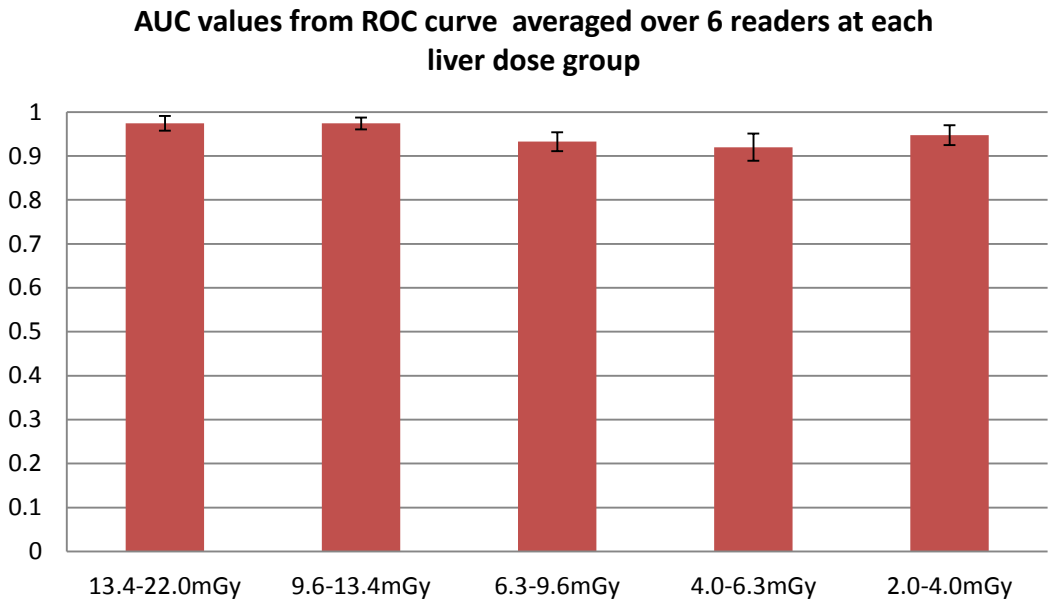


**Figure 9.16 ROC curves averaged over all 6 readers and corresponding AUC values for all five liver dose ranges.**

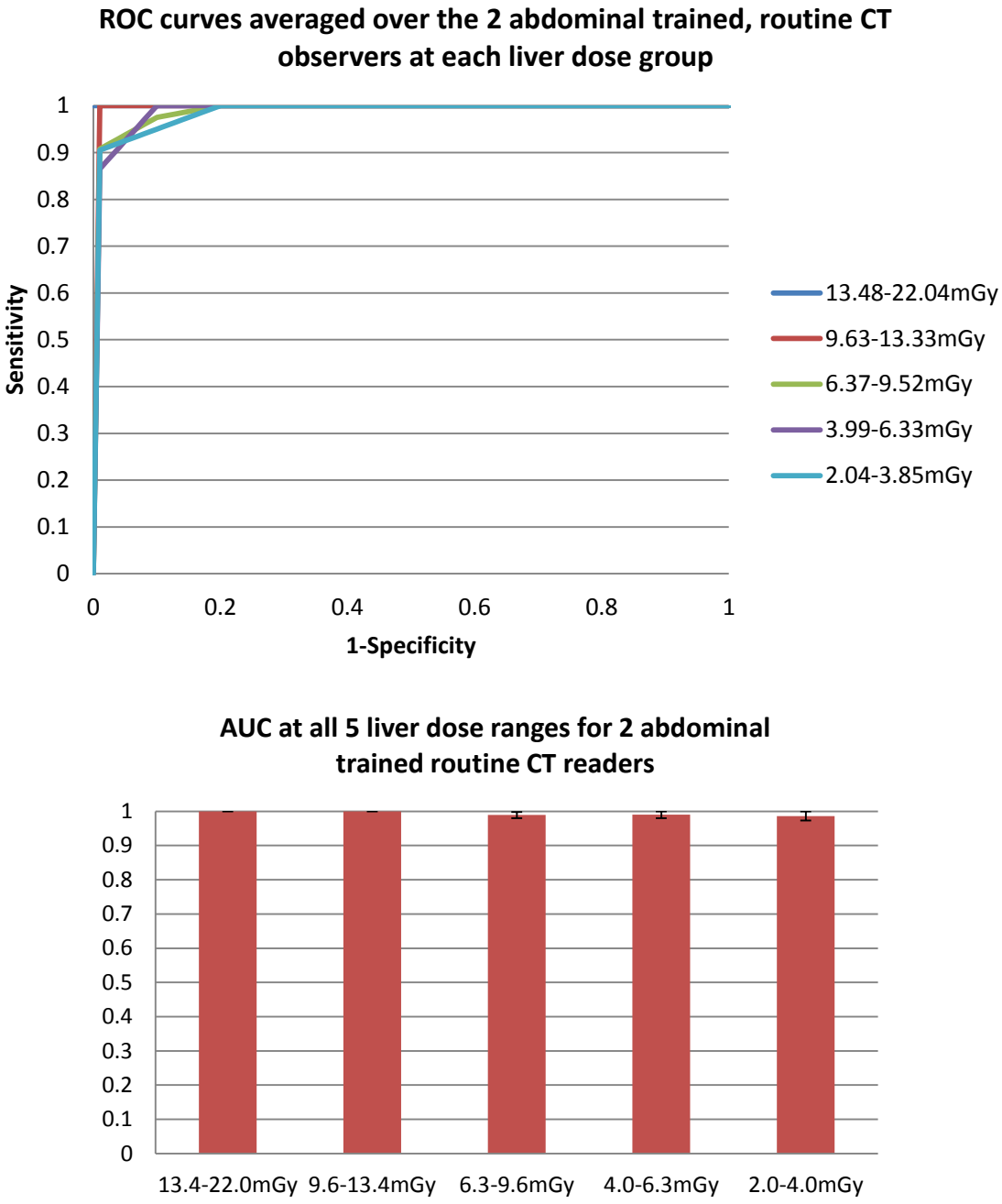


**Figure 9.17 ROC curves and AUC values for all five liver dose ranges for the 2 abdominal trained routine CT readers.**

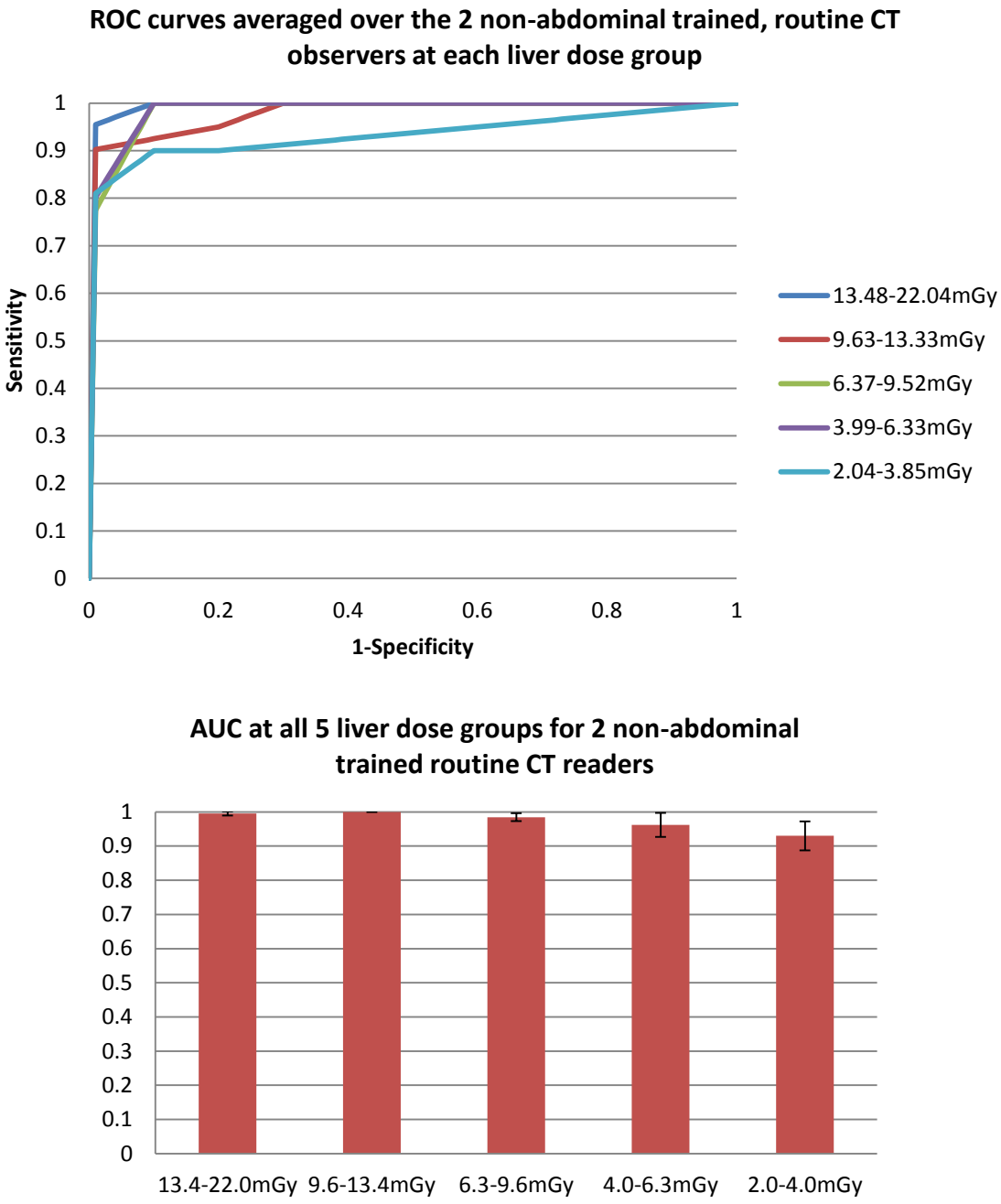


**Figure 9.18 ROC curves and AUC values for all five liver dose ranges for the 2 non-abdominal trained routine CT readers.**

Figure 9.19 shows the ROC curves averaged over the 2 non-abdominal trained occasional CT readers at different liver dose ranges for and the corresponding AUC values. For this group of 2 readers, the overall diagnostic performance is much lower compared to the previous two subgroups. As the dose level decreases from 13.4-22mGy to 9.6-13.4mGy, the performance does not change. But in the ranges of 6.3-9.6mGy and 4.0-6.3mGy, there were noticeable changes of the AUC values. However, when the liver dose is in the range of 2.0-4.0mGy, the AUC value increased again, similar to what was shown in Figure 9.15.

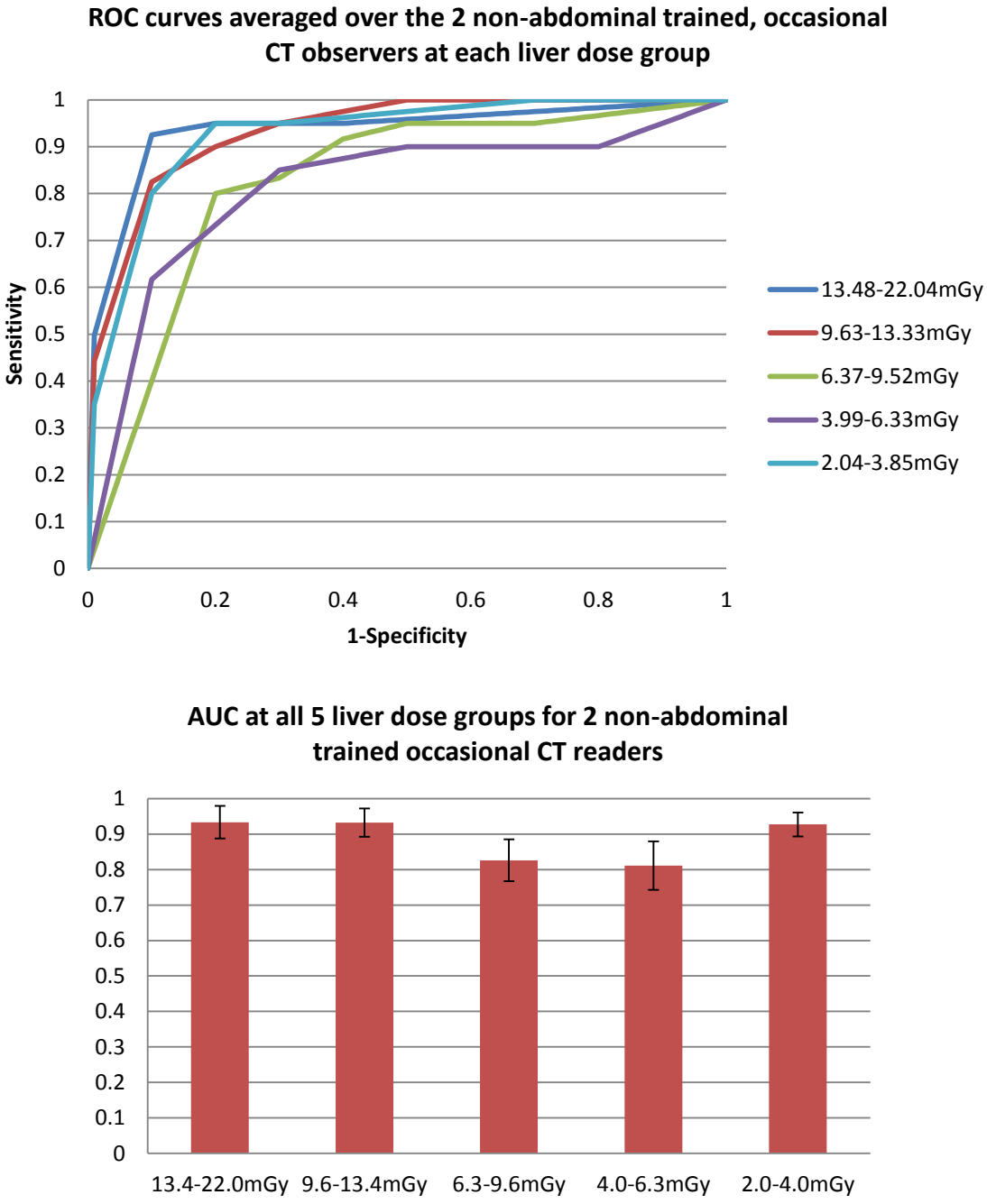


**Figure 9.19 ROC curves and AUC values for all five liver dose ranges for the 2 non-abdominal trained occasional CT readers.**

### 9.3.3. ROC Based on Image Noise

Measured image noise obtained from the standard deviation within a homogeneous region in the liver ranged from 9.6 to 23.7 for patients scanned under the original (100%) conditions which reflect the current clinical techniques. Simulated lower dose images had noise values ranging from 11.8 to 54.8. Therefore, the noise to all 100 image sets (including 20 original patient image sets and 80 simulated image sets at dose levels) ranges from 9.6 to 54.8. Table 9.6 shows the range of measured liver noise for the original and the simulated dose levels (100 image sets in total). The Quality Reference mAs and corresponding CTDIvol values are also shown in Table 9.6 to provide comparison between nominal CTDI dose and measured image noise.

In order to investigate the difference of diagnostic performance across different image noise ranges, the 100 image sets were again stratified into five groups based on image noise obtained from a homogeneous region on the liver of each individual image set, with 20 images sets within each image noise group. The stratified noise ranges are: 9.6 to 14.15, 14.2 to 17.25, 17.3 to 21.1, 21.3 to 25.9, and 25.95 to 54.8. Similar to the stratification strategy based on liver dose, some image noise groups may contain the same patient case at different dose levels. Again there were 120 observation events in each group (20 image sets x 6 observers). In order to give an example of the appearance of these images for each image noise group, Figure 9.20a to Figure 9.20e shows the same slice image for a patient case for different image noise groups, from the group with the lowest noise (9.6 to 14.15) to the group with the highest noise (25.95 to 54.8).

**Table 9.6 Dose level, Quality Reference mAs, $CTDI_{vol}$ and range of measured image noise for original and corresponding simulated lower dose settings.**

| Percent of Original | Qual Ref mAs | $CTDI_{vol}$ | Range of Liver Noise |
|---|---|---|---|
| 100% | 250 | 16.0 mGy | 9.6 to 23.7 |
| 70% | 175 | 11.2 mGy | 11.8 to 29.1 |
| 50% | 125 | 8.0 mGy | 14.1 to 34.6 |
| 30% | 75 | 4.8 mGy | 17.2 to 44 |
| 20% | 50 | 3.2 mGy | 20.7 to 54.8 |

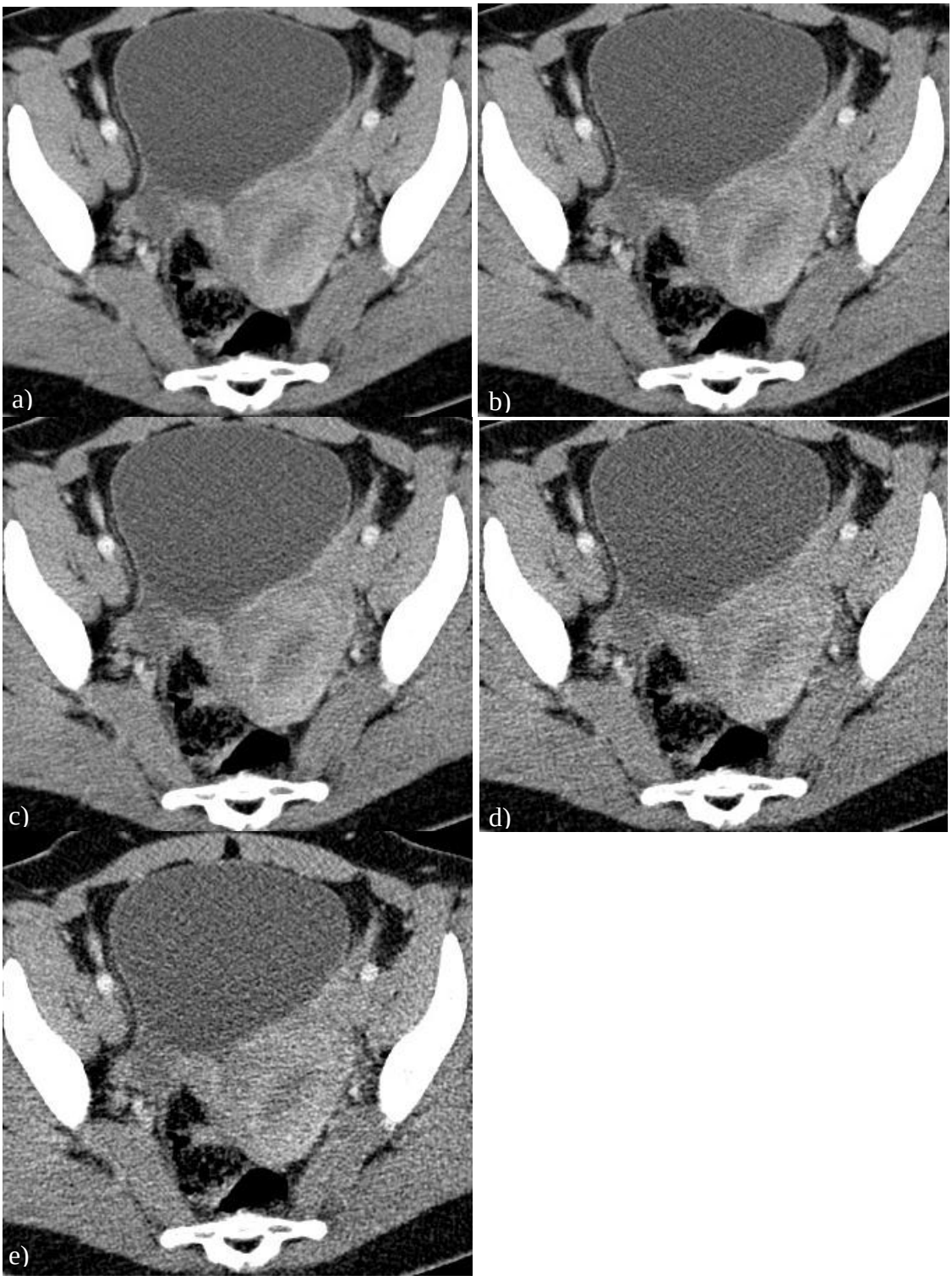


**Figure 9.20 Example images at different image noise groups from low to high.**

ROC curves averaged over all 6 readers for all five different image noise groups and corresponding AUC values are shown in Figure 9.21, with each curve representing an image noise group. These AUC values are almost the same across all the image noise ranges.

Figure 9.22 shows the ROC curves and the AUC values at different image noise groups for the 2 abdominal trained routine CT readers. For this group of 2 readers, the AUC values at 9.6-14.15 image noise range is 1, corresponding to ideal performance. As the image noise increases, the diagnostic performance is nearly constant. The AUC value remains as high as 0.992 even at 25.95-54.8 image noise range. This corresponds to a performance point with a sensitivity of 100% at a specificity of 90% on the ROC curve.

Figure 9.23 shows the averaged ROC curves at different image noise ranges for the 2 non-abdominal trained routine CT readers and the corresponding AUC values. For this group of 2 readers, as the image noise increases, the AUC values kept about the same until the image noise is higher than 21. For example, at 25.95-54.8 image noise range, the AUC value is 0.930. This includes an operation point on the ROC curve with a sensitivity of 90% at a specificity of 90%.

Figure 9.24 shows the averaged ROC curves at different image noise ranges for the 2 non-abdominal trained occasional CT readers and the corresponding AUC values. The overall diagnostic performance for this subgroup is lower compared to the previous two subgroups. In particular, the performance is worst at the least noisy group of image sets (9.6-14.5). The

increase of image noise does not seem to affect the overall diagnostic performance. For example, the AUC value at 25.95-54.8 noise range is actually higher than that at 21.3-25.9 noise range.

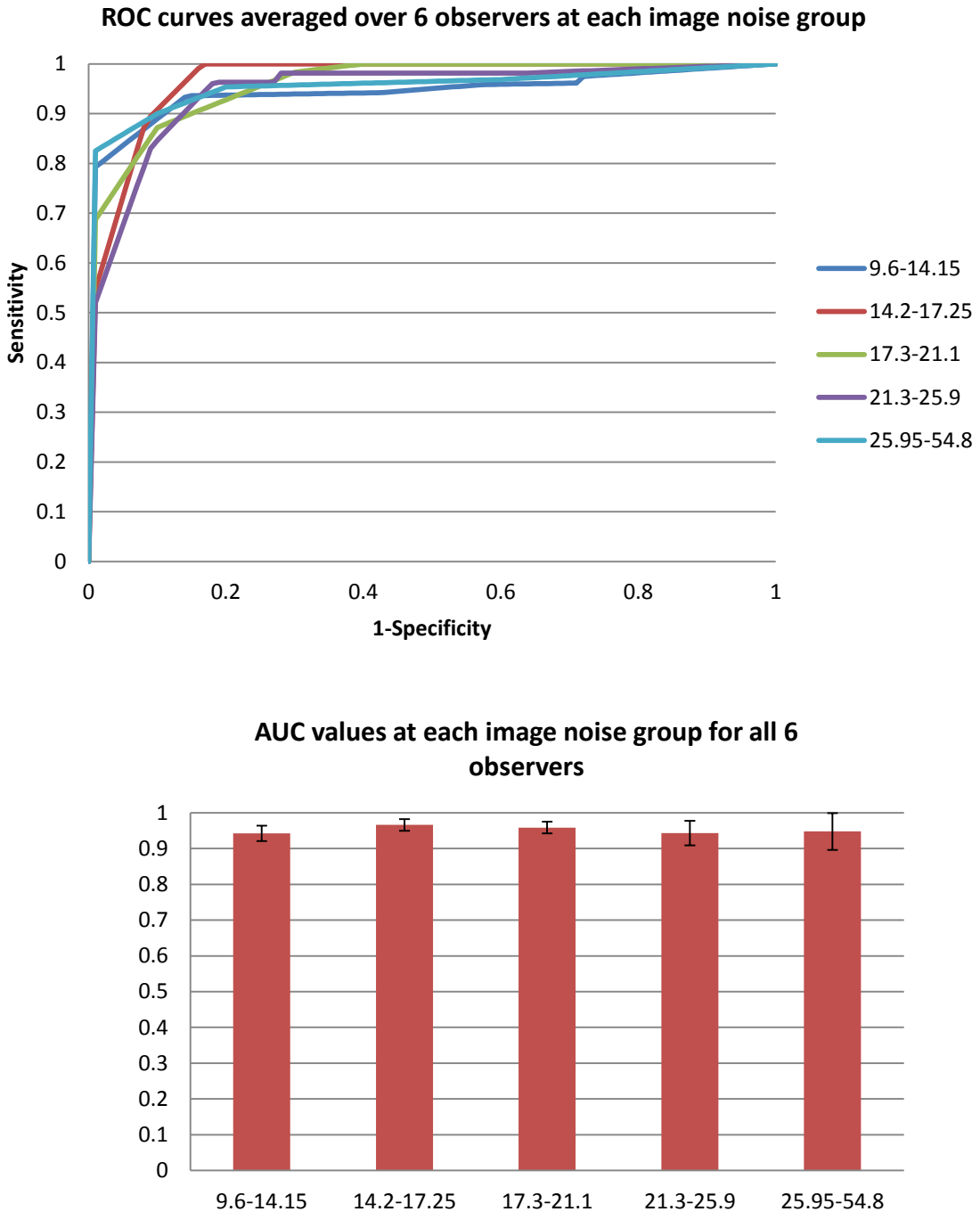


**Figure 9.21 ROC curves and AUC values for all five image noise groups.**

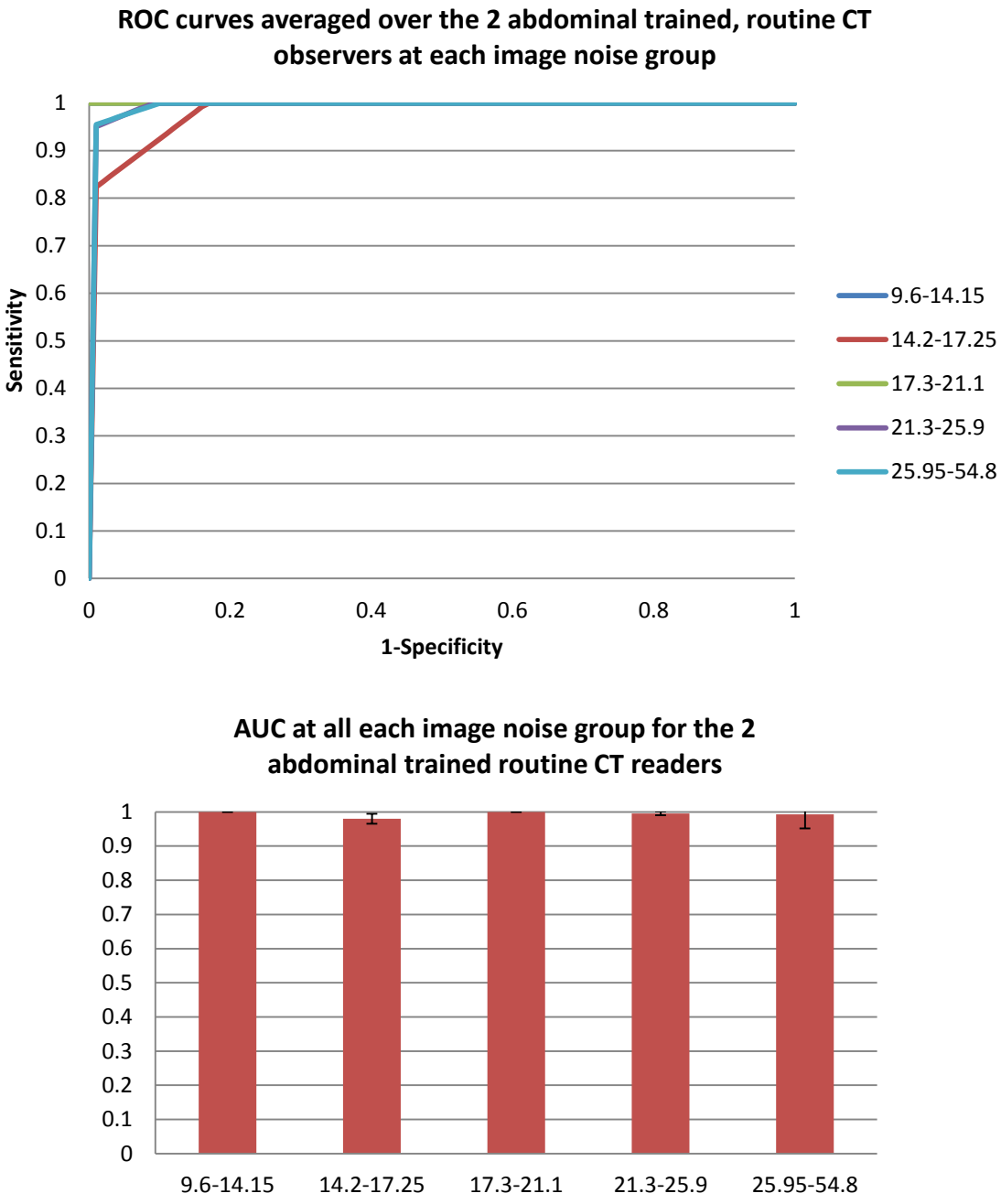


**Figure 9.22 ROC curves and AUC values for all five image noise groups for the 2 abdominal trained routine CT readers.**

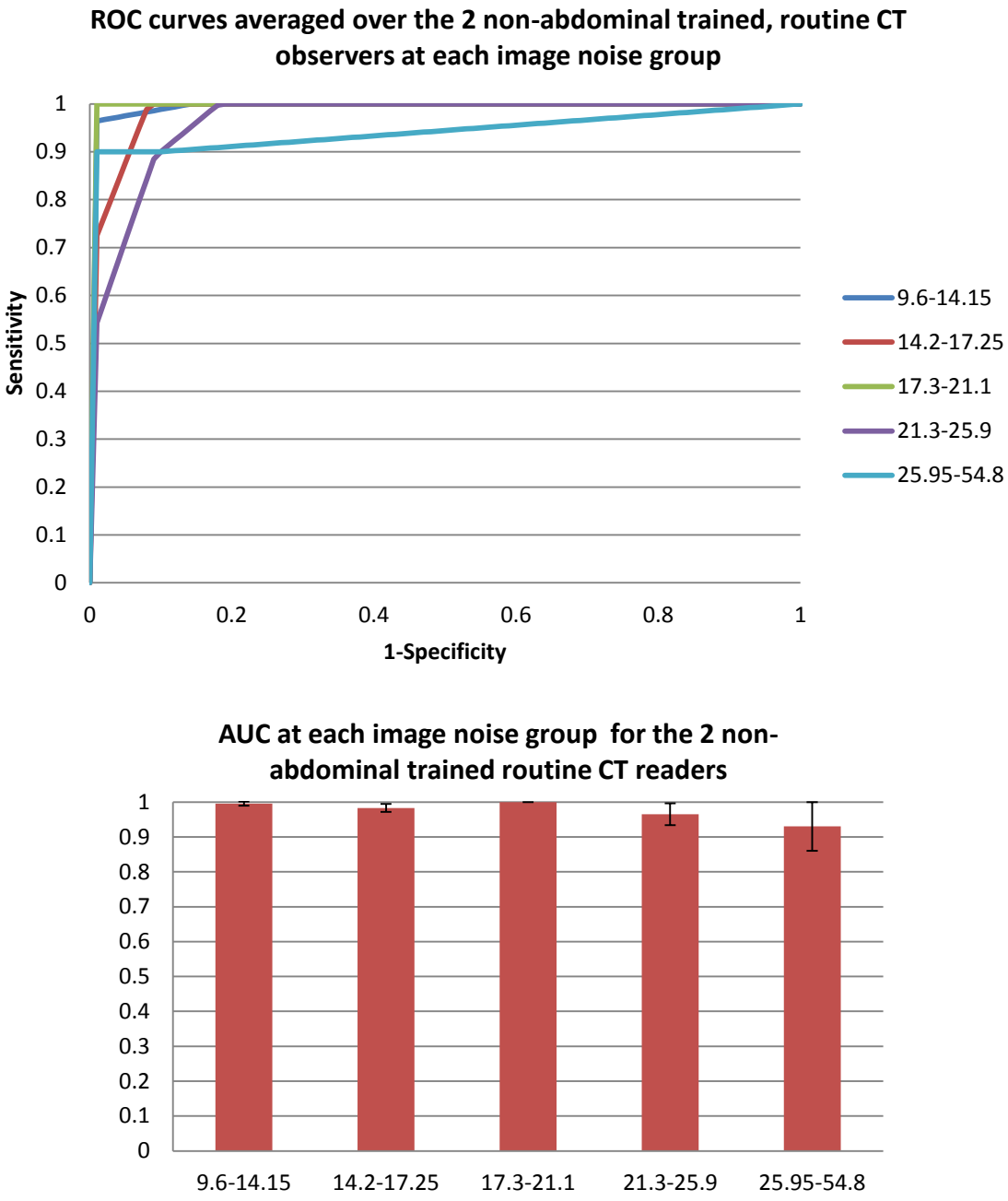


**Figure 9.23 ROC curves and AUC values for all five image noise groups for the 2 non-abdominal trained routine CT readers.**

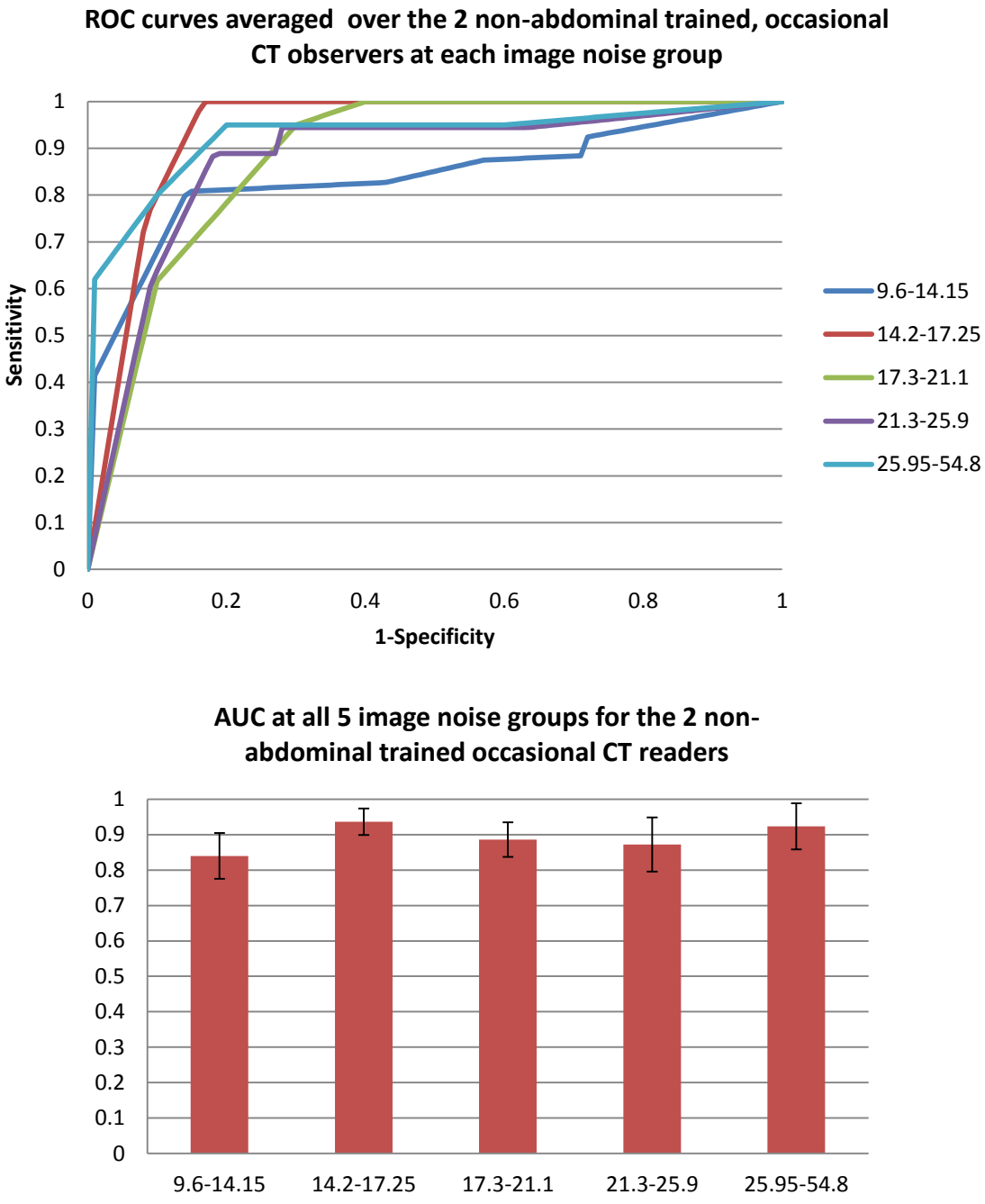


**Figure 9.24 ROC curves and AUC values for all five image noise groups for the 2 non-abdominal trained occasional routine CT readers.**

### 9.3.4. The Interrelationships Between Organ Dose, Noise and Patient Size

In order to investigate the relationship between radiation dose (organ dose) and image quality (simple noise metric in this case), liver dose and the noise of the ROI obtained from liver were studied. Figure 9.25 shows the noise as a function of liver dose in the unit of mGy for 20 patients at all five different dose levels. There are in total 100 data points in this plot (20 patient cases x 5 dose levels). For each patient at different dose levels, the noise should decrease in an exponential manner as the dose increases. This behavior can be observed from Figure 9.25, which basically demonstrated that the algorithm to simulate lower dose images performs within expectation.

Since these patients have different size, the shape and location of the exponential curve for each patient varies in this plot. For example, the data points toward the right lower corner of the graphs represent the image sets with relatively higher dose and relatively lower noise, corresponding to the images at higher dose levels (100% or 70%). In order to emphasize the relationship of the absolute values between noise and liver dose for patients with different sizes, the same plot of noise versus liver dose is shown in Figure 9.26 but with only the 100% dose level data points, with one data point for each of the 20 patients. This graph reveals a complex relationship between liver noise and liver dose, with a couple of outlier data points. It appears that the liver noise increases initially as the liver dose increases. When the liver dose is approximately above 17mGy, the liver noise started to slightly decrease.

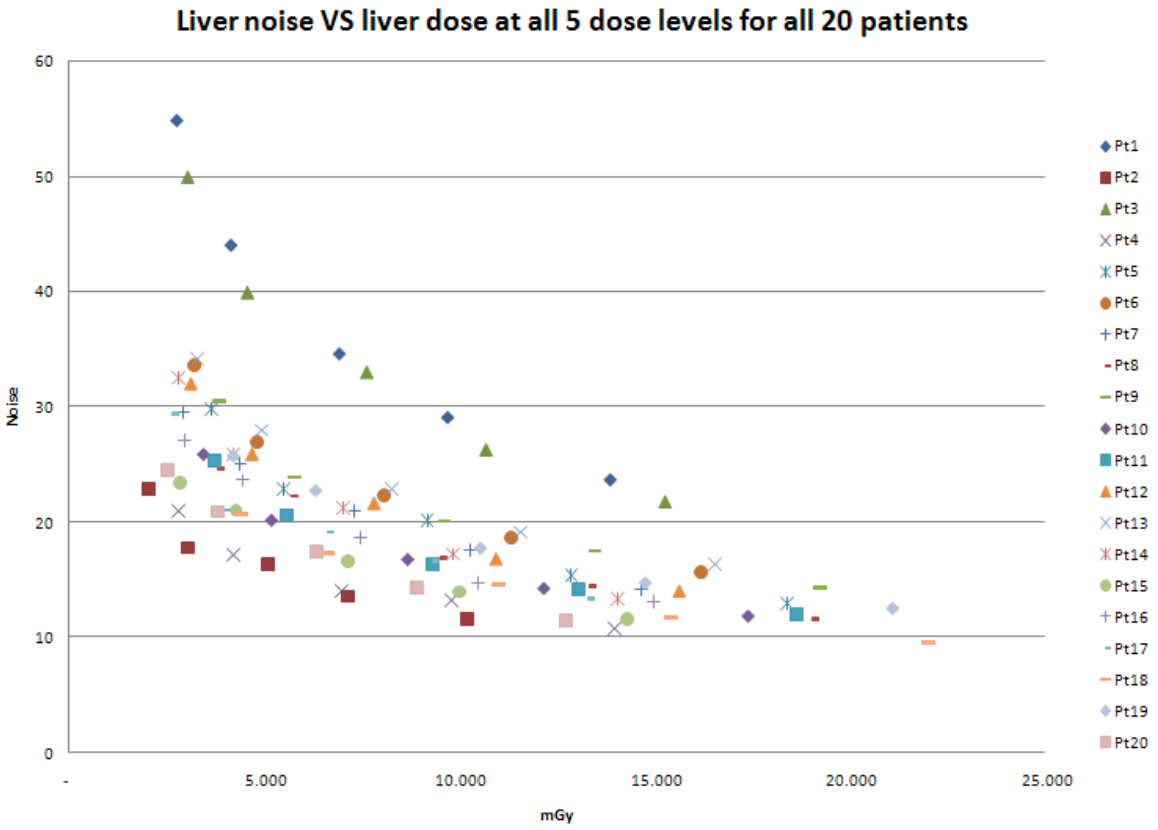


**Figure 9.25 Liver noise as a function of liver dose for all of the 20 patients at all 5 dose levels.**

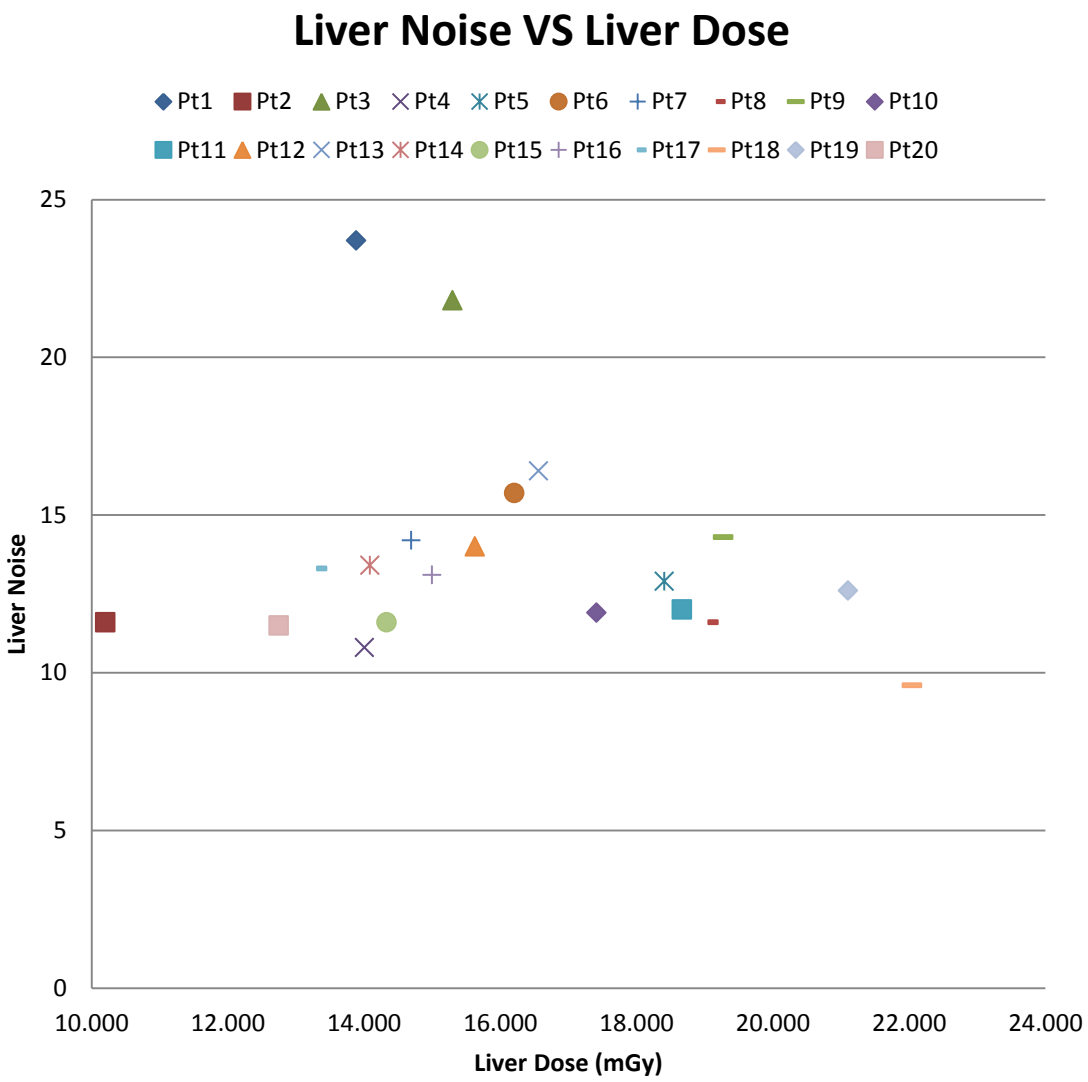


**Figure 9.26 Liver noise as a function of liver dose for all of the 20 patients at the 100% dose level.**

In order to deconstruct this relationship, liver noise as a function of patient perimeter, as well as liver dose as a function of patient perimeter, are shown in Figure 9.27 and Figure 9.28, respectively. Figure 9.27 shows there is general trend of increased liver noise as the patient size increases, with 2 outlier patients with exceptional large size (Patient 1 and Patient 3). The

relationship between liver dose and patient size shown in Figure 9.28 is even more intriguing: for patients with regular sizes (perimeter lower than 120cm), liver dose increases as a function of patient size. However, the liver dose decreased for the two exceptionally large two patients (perimeter higher than 140cm). This is most likely due to the fact that the tube current has reached its maximum for these two patients and cannot be increased to accommodate their size; essentially at this size, the behavior of the TCM is reverting to that of a constant tube current situation, where dose decreases with patient size.

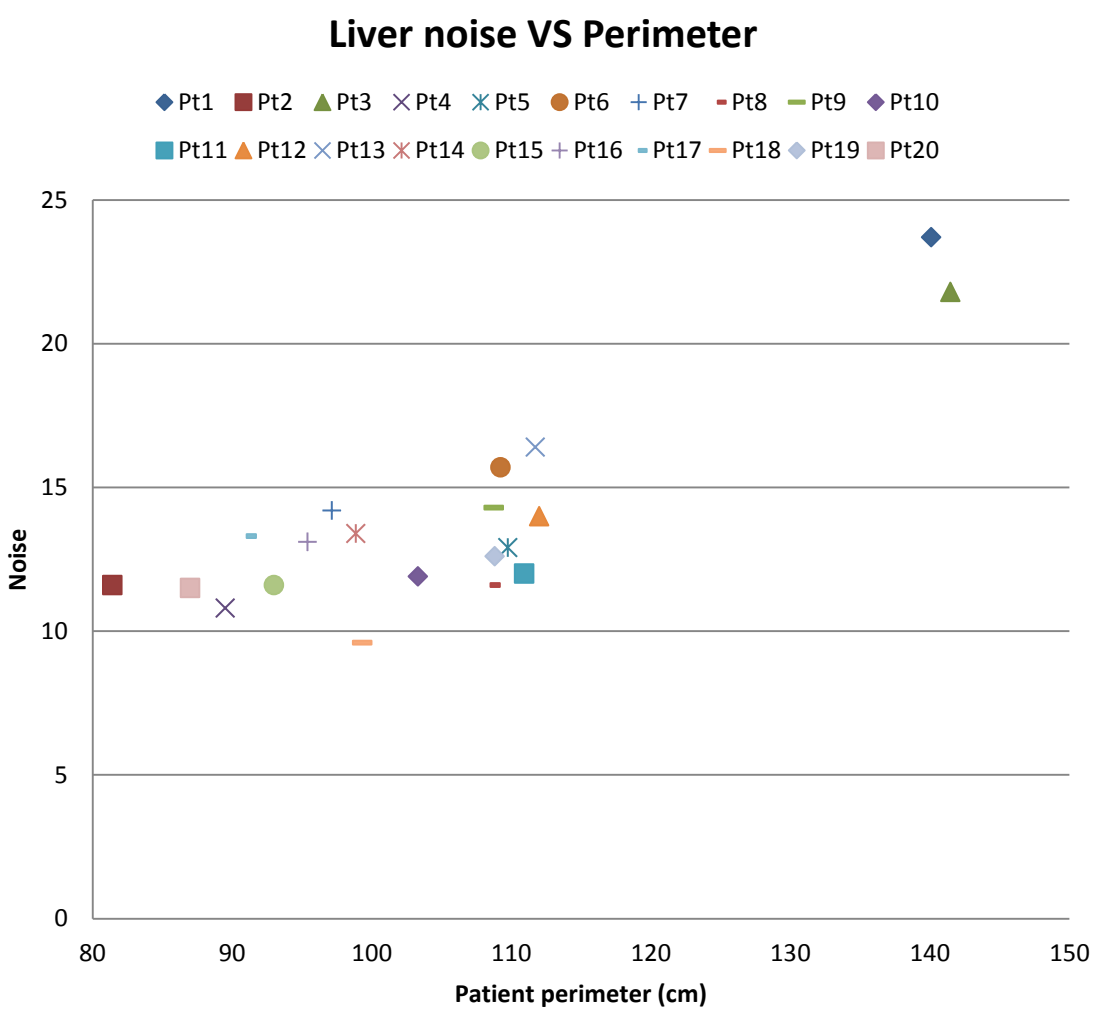


**Figure 9.27 Liver noise as a function of patient perimeter for all of the 20 patients at the 100% dose level.**

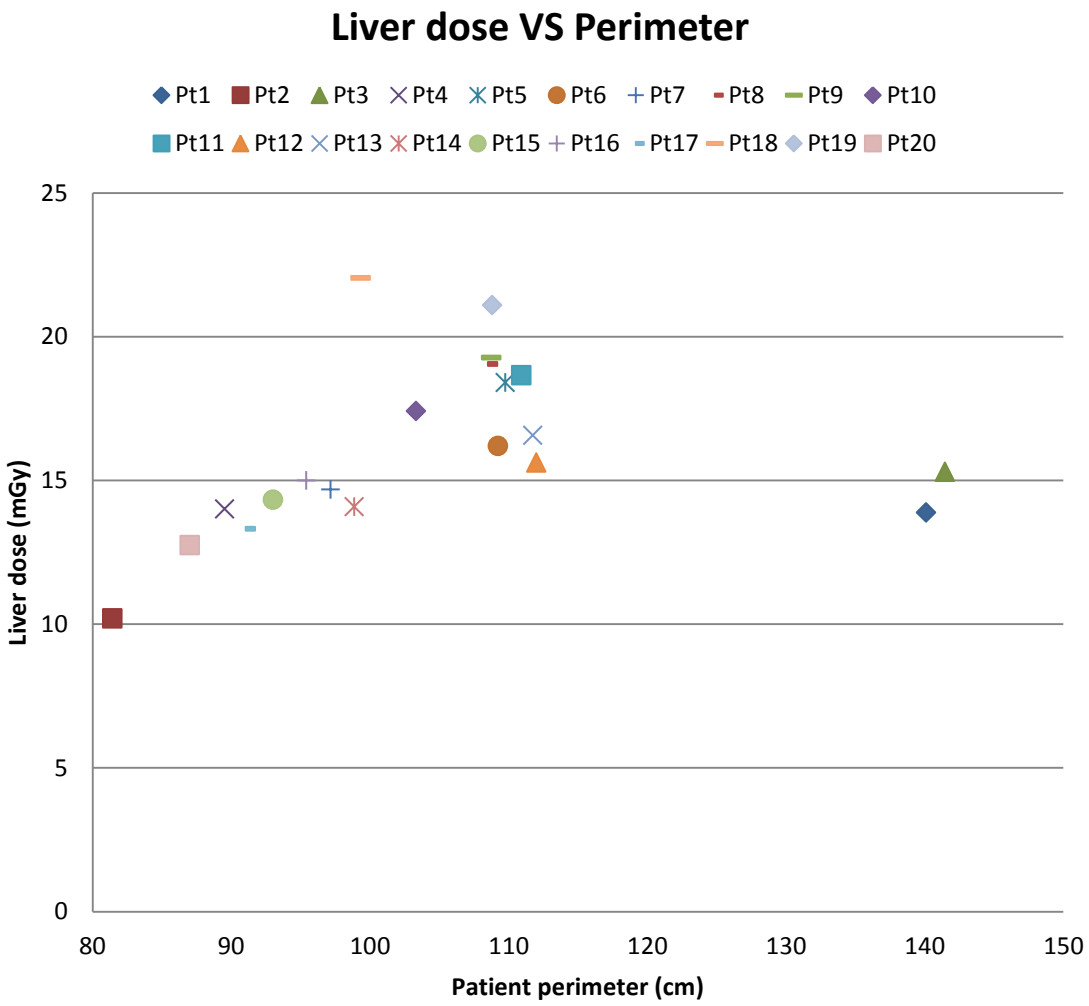


**Figure 9.28 Liver dose as a function of patient perimeter for all of the 20 patients at the 100% dose level.**

### 9.3.5. Relationship Between Subjective and Objective Image Noise

The image noise was subjectively rated by the observers on a 5 point scale for each case at each dose level during each reading session, as described in session 9.2.4. These choices were:

1. Poor, not diagnostically acceptable for interpretation;

2. Suboptimal, worse than routine images with excessive image noise;

3. Acceptable, diagnostic interpretation possible but noiser than routine images;

4. Good, noise similar to routine dose images;

5. Excellent, no image noise.

Additionally, the image noise was measured on each case using ROIs on liver, bladder, and fat. In order to investigate the relationship between subjective and object image noise, the subjective rating was plotted as a function of measured noise at different regions. Figure 9.29 shows the rating as a function of liver noise; Figure 9.30 shows the rating as a function of bladder noise; Finally, Figure 9.31 shows the rating as a function of fat noise. Since there were 100 image sets (20 patients x 5 dose levels) and 6 observers, the total number of data points on each graph was 600.

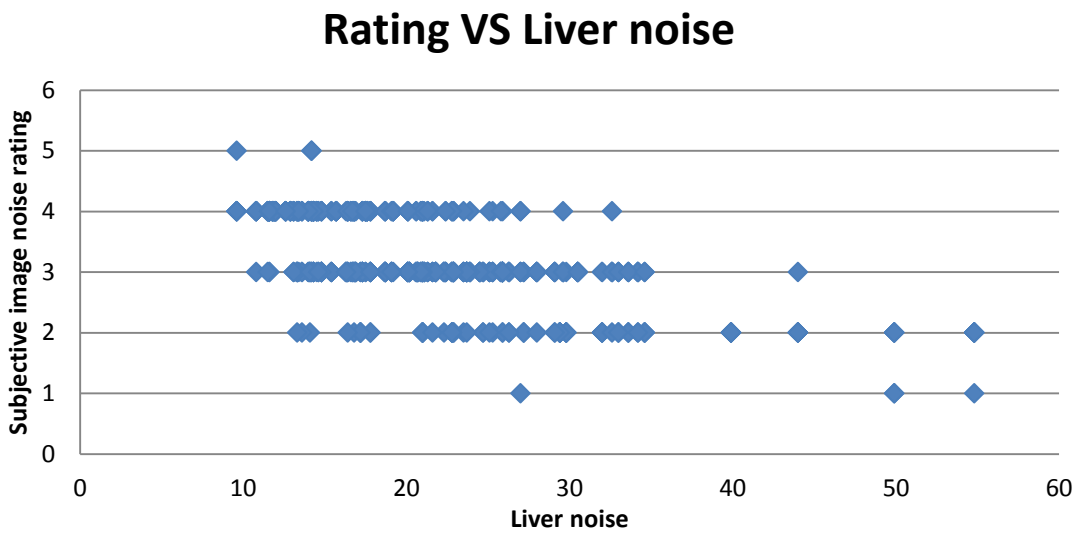


**Figure 9.29 Subjective image noise rating as a function of liver noise.**

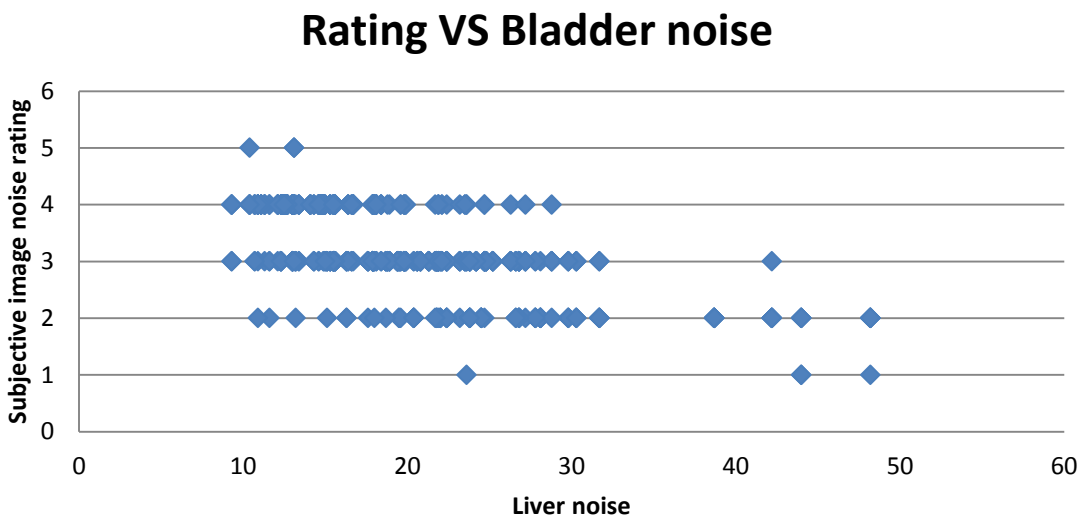


**Figure 9.30 Subjective image noise rating as a function of bladder noise.**

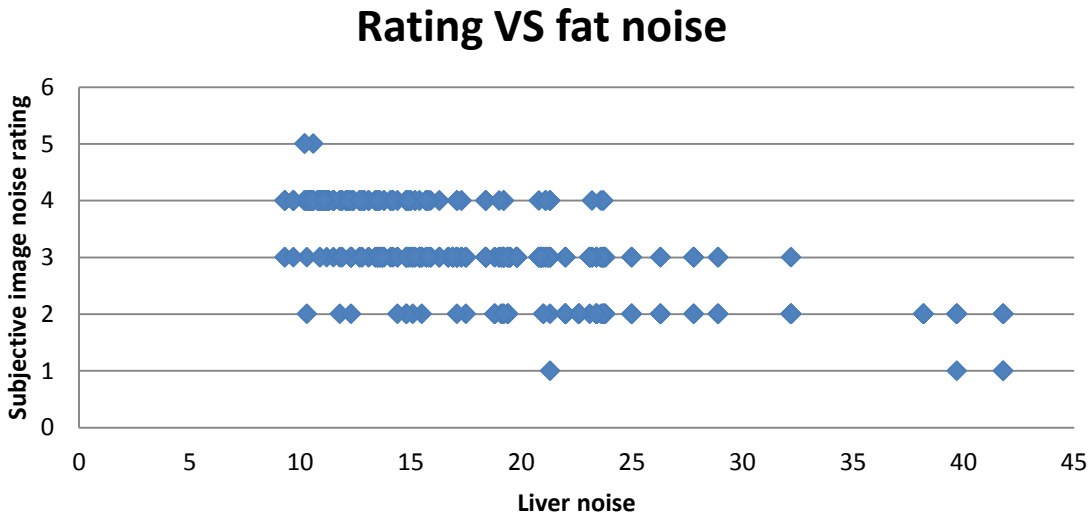


**Figure 9.31 Subjective image noise rating as a function of fat noise.**

The rating of 5 point indicates excellent image quality, while the rating of 1 indicates unacceptable image quality. Therefore a rating of 5 should correspond to lower measured noise

values, while a rating of 1 should correspond to higher measured noise values. Figure 9.29 to Figure 9.31 demonstrate that there were in fact only a few numbers of observations that were rated as excellent or unacceptable. The majority of the observations were rated from 2 to 4, which correspond to suboptimal, acceptable, and good, respectively. There are significant overlaps of the coverage of noise for these three rating levels for noise measurement at all three locations, although there are several outlier data points that yields higher measured noise value for lower image noise ratings.

## 9.4 Discussion and Conclusion

This work investigated the tradeoff between image quality and radiation dose by studying the diagnostic performance across different radiation dose levels for a specific CT clinical task – diagnosis of appendicitis. An observer study was conducted using 20 patient cases which were carefully selected in order to represent a patient population. Six observers with a variety of experience participated in the study and they were required to provide answers to a number of carefully designed clinical relevant questions, including their overall diagnostic impression. In addition to the estimate of diagnostic performance, estimates of the radiation dose to individual organs were obtained using Monte Carlo simulation methods to provide thorough information about the radiation dose to patients. The relationships between diagnostic performance and dose level, organ dose, as well as image noise were investigated.

### 9.4.1. Diagnostic performance at various dose levels

The results of ROC analysis showed that the diagnostic performance averaged over all 6 observers does not decrease dramatically as the radiation dose decreases, at least not over the dose levels used in this study. This can be demonstrated in Figure 9.12, which shows that the differences between AUC values for all five dose levels are very small. The AUC values at different dose levels were all above 0.9. These results are surprisingly informative: the diagnostic performance is reasonably robust even at significantly lower radiation dose levels, e.g., 30% and 20% of the original dose. Statistical analysis demonstrated that there is no significant difference of the AUC values between any of the four lower dose levels and the original 100% dose level.

Nonetheless, these results are based on the averaged performance across all 6 readers with various levels of experience. A more complete understanding about the performance as a function of radiation dose can be obtained by separating subgroups of readers with different experience.

It was demonstrated in Figure 9.13 that for abdominal trained routine CT readers, the AUC values remain consistently high across all dose levels, even when the dose level is 30% and 20% of the original. This performance is surprisingly good given that the radiation dose is only 20% of what is used routinely in clinical practice. This corresponds to $CTDI_{vol}$ of only 3.2mGy at the Quality Reference mAs level. It should be noted that the diagnostic reference level (DRL) for adult abdominal scan is 25mGy[166].

For the non-abdominal trained routine reader group, Figure 9.14 showed the averaged ROC curves and AUC values at different dose levels. It was demonstrated that this group of

observers overall had a slightly lower level of diagnostic performance compared to the previous abdominal specialists group. In terms of the relative diagnostic performance between dose levels, unlike the previous abdominal specialists group, the performance started to degrade at 30% dose level as the radiation dose decreased. Nonetheless, the performance at 50% dose level was very close to the original dose level. This corresponds to $CTDI_{vol}$ of 8.0mGy.

For the 2 non-abdominal trained occasional CT readers who had much less experience in interpreting abdominal CT images, it was demonstrated in Figure 9.15 that the overall diagnostic performance is much lower than the previous two subgroups (abdominal-trained routine CT readers and non-abdominal trained routine CT readers). For example, at the baseline of 100% dose level, the AUC value was 0.901, compared to 0.995 and 1 for the other two groups. However, in terms of the relative diagnostic performance between dose levels within this group of readers, the relative differences between the original 100%, the 70%, and the 50% dose level were still very small. At lower dose levels such as 30%, the AUC value was much lower. However, as the dose level continues to decrease to 20%, there was an increase in the AUC value, which was counter-intuitive. In fact, the performance at 20% was the best for this subgroup, even exceeding the performance at 100% dose level. It is not completely clear the mechanism behind this fact for this subgroup of observers. One possible explanation is that they spent more time and efforts in the diagnosis of the 20% dose level images, which mostly happened during the first and second reading sessions throughout the study. It should be noted that since the number of patient cases is relatively small in this study (20), the consistent bias on

the rating to only a few patients could affect the result of the diagnostic performance. Clearly this requires further study to determine if this phenomenon is reproducible for this group of readers.

After the investigations above which analyzed the observers by different subgroups based on their level of experience in reading abdominal CT images, the results shown in Figure 9.12 could be viewed in a more comprehensive manner: this performance is an average of all 6 observers together, including observers with a variety of experience levels. The small difference in diagnostic performance between original 100%, the 70% and the 50% dose levels applies to all readers. However, the data at the two lowest dose levels, especially at 20% dose levels was largely affected by the unexpected results from the two non-abdominal trained occasional CT readers.

In order to minimize this bias from the two non-abdominal trained occasional CT readers, the ROC curves were averaged over the 4 routine CT readers (2 abdominal trained and 2 non-abdominal trained) to generate the diagnostic performance at each dose level for this larger reader group. This is shown in Figure 9.32. In this larger sub-group consisting of 4 readers, there were 20 patients x 5 dose levels x 4 observers = 400 observation events in total and there were 80 observation events for each dose level. Figure 9.32 demonstrates that for this group of 4 readers, as the dose levels decreases, diagnostic performance starts to degrade at the 30% dose level. At the 20% dose level, the diagnostic performance is noticeably lower than the other dose levels. It should be noted that this represents the results averaged over all the routine CT readers that participated the study. This reader group is probably closest to the settings in a clinical

environment. Similar statistical analysis was performed for this group of readers: the p values for an AUC difference of 0.05 between each of the lower dose levels and the original 100% dose level were also all higher than 0.5. Therefore, based on the results from the cases and the four routine CT readers in this study, there is no statistically significant difference in the diagnostic performance between the original dose level and any of the lower dose levels, including the 30% and 20% dose level. Although a trend of AUC decrease can be observed for 30% and 20% dose level, the statistical analysis results suggested this decrease was not statistically significant, partially due to the small sample size.

For this group of readers, the power calculation indicated that 34 samples of appendicitis subjects (17 positive cases and 17 negative cases) is needed in order to detect the difference of 0.05 between a diagnostic test with an AUC of 0.998 and another diagnostic test with an AUC of 0.95 using a two-sided z-test at a significant level of 0.05.

In summary, there is no difference between diagnostic performance of 100%, 70%, and 50% dose level for all 6 observers. For abdominal-trained routine CT readers, the diagnostic difference is not substantially compromised even at 20% dose levels. This includes an operation point at the ROC curve with a sensitivity 0.95 of and a specificity of 0.9. The corresponding $CTDI_{vol}$ at the Quality Reference mAs level is only 3.2mGy. For non-abdominal trained CT readers, the performance is noticeably reduced at 30% and 20% dose levels.

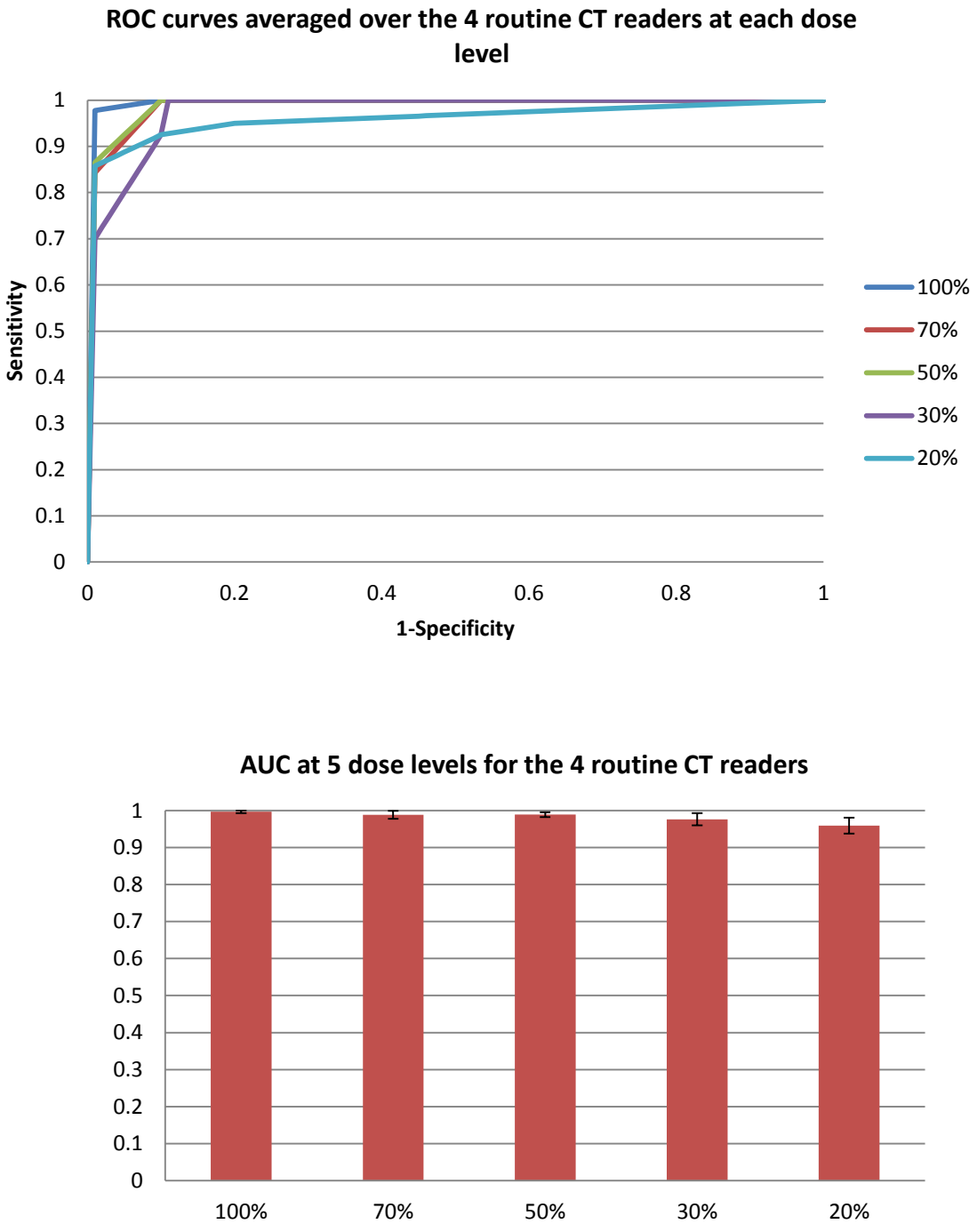


**Figure 9.32 ROC curves and AUC values for all five dose levels for the 4 routine CT readers (including 2 abdominal trained and 2 non-abdominal trained readers).**

### 9.4.2. Diagnostic performance for various organ dose groups

In this analysis, the patient cases were stratified into groups based on the liver dose to investigate the diagnostic performance as a function of absolute organ dose. Similar to Figure 9.12, Figure 9.16 also demonstrated that the diagnostic performance averaged over all 6 observers does not decrease dramatically as the liver dose decreases. The first two groups (13.4-22mGy and 9.6-13.4mGy) had almost the same AUC values. The next two groups (6.3-9.6mGy and 4-6.3mGy) also had very close AUC values but they are lower than that of the first two groups. The AUC value slightly increased for the last group (2-4mGy). The AUC values for all liver dose ranges were all above 0.9. Again, these results are based on the averaged performance across all 6 readers with various levels of experience. The results were further analyzed by separating different reader groups with different levels of experience.

For abdominal trained routine CT readers, the AUC values were 1 when the liver dose is higher than 9.6mGy. As the liver dose decreases, the diagnostic performance remained consistently high across, even at the lowest liver dose range. This performance is surprisingly good given that the radiation dose given to liver is only between 2.0-4.0mGy.

For the non-abdominal trained routine reader group, Figure 9.18 showed that when the liver dose is higher than 9.6mGy, the diagnostic performance is nearly perfect (the AUC values very close to 1). In terms of the relative diagnostic performance between dose levels, unlike the previous abdominal specialists group, where the performance remained consistent at the three lower liver groups, the diagnostic performance for 2 readers started to degrade at 6.3-9.6mGy liver dose range, and continues to degrade as liver dose decreased.

For the 2 non-abdominal trained occasional CT readers who had much less experience in interpreting abdominal CT images, it was demonstrated in Figure 9.19 that the overall diagnostic performance is much lower than the previous two subgroups (abdominal-trained routine CT readers and non-abdominal trained routine CT readers). For example, at the baseline of 100% dose level, the AUC value was 0.927, compared to 1 and 0.995 for the other two groups. In terms of the relative diagnostic performance, the performance is still about the same as long as the liver dose is higher than 9.6mGy. When the liver dose is between 4.0mGy to 9.6mGy, the AUC values are much lower. However, as the liver dose continues to decrease to 2-4mGy, there was a counter-intuitive increase again in the AUC value. This effect was observed previously and analyzed in 9.4.1. This phenomenon is observed again here because the majority of patient cases contained in 2-4mGy liver dose range belong to the 20% dose level virtual scans.

Therefore, the similar diagnostic performance for the 13.4-22mGy and 9.6-13.4mGy liver dose ranges applies to all readers. However, high performance at 2-4mGy liver dose range was largely affected by the unexpected results from the two non-abdominal trained occasional CT readers. In order to minimize this bias, the ROC curves were averaged over the 4 routine CT readers (2 abdominal trained and 2 non-abdominal trained) to generate the diagnostic performance at each liver dose range for this particular reader group. This is shown in Figure 9.33, which demonstrates that when the liver dose is above 9.6mGy (the top two groups), the diagnostic performance is very good, with an AUC value of 0.99 or higher. When the liver dose decreased below 10mGy, the performance started to degrade. While the dose range of 6.3 to 9.6mGy still has an AUC value of 0.986, which corresponds to an operation point with a

sensitivity of 98.7% and a specificity of 90%, as the liver dose decreases to below 6mGy, the performance also degrades noticeably. For example, at the liver dose range of 2.0 to 4.0mGy, the AUC value is 0.928, which corresponds to an operation point with a sensitivity of 92.5% and a specificity of 90%.

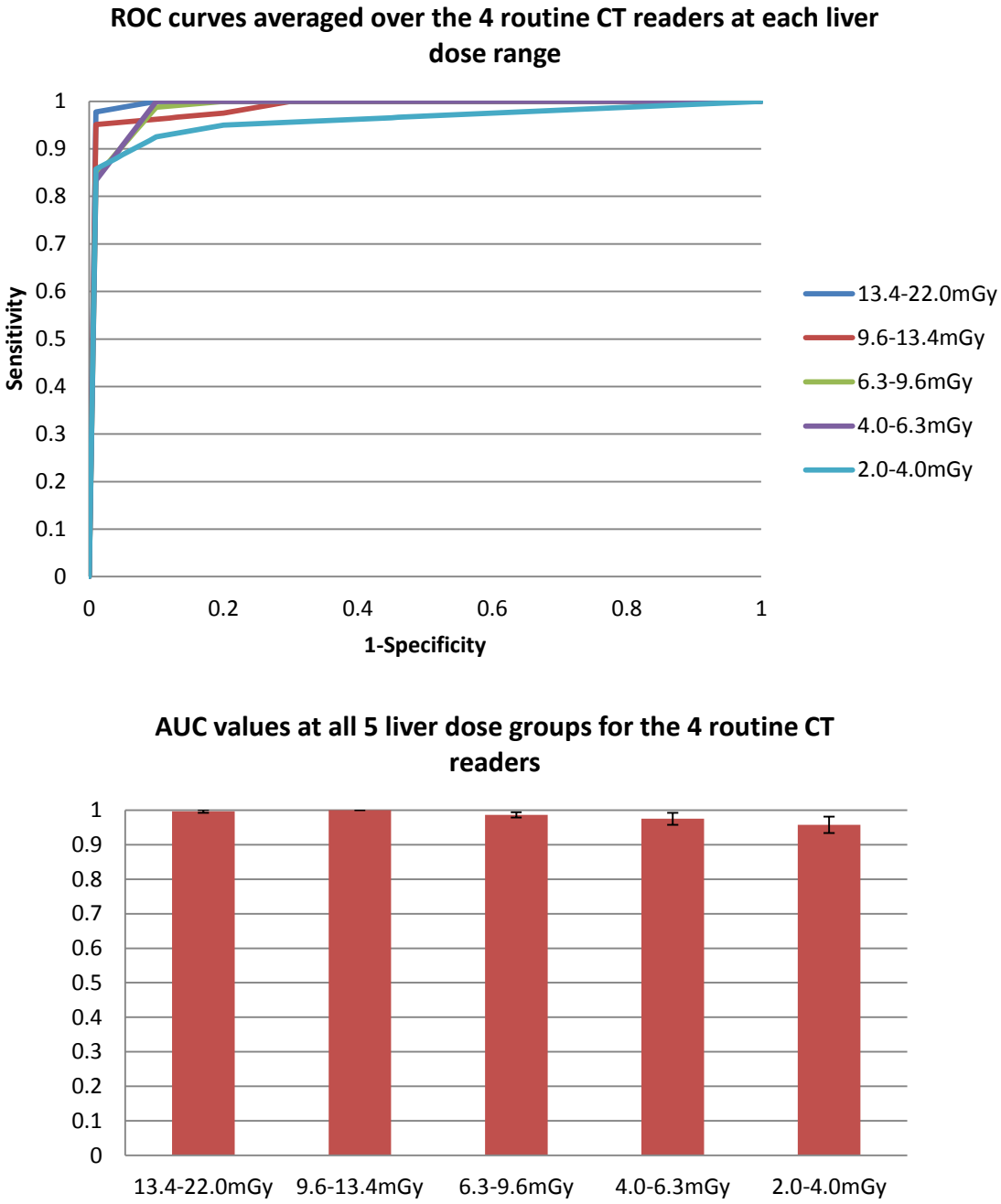


**Figure 9.33 ROC curves and AUC values for all five liver dose ranges for the 4 routine CT readers (including 2 abdominal trained and 2 non-abdominal trained readers).**

In summary, this is the first study to demonstrate a methodology to provide a direct relationship between diagnostic performance (which can be interpreted as benefit) and radiation dose to individual organs (which can be interpreted as risk). The results demonstrated that there is no difference between diagnostic performance using 13.4-22mGy of liver dose and the performance using 9.6-13.4mGy of liver dose for all 6 observers. For abdominal CT specialists, the diagnostic difference is not substantially compromised even using 2-4mGy of liver dose. This includes an operation point at the ROC curve with a sensitivity of 0.95 and specificity of 0.9. In terms of acquisition protocol, this corresponds to the lower end of the liver dose delivered to a patient using 120kVp and 50 effective mAs. For non-abdominal trained CT readers, the performance does decrease when liver dose is lower than approximately 9mGy.

### 9.4.3. Diagnostic performance for various image noise groups

The patient cases were stratified into groups based on the image noise to investigate the diagnostic performance as a function of noise in the images. Figure 9.21 showed that the diagnostic performance averaged over all 6 observers seems to be uncorrelated with image noise. The AUC values for all liver dose ranges were all above 0.9 and no trend of AUC values could be perceived as the image noise changes. Again, results were further analyzed by separating different reader groups.

For abdominal trained routine CT readers, the AUC values are reasonably consistent across all the image noise ranges, and they are all high. For the non-abdominal trained routine reader group, the AUC value started high. But as the image noise increased to be above 21.1, the diagnostic performance started to degrade. For the 2 non-abdominal trained occasional CT

readers, Figure 9.24 showed that that the overall diagnostic performance is much lower than the previous two subgroups. In terms of the relative diagnostic performance, there was not any clear trend that could be observed.

By excluding the 2 non-abdominal trained occasional CT readers, the ROC curves averaged over the 4 routine CT readers (2 abdominal trained and 2 non-abdominal trained) are shown in Figure 9.34. It showed that the image noise range of 9.6-14.15 has ideal performance. As the noise increases to the range of 14.2-17.25, the performance decreases slightly. It increased back to ideal performance as the image noise continues to increase to the range of 17.3-21.1. And from that point on, the performance gradually decreases as the image noise increase.

In summary, for abdominal trained routine CT specialists, the diagnostic performance does not change across all image noise levels. For non-abdominal trained, routine CT readers, the diagnostic performance starts to degrade when the image noise is higher than 21. For non-abdominal trained, occasional CT readers, the diagnostic performance seems to be unrelated to the image noise. Overall, the correlation between diagnostic performance and image noise is weaker than the correlation between diagnostic performance and dose level/liver dose. This indicates that in an image, there are other factors besides noise that determines the diagnosis of appendicitis.

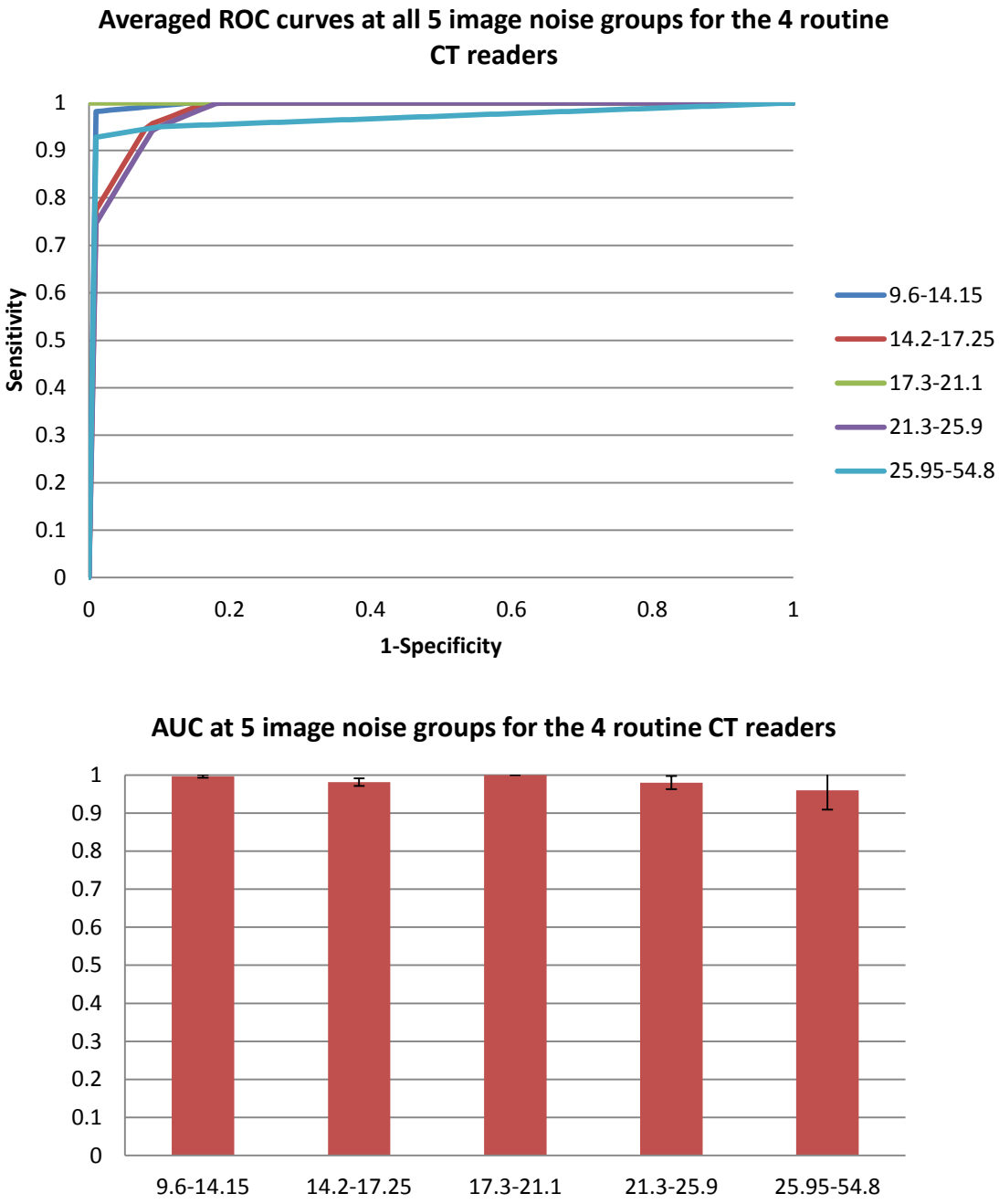


**Figure 9.34 ROC curves and AUC values for all five image noise groups for the 4 routine CT readers (including 2 abdominal trained and 2 non-abdominal trained readers).**

### 9.4.4. The interpretation of the magnitude of the change of AUC values

As described in 9.2.8, AUC is a more comprehensive descriptor than a single sensitivity-specificity point on the ROC curve to evaluate the overall observer performance as the decision criteria changes. However, examining one sensitivity-specificity point may still be of interest to evaluate the change of performance across different dose levels.

In order to provide a rough estimate to interpret changes of AUC value in terms of the change of sensitivity or specificity, one single sensitivity-specificity pair (the operating point closest to the left upper corner on a ROC plot) was selected. Figure 9.35a shows two ROC curves: one original ROC curve and a ROC curve with an AUC that is 0.02 lower. The second AUC value is obtained by reducing the sensitivity for each operating point. The sensitivity-specificity pair of (0.933, 0.9) was changed to (0.903, 0.9) when the AUC value was reduced by 0.02. Figure 9.35b also shows two ROC curves: the original ROC curve and another one with 0.02 lower AUC value achieved by reducing the specificity for each operating point. In this scenario the pair (0.933, 0.9) was changed to (0.933, 0.827) when the AUC value was reduced by 0.02. Therefore, it could be concluded that with a decrease of 0.02 in AUC value for the ROC curve, the sensitivity for a specific operating point could be decreased by 0.03, or the specificity for this specific operating point could be decreased by 0.073. Similarly, a reduction of AUC value by 0.01 corresponds to a reduction of sensitivity of 0.014 or a reduction of specificity of 0.037; a reduction of AUC value by 0.05 corresponds to a reduction of sensitivity of 0.075 or a reduction of specificity of 0.182. This result is summarized in Table 9.7.

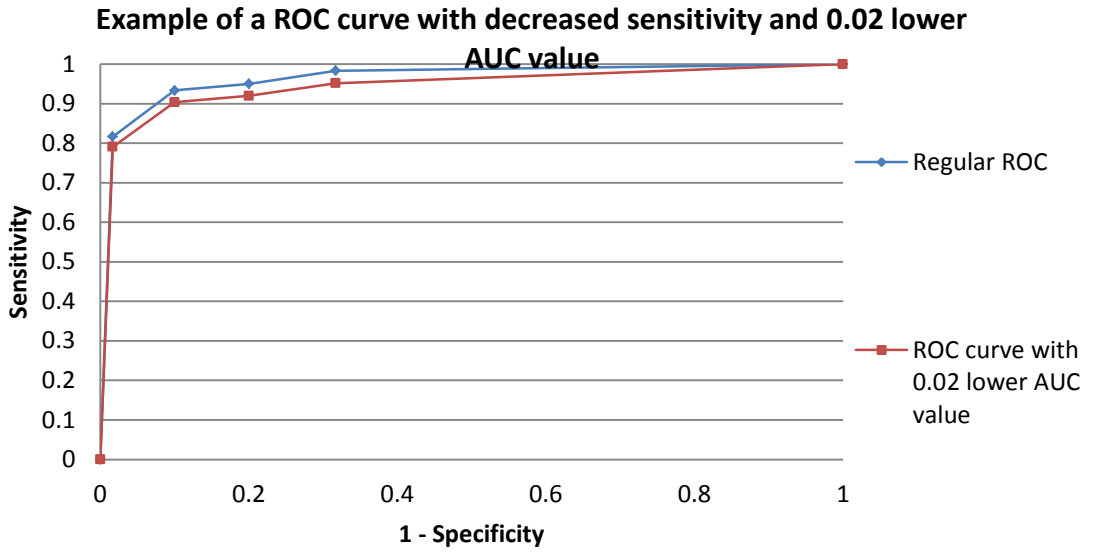


a)

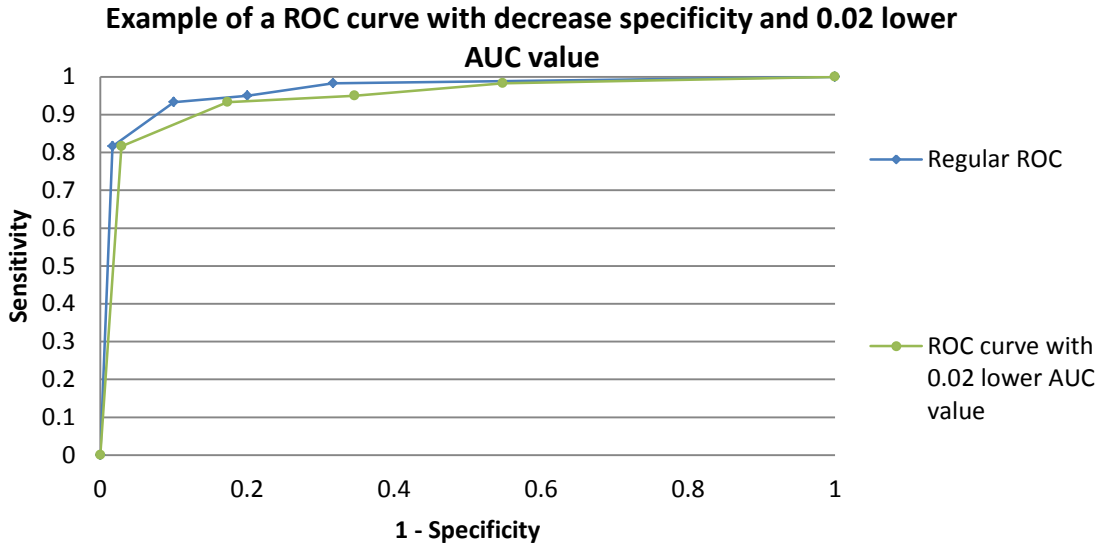


b)

**Figure 9.35 The original ROC curve and another ROC curve with 0.02 lower AUC value achieved by: a) decreased sensitivity at each operating point; b) decreased specificity at each operating point.**

**Table 9.7 The reduction in sensitivity or specificity resulted by the reduction in AUC.**

| Reduction in AUC | Reduction in Sensitivity at 0.9 Specificity | Reduction in Specificity at 0.933 Sensitivity |
|---|---|---|
| 0.05 | 0.075 | 0.182 |
| 0.02 | 0.030 | 0.073 |
| 0.01 | 0.014 | 0.037 |

### 9.4.5. Interrelationships Between Organ Dose, Image Noise and Patient Size

For a fixed tube current CT scan, if all the scan parameters are kept the same (kVp, mAs, collimation, pitch, etc.), patient dose decreases in an exponential fashion as patient size increases because of excessive self-attenuation[167]. This observation led AAPM TaskGroup 204 to develop the Size-Specific Dose Estimate (SSDE) which describes to develop a radiation dose metric that accounts for patient size. In addition, AAPM on-going TaskGroup 220 is investigating the appropriate patient size metric to allow wide deployment of patient size corrections, including SSDE. While these efforts have made good progress towards the direction to develop dose metrics that reflect patient size, however, they assume the scans to be traditional constant tube current scan, which does not address the complexity and subtleties of the effect on radiation dose from TCM. TCM has a very strong interplay with patient size and patient anatomy. This interplay eventually affects patient dose. For example, for chest-abdomen scans, the attenuation in chest region is less than that in the abdomen region. Therefore the tube current is lower in the chest region for a TCM scan, resulting in lower radiation dose. SSDE dose metric is obtained by applying patient size specific conversion factors to a single CTDIvol value  This approach does not taken into account the dose difference to different areas within a scan introduced by TCM.

Since TCM is used in majority of today's scan protocols, it is imperative to investigate the relationship between patient dose and patient size when TCM is on.

In a TCM scan, as the patient size increases, the required tube current is also increased. In some schemes the mAs is increased to maintain constant image noise (for a water phantom with equivalent attenuation), while in other schemes, the function between mAs and patient size may not be purely based on equivalent noise, but some other metrics. In either scheme, the tube current is increased for larger patients. Therefore the dose may actually increase with increased patient size. This may offset the decrease of patient dose when size increases at a constant mAs setting. Figure 9.27 shows that as the patient gets larger, the organ dose actually increases almost in a linear fashion. This is because the increase of mAs outweighs the increase of self-attenuation as the patient gets larger. This result is consistent with previously published results[48,50].

There are 2 outlier data points in Figure 9.27 which correspond to two extra-large patients (perimeter > 140cm). Instead of higher dose, these patients actually received *lower liver dose* compared to the group of patients with smaller sizes. This is because as the patient size increases, the mA increases until the maximum output of tube current is reached. If the patient size continues to increase, the tube current cannot be increased further, and therefore self-attenuation effect dominants, which results in lower patient organ dose. Figure 9.35 shows the tube current as a function of table position for patient 1 (with a perimeter of 140cm), which is one of these two large patients. It shows that the tube current was maxed out at the peak of xy modulation through almost the entire scan. There is essentially no z modulation and hence no

increase of average tube current around the abdomen region, which is the reason that radiation dose to liver does not increase as patient size increases. In contrast, Figure 9.36 shows the tube current scheme for patient 7 (with the perimeter of 97cm), which shows that the tube current is not maxed out.

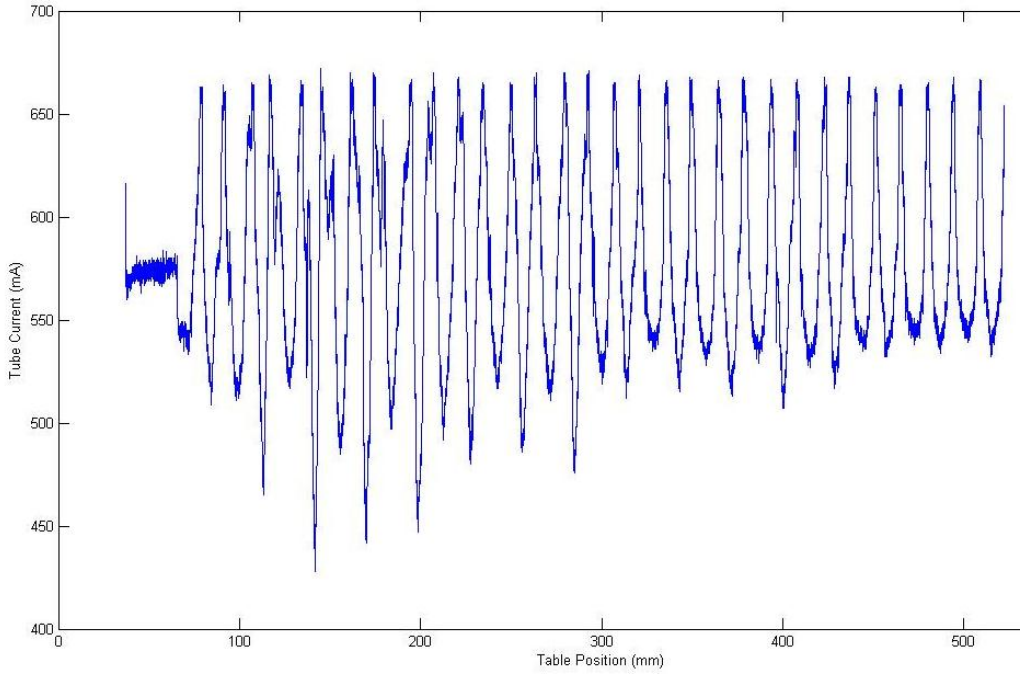


**Figure 9.36 TCM scheme for a very large patient (patient 1). The tube current is maxed out at the peak of xy modulation throughout the whole scan.**

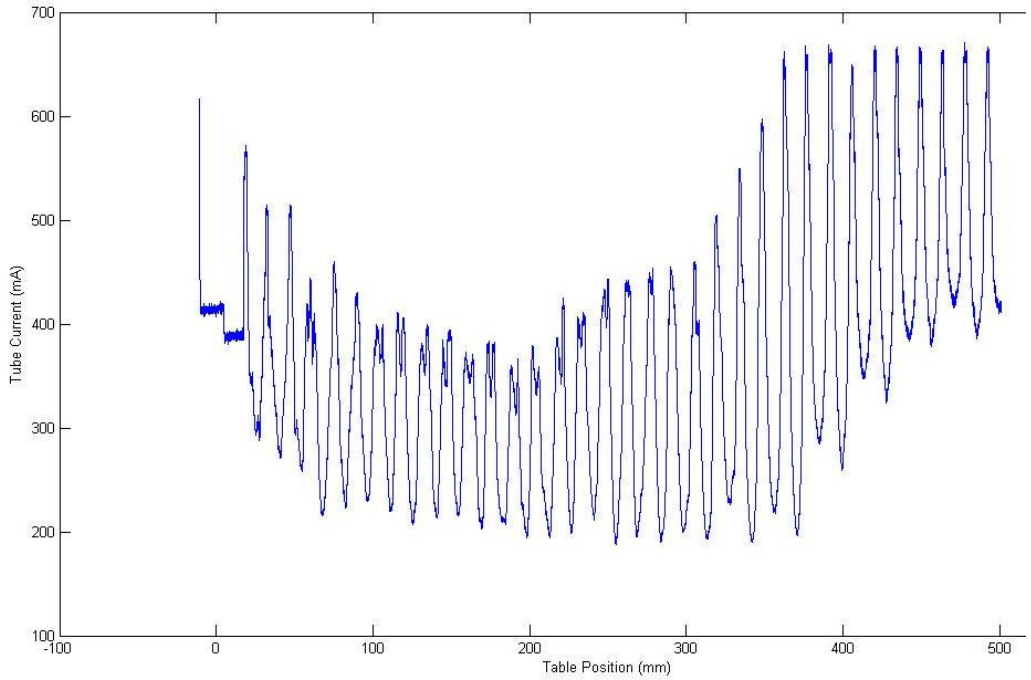


**Figure 9.37 TCM scheme for a regular size patient (patient 7). There is no tube max out for this patient case.**

Therefore, to conclude the behavior of organ dose as a function of the patient size, as the patient size increases, the organ dose also increases since the increase of mAs outweighs the self-attenuation, shown in the trend line in Figure 9.37. However, when the patient size increases to a certain point, the mAs cannot be increased further due to the tube limit. Therefore from that 'threshold' size up, the self-attenuation effect dominates again and organ dose should decrease accordingly. Unfortunately this threshold size cannot be directly observed from Figure 28 because the distribution the sample of patient size is not continuous. However, it can be seen that the organ dose is decreased for the two extra-large patients. Figure 9.37 overlays a curve of SSDE values on top of Figure 9.28 for fixed current scans. When the tube current is maxed out, the organ dose behavior as a function of patient size should be similar to that under fixed current

scans. Therefore, the data points should line up with this curve after the threshold patient size is reached. From this plot it appears the threshold perimeter is approximately 110cm.

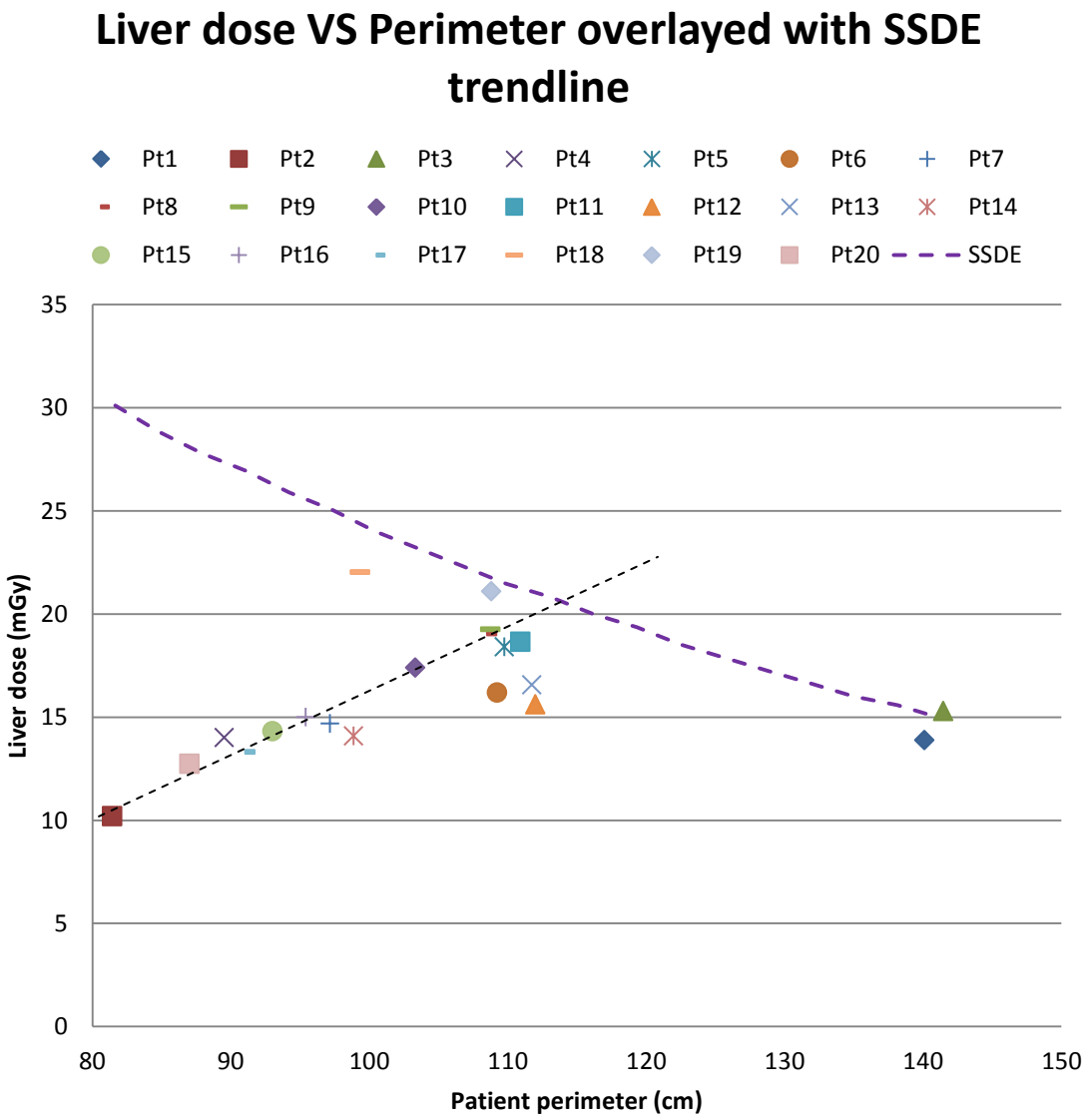


**Figure 9.38 Liver dose and SSDE as a function of patient perimeter for all of the 20 patients at the 100% dose level.**

If all the scan parameters are kept the same, the noise in the image increases with patient size in an exponential fashion. A main goal of TCM is to take into account the difference in attenuation for patient with different sizes by controlling the mA automatically (Automatic Exposure Control). Therefore, mA is usually higher for larger patients. Each manufacturer has its own strategy to control the mA as a function of patient size. For example, GE and Toshiba use Noise Index (NI) and Standard Deviation (SD) as image quality metric to guide the change of mA so that these metrics have the similar value across patients with different sizes[168]. NI and SD are both image noise based metrics. Therefore, these two manufacturers believe the image noise should be kept consistent in order for diagnosis to be on the same level. Siemens however uses another approach by increasing mA slower relative to the increase of image noise as the patient size increase, so that the images of larger patients have relatively higher noise. This is based on the empirical observation that larger patients have more fatty tissue, which makes the low contrast tasks easier. Therefore they can tolerate higher noise. Figure 9.27 exactly shows this mechanism: as the patient size increases, the image noise slightly increases as well. For example, as the patient perimeter increased from 80cm to 110cm, the liver noise gradually approximately increased from 10 to 15. Similarly to the dose plot (Figure 9.28), there are several outlier data points in Figure 9.27 because of tube reaching maximum mA for excessively large patients. As a result, these large size patients (Patient 1 and Patient3) had very high noise (higher than 20).

Since both organ dose and image noise are nearly linearly related to patient size when TCM is on, organ dose and image noise shall also have a nearly linear relationship as the patient

size changes; this was shown in Figure 9.26. Again, there were a few outliers due to the tube current maximum limitation.

As the dose changes, Figure 9.25 showed that the relationships between image noise and organ dose have different behavior for patient with different sizes. For the largest patients such as patient 1 and patient3, the noise-dose curves sit on the top of all the curves. For patients that are fairly large such as patient 6 and patient 13, the curves sit in the middle. And or smallest patients such as patient 2 and patient4, the curves sit at the bottom. Therefore it can be concluded that even when TCM is on, for patient with larger size, more organ dose is needed in order to achieve the same image noise level.

### 9.4.6. Summary and Future Work

This study investigated the tradeoff between diagnostic performance and radiation dose in the CT imaging for ruling out appendicitis. An observer study was designed rigorously in order to minimize bias through the careful selection of the cases, the randomization of the cases for each session, the detailed questions to force observers to perform an actual diagnosis, and so on. Radiation dose to individual organs was accurately estimated to yield a more meaningful picture from a dose perspective. In addition, the interrelationship between image noise, organ dose and patient size under CT scans with tube current modulation was explored.

The results showed that for all the observers, the diagnostic performance is very similar at original, 70% and 50% dose levels. At the dose levels of 30% and 20%, the diagnostic performance behaved different from expectations. For example, it decreased at 30% dose level,

but increased again at 20%. After excluding 2 observers who do not read cross-sectional images on a routine basis, as the dose level goes down, the performance starts to degrade at 30% dose level: the AUC value is lower than the three highest dose levels (100%, 70%, 50%). And the AUC value decreased again from 30% to 20% dose level. Therefore, the results of this study suggest that for this limited sample of patients using this scan protocol, reducing the radiation dose by 50% does not impair the diagnostic performance significantly for all the observers. When the radiation dose is reduced to as low as 30% and 20% of the original scan, one must take comprehensive considerations to balance the tradeoff between the benefits from lower dose and the loss of diagnostic performance in order to achieve maximum benefit to risk ratio. For abdominal trained routine CT readers, the results suggested that the diagnostic performance at 20% dose level is not very different than that at 100%.

This study also for the first time demonstrated that the diagnostic performance is nearly perfect for routine CT readers as long as the radiation dose delivered to liver is higher than 10mGy (including the 13.4-22mGy and 9.6-13.4mGy ranges) in the diagnosis of appendicitis using CT. This is an essential improvement of the current knowledge between diagnostic performance and radiation dose since it directly linked the performance with organ dose, which is a truly meaningful metric to quantify absorbed dose, and even risk to individual patients. As the liver dose goes below 10mGy to the range of 6 to 10mGy, the performance started to degrade slightly. As it continues to decrease to be in the range of 2 to 6mGy (including the 4-6.3mGy range and the 2-4mGy range), there is some considerable loss of diagnostic performance. For

abdominal trained routine CT readers however, the diagnostic performance is good even at the range of 2-4mGy of liver dose.

The diagnostic performance has a weaker correlation with image noise. This indicates that image noise is not the only factor that determines the clinical decision. Other factors such as the amount of fatty tissue also play important roles. When image noise is higher than 21 (including 21.3-25.9 range and 25.95-54.8 range), the diagnostic performance degraded for the 4 routine CT readers.

In summary, the results from this pilot study suggested a lot of opportunities to reduce radiation dose to the patients in today's clinical practice. At least 50% percent dose reduction could potentially achieved by just lowering the mA of the CT scans. This represents the dose reduction achievable from techniques that reduce image quality but maintaining diagnostic outcome. Although this study focuses on the reduction of liver dose in abdominal-pelvis scans, it demonstrates the feasibility to achieve large organ dose reduction in other CT scans types, such as the reduction of eye lens dose in head scans, the reduction of thyroid dose in neck scans, the reduction of breast dose in chest scans, and the reduction of gonads in pelvis scans.

There are several limitations of this study. First, the patient sample size is small. Although tremendous efforts have been put on the selection of the cases to incorporate a wide variation of the phases of the disease and the body habitus of the patients, 20 patients may not represent the clinical image of appendicitis for a much larger population. This is also the reason that this study is served as a pilot study to provide some initial evidence to carry out another full

study on a larger scale of patient cases. Due to the small sample size of the study, the standard errors estimated for all the AUC values are relatively large. Therefore the conclusions in this study are based the trends of the data. But many of them are not statistically significant. Second, the criteria to select the observers may need to be improved. Although in this study we tried to include observers with various years of experience, either currently or in the past, it appeared that there was a large gap of performance between observers who are routinely reading cross-sectional images and observers who are not. It should be a more accurate representation of clinical reality to include only the observers who read cross-sectional images on a routine basis. This issue shall be addressed in the future full study. Third, almost all the observers complained that the viewing platform did not have the function to link coronal view images with axial view images (e.g., once the user click a location on an axial view image, the coronal view images would automatically change to the corresponding slice and location.). They had to manually scroll between slices in both axial and coronal views. It is unclear that how much the lack of this functionality would affect the performance of the observers. But it should definitely be implemented in the future full study.

Future work should include a full study with a much larger sample of patient cases with a more appropriate selection of observers and a better implementation of the viewing platform. For a study with larger sample size, multi-reader, multi-case (MRMC) methodology should be used to account for the components of variation, including within-reader variation (variation of the results based on the same cases and the same readers), reader-sample variation (variation of the results based on the same cases but different readers), and case-sample variation (variation of the

results based on different cases but the same readers)[169]. Also, some data collected in the observer study could be further analyzed. For example, efforts could be made to investigate if the decrease of radiation dose associates with more reading time, and to investigate the correlation between the final diagnosis and each specific finding. In addition, in order to further explore the correlation between diagnostic performance and absolute organ dose, the amount of simulated dose can be adjusted based on the patient's organ dose for the original scan, so that all the patient cases would receive the same amount of organ dose in each organ dose group. For example, for patient 1 and patient 2 with different sizes, their organ doses are different when the same Quality Reference mA was used. By adding different amount of noise into the raw data files for these two patients, it can be achieved that two image sets for these two patients both have 15mGy. From that point, further noise insertion processes could be performed to generate image sets that have 10mGy, 5mGy, 2mGy, and so on. Using this method, there would not be repeating cases in each dose category, so that potential bias could be avoided.

Furthermore, since in this study only the simple noise metric was investigated as an image quality indicator, task-based image quality metrics using mathematical model observers could be explored (80, 81). These model observers have been applied to many other imaging modalities to improve the efficiency of system optimization (82), including nuclear medicine imaging (83-85), mammography (86-89), x-ray dual-energy imaging (90), tomosynthesis and flat-panel cone-beam CT (91-93), and MRI (94). However, relatively few studies have been done in clinical CT (95, 96). Once a set of task-based image quality metrics is determined, they can be

used clinically to efficiently and accurately optimize scanning protocols and radiation dose levels in CT, without the conduct of expensive observer studies.

## Chapter 10 Dissertation Summary and Conclusions

The purpose of the work presented in this dissertation was: 1). to extend the current knowledge of CT dosimetry by introducing detailed dose estimations such as surface dose and peak dose in order to accommodate the emerging needs including dose estimations for deterministic effects; 2). to exploit this detailed dose knowledge to reduce radiation dose for patients without compromising image quality. This include reducing dose to eye lens by varying scan location and gantry angle, as well as reducing dose to specific organs by adjusting tube start angle and table height; 3). to evaluate the technique to reduce radiation dose and image quality while maintaining performance of a diagnostic task by investigating the tradeoff between organ dose and diagnostic outcome. In this dissertation, Monte Carlo simulations were intensively used to obtain detailed and accurate dose quantities to provide thorough perspectives for radiation dose from CT exams.

Chapter 3 introduced the principle of Monte Carlo simulations and the details of the mechanism of UCLA CT Dose Estimation Package. The implementation of the CT source, the scan, as well as the geometry for radiation transport was described. This comprehensive package included multiple scan modes which allow all of today's existing clinical CT exam protocols to be simulated; including intricate details in the acquisition process such as tube start angle and table height. Shown in 8.5, the high accuracy of the simulation results of the package was demonstrated using advanced benchmark strategies within a complex radiation environment.

Radiation dose from CT perfusion exams raised a nationwide public concern, which in turn led many practices to examine the radiation dose for their perfusion scans, using $CTDI_{vol}$ as the dose metric they examined. However, $CTDI_{vol}$ has fundamental limitations in the estimation of peak dose. As an answer, Chapter 4 and Chapter 5 represent the first work to investigate the peak skin dose and eye lens dose delivered to patients in brain perfusion exams using Monte Carlo methods. Look up tables were generated for the estimation of peak doses for any protocol on selected CT scanners. Eye lens dose reduction techniques such as adjusting scan location and tilting the gantry angle were evaluated. In addition, various dose metrics were compared with Monte Carlo results and it was concluded that the TG111 dose metric provides closest estimation to peak skin dose and eye lens dose compared to $CTDI_{vol}$ and IMPACT tool.

The study presented in Chapter 6 was conducted in order to investigate the radiation dose variation on the surfaces of both phantoms and patients in CT scans. This work revealed the complex behavior of surface dose variation as a function of nominal collimation, actual beam width, tube start angle, and the pitch value used in the scan. Since the tube start angle is mostly random in today's helical CT scans, this behavior could cause significant uncertainties in measurements on surface using small dosimeters. In order to overcome these uncertainties, various solutions were proposed and evaluated. It was demonstrated that the FSPP method was a robust approach to minimize surface dose uncertainties.

In the light of the novelty to shift surface dose profile by adjusting the tube start angle, as demonstrated in Chapter 6, the work in Chapter 7 investigated the potential to make use of this

finding to reduce radiation dose to small peripheral organs. Chapter 8 extended this idea to reduce patient dose by combining the adjustment of the tube start angle and the table height. Various experiments were conducted to evaluate the effectiveness of this method including measurements and simulations on both phantoms and patient models under both fixed tube current mode and TCM mode. It was concluded that depending on the patient size, the organ of interest, and the scan protocol, dose reduction up to 60%-70% percent could be achieved without compromising image quality. This proposed a novel method to reduce radiation dose in CT scan while maintaining image quality.

The pilot study presented in Chapter 9 redefined the goal in CT imaging from "maintaining image quality" to be "maintaining performance of a diagnostic task" by investigating dose reductions that reduce image quality, but maintain diagnostic performance for appendicitis. Although this was a feasibility study with small sample sizes, it was illustrated that the diagnostic performance does not have noticeable change at 70% and 50% dose levels. This study also for the first time demonstrated that the performance in the diagnosis of appendicitis using CT is nearly perfect for routine CT readers as long as the radiation dose delivered to liver is higher than 10mGy. This finding for the first time established a relationship between diagnostic performance and organ dose, which facilitates a more comprehensive understanding between benefits and risks in CT imaging.

In conclusion, the culmination of the work presented in this dissertation demonstrated the feasibility and potential to achieve significant dose reduction in CT exams. There is plenty of

room to reduce radiation dose, while reducing image quality but maintaining diagnostic performance. For example, Chapter 9 suggested that radiation dose from CT could be reduced by 50% to 80% simply by decreasing tube current using current technology. Combined with other dose reduction techniques that maintain image quality, such as adjusting tube start angle and table height introduced in Chapter 7 and Chapter 8, the dose reduction could be in the range of 20% to 10% of today's practice. The demonstration of this feasibility in dose reduction is the largest contribution of this dissertation.

Besides the scope of this dissertation, there are many emerging dose reduction technologies, which intend to reduce CT radiation dose while maintaining image quality, such as organ-based tube current modulation[170], dynamic collimation[171], as well as iterative reconstruction technologies. Iterative reconstruction technologies are being investigated and commercialized by all CT vendors and the initial results were very promising. The algorithms correct for low signals in both raw data space and image space by taking the scanner's specific characteristics into account. By using iterative reconstruction techniques, either the image quality could be improved significantly, or radiation dose could be reduced by additional 60% to 80% while maintaining image quality. Figure 10.1 shows two images with and without an iterative reconstruction algorithm called AIDR3D from one of the major CT vendors. Compared to Figure 10.1a, superior image quality could be observed from Figure 10.1b where AIDR3D was used. This translates to a large dose reduction if image quality is maintained. Therefore, with all the technologies, either included in this dissertation or beyond the scope of this dissertation, there is

significant potential to reduce radiation dose in CT by an order of magnitude while preserving excellent diagnostic performance we have to come to expect through the use of CT imaging.

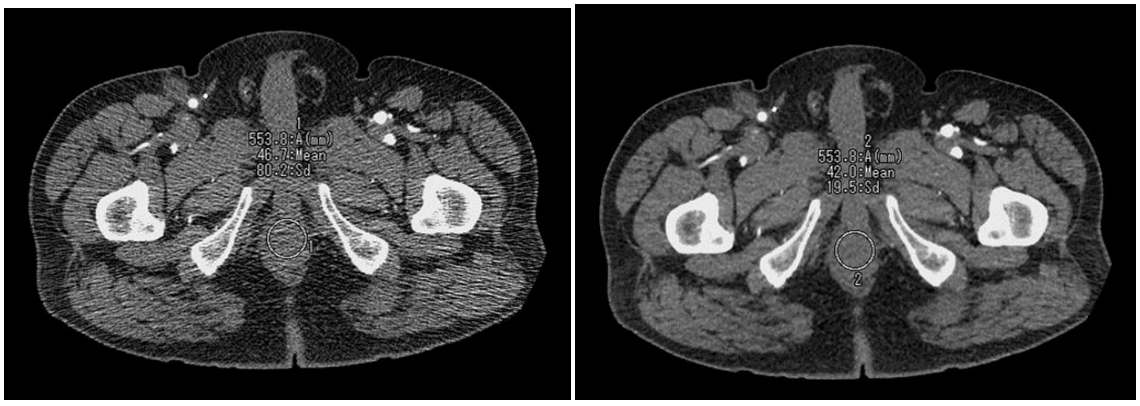


(a) (b)

**Figure 10.1 a) An example image without the use of AIDR3D, an iterative reconstruction algorithm; b) The same example image with the use of AIDR3D, where the image noise is significantly reduced.**

## Reference


1. AAPM. The Measurement, Reporting, and Managementof Radiation Dose in CT. *AAPM report 96* (2008).
2. BEIRVII. Health Risks from Exposure to Low Levels of Ionizing Radiation: BEIR VII. (2006).
3. Brenner, D.J. & Elliston, C.D. Estimated Radiation Risks Potentially Associated with Full-Body CT Screening. *Radiology* **232**, 735-738 (2004).
4. Hall, E.J. & Brenner, D.J. Cancer risks from diagnostic radiology. *Br J Radiol* **81**, 362-378 (2008).
5. Mettler, F.A., Jr., *et al.* Medical Radiation Exposure in the U.S. in 2006: Preliminary Results. *Health Physics* **95**, 502-507 510.1097/1001.HP.0000326333.0000342287.a0000326332 (2008).
6. NCRP. Ionizing Radiation Exposure of the Population of the United States. in *Report No. 160* (2009).
7. California Health and Human Services Agency, 2567 Mad River Community Hospital. (22 Jan. 2009).
8. http://www.nytimes.com/imagepages/2009/10/16/us/16radiationCA01ready.html.
9. ICRP. Recommendations of the International Commission on Radiological Protection. in *ICRP Publication 60*, Vol. 21 1-32 (1991).
10. ICRP. Relative biological effectiveness (RBE), quality factor (Q), and radiaiton weighting factor (w(R)). A report of the International Commission on Radiological Protection. in *Ann ICRP*, Vol. 33 1-117 (2003).
11. ICRP. Recommendations of the International Commission on Radiological Protection. in *ICRP publication 103*, Vol. 37 1-332 (2007).

12. Berrington de Gonzalez, A., *et al.* Projected cancer risks from computed tomographic scans performed in the United States in 2007. *Arch Intern Med* **169**, 2071-2077 (2009).

13. O'Connor, M.K. BEIR VII: what it does and doesn't say. in *AAPM* (Vancouver, 2011).

14. www.imagegently.org. (Image Gently).

15. http://imagewisely.org/. (Image Wisely).

16. FDA. White Paper: Initiative to Reduce Unnecessary Radiation Exposure from Medical Imaging. (2010).

17. Joint Commission, Sentinel Event Alert. in *http://www.jointcommission.org/assets/1/18/sea_471.pdf* (2011).

18. State of California. Senate Bill 1237. (2010).

19. McCollough, C.H., *et al.* Strategies for reducing radiation dose in CT. *Radiol Clin North Am* **47**, 27-40 (2009).

20. McNitt-Gray, M.F. AAPM/RSNA Physics Tutorial for Residents: Topics in CT. Radiation dose in CT. *Radiographics* **22**, 1541-1553 (2002).

21. McCollough, C.H. CT dose: how to measure, how to reduce. *Health Phys* **95**, 508-517 (2008).

22. Brenner, D.J. Is it time to retire the CTDI for CT quality assurance and dose optimization? *Med Phys* **32**, 3225-3226 (2005).

23. Dixon, R.L. & Ballard, A.C. Experimental validation of a versatile system of CT dosimetry using a conventional ion chamber: beyond CTDI100. *Med Phys* **34**, 3399-3413 (2007).

24. Dixon, R.L., Munley, M.T. & Bayram, E. An improved analytical model for CT dose simulation with a new look at the theory of CT dose. *Med Phys* **32**, 3712-3728 (2005).

25. Dixon, R.L. A new look at CT dose measurement: beyond CTDI. *Med Phys* **30**, 1272-1280 (2003).

26. McCollough, C.H., *et al.* CT dose index and patient dose: they are not the same thing. *Radiology* **259**, 311-316.

27. Cody, D.D., *et al.* Strategies for formulating appropriate MDCT techniques when imaging the chest, abdomen, and pelvis in pediatric patients. *AJR Am J Roentgenol* **182**, 849-859 (2004).

28. Einstein, A.J., Henzlova, M.J. & Rajagopalan, S. Estimating risk of cancer associated with radiation exposure from 64-slice computed tomography coronary angiography. *JAMA* **298**, 317-323 (2007).

29. Hurwitz, L.M., *et al.* Radiation dose from contemporary cardiothoracic multidetector CT protocols with an anthropomorphic female phantom: implications for cancer induction. *Radiology* **245**, 742-750 (2007).

30. Hurwitz, L.M., *et al.* Radiation dose to the fetus from body MDCT during early gestation. *AJR Am J Roentgenol* **186**, 871-876 (2006).

31. Hurwitz, L.M., *et al.* Effective dose determination using an anthropomorphic phantom and metal oxide semiconductor field effect transistor technology for clinical adult body multidetector array computed tomography protocols. *J Comput Assist Tomogr* **31**, 544-549 (2007).

32. Hurwitz, L.M., *et al.* Radiation dose to the female breast from 16-MDCT body protocols. *AJR Am J Roentgenol* **186**, 1718-1722 (2006).

33. Price, R., Halson, P. & Sampson, M. Dose reduction during CT scanning in an anthropomorphic phantom by the use of a male gonad shield. *Br J Radiol* **72**, 489-494 (1999).

34. Thomton, F.J., Paulson, E.K., Yoshizumi, T.T., Frush, D.P. & Nelson, R.C. Single versus multi-detector row CT: comparison of radiation doses and dose profiles. *Acad Radiol* **10**, 379-385 (2003).

35. Duggan, L., Hood, C., Warren-Forward, H., Haque, M. & Kron, T. Variations in dose response with x-ray energy of LiF:Mg,Cu,P thermoluminescence dosimeters: implications for clinical dosimetry. *Phys Med Biol* **49**, 3831-3845 (2004).

36. Turner, A., *et al.* The Energy Dependence of Small Volume Ionization Chambers and Solid State Detectors at Diagnostic Energy Ranges for CT Dosimetry - Assessment in Air and in Phantom. in *American Association of Physics in Medicine annual meeting* (2011).

37. Zhang, D., *et al.* Change in X-Ray CT Spectra Inside of Dosimetry Phantoms: Beam Hardening Or Beam Softening? in *American Association of Physics in Medicine annual meeting* (2011).

38. Boone, J.M. Dose spread functions in computed tomography: a Monte Carlo study. *Med Phys* **36**, 4547-4554 (2009).

39. Deak, P., van Straten, M., Shrimpton, P.C., Zankl, M. & Kalender, W.A. Validation of a Monte Carlo tool for patient-specific dose simulations in multi-slice computed tomography. *Eur Radiol* **18**, 759-772 (2008).

40. Gu, J., Bednarz, B., Caracappa, P.F. & Xu, X.G. The development, validation and application of a multi-detector CT (MDCT) scanner model for assessing organ doses to the pregnant patient and the fetus using Monte Carlo simulations. *Phys Med Biol* **54**, 2699-2717 (2009).

41. Jarry, G., DeMarco, J.J., Beifuss, U., Cagnon, C.H. & McNitt-Gray, M.F. A Monte Carlo-based method to estimate radiation dose from spiral CT: from phantom testing to patient-specific models. *Physics in Medicine and Biology*, 2645 (2003).

42. Lee, C., *et al.* Organ and effective doses in pediatric patients undergoing helical multislice computed tomography examination. *Med Phys* **34**, 1858-1873 (2007).

43. Li, X., *et al.* Patient-specific radiation dose and cancer risk estimation in CT: part I. development and validation of a Monte Carlo program. *Med Phys* **38**, 397-407.

44. Perisinakis, K., Tzedakis, A. & Damilakis, J. On the use of Monte Carlo-derived dosimetric data in the estimation of patient dose from CT examinations. *Med Phys* **35**, 2018-2028 (2008).

45. Imaging Performance Assessment of CT Scanners Group, "ImPACT CT patient dosimetry calculator," 2006, available at http://www.impactscan.org.

46. Kubo, T., *et al.* Radiation dose reduction in chest CT: a review. *AJR Am J Roentgenol* **190**, 335-343 (2008).

47. Kalender, W.A., *et al.* Dose reduction in CT by on-line tube current control: principles and validation on phantoms and cadavers. *Eur Radiol* **9**, 323-328 (1999).

48. Angel, E., *et al.* Dose to radiosensitive organs during routine chest CT: effects of tube current modulation. *AJR Am J Roentgenol* **193**, 1340-1345 (2009).

49. Straten, M.v., Deak, P., Shrimpton, P. & Kalender, W.A. The effect of angular and longitudinal tube current modulations on the estimation of organ and effective doses in x-ray computed tomography. *Medical Physics* **36**, 4881-4889 (2009).

50. Angel, E., *et al.* Monte Carlo simulations to assess the effects of tube current modulation on breast dose for multidetector CT. *Physics in Medicine and Biology*, 497 (2009).

51. Wessling, J., *et al.* The effect of dose reduction and feasibility of edge-preserving noise reduction on the detection of liver lesions using MSCT. *Eur Radiol* **17**, 1885-1891 (2007).

52. Kalra, M.K., *et al.* Chest CT performed with z-axis modulation: scanning protocol and radiation dose. *Radiology* **237**, 303-308 (2005).

53. Kubo, T., *et al.* 3-dimensional adaptive raw-data filter: evaluation in low dose chest multidetector-row computed tomography. *J Comput Assist Tomogr* **30**, 933-938 (2006).

54. Lee, E., *et al.* Radiation dose reduction and image enhancement in biological imaging through equally-sloped tomography. *J Struct Biol* (2008).

55. Chen, G.H., Tang, J. & Leng, S. Prior image constrained compressed sensing (PICCS): a method to accurately reconstruct dynamic CT images from highly undersampled projection data sets. *Med Phys* **35**, 660-663 (2008).

56. Funama, Y., *et al.* Radiation dose reduction without degradation of low-contrast detectability at abdominal multisection CT with a low-tube voltage technique: phantom study. *Radiology* **237**, 905-910 (2005).

57. Kalender, W.A., Deak, P., Kellermeier, M., van Straten, M. & Vollmar, S.V. Application- and patient size-dependent optimization of x-ray spectra for CT. *Med Phys* **36**, 993-1007 (2009).

58. Primak, A.N., Ramirez Giraldo, J.C., Liu, X., Yu, L. & McCollough, C.H. Improved dual-energy material discrimination for dual-source CT by means of additional spectral filtration. *Med Phys* **36**, 1359-1369 (2009).

59. Schindera, S.T., *et al.* Hypervascular liver tumors: low tube voltage, high tube current multi-detector row CT for enhanced detection--phantom study. *Radiology* **246**, 125-132 (2008).

60. Siegel, M.J., Schmidt, B., Bradley, D., Suess, C. & Hildebolt, C. Radiation dose and image quality in pediatric CT: effect of technical factors and phantom size and shape. *Radiology* **233**, 515-522 (2004).

61. Yu, L., Li, H., Fletcher, J.G. & McCollough, C.H. Automatic selection of tube potential for radiation dose reduction in CT: a general strategy. *Med Phys* **37**, 234-243.

62. Khatonabadi, M., *et al.* Organ Dose-based Adjustment of mAs When Using Lower kVp for Adult and Pediatric Chest CT. in *Radiological Society of North America annual meeting* (2011).

63. Kalra, M.K., *et al.* Strategies for CT radiation dose optimization. *Radiology* **230**, 619-628 (2004).

64. Sohaib, S.A., *et al.* The effect of decreasing mAs on image quality and patient dose in sinus CT. *Br J Radiol* **74**, 157-161 (2001).

65. Udayasankar, U.K., *et al.* Low-dose nonenhanced head CT protocol for follow-up evaluation of children with ventriculoperitoneal shunt: reduction of radiation and effect on image quality. *AJNR Am J Neuroradiol* **29**, 802-806 (2008).

66. Rizzi, E.B., Schinina, V., Gentile, F.P. & Bibbolino, C. Reduced computed tomography radiation dose in HIV-related pneumonia: effect on diagnostic image quality. *Clin Imaging* **31**, 178-184 (2007).

67. Shah, R., Gupta, A.K., Rehani, M.M., Pandey, A.K. & Mukhopadhyay, S. Effect of reduction in tube current on reader confidence in paediatric computed tomography. *Clin Radiol* **60**, 224-231 (2005).

68. Kalra, M.K., *et al.* Clinical comparison of standard-dose and 50% reduced-dose abdominal CT: effect on image quality. *AJR Am J Roentgenol* **179**, 1101-1106 (2002).

69. Prasad, S.R., Wittram, C., Shepard, J.A., McLoud, T. & Rhea, J. Standard-dose and 50%-reduced-dose chest CT: comparing the effect on image quality. *AJR Am J Roentgenol* **179**, 461-465 (2002).

70. MacKenzie, J.D., *et al.* Reduced-dose CT: effect on reader evaluation in detection of pulmonary embolism. *AJR Am J Roentgenol* **189**, 1371-1379 (2007).

71. Mayo, J.R., *et al.* Reduced radiation dose helical chest CT: effect on reader evaluation of structures and lung findings. *Radiology* **232**, 749-756 (2004).

72. McCollough, C.H., Guimaraes, L. & Fletcher, J.G. In defense of body CT. *AJR Am J Roentgenol* **193**, 28-39 (2009).

73. Waters, L.S. MCNPX User's Manual, Version 2.4.0. *Los Alamos National Laboratory report* LA-CP-02-408 (2002).

74. Waters, L.S. MCNPX Version 2.5.C. *Los Alamos National Laboratory report* LA-UR-03-2202 (2003).

75. Turner, A.C., *et al.* A method to generate equivalent energy spectra and filtration models based on measurement for multidetector CT Monte Carlo dosimetry simulations. *Medical Physics* **36**, 2154-2164 (2009).

76. ICRU. Tissue Substitutes in Radiation Dosimetry and Measurement. *ICRU Report No. 44* (1989).

77. Attix, F.H. *Introduction to Radiological Physics and Radiation Dosimetry*, (Viley - VCH, 2004).

78. Wintermark, M. Brain perfusion-CT in acute stroke patients. *European Radiology Supplements* **15**, d28-d31 (2005).

79. Miles, K.A. Perfusion imaging with computed tomography: brain and beyond. *Eur Radiol* **16 Suppl 7**, M37-43 (2006).

80. Miles, K., Eastwood, J.D. & König, M. *Multidetector computed tomography in cerebrovascular disease : CT perfusion imaging*, (Informa Healthcare, Abinfdon, Oxon, 2007).

81. Chodick, G., *et al.* Risk of cataract after exposure to low doses of ionizing radiation: a 20-year prospective cohort study among US radiologic technologists. *Am J Epidemiol* **168**, 620-631 (2008).

82. Minamoto, A., *et al.* Cataract in atomic bomb survivors. *Int J Radiat Biol* **80**, 339-345 (2004).

83. Nakashima, E., Neriishi, K. & Minamoto, A. A reanalysis of atomic-bomb cataract data, 2000-2002: a threshold analysis. *Health Phys* **90**, 154-160 (2006).

84. Neriishi, K., *et al.* Postoperative cataract cases among atomic bomb survivors: radiation dose response and threshold. *Radiat Res* **168**, 404-408 (2007).

85. DeMarco, J.J., *et al.* A Monte Carlo based method to estimate radiation dose from multidetector CT (MDCT): cylindrical and anthropomorphic phantoms. *Physics in Medicine and Biology*, 3989 (2005).

86. Petoussi-Henss, N., Zankl, M., Fill, U. & Regulla, D. The GSF family of voxel phantoms. *Physics in Medicine and Biology*, 89 (2002).

87. AAPM. http://www.aapm.org/pubs/CTProtocols/documents/AdultBrainPerfusionCT_2011-01-11.pdf. (2010).

88. Shuren, J. http://www.fda.gov/Radiation-EmittingProducts/RadiationSafety/RadiationDoseReduction/ucm232551.htm. (2010).

89. McCollough, C.H., S.Leng & et.al. CT Dose index(CTDI) and patient dose: they are not the same thing. *Radiology* **259**, 311-316 (2011).

90. ICRP. Recommendations of the International Commission on Radiological Protection. *ICRP publication 60* (1991).

91. ICRP. Avoidance of radiation injuries from medical interventional procedures. *ICRP Publication 85* **30**, 21 (2000).

92. Worgul, B.V., *et al.* Cataracts among Chernobyl clean-up workers: implications regarding permissible eye exposures. *Radiat Res* **167**, 233-243 (2007).

93. Medical electrical equipment - Part 2-44: Particular requirements for the basic safety and essential performance of X-ray equipment for computed tomography. IEC 60601-2-44 3rd edition. (2009).

94. DeMarco, J.J., *et al.* Estimating radiation doses from multidetector CT using Monte Carlo simulations: effects of different size voxelized patient models on magnitudes of organ and effective dose. *Physics in Medicine and Biology*, 2583 (2007).

95. Lee, C., *et al.* Organ and effective doses in pediatric patients undergoing helical multislice computed tomography examination. *Medical Physics* **34**, 1858-1873 (2007).

96. Bauhs, J.A., Vrieze, T.J., Primak, A.N., Bruesewitz, M.R. & McCollough, C.H. CT dosimetry: comparison of measurement techniques and devices. *Radiographics* **28**, 245-253 (2008).

97. AAPM. Comprehensive Methodology for the Evaluation of Radiation Dose in X-Ray Computed Tomography. *AAPM report NO. 111* (2010).

98. DeMarco, J.J., Solberg, T.D. & Smathers, J.B. A CT-based Monte Carlo simulation tool for dosimetry planning and analysis. *Medical Physics* **25**, 1-11 (1998).

99. Zankl, M., Fill, U., Petoussi-Henss, N. & Regulla, D. Organ dose conversion coefficients for external photon irradiation of male and female voxel models. *Physics in Medicine and Biology*, 2367 (2002).

100. Angel, E., *et al.* Radiation Dose to the Fetus for Pregnant Patients Undergoing Multidetector CT Imaging: Monte Carlo Simulations Estimating Fetal Dose for a Range of Gestational Age and Patient Size. *Radiology* **249**, 220-227 (2008).

101. Perisinakis, K., Tzedakis, A. & Damilakis, J. On the use of Monte Carlo-derived dosimetric data in the estimation of patient dose from CT examinations. *Medical Physics* **35**, 2018-2028 (2008).

102. Turner, A.C., *et al.* The feasibility of a scanner-independent technique to estimate organ dose from MDCT scans: using CTDIvol to account for differences between scanners. *Med Phys* **37**, 1816-1825.

103. Turner, A.C., *et al.* The feasibility of a scanner-independent technique to estimate organ dose from MDCT scans: using CTDIvol to account for differences between scanners. *Med Phys* **37**, 1816-1825 (2010).

104. McNitt-Gray, M.F. AAPM/RSNA Physics Tutorial for Residents: Topics in CT: Radiation Dose in CT. *Radiographics* **22**, 1541-1553 (2002).

105. Shope, T., Gagne, R. & Johnson, G. A method for describing the doses delivered by transmission x-ray computed tomography. *Medical Physics* **8**, 488-495 (1981).

106. *Department of Health and Human Services, Food and Drug Administration. 21 CFR Part 1020: Diagnostic x-ray systems and their major components; amendments to performance standard--FDA. Final rule.*, (1984).

107. IEC 60601-2-44. Medical electrical equipment - Part 2-44: Particular requirements for the safety of X-ray equipment for computed tomography. (2002).

108. American Association of Physicists in Medicine. The Measurement, Reporting, and Managementof Radiation Dose in CT. Report NO. 96. (2008).

109. Menzel, H., Schibilla, H. & D, T. (eds.). *European guidelines on quality criteria for computed tomography* (European Commission, Luxembourg, 2000).

110. Dixon, R.L. A new look at CT dose measurement: Beyond CTDI. *Medical Physics* **30**, 1272-1280 (2003).

111. Hurwitz, L.M., *et al.* Radiation Dose to the Female Breast from 16-MDCT Body Protocols. *Am. J. Roentgenol.* **186**, 1718-1722 (2006).

112. Hurwitz, L.M., *et al.* Radiation Dose to the Fetus from Body MDCT During Early Gestation. *Am. J. Roentgenol.* **186**, 871-876 (2006).

113. Jaffe, T.A., *et al.* Early First-Trimester Fetal Radiation Dose Estimation in 16-MDCT Without and With Automated Tube Current Modulation. *Am. J. Roentgenol.* **190**, 860-864 (2008).

114. Deak, P., Straten, M.v., Shrimpton, P.C., Zankl, M. & Kalender1, W.A. Validation of a Monte Carlo tool for patient-specific dose simulations in multi-slice computed tomography *European Radiology* **18**, 759-772 (2008).

115. DeMarco, J.J., *et al.* A Monte Carlo based method to estimate radiation dose from multidetector CT (MDCT): cylindrical and anthropomorphic phantoms. *Physics in Medicine and Biology* **50**, 3989-4004 (2005).

116. DeMarco, J.J., *et al.* Estimating surface radiation dose from Multidetector CT: Cylindrical phantoms, Anthropomorphic phantoms and Monte Carlo Simulations. in *SPIE* (MI 5745-13, 2005).

117. DeMarco, J.J., *et al.* Estimating radiation doses from multidetector CT using Monte Carlo simulations: effects of different size voxelized patient models on magnitudes of organ and effective dose. *Physics in Medicine and Biology* **52**, 2583-2597 (2007).

118. Jarry, G., DeMarco, J.J., Beifuss, U., Cagnon, C.H. & McNitt-Gray, M.F. A Monte Carlo-based method to estimate radiation dose from spiral CT: from phantom testing to patient-specific models. *Physics in Medicine and Biology* **48**, 2645-2663 (2003).

119. DeMarco, J., Solberg, T. & Smathers, J. A CT-based Monte Carlo simulation tool for dosimetry planning and analysis. *Medical Physics* **25**, 1-11 (1998).

120. http://www.cirsinc.com/products/all/33/atom-dosimetry-verification-phantoms/?details=specs.

121. Vrieze, T., Bauhs , J. & McCollough, C. Use of Spiral Scan Acquisitions for CT Dose Measurements: Selection of Optimal Pitch Values to Ensure Reproducible Results. in *Radiological Society of North America (RSNA)* 245 (Chicago, 2007).

122. Petoussi-Henss, N., Zankl, M., Fill, U. & Regulla, D. The GSF family of voxel phantoms. *Physics in Medicine and Biology* **47**, 89-106 (2002).

123. NCRP. Ionizing Radiation Exposure of the Population of the United States. *NCRP Report No. 160* (2009).

124. McCollough, C.H., Bruesewitz, M.R. & Kofler, J.M., Jr. CT Dose Reduction and Dose Management Tools: Overview of Available Options. *Radiographics* **26**, 503-512 (2006).

125. Paul, J.-F. & Abada, H. Strategies for reduction of radiation dose in cardiac multislice CT. *European Radiology* **17**, 2028-2037 (2007).

126. Udayasankar, U.K., *et al.* Low-Dose Nonenhanced Head CT Protocol for Follow-Up Evaluation of Children with Ventriculoperitoneal Shunt: Reduction of Radiation and Effect on Image Quality. *AJNR Am J Neuroradiol* **29**, 802-806 (2008).

127. Szucs-Farkas, Z., *et al.* Patient Exposure and Image Quality of Low-Dose Pulmonary Computed Tomography Angiography: Comparison of 100- and 80-kVp Protocols. *Investigative Radiology* **43**, 871-876 (2008).

128. ICRP. RECOMMENDATIONS OF THE ICRP. *ICRP publication 103* (2008).

129. Health Risks from Exposure to Low Levels of Ionizing Radiation: BEIR VII. (2006).

130. Zhang, D., *et al.* Variability of surface and center position radiation dose in MDCT: Monte Carlo simulations using CTDI and anthropomorphic phantoms. *Medical Physics* **36**, 1025-1038 (2009).

131. Dixon, R.L. & Ballard, A.C. Experimental validation of a versatile system of CT dosimetry using a conventional ion chamber: Beyond CTDI[sub 100]. *Medical Physics* **34**, 3399-3413 (2007).

132. Moore, K. & Persaud, T. *The developing human*, (Saunders, Philadelphia, 1998).

133. Matsubara, K., *et al.* Misoperation of CT automatic tube current modulation systems with inappropriate patient centering: phantom studies. *AJR Am J Roentgenol* **192**, 862-865 (2009).

134. Toth, T., Ge, Z. & Daly, M.P. The influence of patient centering on CT dose and image noise. *Med Phys* **34**, 3093-3101 (2007).

135. Alderson Lung/Chest Phantom http://www.rsdphantoms.com/rd_lung.htm In. Long Beach, CA: Radiological Support Devices

136. Petoussi-Henss, N., Zanki, M., Fill, U. & Regulla, D. The GSF family of voxel phantoms. *Phys Med Biol* **47**, 89-106 (2002).

137. Zankl, M., Eckerman, K.F. & Bolch, W.E. Voxel-based models representing the male and female ICRP reference adult--the skeleton. *Radiat Prot Dosimetry* **127**, 174-186 (2007).

138. ACR. http://www.acr.org/accreditation/computed/qc_forms/Phantom_Testing_Instruction_Final.aspx. *Accessed 4/8/2012*.

139. Mayo, J.R., *et al.* Simulated dose reduction in conventional chest CT: validation study. *Radiology* **202**, 453-457 (1997).

140. Joo, S.M., *et al.* Detection of the normal appendix with low-dose unenhanced CT: use of the sliding slab averaging technique. *Radiology* **251**, 780-787 (2009).

141. Seo, H., *et al.* Diagnosis of acute appendicitis with sliding slab ray-sum interpretation of low-dose unenhanced CT and standard-dose i.v. contrast-enhanced CT scans. *AJR Am J Roentgenol* **193**, 96-105 (2009).

142. Keyzer, C., *et al.* Acute appendicitis: comparison of low-dose and standard-dose unenhanced multi-detector row CT. *Radiology* **232**, 164-172 (2004).

143. Kim, S.Y., *et al.* Acute appendicitis in young adults: low- versus standard-radiation-dose contrast-enhanced abdominal CT for diagnosis. *Radiology* **260**, 437-445.

144. Platon, A., *et al.* Evaluation of a low-dose CT protocol with oral contrast for assessment of acute appendicitis. *Eur Radiol* **19**, 446-454 (2009).

145. Ciaschini, M.W., Remer, E.M., Baker, M.E., Lieber, M. & Herts, B.R. Urinary calculi: radiation dose reduction of 50% and 75% at CT--effect on sensitivity. *Radiology* **251**, 105-111 (2009).

146. Frush, D.P., *et al.* Computer-simulated radiation dose reduction for abdominal multidetector CT of pediatric patients. *AJR Am J Roentgenol* **179**, 1107-1113 (2002).

147. Karmazyn, B., *et al.* CT with a computer-simulated dose reduction technique for detection of pediatric nephroureterolithiasis: comparison of standard and reduced radiation doses. *AJR Am J Roentgenol* **192**, 143-149 (2009).

148. van Gelder, R.E., *et al.* CT colonography at different radiation dose levels: feasibility of dose reduction. *Radiology* **224**, 25-33 (2002).

149. Fefferman, N.R., *et al.* Appendicitis in children: low-dose CT with a phantom-based simulation technique--initial observations. *Radiology* **237**, 641-646 (2005).

150. Keyzer, C., *et al.* MDCT for suspected acute appendicitis in adults: impact of oral and IV contrast media at standard-dose and simulated low-dose techniques. *AJR Am J Roentgenol* **193**, 1272-1281 (2009).

151. Massoumzadeh, P., Don, S., Hildebolt, C.F., Bae, K.T. & Whiting, B.R. Validation of CT dose-reduction simulation. *Med Phys* **36**, 174-189 (2009).

152. CT Accreditation Program Requirements. (American College of Radiology, Reston, VA, 2011).

153. Boone, J.M. Determination of the presampled MTF in computed tomography. *Med Phys* **28**, 356-360 (2001).

154. Siewerdsen, J.H., Cunningham, I.A. & Jaffray, D.A. A framework for noise-power spectrum analysis of multidimensional images. *Med Phys* **29**, 2655-2671 (2002).

155. Brown, M., *et al.* The Use of a Simple Contrast to Noise Ratio (CNR) Metric to Predict Low Contrast Resolution Performance in CT. in *American Association of Physics in Medicine annual meeting* (2009).

156. Howell, J.M., *et al.* Clinical policy: Critical issues in the evaluation and management of emergency department patients with suspected appendicitis. *Ann Emerg Med* **55**, 71-116.

157. Hernanz-Schulman, M. CT and US in the diagnosis of appendicitis: an argument for CT. *Radiology* **255**, 3-7.

158. Jo, Y.H., *et al.* The accuracy of emergency medicine and surgical residents in the diagnosis of acute appendicitis. *Am J Emerg Med* **28**, 766-770.

159. Brown, M.S., *et al.* An architecture for computer-aided detection and radiologic measurement of lung nodules in clinical trials. *Cancer Inform* **4**, 25-31 (2007).

160. Metz, C.E. ROC analysis in medical imaging: a tutorial review of the literature. *Radiol Phys Technol* **1**, 2-12 (2008).

161. Wagner, R.F., Beiden, S.V., Campbell, G., Metz, C.E. & Sacks, W.M. Assessment of medical imaging and computer-assist systems: lessons from recent experience. *Acad Radiol* **9**, 1264-1277 (2002).

162. Hillis, S.L., Berbaum, K.S. & Metz, C.E. Recent developments in the Dorfman-Berbaum-Metz procedure for multireader ROC study analysis. *Acad Radiol* **15**, 647-661 (2008).

163. Metz, C.E. ROC methodology in radiologic imaging. *Invest Radiol* **21**, 720-733 (1986).

164. Wagner, R.F., Metz, C.E. & Campbell, G. Assessment of medical imaging systems and computer aids: a tutorial review. *Acad Radiol* **14**, 723-748 (2007).

165. Metz, C.E. Some practical issues of experimental design and data analysis in radiological ROC studies. *Invest Radiol* **24**, 234-245 (1989).

166. ACR. CT Accreditation Program Requirements.

167. Turner, A.C., *et al.* The feasibility of patient size-corrected, scanner-independent organ dose estimates for abdominal CT exams. *Med Phys* **38**, 820-829 (2011).

168. McCollough, C.H., Bruesewitz, M.R. & Kofler, J.M., Jr. CT dose reduction and dose management tools: overview of available options. *Radiographics* **26**, 503-512 (2006).

169. Roe, C.A. & Metz, C.E. Variance-component modeling in the analysis of receiver operating characteristic index estimates. *Acad Radiol* **4**, 587-600 (1997).

170. Duan, X., *et al.* Dose reduction to anterior surfaces with organ-based tube-current modulation: evaluation of performance in a phantom study. *AJR Am J Roentgenol* **197**, 689-695 (2011).

171. Zhang D & McNitt-Gray, M. The Reduction of Radiation Dose to Thyroid When Using Dynamic Collimation during Thoracic CT Exams. in *Radiological Society of North America (RSNA) annual meeting* (Chicago, 2011).